Quantifying collateral flow pathways in the brain



Flora Kennedy McConnell

St John's College

University of Oxford

A thesis submitted for the degree of

Doctor of Philosophy

Trinity Term 2017

Acknowledgements

This thesis would not have been possible without the excellent advice and support of my supervisors Dr Stephen Payne, Dr Michael Chappell, and Dr Thomas Okell: to each, I owe a great debt of thanks.

I am sincerely grateful for my formal sources of support. For example, I received funding from the RCUK Digital Economy Programme via the CDT in Healthcare Innovation. Also, throughout this DPhil., St John's College has provided me with a home, a community and many opportunities that have allowed me to grow. Furthermore, the outstanding care that I have received from the Oxford Adult Cystic Fibrosis Centre has allowed me to stay well, and continue my DPhil. whilst working through the various health challenges with which I have been presented.

I have been very lucky in Oxford to find friends who have expanded my outlook and my interests. I am grateful to know people who support me, challenge me, focus me (and distract me): Emma Claussen, Caitlin Clunie-O'Connor, Jon Daly, Wahbi El-Bouri, Katherine Fender, Chris Harrison, Nick Higgins, Joao Jorge, Jamil Mokhtarudin, Chang Sub Park, George Qian, Thais Roque, and Eden Tanner.

Finally, I would certainly not have made it this far without the immeasurable support of my family. To my siblings, siblings-in-law, and niece: Calum and Claire, and Isla, Andrew, and Esme, thank you for being role models, supporters and friends. And, to my parents Pat McConnell and Jack (Andrew) Kennedy, thanks, for your ceaseless love and support, and for feeding, housing and enduring me in the final months of this thesis. I am immensely grateful to you all.

Abstract

Ischaemic stroke is a major cause of death and disability worldwide. Cerebral autoregulation, which can be impaired during acute stroke, and collateral flow to brain tissue through the circle of Willis, both play a role in preventing tissue infarction. The configuration of the arterial circle varies between individuals. Thus, personalised modelling of the cerebral arterial network, to determine the potential for collateral flow, can be of significant value in the clinical context of stroke.

The interaction between autoregulation and collateral flow remains poorly understood. In this study, steady-state physiological models of the cerebral arterial network, including several common variants of the circle of Willis, were coupled to a spatially variable mathematical representation of cerebral autoregulation. The resulting model was used to simulate various arterial occlusions, as well as bilateral and unilateral impairment of autoregulation, in each structural variant. The work identified few circle of Willis variants that present either particularly high-risk or particularly low-risk of cerebral ischaemia. Instead it was found that most variants are dependent upon the bilateral function of autoregulation to facilitate collateral flow and preserve cerebral blood flows. When autoregulation was impaired unilaterally, downstream of an occlusion, blood flows in the contralateral hemisphere were preserved at the expense of the ipsilateral tissue at risk.

Arterial network models have in the past been personalised using structural, rather than functional, angiography measurements. This thesis presents a novel model-based method for absolute blood volume flow rate quantification in short arterial segments using dynamic magnetic resonance angiography data. The work also investigated the additional information that can be obtained from such functional angiography. The flow quantification technique was found to accurately estimate flows in shorter arterial segments than an existing technique. However, improvements to noise performance, and strategies for rejection of contaminating signals from overlapping vessels within the imaging plane, are required before the technique can be applied to personalised cerebral arterial network modelling.

Contents

Related publications and presentations **vii**

List of Abbreviations **viii**

1 Introduction **1**
1.1 Motivation . . . 1
1.2 The blood supply to the brain . . . 2
1.3 Recanalisation therapies . . . 2
1.4 Treatment of arterial stenosis . . . 3
1.5 Mathematical modelling . . . 4
1.6 Thesis outline . . . 5

2 Literature review **7**
2.1 Physiology . . . 7
2.1.1 The cerebral blood supply . . . 9
2.1.2 Disorders of the cerebral blood supply . . . 10
2.1.3 Collateral circulation . . . 12
2.1.4 Cerebral autoregulation . . . 15
2.2 Models of the cerebral vasculature . . . 18
2.3 Cerebrovascular angiography . . . 22
2.3.1 Transcranial doppler ultrasound . . . 22
2.3.2 X-ray digital subtraction angiography . . . 23
2.3.3 Computed tomography angiography . . . 24
2.3.4 Contrast enhanced MRA . . . 24
2.3.5 Time-of-flight MRA . . . 24
2.3.6 Phase contrast MRA . . . 25
2.3.7 Arterial spin labelling MRA . . . 25
2.4 Arterial spin labelling . . . 26
2.4.1 Methods of creating contrast . . . 27
2.4.2 Vessel-selective labelling . . . 29
2.4.3 Kinetic modelling of ASL in perfusion imaging . . . 31
2.4.4 Modelling of ASL in angiography . . . 33
2.5 Summary . . . 37

3 Network Model **39**
3.1 Introduction . . . 39
3.2 Model equations . . . 40
3.2.1 The cerebral arterial network . . . 40
3.2.2 The cerebral territories . . . 41
3.3 Results . . . 52
3.3.1 Healthy flows . . . 52
3.3.2 Arterial occlusions . . . 54
3.4 Discussion . . . 59
3.4.1 Healthy flows . . . 59
3.4.2 Arterial occlusions . . . 63
3.4.3 Analysis of the model . . . 67
3.5 Summary . . . 71

4 ASL angiography models **72**
4.1 Theory . . . 74
4.1.1 Pulsed arterial spin labelling . . . 76
4.1.2 Pseudo-continuous arterial spin labelling . . . 80
4.2 Materials and methods . . . 84
4.2.1 Data . . . 84
4.3 Parameter estimation . . . 85
4.3.1 Calibration factor . . . 87
4.3.2 Vessel regions . . . 87
4.3.3 Constraints . . . 88
4.3.4 Curve fitting . . . 90
4.3.5 Experiments performed . . . 94
4.4 Results . . . 96
4.4.1 Phantom data . . . 96
4.4.2 Human data testing . . . 102
4.5 Discussion . . . 110
4.5.1 Flow phantom validation . . . 111
4.5.2 Human results . . . 113
4.6 Summary . . . 119

5 Tracer Model **121**
5.1 Introduction . . . 121
5.2 Model equations . . . 122
5.2.1 Junctions and bifurcations . . . 124
5.2.2 The final node in each vessel . . . 125
5.2.3 ASL labelling conditions . . . 125

5.2.4 Decay . . . 128
5.3 Materials and methods . . . 128
5.4 Results . . . 129
5.5 Discussion . . . 140
5.5.1 The tracer model . . . 140
5.5.2 Circle of Willis variant results . . . 141
5.6 Summary . . . 147

6 Conclusions and future work **149**
6.1 Conclusions . . . 149
6.1.1 Network modelling . . . 149
6.1.2 Flow quantification . . . 151
6.1.3 Model personalisation . . . 152
6.2 Future work . . . 153
6.2.1 Measurements of arterial blood flows . . . 153
6.2.2 Model personalisation . . . 154
6.3 Summary . . . 156

Appendices

A **159**
A.1 Blood flow rates through the circle of Willis from network simulations 159

References **173**

Related publications and presentations

2017 . F. Kennedy McConnell, S. Payne, "Autoregulating Cerebral Tissue Selfishly Exploits Collateral Flow Routes Through the Circle of Willis", *Acta Neurochirurgica Supplement, in press*, [**2016 Conference poster** and **invited journal article**].

2017 . F. Kennedy McConnell, S. Payne, "The Dual Role of Cerebral Autoregulation and Collateral Flow in the Circle of Willis after Major Vessel Occlusion", *IEEE Transactions on Biomedical Engineering*, vol. 64, no. 8, pp. 1793-1802 [**Journal article**].

2015 . FA. Kennedy McConnell, SJ. Payne, MA. Chappell, TW. Okell, Filed: Nov. 2015. Estimation of Blood Flow Rates. U.S. Patent Publication no: $2016-0128601$. Application no: 14/938250. [**Patent Pending**].

2015 . F. Kennedy McConnell, T. Okell, M. Chappell, S. Payne, "Quantification of flow rates in short vessel segments from arterial spin labeling dynamic angiography", *ISMRM* 23^{rd} *Annual Meeting & Exhibition, Toronto, Canada.* [**Short invited presentation** to the ISMRM Study Group on MR Flow and Motion Quantification, and **poster**].

List of Abbreviations

1-D, 2-D, 3-D One-, two-, or three-dimensional, referring in this thesis to spatial dimensions in arterial network models and in angiography images.

A1 . . . . . Proximal segment of an anterior cerebral artery.

A2 . . . . . Segment of an anterior cerebral artery immediately distal to the junction with the anterior communicating artery.

ABP . . . . . Arterial blood pressure.

ACA . . . . . Anterior cerebral artery.

ACoA . . . . . Anterior communicating artery.

ASITN . . . . American Society of Intervention and Therapeutic Neuroradiology.

ASL . . . . . Arterial spin labelling.

AVM . . . . . Arteriovenous malformation.

BA . . . . . Basilar artery.

CASL . . . . . Continuous arterial spin labelling.

CBF . . . . . Cerebral blood flow.

CE . . . . . Contrast enhanced.

CTA . . . . . Computed tomography angiography.

DSA . . . . . Digital subtraction angiography.

I1 . . . . . Proximal segment of an internal carotid artery.

I2 . . . . . Distal segment of an internal carotid artery.

ICA . . . . . Internal carotid artery.

LACA . . . . . Left anterior cerebral artery.

LICA . . . . . Left internal carotid artery.

LMCA . . . . Left middle cerebral artery.

LPCA . . . . . Left posterior cerebral artery.

LPCoA . . . . Left posterior communicating artery.

LVA . . . . . Left vertebral artery.

MCA . . . . . Middle cerebral artery.

MRA . . . . . Magnetic resonance angiography.

MRI . . . . . Magnetic resonance imaging.

P1 . . . . . Proximal segment of a posterior cerebral artery.

P2 . . . . . Segment of a posterior cerebral artery immediately distal to the junction with the posterior communicating artery.

PASL . . . . . Pulsed arterial spin labelling.

PCA . . . . . Posterior communicating artery.

PCASL . . . . Pseudo-continuous arterial spin labelling.

PCoA . . . . . Posterior communicating artery.

PID . . . . . Proportional-integral-derivative.

RACA . . . . . Right anterior cerebral artery.

RF . . . . . Radio frequency.

RICA . . . . . Right internal carotid artery.

RMCA . . . . Right middle cerebral artery.

ROI . . . . . Region of interest.

RPCA . . . . . Right posterior cerebral artery.

RPCoA . . . . Right posterior communicating artery.

RVA . . . . . Right vertebral artery.

SENTIS . . . . Safety and Efficacy of NeuroFlo Technology in Ischaemic Stroke.

SNR . . . . . Signal to noise ratio.

TCD . . . . . Transcranial doppler ultrasound.

TIA . . . . . Transient ischaemic attack.

TOF . . . . . Time-of-flight.

VA . . . . . Vertebral artery.

VE . . . . . Vessel-encoded.

VEPCASL . . Vessel-encoded pseudo-continuous arterial spin labelling.

1 Introduction

1.1 Motivation

Brain tissue has very high metabolic demands [1]. As a result, reductions in blood supply can rapidly lead to impaired tissue function (ischaemia), and cell death (infarction). Stroke is a disease of the blood supply to the brain. It is defined as 'rapidly developing clinical signs of focal (or global) disturbance of cerebral function, with symptoms lasting 24 hours or longer, or leading to death, with no apparent cause other than of vascular origin' [2]. Around 85% of all strokes are classed as ischaemic [2], meaning that brain tissue is deprived of blood, typically due to narrowing or blockage of an artery of the cerebral blood supply. The remaining 15% of strokes are haemorrhagic [2], in which blood vessel rupture leads to bleeding in or around the brain.

In the UK the incidence of stroke is 2-3/1000 per year [2]. It is the fourth most common cause of death, leading to more than 40,000 deaths per year [3], and it is the leading cause of adult disability, with two-thirds of stroke survivors leaving hospital with some functional impairment [3]. Of the over 1.2 million stroke survivors in the UK [3], around 300,000 live with significant disability [2]. It is estimated that the total annual societal cost of stroke in the UK is £9 *billion* [2],

[3], a figure which takes into account the costs of acute and ongoing medical care, social and informal care, and the cost of lost productivity and disability.

1.2 The blood supply to the brain

The brain's arterial network can be very robust to disturbances in cerebral blood supply. Interconnections exist between the large arteries at the base of the brain, and between smaller downstream arteries [4]. These arterial interconnections are known as 'collateral' arteries as they provide alternative flow routes through which blood can be supplied to tissue deprived of blood by arterial stenosis (narrowing) or occlusion (blockage). In addition to these potentially protective vessels, homeostatic mechanisms act at the level of the small arteries and arterioles to maintain the cerebral environment. These mechanisms maintain cerebral blood flow, oxygen supply and concentrations of metabolites in response to changes in arterial blood pressure and the metabolic demands of cerebral tissue [5], [6]. This control is enacted by changing the resistance of small arteries and arterioles through constriction and dilation of these vessels. These mechanisms are known collectively as 'cerebral autoregulation'.

The combination of collateral flow routes and cerebral autoregulation can provide significant protection during disturbance of the arterial blood supply to the brain [5], [7], [8]. However, as will be discussed in Chapter 2, there is considerable variability between individuals in the existence, structure and function of collateral vessels [9]–[11]. Furthermore, the function of cerebral autoregulation can be impaired in a spatially heterogeneous fashion in cerebral arterial stenosis, and in stroke [12].

1.3 Recanalisation therapies

One of the primary aims of acute ischaemic stroke care is the rapid restoration of blood flow, or 'recanalisation'. This is done in an attempt to salvage ischaemic tissue which has not yet progressed to infarction. The region of potentially salvageable

tissue around the infarct core is known as the ischaemic penumbra. It is thought that both the size of the infarct core [8], and the time span over which the ischaemic penumbra remains viable [13], are related to the ability of the cerebral arterial network to provide collateral blood flow.

There are currently two treatments that can be used to restore blood flow through an occluded artery. These are intravenous or intra-arterial thrombolysis, and trans-arterial mechanical clot removal. Thrombolytic, or so called 'clot-busting', agents act to break down a blood clot in order to reopen the artery it occludes [2]. Mechanical clot removal involves the intra-arterial delivery of a clot retrieval device to collect and remove the material occluding an artery. Both of these therapies are of greater benefit to the patient when administered early after stroke onset [14]. The window of opportunity for the use of thrombolytic agents is just 4.5 hours after stroke onset [2]. After this time window has passed, the potential benefit from the therapy is so reduced that the treatment is more likely to harm the patient by causing haemorrhage [2]. Trials of mechanical clot removal devices have generally aimed at recanalisation within 6 hours of stroke onset [2]. The existence of these therapeutic windows reflects the fact that the ischaemic penumbra is short lived. Many proposed 'neuroprotective' treatments have aimed to extend the therapeutic window of opportunity by slowing the progression of ischaemic tissue damage. One of these, therapeutic hypothermia, has shown promise in computational studies [15], animal models [16], and small trials in humans [2], [17], but is not currently used clinically in the context of stroke.

1.4 Treatment of arterial stenosis

Arterial stenoses can also cause neurological symptoms, such as a stroke or transient ischaemic attack (TIA). TIA is often thought of as a mini-stroke, in which the signs of disturbance of cerebral function do not persist beyond 24 hours. TIA is a risk factor for subsequent stroke [2], as TIA patients have an average risk of suffering a stroke within the first seven days after the TIA of around 10%, with the risk

reducing after the first seven days have passed.

Surgical procedures aimed at widening the affected arterial lumen, such as carotid endarterectomy (open surgical correction of stenosis through removal of fatty plaque material from the arterial wall), and trans-arterial angioplasty (balloon widening) and stenting (widening and reinforcement through the placement of a permanent wire mesh structure) [18], have been shown to significantly reduce the risk of stroke in patients with symptomatic carotid artery stenosis [2]. The most commonly performed procedure, carotid endarterectomy, has been shown to be very effective at preventing stroke [2]. However, the procedure involves clamping one of the major arteries that carries blood to the brain [18]. In doing this, surgeons rely on collateral blood flow from the remaining arteries to supply downstream cerebral tissue during the procedure. In patients with insufficient collateral routes, a shunt can be placed to bypass the clamped vessel sections in order to preserve near normal blood supply to the brain [18].

1.5 Mathematical modelling

Mathematical modelling of the blood supply to the brain presents an opportunity to examine the performance of different cerebral arterial networks under various conditions of arterial stenoses and occlusions. Furthermore, the ability to rapidly personalise cerebral arterial network models, such that they accurately represent blood delivery to the brain of an individual subject, can allow observation of the consequences of a variety of disease pathologies in that particular patient. Accurate modelling simulations of this kind can be of great clinical value in the contexts of stroke and arterial stenosis.

In stroke, the use of personalised arterial network models that account for collateral blood flow, and the interaction of cerebral autoregulation with this flow, may help to identify good candidates for thrombolysis and mechanical clot removal, and to adapt the therapeutic window on a patient-specific basis. Just as importantly,

such models could help to identify poor candidates for recanalisation therapies. In these patients, the presence of an unfavourable cerebral arterial network may negate the possibility of recanalisation [13] and, instead, leave them vulnerable to the potentially deadly side effect of such treatment, namely haemorrhage within the infarct core [19].

In cases of stenoses of the arteries supplying the brain, personalised models may permit identification of patients most at risk of subsequent stroke. They may also help to identify those at risk of very severe stroke, based on the lack of available collateral blood flow routes to brain tissue within the vascular territory of the stenosed artery. These patients could then be prioritised as those who would most benefit from therapies aimed at widening the affected arterial lumen, such as carotid endarterectomy. Personalised arterial network models could also be used to identify patients most in need of additional cerebral blood supply via a shunt during this surgical procedure.

1.6 Thesis outline

This thesis is concerned with personalised mathematical modelling of the cerebral arterial network. The work is presented in the following five chapters, which are briefly summarised below.

Chapter 2 introduces the cerebral arterial network, including arteries that provide collateral flow routes, and cerebral autoregulation, before briefly reviewing published literature which has considered these potentially protective mechanisms in the context of stroke. The chapter then reviews the body of literature relating to existing mathematical models of the cerebral arterial network. This section considers the features of the network included within the models, and the methods that some authors have used to personalise these models. The chapter also examines the types of imaging data commonly used to assess the structure and functionality of the arteries of interest. Finally Chapter 2 describes arterial spin labelling magnetic

resonance angiography, a non-toxic, non-invasive imaging modality which has been used to quantify blood flow rates in the cerebral arteries.

Chapter 3 presents the development of a steady state mathematical model of the arterial network supplying the brain, which includes the large collateral flow routes, and is coupled to a steady state model of cerebral autoregulation. The model was used to consider the interaction of collateral flow and autoregulation in a range of structural variants of the cerebral arterial network, under conditions of arterial occlusion.

Chapter 4 presents the development of a model-based method for blood volume flow rate quantification from time-resolved magnetic resonance angiography images. The proposed quantification is validated against images of a flow phantom, and tested on images of the cerebral blood supply of healthy volunteers.

Chapter 5 considers the inclusion of information from imaging data into a mathematical model of the cerebral arterial network, by modelling the transport of an angiography imaging tracer through a subset of the networks presented in Chapter 3. The chapter also considers the extent to which structural information about an individual's arterial network can be obtained from cerebral angiography data like that analysed in Chapter 4.

Chapter 6 summarises the work presented in this thesis and the results that were obtained, then discusses the techniques used, and the conclusions that can be drawn from the work. Finally, this chapter provides suggestions for future work which could improve some of the methods developed in the preceding chapters, and build upon this work. These suggestions of future work will help to work towards the eventual goal of the use of mathematical models of the cerebral arterial network, that can be rapidly and accurately personalised, in clinical decision making.

2
Literature review

This chapter presents a description of the cerebral arterial network, including details of features of the network, i.e. collateral flow and cerebral autoregulation, which afford protection against ischaemia. The chapter then goes on to review the existing body of literature detailing mathematical models of the human cerebral arterial tree, and the progress that has been made towards personalising such models to represent the cerebral blood supply of individual patients. The chapter then discusses the imaging modalities that can be used to obtain structural and functional information about blood flow in arteries. Finally, the chapter examines the magnetic resonance angiography technique of arterial spin labelling, which presents an opportunity for fast, non-invasive, non-toxic, repeatable imaging of blood flow in the cerebral arteries, and which may have the potential to provide both structural and functional information about the circle of Willis from a single acquisition.

2.1 Physiology

Blood continuously circulates around the body carrying oxygen and nutrients to its cells and removing waste products. This transport takes place in the arterial and venous systems. Blood is initially carried away from the heart in elastic arteries, which are the aorta and the branches of the aortic arch [20]. These are able to expand

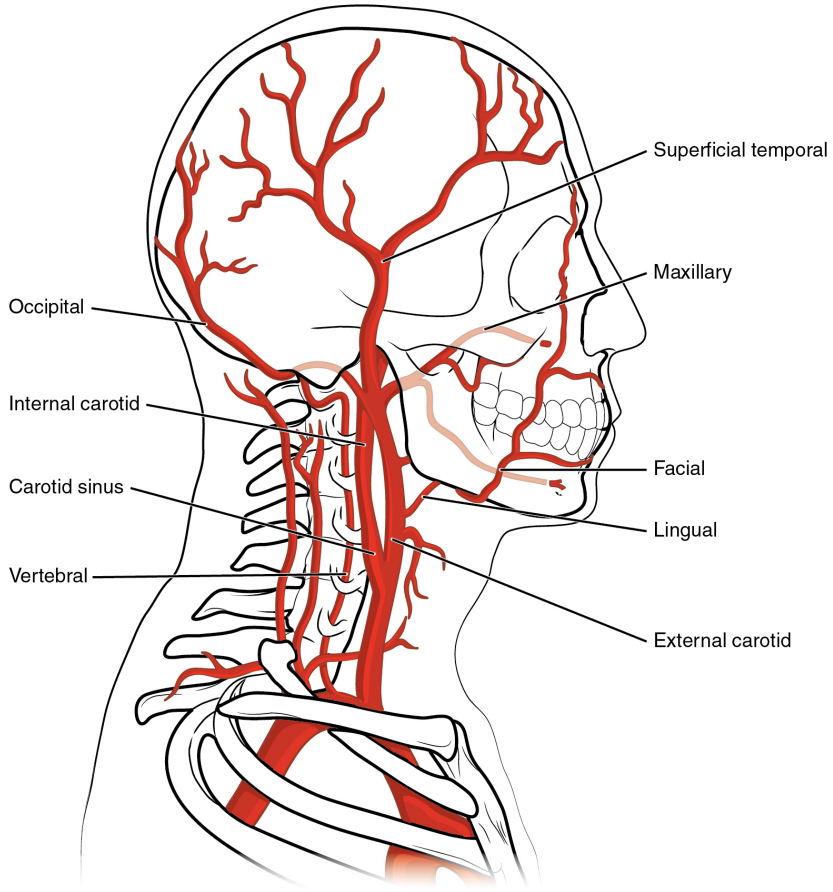


Figure 2.1: Illustration of the arteries supplying blood to the head. Reproduced without changes from OpenStax College under license http://creativecommons.org/licenses/by/3.0

radially and have elastic walls to constrain the pulse pressure wave generated by the heart muscle. Large and small muscular arteries transport blood to organs and their subsections, then smaller arterioles with less muscular walls distribute blood throughout tissue regions within organs. From there, very thin-walled capillaries allow molecular exchange to take place between blood and tissue. Blood leaving the capillaries (excluding those involved in gas exchange in the lungs) contains reduced levels of oxygen and glucose, and higher levels of metabolic waste products such as carbon dioxide. This blood collects in the venules, then the larger veins, which return it to the heart.

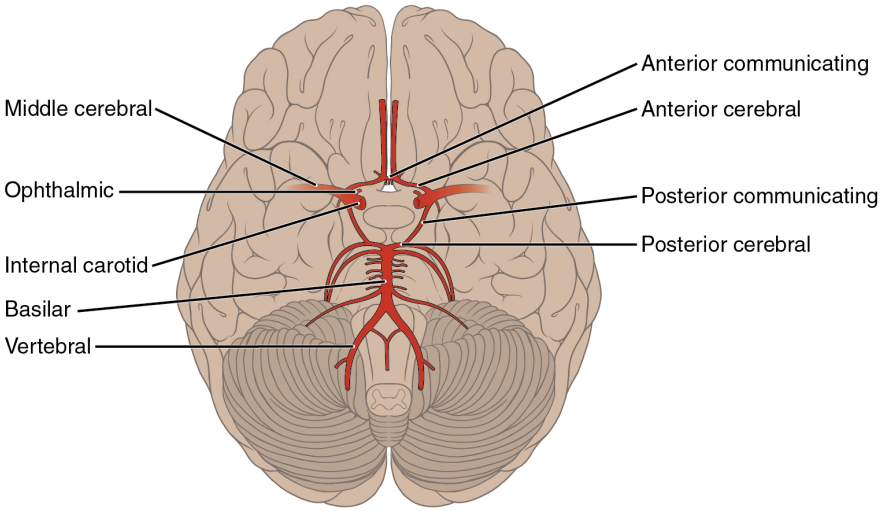


Figure 2.2: Illustration of the arteries of the circle of Willis. Reproduced without changes from OpenStax College under license http://creativecommons.org/licenses/by/3.0

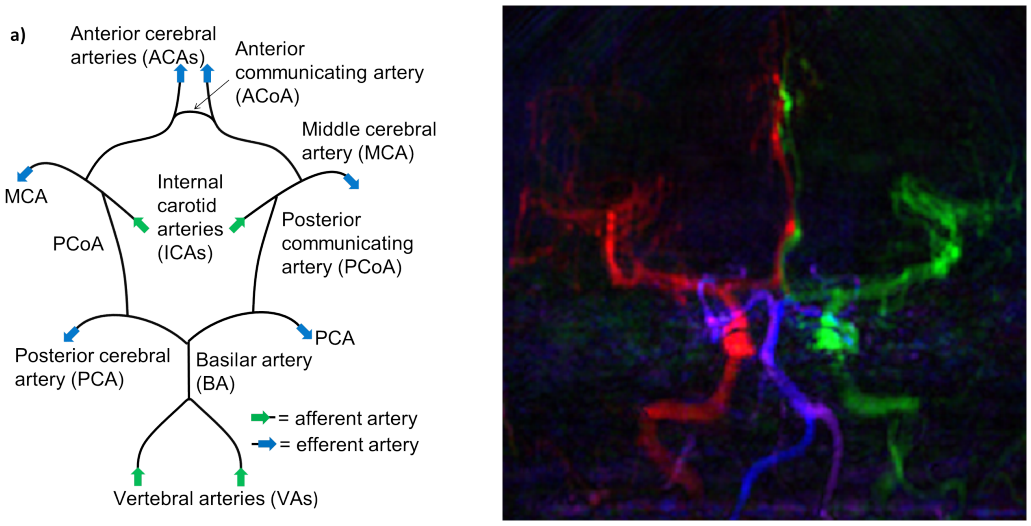
2.1.1 The cerebral blood supply

Figure 2.1 shows the arteries that carry blood to the head. These are the paired vertebral arteries and common carotid arteries. At approximately the level of the 3rdcervical vertebra, each common carotid artery bifurcates into an external carotid artery, which largely supplies the external structures of the head, and an internal carotid artery, which enters the cranial cavity to supply the brain (Figure 2.2). The vertebral arteries ascend the neck to above the 1stcervical vertebra, where they unite to form the basilar artery (Figure 2.2) [21].

Blood is supplied to the brain via the circle of Willis (Figures 2.2 and 2.3a), an arterial ring at the base of the brain. Oxygenated blood arrives in the circle of Willis through the four inflow (afferent) arteries. Anteriorly, these are the left and right internal carotid arteries (ICAs) and posteriorly, the left and right vertebral arteries (VAs), which anastomose to form the basilar artery (BA). From the circle of Willis, blood is distributed to brain tissue via the outflow (efferent) arteries: the left and right anterior, middle and posterior cerebral arteries (ACAs, MCAs and PCAs respectively). The anterior and posterior parts of the circle of Willis are connected by the posterior communicating arteries (PCoAs), and the ring structure

is completed by the anterior communicating artery (ACoA) which connects the left and right sides [4].

Throughout this thesis, the arterial segments that make up the ring of the circle of Willis, i.e. the distal segments of the ICAs, the proximal segments of the ACAs and PCAs, the PCoAs, and the ACoA, will be collectively referred to as the 'circulus' arteries. Although not shown in the schematic (Figure 2.3a), most of the afferent, efferent and circulus arteries of the circle of Willis give rise to further small arteries along their lengths that supply structures deep within the brain. Along the VAs and BA, these small arteries also supply blood to structures in the neck and to low-lying structures in the head [4].



(a) Schematic **(b)** Cerebral angiogram

Figure 2.3: (a) Simplified schematic of the arteries that make up the circle of Willis; and (b) Example vessel-encoded arterial spin labelling angiography image of the circle of Willis, generated using the data collected by [22].

2.1.2 Disorders of the cerebral blood supply

Continuity of blood supply is essential for tissue health, particularly brain tissue which has very limited stores of glucose [1], and very high metabolic demands: despite only constituting around 2% of normal body mass, the brain receives around 15% of the total cardiac output [23]. Thus, reductions in cerebral blood flow, rapidly

lead to depletion of energy stores and to tissue damage and death. In such cases, the health of cerebral tissue is heavily dependent on the severity and duration of ischaemia. Maintenance of the blood supply to the brain is, therefore, vital in order to sustain normal neurological functioning. Vascular damage that leads to neurological dysfunction, or stroke, can be of two main types, ischaemic and haemorrhagic.

Ischaemic stroke

Ischaemic strokes account for 85% of all strokes. They are generally caused by stenosis or occlusion of an artery of the cerebral vasculature, which leaves downstream tissue vulnerable to deprivation of blood supply. When exposed to ischaemic conditions, brain tissue can rapidly die due to lack of oxygen, or remain alive in a hypoperfused state for some time [2].

Ischaemic stroke may have any of a number of causes. The most common cause, and most relevant to the context of this study, is atherosclerosis of the large arteries. Atherosclerosis is a disease causing the formation of thick, fibrous plaques in arterial walls [24]. The surface of an atherosclerotic plaque may facilitate the formation of a blood clot (thrombus), which could occlude the artery locally, or embolise and occlude a distal vessel, causing stroke. Alternatively, a stenotic plaque may simply grow so large that it prevents sufficient blood flow through the vessel [24].

Haemorrhagic stroke

The remaining 15% of strokes are haemorrhagic strokes, caused by blood vessel rupture which leads to bleeding in or around the brain and subsequent compression of brain tissue. Typically such ruptures occur due to abnormalities of the cerebral vasculature. For example, a cerebral aneurysm is an out-pouching (saccular aneurysm) from, or dilation (fusiform aneurysm) of, an artery caused by weakness in the vessel wall [25]. Saccular aneurysms tend to form at branching points in the circle of Willis and proximal arteries [24]. Rupture of a cerebral aneurysm is one cause of haemorrhage. An arteriovenous malformation (AVM) is a collection of enlarged blood vessels that creates an abnormal connection between one or

more feeding arteries and draining veins [24]. An AVM can divert blood from the capillary networks of nearby regions of brain tissue and thereby cause tissue ischaemia, or rupture of an AVM results in intracerebral haemorrhage. It is also the case that some haemorrhagic strokes develop in areas of ischaemia; a process known as haemorrhagic transformation [26].

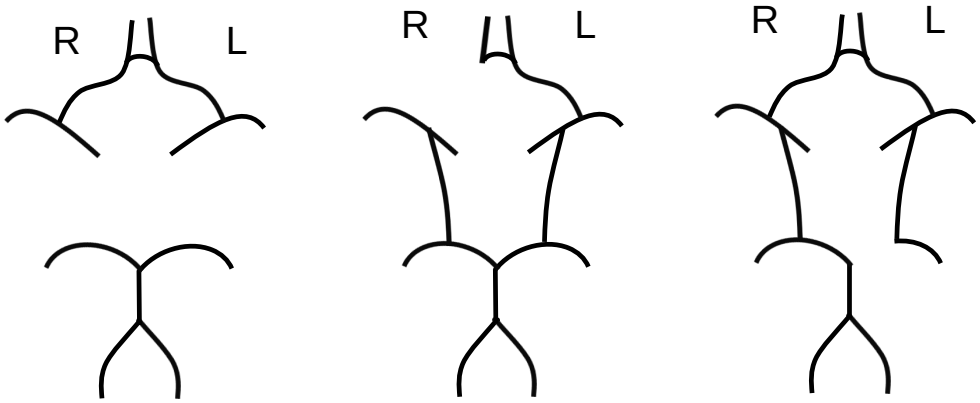
2.1.3 Collateral circulation

Primary collateral flow

Figure 2.3a shows the 'textbook' configuration of the circle of Willis. However, between individuals there is considerable variability in the structure of the circle. A study by Alpers *et al.* [9] examined 350 human brains with no evidence of vascular pathology, other than atherosclerosis, and found that only 52% possessed the complete circle structure. Another investigation, by Riggs *et al.* [10], examined the brains of 994 patients who had presented with signs of neurological dysfunction, and found that only 19% of the patient group had a complete circle of Willis.

Particularly common structural variations include: absence of one, or both, of the PCoAs (Figure 2.4a); absence of the proximal segment of one ACA (the ACAA1, shown in Figure 2.4b); and absence of the proximal segment of one PCA (the PCAP1, shown in Figure 2.4c). Measurement studies suggest that these structural variants occur in 5–15% of people [9]–[11].

Through the potentially redundant communicating arteries (Figure 2.3a), the circle of Willis provides the brain with primary collateral (i.e. alternative) flow pathways. In the event of vessel occlusion, the severity of downstream tissue ischaemia is affected both by the degree of occlusion and by the extent to which the collateral circulation can compensate for the deficit in cerebral blood flow (CBF) [27]. The collateral flow pathways potentially enable blood to bypass a vessel blockage and continue to supply hypoperfused tissue [27].



(a) Absent right and left PCoAs

(b) Absent right proximal ACA

(c) Absent left proximal PCA

Figure 2.4: Three possible variants of the circle of Willis.

Secondary collateral flow

In addition to the primary collateral flow routes provided by the circle of Willis, there exist more indirect secondary collateral flow routes which can bolster CBF to ischaemic tissue. Blood from branches of the external carotid artery (Figure 2.1), such as the facial, maxillary, middle meningeal and occipital arteries, can be redirected to intracranial vessels such as the ophthalmic artery via anastamoses [28]. Furthermore, intracranial arteries which do not normally feed the tissue territory at risk can also provide secondary collateral flow. Examples include the ophthalmic artery and leptomeningeal vessels [27]. These routes are more indirect than the arteries of the circle of Willis and develop over time, making them potentially less valuable in episodes of acute ischaemia [28].

Benefits of collateral flow

Due to anatomical variations in the structure of the circle of Willis, the extent to which the collateral circulation can stabilise CBF in the event of a disruption to the supply varies considerably between individuals [27]. The presence of good collateral flow routes in the cerebral circulation is likely to prove advantageous in the event of steno-occlusive cerebrovascular disease. This has been seen in the results of Henderson *et al.* [7] who studied angiographically identified collaterals in patients

with severe carotid artery stenosis. They found that patients without collaterals supplying the tissue territories downstream of ICA stenosis have a higher risk of stroke and TIA than patients with collaterals. Henderson *et al.* [7] concluded that angiographic assessment of collaterals may be a useful tool for identifying those patients with carotid artery stenosis who are at higher risk of stroke.

In 2011, Bang *et al.* [13] studied 222 patients with acute ischaemia in the MCA territory who had undergone conventional X-ray digital subtraction angiography (DSA) in advance of endovascular therapy. The therapy consisted of either interarterial thrombolysis or mechanical clot removal. The collateral grading scale of the American Society of Intervention and Therapeutic Neuroradiology (ASITN)[29] was used. Patients with ASITN scores of 0-1 had 'poor' collaterals, scores of 2-3 were described as 'good' collaterals and a score of 4 indicated 'excellent' collaterals. The study found that complete recanalisation, defined as recovery of perfusion, was achieved in a higher proportion of patients with collaterals graded as excellent prior to treatment than in those with good collaterals, who in turn had a higher rate of recanalisation than those with poor collaterals. In the same patient group, Bang *et al.* [19] observed haemorrhagic transformation in 46.4% of patients, finding that it occurred most frequently in patients with poor collaterals in whom recanalisation was achieved. It is possible that ischaemic tissue damage had occurred more rapidly in these patients due to reduced collateral supply to the affected tissue, leaving them with a greater risk of haemorrhagic transformation after recanalisation therapy [29].

These studies were in agreement with the results of Angermaier *et al.* [8] who used computed tomography angiography (CTA) to assess the degree of pre-treatment collateral flow in 25 acute stroke patients who underwent interarterial thrombolysis within 6 hours of symptom onset. They found that a high pre-treatment CTA collateral score (indicating good collateral blood supply in the region of affected tissue) was associated with a smaller infarct volume 5 days after treatment.

A 2013 study by Schellinger *et al.* [30] considered the circle of Willis in patients in the SENTIS (Safety and Efficacy of NeuroFlo Technology in Ischaemic Stroke) trial, on whom vascular imaging was performed at baseline. The NeuroFlo procedure aims to enhance cerebral perfusion during acute ischaemic stroke through short-term (45 minutes), partial occlusion of the abdominal aorta, achieved using an intra-arterial balloon catheter, in order to augment the cerebral blood supply [31]. The process relies on cerebral collateral flow pathways to distribute some of the resulting increase in CBF to regions of ischaemic tissue downstream of an arterial occlusion. The study by Schellinger *et al.* [30] found that a 'favourable vascular profile', defined as the combination of (1) a complete circle of Willis, including visualised communicating arteries, and (2) mean arterial blood pressure continuously $> 65\ mmHg$ for the first 12 hours after the NeuroFlo procedure, independently predicted good outcome in acute stroke patients. The results of these studies highlight the potential use of angiographic assessment of collateral circulation as a tool for patient selection, and outcome prediction, for endovascular therapy.

2.1.4 Cerebral autoregulation

The cerebral vasculature is highly responsive and, when healthy, is able to meet the substantial metabolic demands of brain tissue in spite of continuous changes in tissue activity and in perfusion pressure (blood pressure minus intracranial pressure), for example due to the oscillations of pulse wave pressure and changes in posture. Cerebral autoregulation is an umbrella term describing a complex phenomenon resulting from several physiological mechanisms that maintain near-constant cerebral blood flow over wide ranges of perfusion pressure [5]. The combined protective effect of these mechanisms is enacted through dilation of resistance vessels, primarily the small arteries and arterioles, in response to perfusion pressure reduction, and through constriction of these vessels in response to raised perfusion pressure (Figure 2.5).

Equation 2.1 gives Poiseuille's law, which relates the pressure drop across an artery ΔP, to the arterial blood flow, Q, in terms of blood viscosity, μ, and the vessel's length, l, and radius r. Poiseuille's equation gives vessel resistance, R, as inversely proportional to the fourth power of radius, r, which means that large changes in flow, Q, can result from small changes in vessel radius and thus, very fine control of CBF is possible. Such changes in radius are brought about through alteration of arteriolar compliance, controlled by the level of activation of the smooth muscle cells in the vessel wall.

$$\frac{\Delta P}{Q} = \frac{8\mu l}{\pi r^4} = R \tag{2.1}$$

It is thought that cerebral autoregulatory control has three main drivers: a myogenic response, metabolic control and neurogenic control [32]. The 'myogenic response' describes the contraction of vascular smooth muscle cells in response to an increase in arterial blood pressure (ABP) and an accompanying increase in CBF, and relaxation in response to a reduction in ABP. Changes in CBF also affect cerebral metabolism. For example an increase in CBF, without a corresponding increase in demand for oxygen and glucose, will lead to a reduction in the concentration of metabolic products within brain tissue, such as carbon dioxide [6]. In order to match supply and demand, this decrease in CO_2 concentration will lead to vasoconstriction and subsequent CBF reduction. Similarly, where low CBF leads to raised concentrations of metabolic products, vasodilation acts to increase CBF. This 'metabolic control' is thought to be mediated through changes in the release rates of vasodilating metabolites [5]. Additionally, there is some evidence that sympathetic neural activity may be involved in the control of CBF, although this mechanism remains very poorly understood [5], [6], [32].

In modelling studies, the overall cerebral autoregulatory response is generally considered in two parts. The first of these is static autoregulation (Figure 2.5), which can be considered as the steady-state response to changes in ABP, acting over time scales longer than approximately 30 *seconds*. The second part of the autoregulatory

response is dynamic autoregulation, which rapidly (within $2 - 10$ *seconds*) acts to return CBF to its baseline value following a sudden change in ABP [6].

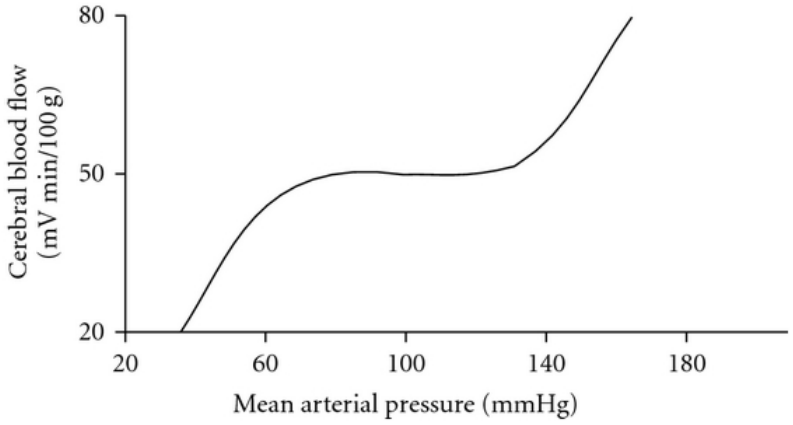


Figure 2.5: Static autoregulation curve showing variation of CBF with mean ABP. Figure reproduced without changes from [33] under license http://creativecommons.org/licenses/by/3.0

Autoregulation in cerebrovascular disease

Payne [5] collated information from a vast array of studies of cerebral autoregulation in physiological and pathophysiological conditions and concluded that autoregulation is impaired in a number of cerebrovascular diseases. In carotid artery stenosis, several studies have indicated that autoregulation can be impaired ipsilateral to the stenosed artery [34]–[37], with others showing that recanalisation procedures, such as carotid stenting and carotid endarterectomy performed on the stenosed artery, are able to restore the autoregulatory ability of the downstream vasculature [34], [38].

In stroke, a number of studies have found that autoregulation is impaired in both hemispheres, even in minor stroke [39]–[41]. Some studies conclude that impairment of autoregulation may occur to a greater extent in the ipsilateral hemisphere initially [12], and then worsen and spread to the contralateral hemisphere over a period of days [42]–[44]. It is possible that the pattern of impairment of the autoregulation response is dependent upon the vascular cause of the stroke, for example large-artery atherosclerosis or small-artery occlusion [12], [41].

Autoregulation and collateral flow

Cerebral autoregulation and collateral flow both potentially protect and maintain blood flow to cerebral tissue but the interaction between the two mechanisms is poorly understood. In 2003, Reinhard *et al.* [45] examined the relationship between different patterns of collateral flow and impairment of cerebral autoregulation in patients with carotid artery stenosis or occlusion. They found that, in patients with flow through the primary collateral routes alone, there was no statistically significant impairment of autoregulation ipsilateral to the stenosis or occlusion. In contrast, detected activation of secondary collateral flow routes, with or without flow through primary routes, was significantly associated with impaired autoregulation ipsilateral to the diseased artery. Furthermore, when anterior collateral flow, defined as either flow through the ACoA or as reversal of flow through the proximal segment of the ipsilateral ACA, was absent, there was found to be even poorer autoregulation. The authors suggested that activation of the secondary collateral pathways may occur when the primary pathways are insufficient to maintain the health of ischaemic tissue.

2.2 Models of the cerebral vasculature

The complex behaviour of the cerebrovascular network remains an active area of research. To date there have been many mathematical modelling studies of the cerebral arterial network. Such models are produced to provide greater understanding of cerebrovascular physiology and pathophysiology, with the eventual aim that personalised modelling will be used to aid treatment decisions for both acute and chronic cerebrovascular disease. Existing models of the cerebral arterial network invoke a wide variety of modelling techniques and assumptions. Models vary in terms of the extent of the arterial network encompassed, the modelling assumptions made about the arterial walls and the characteristics of the flow within them, their dimensionality, and their representation of the vascular territories beyond the cerebral arteries.

Many early modelling studies of the human circle of Willis were carried using physical models. These physical analogues were either hydraulic [46]–[50], or electrical [49], [51]. Early mathematical simulations of blood flow in the human circle of Willis include works by Duros and Nadvornik [52], Hillen *et al.* [53], [54], and Zagzoule and Marc-Vergnes [55]. Among the earliest of these is the 1986 modelling work of Hillen *et al.* [53]. This study used a non-linear 1D model of a well-balanced circle of Willis with elastically-varying arterial walls, to show that flows into and around the circle are dominated by vessel resistances, which increase as vessel cross-section decreases. Flows away from the circle are dominated by peripheral resistances, which represent the resistance of the downstream arterial and capillary networks.

In 1988, Hillen *et al.* [54] produced a lumped parameter model of the circle of Willis which used the Poiseuille equation (equation 2.1) to model each artery as a resistance to blood flow. They concluded that this simplified linear model was able to determine fluxes through the arteries of the circle of Willis within 10% of those calculated in their 1986 work [53]. The differences in flow, which were a result of the larger time-averaged diameters of the vessels in the pulsatile model, did not affect the distribution of flows around the circle.

One study of particular interest to the work presented in this thesis, and which has formed the basis of further modelling studies [56], [57] is that of Alastruey *et al.* [58]. In 2007, Alastruey *et al.* [58] used a non-linear 1D network model with elastically deformable arterial walls to examine the differences in cerebral blood flows provided by common anatomical variations of the circle of Willis. They used the model to investigate the effects of ICA and VA occlusion on the efferent flows provided by each circle variant, in order to identify those variants at higher risk of ischaemia. Studies by Devault *et al.* [59] and Perdikaris *et al.* [60] have since produced similar 1D models of the network in which the deformation behaviour of

the arterial walls was modelled as viscoelastic.

The vast majority of these models of the cerebral vasculature have neglected the effects of autoregulation, choosing instead to represent the cerebral vascular bed as a passive resistance to blood flow; an approach that Piechnik *et al.* [61] asserted was unrealistic. Understanding of the interaction between autoregulation and collateral flow through the circle of Willis is essential, especially as autoregulation can be disturbed during acute ischemia, when treatment decisions are most critical [32].

Dynamic control of CBF has been incorporated into network models through control of peripheral resistances in order to maintain efferent flow rates. In 2002 Ferrandez *et al.* [62] used proportional-integral control techniques to vary the peripheral resistances of a non-linear 2D model of the circle of Willis with rigid-walled vessels. They allowed the peripheral resistances, representing the vasculature between the cerebral arteries and the venous system, to be varied from their reference values by $\pm 95\%$ in order to correct efferent flow deviations from their set-point values. Ferrandez *et al.* used this model to examine the response of five single-vessel variations of the circle of Willis structure to a pressure drop in an afferent artery. Based on analysis of their modelling results, they concluded that 2D modelling did not significantly improve upon the information obtained using 1D models.

In 2004 Moorhead *et al.* [63] used proportional-integral-derivative control techniques to vary the equivalent peripheral resistances in their lumped-parameter model of the circle of Willis. They also allowed variation of these resistances by 95% above and below their reference values, and used their model to examine the performance of circle of Willis variants during simulations of afferent vessel stenosis.

Many authors [57], [64]–[69] have attempted to incorporate physiological models of autoregulatory control of efferent flows into their models of the circle of Willis. In a study by Lodi and Ursino [64], and in a study by Ryu *et al.* [67], this control

was modelled as a dynamic process, based on arteriolar volume changes. However, neither work considered individual variations in the structure of the circle of Willis and the resulting differences in capacity for collateral flow.

Alastruey *et al.* [65] coupled their earlier 1D flow model [58] to an autoregulation model in which the concentration of CO_2 in brain tissue was the driving force for changes in peripheral cerebrovascular resistance, with deviations in CO_2 concentration from the set-point value causing sigmoidal variation in resistance. The range of values within which the resistance of the cerebral vascular network, R_p could vary was: $0.74R \leq R_p \leq 1.3R$, where R is the set-point value of the peripheral resistance. Moore and David [68] coupled a very similar model of autoregulation to a 3D flow model of the circle of Willis, and further autoregulation models focussing on the metabolic component of the cerebral autoregulatory response have since been proposed [57], [69].

Liang *et al.* [66] modelled autoregulation by fitting a polynomial to the classic static autoregulation curve (Figure 2.5) relating cerebral perfusion pressure to CBF. Using the fitted polynomial to impose negative feedback based on CBF, they adjusted the resistances of the cerebral arterioles in their four-compartment model of the cerebral vasculature, which was coupled to a non-linear 1D model of the circle of Willis. They used their model to consider the influence of several structural variants on the risk of cerebral hyperperfusion after carotid artery surgery.

All of the early models of the cerebral arterial network based the structure of the arterial tree on averaged measurements from a variety of anatomical studies. However, many of the more recent modelling studies have used anatomical, and sometimes functional, angiography imaging data (which will be discussed in more detail in Section 2.3) to take steps towards personalising their models to individual human subjects.

The first model to include patient-specific arterial geometry was the 2002 work of Cebral *et al.* [70]. This study used contrast enhanced (CE) magnetic resonance angiography (MRA) images to construct a computational representation of the carotid bifurcation, and used phase-contrast MRA (PC MRA) to obtain physiologic boundary conditions. These boundary conditions took the form of flow velocity measurements, which were imposed above and below the bifurcation.

Since the work of Cebral *et al.* [70], a large number of modelling studies have followed a similar procedure, using a variety of structural angiography imaging techniques, such as time-of-flight (TOF) MRA [68], [71]–[77], contrast-enhanced MRA (CE MRA) [78], CTA [79]–[81], and X-ray DSA [81], to construct a finite-element computational domain over which the Navier-Stokes equations were solved to simulate blood flow. Some of studies have also used in vivo flow velocity measurements, made using PC MRA [68], [75] or Doppler ultrasound [59], [78], [79], [81], either to determine inlet velocity profiles to impose as boundary conditions, to calibrate their model, or to validate their results.

2.3 Cerebrovascular angiography

Imaging is essential in the diagnosis of, and treatment planning for, cerebrovascular disease. Visualisation of the arterial lumen (angiography) can be used to detect stenoses, occlusions, aneurysms, and other vascular malformations. Also, as discussed in Section 2.1.3, angiography allows the detection of collateral blood flow routes and can therefore be used to identify good candidates for endovascular therapies [7], [8], [13], [19]. The techniques discussed in this section have all been used to image the cerebral blood supply [2] and some have been used to develop patient specific models of the cerebral arterial network.

2.3.1 Transcranial doppler ultrasound

Transcranial doppler ultrasound (TCD) imaging can be used to monitor the major cerebral arteries i.e. the carotids, vertebrals and parts of the circle of Willis. It

is useful for identification of collateral routes in the circle [29] and for detection of stenoses or occlusions in the intracranial circulation [2], [82]. TCD can also be used to calculate blood flow velocities due to its high temporal resolution. This, combined with the fact that the technique is non-invasive and non-toxic, means that it is suitable for continuous monitoring of the cerebral blood supply during treatment and at the bedside [2].

Until recently, TCD was able to provide flow velocity information but the technique only detected the component of velocity perpendicular to the ultrasound probe [83] and it could not be used to quantify volumetric flow rates in the arteries of the circle of Willis [2]. A study by Correia *et al.* [84] has now demonstrated quantification of blood volume flow rates in the common carotid arteries using 4D ultrasound flow imaging. However, the application of this imaging technique to all of the arteries of the circle of Willis may be limited, due to poor transmission of ultrasound through most of the bones of the cranium [2], making some of the intracranial vessels difficult to visualise.

2.3.2 X-ray digital subtraction angiography

X-ray DSA is often called 'conventional angiography'. Due to its high spatial and temporal resolution, it is thought of as the gold standard for visualising cerebrovascular anatomy and disease. DSA can also be useful in detecting collateral flow [85]. The X-ray DSA technique involves placing an intra-arterial catheter upstream of the vessel of interest [85]. The catheter is used to inject a bolus of radio-opaque contrast agent. A pre-contrast image of the field of view is subtracted from the later images, leaving only the signal from the vessels containing contrast agent. In spite of its status as the gold standard in cerebral angiography, the use of X-ray DSA is declining; it is now generally reserved for cases that could involve intra-arterial intervention [27], [82], [85]. This decline in use is due to the fact that X-ray DSA is an invasive and time-consuming procedure, which involves injecting a potentially harmful contrast agent and exposing the patient to ionising

radiation [85]. The decline could also be explained by the increasing availability of non-invasive angiography techniques such as MRA.

2.3.3 Computed tomography angiography

CTA provides three-dimensional reconstructions of the cerebral vasculature. The images are acquired by injecting an intravenous contrast agent and then moving the patient through a rotating X-ray beam [2], [82]. The spatial resolution of CTA is excellent, and good X-ray transmission through the bones of the cranium means that the intracranial vessel anatomy can be successfully visualised and disease of the large vessels, such as the MCAs, can be detected [82], [85], [86]. However, CTA is not a time-resolved imaging technique, so gives no insight into blood flow patterns. Also, as with X-ray DSA, CTA images are acquired using X-rays, and patients are injected with a potentially toxic radio-opaque contrast agent [85].

2.3.4 Contrast enhanced MRA

In CE MRA, intravenous injection of a gadolinium-based paramagnetic contrast agent is used to visualise the cerebral vasculature in MR images [87]. The use of a contrast agent results in a high signal-to-noise ratio (SNR) which, coupled with the high spatial resolution of MRI, provides excellent visualisation of the brain-feeding arteries [87]. CE MRA is useful for detecting vessel stenoses and is better at differentiating between stenoses and occlusions than other MRA techniques [2]. However, similar to other contrast enhanced angiography techniques, the injection of contrast is invasive and the contrast agent itself is potentially toxic [87].

2.3.5 Time-of-flight MRA

TOF MRA capitalises on the fact that the radio-frequency (RF) pulses used to produce MR images 'saturate' the magnetisation of spins in the imaging plane. Angiographic images can be obtained because blood flowing into the imaging plane is not saturated, meaning that there is contrast between blood and the surrounding tissue [87], [88]. TOF MRA is a non-invasive technique that can be

used to image arterial morphology, and to identify stenoses in the large cerebral arteries [2]. However, the detected signal is flow-dependent meaning that slow flow can appear absent on TOF images. This effect can lead to overestimation of the degree of vessel stenosis, so occlusions detected using this technique often require further investigation [2].

2.3.6 Phase contrast MRA

PC MRA is a non-contrast technique that utilises the phase shift in the MR signal from blood as it moves through a magnetic field [87], [88]. PC MRA is an intrinsically quantitative method of imaging blood flow because the phase of the measured signal is proportional to the velocity of the blood [87]. This angiography technique can be used to determine the direction of blood flow in a vessel because flow in opposite directions causes opposite phase changes in the signal [87]. This is particularly useful for detecting collateral flow in the circle of Willis. Furthermore, PC MRA is more capable of differentiating between slow and absent flow than TOF MRA. However, both PC and TOF MRA suffer signal loss in regions of turbulent flow [2].

In 2007, Bammer *et al.* [89] used a time-resolved PC MRI technique to produce 3D velocity vector fields for the major intracranial arteries. They used the measured flow velocity information, together with measurements of the arteries' cross-sectional areas, to estimate blood flow rates in the circle of Willis. The measured blood flow rates were lower than values from literature measured using TCD, a difference that they suggested was due to averaging the signal over a larger volume and time step than used in TCD, leaving PC MRA less sensitive to higher flow velocities.

2.3.7 Arterial spin labelling MRA

Arterial spin labelling (ASL) is a non-invasive MRI technique, whereby the water in arterial blood is used as an endogenous contrast agent. This imaging modality avoids the potential harms of X-ray, CT, and CE MRA techniques, and recently methods have been devised to measure flow rates directly in the arteries of the circle of Willis

[90], [91]. Blood volume flow rate quantification using ASL MRA is one of the focal points of this thesis, hence, a more detailed discussion of ASL is presented below.

2.4 Arterial spin labelling

ASL is a process in which the longitudinal magnetisation of protons in arterial blood water is 'labelled' by a 180° RF inversion pulse applied to the arteries proximal to the imaging region of interest. When the inverted arterial blood reaches the imaging plane, a 'label' image, which shows the presence of the labelled blood water, is produced. ASL has, to date, found most use in imaging CBF in the context of estimating local brain tissue perfusion [92], [93]. In perfusion imaging, labelled blood water flows into tissue and exchanges into the tissue water pool, with the result that the label is observed as a perturbation of brain tissue magnetisation [94].

In perfusion imaging, ASL is a technique with an inherently low SNR. This is a consequence of the fact that, in one second, perfusion replaces only a small proportion of the water in tissue with arterial blood water. Thus, the inflowing labelled blood water only perturbs the magnetisation of the imaged tissue by $\sim 1 - 3\%$ [94]. To improve SNR, the image acquisition procedure is repeated without arterial blood water inversion, allowing a 'control' image to be made. Then, by subtraction of the 'label' image from the 'control' image, the MR signal contribution from static background tissue can be removed, producing an ASL difference image [92].

Another factor which affects the SNR of ASL images, and limits the time over which images can be acquired, is relaxation of the longitudinal magnetisation of the arterial blood water protons. The process of longitudinal relaxation or 'T_1 decay' occurs over a few seconds as labelled water protons gradually return to the non-inverted state [92]. Generally, to improve SNR, ASL perfusion images are acquired at low spatial resolution [94]. Furthermore, multiple repetitions of the label-control acquisition process are performed, and the final ASL image is then an

average over all of the repetitions [95].

ASL angiography imaging of the circle of Willis can also be achieved, and can generally be acquired at higher SNRs than are possible in perfusion imaging. Like perfusion, the process of angiography acquisition involves subtraction to remove static tissue signal. Compared to perfusion, it involves shifting the imaging plane so that it covers the arteries in the neck, and the circle of Willis, in order to acquire both 'label' and 'control' images of the circle of Willis. However, the concentration of labelled blood in the arteries of the circle is high and, as the images are acquired closer to the location of label generation, there is very little time for longitudinal relaxation to occur between labelling and imaging [22]. The high SNR of ASL angiography means that the images can be acquired at higher spatial and temporal resolution than perfusion images [94].

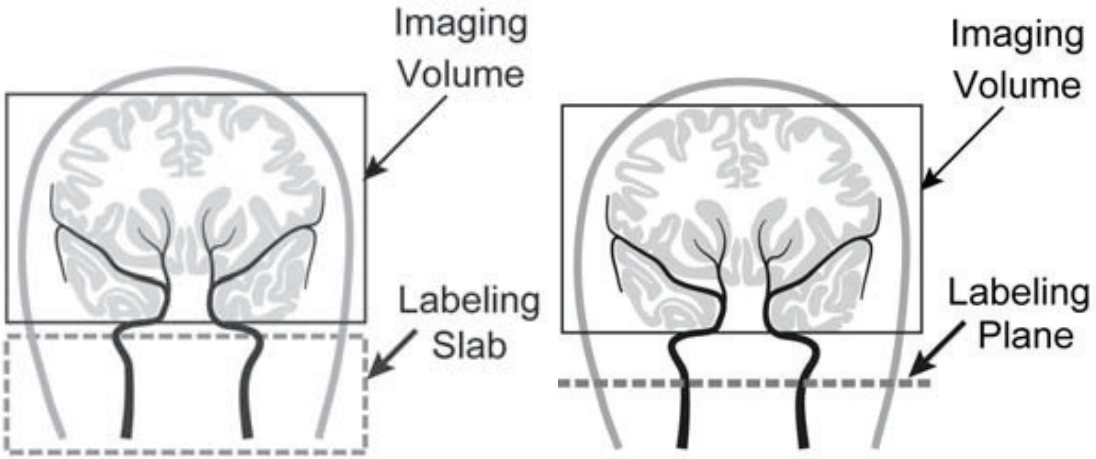
2.4.1 Methods of creating contrast

Generally speaking, there are two techniques for acquiring ASL perfusion images. They are: continuous ASL (CASL) and pulsed ASL (PASL).

CASL involves protracted application of an inversion pulse (for up to several seconds) to a very thin labelling plane, proximal to the imaging plane. As blood flows through this plane its longitudinal magnetisation is inverted in a process known as 'flow-driven adiabatic inversion' [94]. Pseudocontinuous ASL (PCASL) is similar to CASL, in that blood is inverted in a thin labelling plane (Figure 2.6b), but the inversion is achieved using a long train of very short RF pulses, rather than one continuous pulse [92], [96]. Compared with CASL, PCASL greatly reduces magnetisation transfer effects [92], and is easier to implement using clinical scanner hardware [97].

PASL involves briefly (for around $10\,ms$) applying a 180° inversion pulse to a thick labelling band close, and proximal, to the imaging plane (Figure 2.6a). This

allows a fairly large volume of arterial blood to be rapidly labelled [94].



(a) PASL **(b)** PCASL

Figure 2.6: Schematic representations of (a) PASL, and (b) PCASL labelling for perfusion imaging. In angiography the imaging volume is positioned lower, at the level of the circle of Willis. Images reproduced, with permission and without changes, from Wong [94].

There are specific advantages to both pulsed and continuous/pseudocontinuous ASL. For example, PASL has a higher labelling efficiency than either CASL or PCASL, and in PASL the labelling efficiency is not affected by the flow velocity of blood [94]. Furthermore, the brevity of the PASL labelling period allows image acquisition to begin much earlier than in CASL or PCASL and, therefore, means that the inflow of labelled blood into the imaging plane can be visualised. An advantage of CASL/PCASL is that the two techniques create ASL labelled blood boluses of a known duration equal to the labelling duration [92], a factor which is valuable in blood flow quantification. In PASL, unless a labelling adaptation which truncates the bolus at a specified duration is used [98], only the spatial width of the labelled blood bolus is known. Finally, the use of CASL/PCASL conveys an SNR advantage over PASL because the narrow labelling plane can be located at the distal edge of the corresponding PASL labelling slab [94]. In CASL/PCASL, blood water is labelled as it flows through the labelling plane, rather than all at once, which means that, on average, the blood is labelled closer to the time of

image acquisition than blood labelled by PASL and, as a result, undergoes less longitudinal relaxation prior to imaging.

Longitudinal relaxation can be described mathematically as the concentration, c, of the ASL label in blood decreasing over time from its initial value, as the longitudinal magnetisation of labelled water protons decays, at a rate determined by T_{1b}, the longitudinal relaxation time of arterial blood [92]. This effect is described in ASL signal models using a multiplicative exponential decay term [92]:

$$c_p(t) = c_0 e^{-t/T_{1b}} \qquad \text{for PASL} \tag{2.2}$$

$$c_c(t) = c_0 e^{-\Delta t/T_{1b}} \qquad \text{for CASL and PCASL} \tag{2.3}$$

where t is the time since PASL labelling, and Δt is the time that has passed since each part of the CASL/PCASL blood bolus was labelled. T_{1b} values are typically around 1.65 *seconds* at 3 Tesla, and 1.35 *seconds* at 1.5 Tesla [95], [99]. Differences in labelling and the difference in T_1 decay of PASL and CASL/PCASL cause the resulting labelled blood boluses to have different temporal profiles.

2.4.2 Vessel-selective labelling

Methods have been devised to perform both pulsed, and pseudo-continuous ASL of blood in individual arteries that supply the brain. The ability to perform vessel-selective labelling allows matching of blood in cerebral arteries and tissue territories, to the afferent arteries involved in their supply. This replicates a particularly valuable feature of X-ray DSA, as it permits determination of the extent to which each afferent artery contributes to the blood supply of a particular vessel or tissue region and the origins of any collateral blood supply to a vessel or tissue.

Several single-vessel labelling techniques have been proposed. In PASL these techniques involve orienting the labelling slab such that it only covers a single artery [100]–[103]. In CASL, some techniques have involved restriction of the labelling plane through the use of a separate transmit coil specifically for labelling

[104]–[108]. Other vessel-selective CASL techniques involving continuous rotation of the labelling plane [109], [110], and PCASL techniques in which gradient pulses are applied between RF pulses [111], [112], are able to restrict efficient labelling to a single point.

In PCASL, the application of gradient pulses between successive RF pulses can also allow modulation of labelling efficiency across the labelling plane [113]. For example, in 2007, Wong *et al.* [113] used this PCASL technique to selectively label and control combinations of different vessels in the neck in one acquisition. They modulated the PCASL labelling efficiency across the labelling plane, such that some of the vessels were labelled and some were controlled. Varying the locations of the labelled and controlled parts of the labelling plane, over several acquisitions, meant that labelling of each artery was uniquely encoded. During post-processing of the acquired images, Wong *et al.* [113] were able to separate the ASL signal contributions from the RICA, LICA and BA, and then to produce vascular tissue territory maps. These maps showed the areas of brain tissue perfused by each of the three vessels. Several methods for separation of these encoded vascular signals have been proposed, some which allow for the presence of blood from more than one supply in a voxel [114]–[117], and others which do not [113], [118].

Much of the vessel-selective ASL literature describes the application of these labelling techniques to vascular territory mapping in perfusion imaging. However, as mentioned above and of particular interest in this work, vessel-selective labelling in angiography has also been used for visualisation of collateral blood flow through the circle of Willis [22], [90], [100], [101], [119], [120]. One example of particular relevence to the work of this thesis is a 2006 study by van Osch *et al.* [90] in which a PASL technique was used to perform 2D thick-slab, quantitative, non-invasive, dynamic MRA of the circle of Willis. They acquired vessel-selective ASL images by positioning the thick labelling band so that the inversion pulse was restricted to a single artery proximal to the circle of Willis. They labelled one of the afferent

arteries and observed the flow of the ASL blood bolus through the imaging plane. They then repeated the process on the remaining afferent arteries.

Vessel-encoded ASL MRA

In 2010, Okell *et al.* [22] used the vessel encoding (VE) technique of Wong *et al.* [113], described above, to produce vessel-encoded PCASL (VEPCASL) cerebral angiograms rather than tissue perfusion maps. Okell *et al.* [22] selectively labelled the four brain-feeding arteries in the neck (ICAs and VAs) and then acquired a time series of MR images of the circle of Willis in transverse and coronal views. The time for which the labelling pulse was applied ($1000\,ms$) determined the duration of the bolus of ASL labelled blood that flowed through the circle of Willis. The image time series was used to observe the passage of this bolus of blood through the circle. The 'label' and 'image' steps were repeated, with different neck vessel combinations labelled and controlled each time.

After image acquisition, VE angiograms showing the flow of blood, from each of the four supply arteries, were produced. This involved identification of the ASL signals that originated in each supply vessel from the raw data. To extract these signals, Okell *et al.* [22] adapted the Bayesian inference model of Chappell *et al.* [22], [121]. In every voxel in a VEPCASL image, Okell *et al.* [22] determined which group of supply vessels the labelled blood was likely to have come from, based on how well the Chappell *et al.* [121] model described the ASL signal. Figure 2.3b shows one of the VEPCASL angiograms obtained by Okell *et al.* [22] with the four different colours showing the ASL signals from blood labelled in each of the four afferent arteries.

2.4.3 Kinetic modelling of ASL in perfusion imaging

In perfusion imaging, quantification of voxel-wise CBF relies on the use of a kinetic model of blood delivery to brain tissue. For perfusion data acquired at a single time point, simple models are used [95] and these can be inverted analytically

to calculate CBF. For dynamic ASL perfusion acquisitions, a kinetic model like that described by Buxton *et al.* [122] can be fitted to the measured signal-time curve in a voxel to estimate CBF:

$$\Delta M(t) = 2M_{0b} f \int_0^t AIF(t')R(t-t')dt' \tag{2.4}$$

where $\Delta M(t)$ is the magnetisation time series measured in a voxel, M_{0b} is the equilibrium magnetisation of arterial blood, a calibration factor which is typically estimated from a proton-density image of the tissue of interest. In equation 2.4, f is CBF, $AIF(t)$ is an arterial input function, and $R(t)$ is the residue function which, after bolus arrival, describes the proportion of the label that remains within the voxel.

Bolus dispersion

Inversion of the magnetisation of blood water by PASL, CASL or PCASL labelling creates a bolus with a profile close to the well-defined, box-car shape [92]. Transit through the cerebral vasculature will cause such a bolus to disperse. This means that the bolus will spread out, smoothing its temporal profile away from the ideal box-car. Dispersion of the bolus is the result of an arterial blood velocity profile that cannot be described by ideal 'plug flow', as blood close to the vessel wall travels more slowly than blood in the vessel centre. Bolus dispersion also results from the fact that different parts of the bolus may travel different distances to reach the imaged voxel, and ASL labelled water molecules in the bolus may diffuse into the unlabelled blood [123].

The work of Buxton *et al.* [122] (equation 2.4) modelled a plug-flow blood velocity profile and thereby neglected to model the effects of bolus dispersion between the labelling and imaging planes. Some attempts have been made to incorporate the effects of dispersion into this standard model of the ASL perfusion signal [123]–[125]; more recently similar methods have been applied in the context of ASL angiography [126], [127]. Most of this work has involved modelling the statistical distribution of labelled blood arrival times at the imaging voxel, in the form of dispersion kernels.

When convolved with the ideal ASL temporal profile, dispersion kernels give models of the dispersed bolus profile in the imaging voxel [123], [126], [127]. Another approach has been to consider the development of the bolus shape by assuming steady laminar fluid flow in an artery. Gallichan and Jezzard [124] considered dispersion resulting from a quadratic, Hagen-Poiseuille arterial blood flow profile and geometrically modelled the evolution of the shape of the bolus as it travelled along a vessel to the imaging voxel. Kazan *et al.* [125] assumed a velocity profile that was somewhere between plug-flow and quadratic laminar flow, to account for dispersion effects, and modelled the mass transport of the ASL label between the labelling plane and the imaging plane.

The techniques that model dispersion arising from an assumed flow profile are advantageous in that the dispersion model parameters estimated from the ASL data have obvious physical meaning. This is because the techniques address the underlying causes of dispersion, rather than focusing on quantifying its effects. However, estimation of these model parameters is generally more computationally costly, due to increased model complexity [127].

2.4.4 Modelling of ASL in angiography

As well as using ASL MR cerebral angiograms for anatomical imaging, and in order to map the distribution of blood from specific afferent arteries, attempts have been made to obtain quantitative information about cerebral blood flow using vessel-selective ASL MRA techniques [90], [91]. Similar to the approaches to CBF quantification in ASL perfusion imaging (Section 2.4.3), such studies have involved modelling the MR signals detected in arteries after ASL labelling, then fitting the modelled signals to those measured in order to estimate model parameters.

PASL

The 2006 study by van Osch *et al.* [90], outlined in Section 2.4.2, attempted to perform quantitative, vessel-selective PASL MRA. After selective ASL vessel

labelling, van Osch *et al.* [90] measured the ASL signal in an input region of voxels positioned inside a major artery (distal to the labelling band but proximal to the circle of Willis). They then modelled the ASL signal in a region-of-interest (ROI) covering part of an artery of the circle of Willis. The signal model accounted for the attenuating effects of longitudinal relaxation of the ASL label. The ASL signal was also attenuated as a result of repeated perturbation of the label by the readout RF excitation pulses it experienced as it passed through the imaging region. van Osch *et al.* [90] accounted for this effect in their ASL angiography model (equation 2.6) by modification of the longitudinal relaxation time of arterial blood T_{1b} [128]:

$$\frac{1}{T_{1m}} = \frac{1}{T_{1b}} - \frac{\ln\left[\cos\alpha\right]}{T_R} \tag{2.5}$$

where T_{1m} was the effective longitudinal relaxation time of the blood in the imaging plane, α was the flip angle of the RF excitation pulses and T_R was the pulse repetition time.

van Osch *et al.* [90] estimated the fraction of time ($1-\beta$ in equation 2.6) the label experienced imaging pulses (i.e. the fraction of time that the labelled blood was in the imaging plane) based on an assumed blood flow rate and vessel length, and applied the two relaxation times T_{1b} and T_{1m} proportionately. With the T_1 and RF attenuating effects included, the resulting ROI signal was modelled as a delayed and scaled version of the signal in the input region, $\hat{S}_{CA}(t)$, integrated over the volume of the ROI (equation 2.6).

$$\frac{S_{ROI}(t)}{e\left[-t\left(\frac{\beta}{T_1}+\frac{1-\beta}{\tau}\right)\right]} \approx \frac{BF_{ROI}}{V_{CA}} \cdot \int_{t-\bar{t}-TA}^{t-TA} \frac{\hat{S}_{CA}(t')}{e\left[-\frac{t'}{T_1}\right]}\,\mathrm{d}t' \tag{2.6}$$

where $S_{ROI}(t)$ was the MR signal in the ROI, BF_{ROI} was the flow rate of blood through the ROI, TA was the time taken for blood to flow from the input region to the ROI, $\bar{t}$ was the time taken for blood to flow through the ROI, V_{CA} was the volume of all of the voxels included in the input signal measurement.

van Osch *et al.* [90] were able to calibrate their model by using a separate high resolution scan performed for input signal ($\hat{S}_{CA}(t)$) measurement. They did this by ensuring that their input region was positioned inside an ICA or the BA, and only contained voxels that were assumed to be entirely filled with labelled blood, hence the blood volume that produced the ASL signal in the input region, V_{CA}, was known. Minimising the sum-of-squared-differences between the measured and modelled ROI signals allowed for estimation of the model parameters and, thus, for estimation of the blood flow rate BF_{ROI}. van Osch *et al.* [90] attempted to validate their technique of estimating blood flow using a circle of Willis phantom. Their estimates were highly correlated with the true flow rates, but underestimated the true flow by 10-15%.

PCASL

In 2013, Okell *et al.* [91] proposed a model-based method for blood volume flow rate quantification using 2D thick-slab, dynamic, vessel-encoded PCASL angiography images of the cirlce of Willis [22]. By using PASL, van Osch *et al.* were able to visualise the inflow of the ASL labelled blood bolus into the circle of Willis. However, the significantly longer labelling duration of PCASL meant that Okell *et al.* [22] were only able to observe the outflow of the bolus.

In an effort to visualise the bolus inflow, Okell *et al.* [126] developed a kinetic model of the ASL signal in a VEPCASL image voxel:

$$S(t) = A \int_{-\infty}^{\infty} c_{in}(t - t' - \Delta t) D(t') T(\Delta t, t', t) \Psi(\Delta t, t', t) \, \mathrm{d}t' \tag{2.7}$$

The model assumed that the concentration of the ASL label generated in the labelling plane, c_{in}, could be modelled as a rectangular pulse of duration τ. The ASL signal measured in a downstream voxel, $S(t)$, was assumed to be proportional to the volume of the ASL label in that voxel, $A_i = S_0 v_i$. This volume was modelled as a delayed (by the arrival time Δt) version of the rectangular concentration pulse, integrated over the volume of the voxel. The model included a term to account for longitudinal relaxation, $T(\Delta t, t', t)$, (equation 2.3), and a term to account for the

signal attenuating effects of the applied RF imaging pulses, $\Psi(\Delta t, t', t)$. Dispersion of the bolus during transit through the vasculature was modelled using a dispersion kernel, $D(t')$, which took the form of a gamma variate function.

Fitting the kinetic model (equation 2.7) voxel-wise to the VEPCASL signals allowed Okell *et al.* [126] to visualise the complete passage of the ASL bolus through the circle of Willis. They were also able to generate maps of their estimated model parameters across the circle and thereby derive information about relative blood flow rates in the cerebral vessels. Unfortunately, this information was not fully quantitative because the measured ASL difference signal per unit volume of labelled blood, S_0, was unknown. In Okell *et al.* [91], this parameter was estimated, meaning that absolute blood volumes could be calculated. The parameter was estimated by fitting a simple model of the variation of the scaling parameter A across the diameter, $\bar{d}$, of an artery:

$$A_{tot}(d) = \begin{cases} S_0 \Delta x \Delta y \sqrt{\bar{d}^2 - 4\left(d - d_0\right)^2}, & |d - d_0| \leq \bar{d}/2 \\ 0 & |d - d_0| > \bar{d}/2 \end{cases} \tag{2.8}$$

where Δx and Δy are the two smaller voxel dimensions i.e. not the slab-thickness, and d_0 is the centre of the artery.

Okell *et al.* [91] located imaged vessels which ran parallel to the imaging plane and, assuming circular cross-sections, estimated the model parameters S_0 and $\bar{d}$ by fitting equation 2.8 (Figure 2.7). Then, in order to estimate flow rates, a vessel region large enough to encompass the entire simulated bolus was defined, and the measured volumes of labelled blood in the individual voxels in that vessel region were summed, to estimate the total volume of labelled blood that flowed through the trunk vessel during the labelling duration. This permitted eventual, calculation of blood flow rates. The Okell *et al.* method was able to measure flow rates in a phantom with a systematic underestimation of only $2 \pm 3\%$. However, the requirement that the vessel region encompass the entire simulated ASL bolus meant

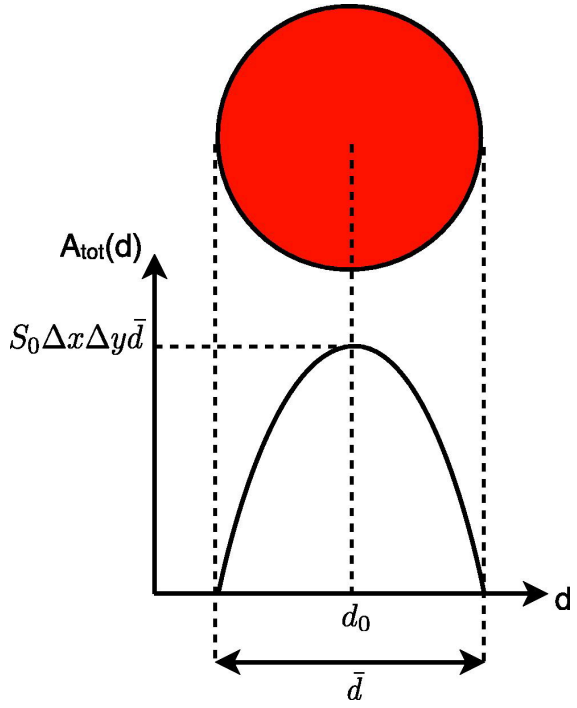


Figure 2.7: Arterial geometry (shown in red) assumed by Okell *et al.* [91] in order to estimate the calibration factor S_0 from 2D thick-slab angiography images of the circle of Willis, such as that seen in Figure 2.3b. Reproduced without changes from [91] under license http://creativecommons.org/licenses/by/3.0

that blood flow measurements could only be taken from the large afferent and efferent arteries of the circle of Willis, and not from the smaller circulus arteries.

2.5 Summary

In a clinical context, vascular surgeries such as aortic arch repair [11] and carotid endarterectomy [129] rely on collateral flow thorough the circle of Willis to perfuse cerebral tissue adequately while one or both of the ipsilateral afferent arteries are intentionally occluded. In stroke patients, the presence of good collateral routes on angiography has been shown to be associated with smaller infarct volumes [8], and improved outcomes of endovascular recanalisation therapies [13], [19]. The work described in this thesis aims to use mathematical modelling to explore the extent to which collateral flow through the circle of Willis and cerebral autoregulation, individually and in combination, ensure blood flows through the cerebral arteries in the event of afferent vessel occlusion. A fuller understanding of these factors may

allow assessments of collateral flow and autoregulation, and personalised cerebral arterial network models, to be used as predictors of outcome in cerebrovascular diseases and interventions.

3
Network Model

3.1 Introduction

As outlined in Chapter 2, autoregulation and collateral blood flow through the circle of Willis both play a role in maintaining cerebral blood flows in the event of arterial occlusion. However, the interaction between the two mechanisms remains poorly understood. To investigate this interaction, a one-dimensional steady state model of the cerebral arterial network was created, and is presented in this chapter [1]. Common structural variants of the circle of Willis, together with less common configurations that present particular risk of stroke, were recreated using the network model coupled with: (1) a steady state physiological model of cerebral autoregulation, (2) one wherein the cerebral vascular bed was modelled as a passive resistance, and (3) a model in which the hemisphere contralateral to the occluded artery autoregulates and the ipsilateral hemisphere does not. These three models were used in turn to simulate various conditions of internal carotid and vertebral artery occlusion.

[1] Large parts of the work presented in this chapter have been published in the following articles:
F. Kennedy McConnell and S. Payne, "The Dual Role of Cerebral Autoregulation and Collateral Flow in the Circle of Willis after Major Vessel Occlusion", *IEEE Transactions on Biomedical Engineering*, vol. 64, no. 8, pp. 1793-1802, 2017.
F. Kennedy McConnell and S. Payne, "Autoregulating Cerebral Tissue Selfishly Exploits Collateral Flow Routes Through the Circle of Willis", *Acta Neurochirurgica Supplement, in press.*

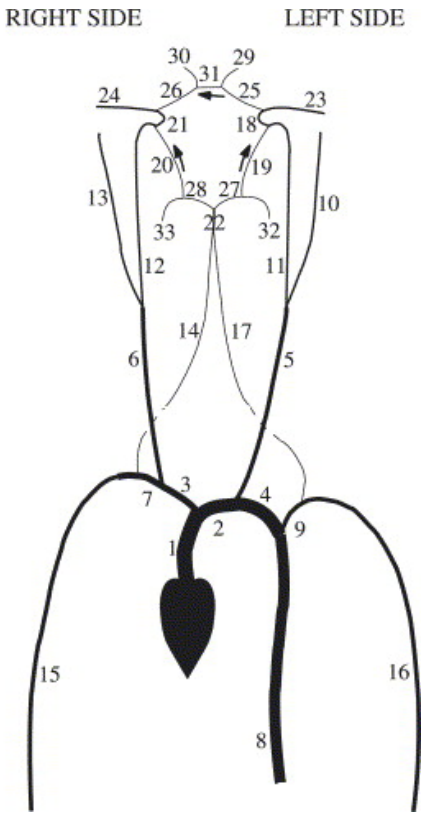


Figure 3.1: Schematic showing the extent of the arterial domain modelled in this chapter. The arrows indicate the direction of blood flow through the communicating arteries that was defined as positive in this work, and the numbers are used identify each artery in Table 3.1. Reproduced with permission from Alastruey *et al.* [58].

3.2 Model equations

3.2.1 The cerebral arterial network

A schematic of the network of arteries that supply blood to the brain was included in the work of Alastruey *et al.* [58], and is reproduced in Figure 3.1. This simplified arterial tree is the basis of the network model presented here. The circle of Willis portion of the modelled network is shown in Figure 3.2a. The anatomical and physiological parameters used to define the structure and function of the arteries were also taken directly from Alastruey *et al.* [58] (Table 3.1). In the work presented here, the network was modelled in steady state, meaning that fluctuations in arterial pressure and blood flow with the cardiac cycle were not considered. This approach was taken because the ability of collateral flow and autoregulation to maintain CBF is of interest over time scales significantly longer than the cardiac cycle.

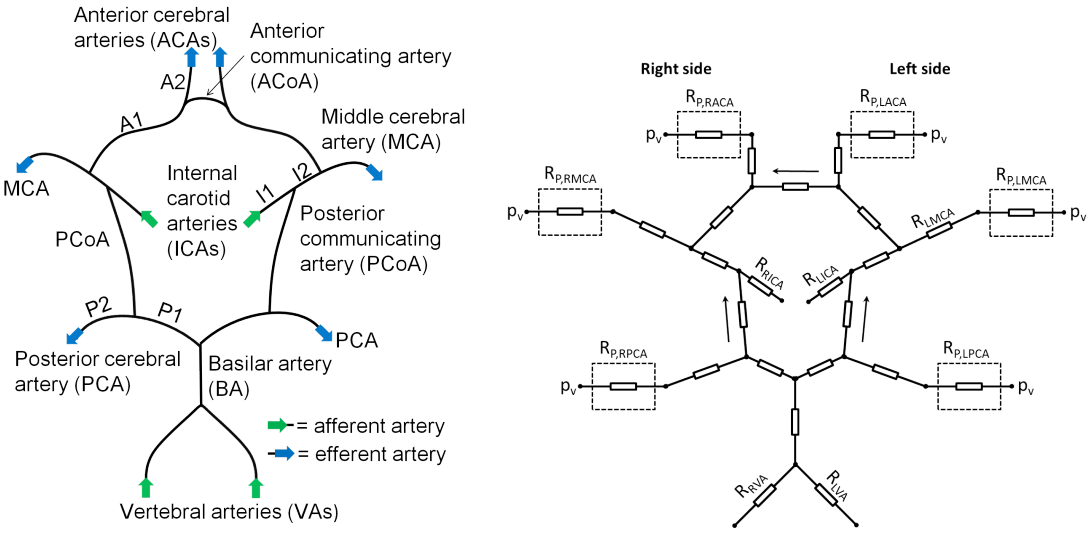


Figure 3.2: (a) Schematic and (b) equivalent resistance model representations of the full circle of Willis (which will be referred to as 'variant 1' throughout this chapter). The arrows in (b) indicate the direction of blood flow through the communicating arteries that was defined as positive in this work.

Poiseuille's equation, which assumes fully-developed, laminar fluid flow, was used to define flow through the vessels of the network. The equation relates blood flow Q through a vessel, to the pressure drop ΔP across it:

$$\frac{\Delta P}{Q} = \frac{8\mu l}{\pi r^4} = R = \frac{1}{G} \tag{3.1}$$

where l and r are vessel length and radius respectively, R denotes the resistance of the vessel to flow, G refers to the flow conductance, and μ is the viscosity of blood, which is taken here to be 4.5 $mPas$ [58].

3.2.2 The cerebral territories

Using Poiseuille's equation, the arterial network becomes analogous to a series of interconnected resistances, the circle of Willis portion of which is shown in Figure 3.2b. In this structure, each of the terminal arteries (i.e. those at the limits of the modelled network: the brachials, the thoracic aorta, the external carotids, and the six cerebral arteries) is coupled with a peripheral resistance which accounts

Table 3.1: Physiological data used in modelling – all values taken from Alastruey *et al.* [58]. Numbers in the leftmost column identify each artery in Figure 3.1.

	Artery	Length	Radius	Peripheral resistance
	Units	mm	mm	mmHg s/ml
1	Ascending aorta	40	12	—
2	Aortic arch 1	20	11.2	—
3	Brachiocephalic	34	6.2	—
4	Aortic arch 2	39	10.7	—
5	Left common carotid	208	2.5	—
6	Right common carotid	177	2.5	—
7	Right subclavian	34	4.23	—
8	Thoracic aorta	156	9.99	1.35
9	Left subclavian	34	4.23	—
10	Left external carotid	177	1.5	40.73
11	LICA I1	177	2.0	—
12	RICA I1	177	2.0	—
13	Right external carotid	177	1.5	40.73
14	RVA	148	1.36	—
15	Right brachial	422	4.03	20.10
16	Left brachial	422	4.03	20.10
17	LVA	148	1.36	—
18	LICA I2	5	2.0	—
19	LPCoA	15	0.73	—
20	RPCoA	15	0.73	—
21	RICA I2	5	2.0	—
22	BA	29	1.62	—
23	LMCA	119	1.43	44.78
24	RMCA	119	1.43	44.78
25	LACAA1	12	1.17	—
26	RACAA1	12	1.17	—
27	LPCAP1	5	1.07	—
28	RPCAP1	5	1.07	—
29	LACAA2	103	1.2	63.61
30	RACAA2	103	1.2	63.61
31	ACoA	3	0.74	—
32	LPCAP2	86	1.05	83.11
33	RPCAP2	86	1.05	83.11

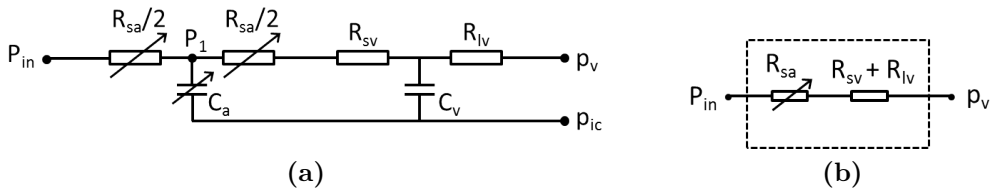


Figure 3.3: Electrical equivalent circuit representations of the autoregulation model of Payne [130]: a) the full dynamic model; and b) its steady state equivalent. The parameter R_{sa} represents the resistance of the small arteries and arterioles, R_{sv} is the resistance of the capillaries and small veins, R_{lv} is the resistance of the large veins. The parameter C_a is the arteriolar compliance, and C_v is the venous compliance. The parameter P_{in} is the pressure at the inlet to the arteriolar compartment, p_v is the venous pressure, and p_{ic} is the intracranial pressure.

for the total resistance of the arterial network between the terminal vessel and the venous system. The peripheral resistances were used to calculate the pressures and flow rates at the distal ends of the terminal arteries:

$$p = p_v + R_p Q \tag{3.2}$$

where p_v is the pressure of the venous system, which, as in Alastruey *et al.* [58], was taken to be 5 $mmHg$ (666.7 Pa). The network model was then adapted to take account of CBF autoregulation by the brain's arteriolar network. This involved adapting the peripheral resistances R_p (shown in dashed boxes in Figure 3.2b) using the small artery, capillary, and venous components of the Payne [130] autoregulation equivalent circuit model.

At steady state, the Payne model (Figure 3.3a) condenses to two resistances connected in series. These include a variable resistance, representing the small arteries and arterioles, and a fixed resistance, representing the capillaries, and the small and large veins (Figure 3.3b). The peripheral resistances from the non-autoregulating model were thus replaced with the resistances in Figure 3.3b. In order to match the autoregulating and non-autoregulating network models under baseline conditions, it was assumed that $\overline{R_{sa}} + R_v = R_p$, where R_{sa} is the variable resistance of the regulating small arteries and arterioles, and $\overline{R_{sa}}$ represents its baseline value. Also $R_v = R_{sv} + R_{lv}$, where R_{sv} is the resistance of the capillaries

and small veins, and R_{lv} is the resistance of the large veins. The partitioning of the peripheral resistances was done by matching the ratios of $\overline{R_{sa}}$:R_v used by Payne [130].

The resistance of a blood vessel is related to its radius, according to equation 3.1. In the autoregulation model, a vessel's resistance is thus assumed to be related to its volume by:

$$\frac{V_{sa}}{\overline{V_{sa}}} = \sqrt{\frac{\overline{R_{sa}}}{R_{sa}}} \tag{3.3}$$

where V_{sa} is the volume of the arteriolar compartment and $\overline{V_{sa}}$ denotes its value under baseline conditions.

Arterial compliance, C_a relates the rates of change of arterial volume and pressure:

$$\frac{dV_{sa}}{dt} = \frac{d[C_a \cdot (P_1 - P_{ic})]}{dt} \tag{3.4}$$

which, at steady-state, reduces to:

$$V_{sa} - \overline{V_{sa}} = C_a\,(q) \cdot (P_1 - P_{ic}) - \overline{C_a} \cdot (\overline{P_1} - P_{ic}) \tag{3.5}$$

where P_{ic} is the intracranial pressure and P_1 is the pressure of the arteriolar compartment.

Cerebral blood flow is regulated by adjusting the compliance of the arteriolar compartment based on a negative feedback parameter proportional to the deviation in flow from baseline. Payne [130] modelled this change in arteriolar compliance using an asymmetrical sigmoidal curve:

$$C_a\,(q) = \overline{C_a} + \frac{1}{2}\begin{cases} \Delta C_a^{+} tanh\Big[-\frac{2G_q}{\Delta C_a^{+}}\left(\frac{q-\overline{q}}{\overline{q}}\right)\Big], & \text{if } q < \overline{q} \\ \Delta C_a^{-} tanh\Big[-\frac{2G_q}{\Delta C_a^{-}}\left(\frac{q-\overline{q}}{\overline{q}}\right)\Big], & \text{if } q > \overline{q} \end{cases} \tag{3.6}$$

where $\overline{C_a}$ is the baseline arterial compliance. ΔC_a^{+} and ΔC_a^{-} define the upper and lower limits on the value of compliance respectively, $\overline{q}$ is the baseline healthy flow through the afferent artery, and G_q is the gain of the flow feedback mechanism.

Thus, an equation relating P_{in}, pressure at the distal end of a cerebral artery, to q, flow through that artery, can be found:

$$\begin{aligned}\left[\frac{P_{in}-P_v-qR_v}{q}\right]\cdot[&C_a\left(q\right)\left(P_{in}-2P_{ic}+P_v+qR_v\right)\\&-\overline{C_a}(2\overline{P_{in}}-2P_{ic}-\overline{q}\overline{R_{sa}})+2\overline{V_{sa}}]^2\\&-4\overline{R_{sa}V_{sa}}^2=0\end{aligned}\tag{3.7}$$

Equation 3.7 can be solved numerically to calculate q for any value of the arterial input pressure P_{in}.

Numerical solution

At arterial bifurcations and junctions, the pressure was set to be equal in all vessels at each node. The pressure at all but the first and last nodes in the network is thus given by a linear equation of the form:

$$\sum_{i=2}^{n-1}(P_i-P_j)G_{ij}=S_i\tag{3.8}$$

where G_{ij} is the flow conductance of a vessel connecting node i to every other node j. If i is not connected to a node j then $G_{ij}=0$. S_i is a source term equal to the blood flow in at node i. Due to conservation of mass, this term should be zero for all nodes other than those at the input from the heart, and the output to the venous system. However, rather than fixing these flows as boundary conditions, modified nodal analysis was used to impose pressure boundary conditions at the input and outputs of the network. This system of linear equations was put into the following matrix form:

$$\mathbf{BP}=\mathbf{S}\tag{3.9}$$

where $\mathbf{B}$ is a matrix of vessel conductance terms, vector $\mathbf{P}$ contains the pressure at each node, and $\mathbf{S}$ is the vector of source terms. In matrix form:

$$\left[\begin{array}{cccc:cc}\sum_n G_{11} & -G_{12} & \cdots & -G_{1n} & 1 & 0\\ -G_{21} & \sum_n G_{22} & \cdots & -G_{2n} & 0 & 0\\ \vdots & \vdots & \ddots & \vdots & \vdots & \vdots\\ -G_{(n-1)1} & \cdots & \cdots & -G_{(n-1)n} & 0 & 0\\ -G_{n1} & \cdots & \cdots & \sum_n G_{nn} & 0 & 1\\ \hdashline 1 & 0 & \cdots & 0 & 0 & 0\\ 0 & 0 & \cdots & 1 & 0 & 0\end{array}\right]\left[\begin{array}{c}P_h\\P_2\\\vdots\\P_{n-1}\\P_n\\\hdashline S_1\\S_n\end{array}\right]=\left[\begin{array}{c}S_1\\S_2\\\vdots\\S_{n-1}\\S_n\\\hdashline P_h\\P_n\end{array}\right]\tag{3.10}$$

The rows of matrix **B** below the horizontal dashed line allow the inclusion of pressure boundary conditions at the input and outputs of the network. The columns to the right of the vertical dashed line allow the inflow S_1 and outflow S_n to be included as parameters to be found, rather than being boundary conditions. Finding vector **P** involves inversion of this matrix equation, performed here using Gaussian elimination. The resulting node pressure values are then used to find the flow rates of blood in all of the arteries in the network.

The autoregulation model was expressed in matrix form, in the same way as in equation 3.10. The pressure at the start of the aorta, P_h, and the venous pressure remained as boundary conditions. However, the pressures at the distal ends of the cerebral arteries were calculated using equation 3.7 and imposed in the matrix system in the same way as the boundary conditions, i.e. in equation 3.10 the flow rates were included as additional rows below the dashed line in the **P** vector, with the calculated corresponding pressures imposed below the dashed line in the **S** vector. The autoregulation matrix equation, and equation 3.7, were then solved using the following iterative scheme:

1. The non-autoregulating version of the model was run, under healthy conditions, to establish a baseline.

2. Vessel number, m, and iteration number, a, were initially set to $m = 1$ and $a = 0$.

3. Cerebral artery flows, and distal pressure values from Step 1 were used as the baseline pressures and flows in the autoregulation model, and initial estimates of the pressures at the distal ends of the six cerebral arteries, $P_{m,0}$, were made.

4. Set $a = a + 1$

5. (a) Equation 3.7 was solved for vessel m to find a new estimate, $\hat{P}_{m,a}$, for the pressure in vessel m.

(b) The pressure in vessel m was updated, according to equation 3.11, while the pressures in the five remaining cerebral arteries were held constant.

$$P_{m,a} = P_{m,a-1} + r \times \left(\hat{P}_{m,a} - P_{m,a-1}\right) \tag{3.11}$$

where r was a selected parameter used to ensure convergence.

(c) The autoregulation model matrix equation was solved to find the flows in the network, given the updated value of $P_{m,a}$. This gave updated values of flow in the six cerebral arteries.

6. Step 5 was repeated for the remaining cerebral arteries $m = 2$ to $m = 6$.

7. Steps 4, 5 and 6 were repeated until the solution converged.

The iterative scheme was assumed to have converged upon a solution when the maximum difference between the flow rate in any of the six cerebral arteries at iteration a, and its value at iteration $a - 6$ had remained less than $0.01ml/s$ for 100 iterations. The solution was then checked to ensure that flow was conserved throughout the arterial network. The number of iterations required to reach convergence, and thus the required computational time, depended on the circle variant and the afferent artery occlusion condition under consideration. Convergence was always achieved in under 3000 iterations. For example, when the LICA of the complete circle of Willis (Figure 3.2a) was occluded, the iterative scheme converged on a solution to the autoregulating model in 76 seconds, after 1327 iterations.

Parameter values

As indicated in Section 3.2.1, the parameters used to create the network model: vessel lengths and radii and peripheral resistances, were taken from Alastruey *et al.* [58]. For arteries proximal to the circle of Willis, the vessel length and radius data were originally taken from the work of Stergiopulos *et al.* [131]. For the arteries of the circle of Willis, the data were originally taken from Fahrig *et al.* [50]. The peripheral resistance values were calculated by Alastruey *et al.* [58], assuming that the distal end of each cerebral artery was coupled to a three-element model

consisting of a resistance, R_1, in series with a parallel combination of a second resistance, R_2 and a capacitor. The values of R_1 were fixed to the characteristic impedances of the associated terminal arteries. To determine the values of R_2, the total resistance of the arterial network was taken to be $R_T = 1.34 \times 10^8\ Pa\ s\ m^{-3}$ [58], [131] and the peripheral resistances $R_p = R_1 + R_2$ apportioned, such that 15% of the cardiac output goes to the head, 5% goes to each arm, and 75% goes to the rest of the body [58]. The blood flow to the head was split between the six cerebral arteries and the two external carotid arteries in proportion to the initial cross-sectional area of the associated terminal artery [58]. In the work described in this thesis, the inlet pressure at the aorta (P_h) was determined as the pressure that provided cardiac output, through the healthy 'full circle' network, equal to the time average of the cardiac output flow function used by Alastruey *et al.* [58].

The parameters used to define the autoregulatory model: $\overline{C_a}$, ΔC_a^+, ΔC_a^-, $\overline{V_{sa}}$, and G_q, were taken from Payne [130]. However, the parameter values that Payne used represent the arterioles supplying the whole brain. In this work, a scaled down version of Payne's cerebral autoregulation model was connected to each of the cerebral arteries, representing the vascular networks beyond the circle of Willis. Hence, each of the model parameters was scaled down accordingly. For $\overline{V_{sa}}$ this was done using equation 3.3 and values of $\overline{R_{sa}}$, which were calculated from the peripheral resistances of the non-autoregulating model. Then, the remaining autoregulation model parameters were scaled down by the same proportion as $\overline{V_{sa}}$. The resulting parameter values used to define the autoregulating part of the model are given in Table 3.2.

Simulations

As already discussed in Chapter 2, the structure of the circle of Willis is widely variable. One key aim of this work was to investigate the effect of variations in the structure of the circle of Willis on its capacity for collateral flow. The circle configurations considered were those identified by Papantchev *et al.* [11]. These are

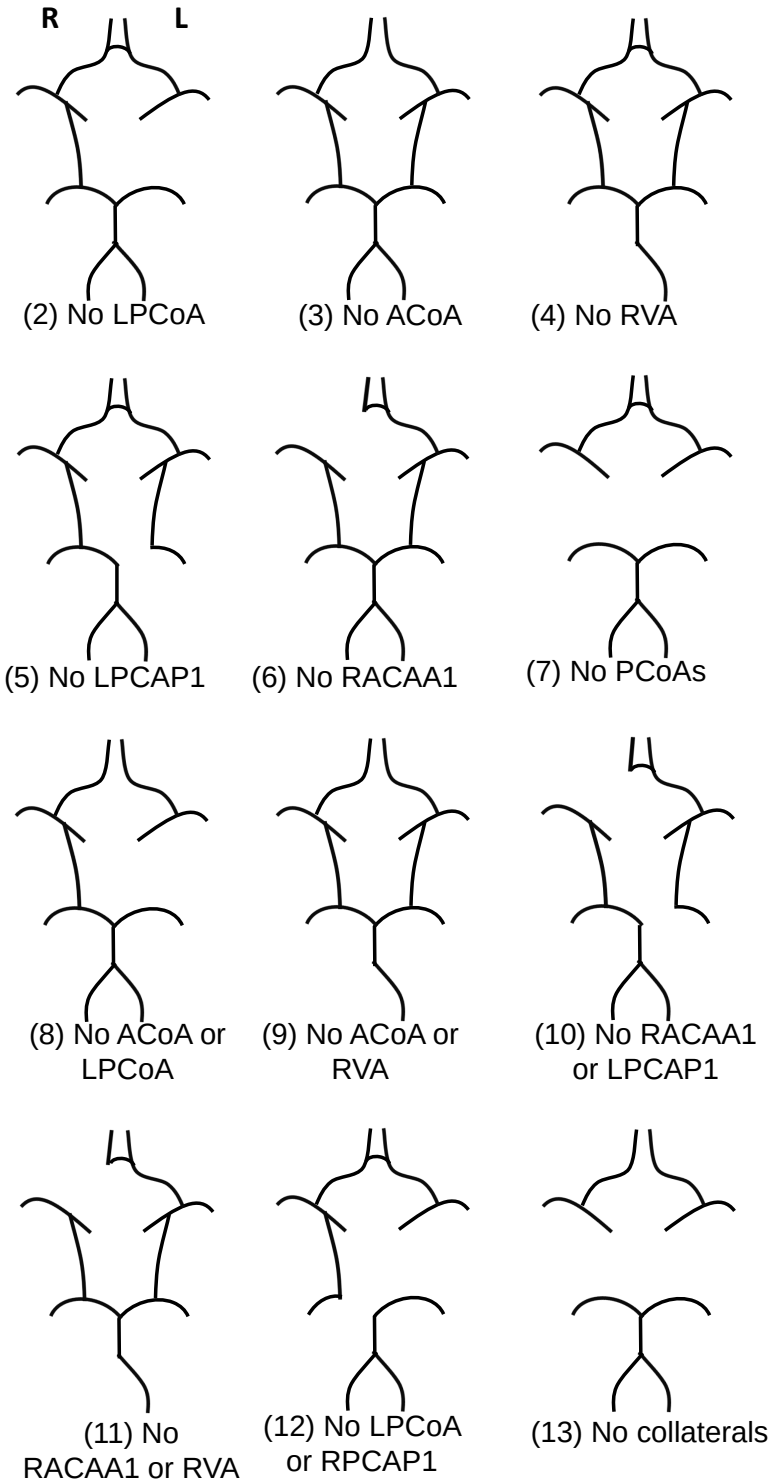


Figure 3.4: Twelve of the thirteen circle of Willis variants considered in arterial network modelling simulations. The full circle of Willis (variant 1) is shown in Figure 3.2a.

Table 3.2: Autoregulation model parameter values

Parameter	Units	MCAs	PCAs	ACAs	Whole network	Payne [130]
$\overline{V_{sa}}$	ml	4.71	3.46	3.96	—	12
G_q	ml/mmHg	1.18	0.87	0.99	—	3.0
$\overline{C_a}$	ml/mmHg	0.08	0.06	0.07	—	0.21
ΔC_a^+	ml/mmHg	1.13	0.83	0.95	—	2.87
ΔC_a^-	ml/mmHg	0.06	0.05	0.05	—	0.16
$\overline{R_{sa}}$	mmHg s/ml	32.60	60.50	46.31	—	5.03
R_v	mmHg s/ml	12.18	22.61	17.30	—	1.88
P_h	mmHg	—	—	—	108	—
P_v	mmHg	—	—	—	5	6
P_{ic}	mmHg	—	—	—	10	10

illustrated in Figures 3.2a, which shows variant 1, and 3.4 (variants 2–6, and 8–11), together with two additional, commonly occurring networks [132]: both PCoAs absent (variant 7 in Figure 3.4); and one PCoA absent with the contralateral PCA P1 segment also absent (variant 12 in Figure 3.4). Another additional variant (variant 13 in Figure 3.4), which has not been identified from anatomical or imaging studies, but was proposed in this work to provide the most extreme case of a circle of Willis without any potential for collateral flow (i.e. missing both PCoAs and the ACoA) was also considered.

For each circle of Willis configuration, three scenarios concerning the status of the cerebral autoregulatory response were considered (Figure 3.5): Scenario (1) none of the cerebral territories autoregulating, Scenario (2) all of the cerebral territories autoregulating, and Scenario (3) only those cerebral territories contralateral to the occluded afferent artery autoregulating (see Section 2.1.4). The three scenarios were simulated for every circle variant in order to:

1. Examine the flows through the cerebral and communicating arteries under baseline conditions, i.e. when none of the afferent arteries was occluded.

2. Examine the effect of the following occlusion conditions:

   (a) Partial occlusion of the LICA

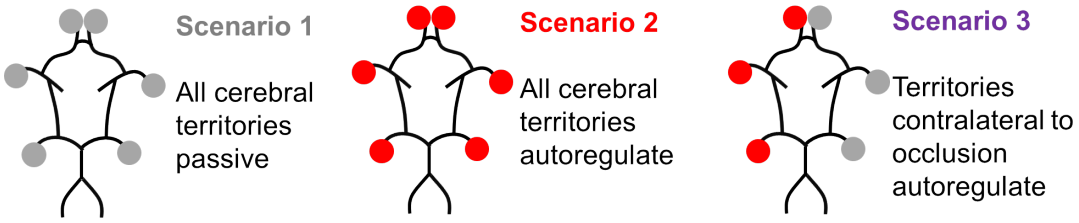


Figure 3.5: Three autoregulation scenarios were simulated in each circle of Willis variant.

(b) Total occlusion of the LICA

(c) Total occlusion of the LVA

(d) Partial occlusion of the LICA and total occlusion of the RICA

(e) Total occlusion of the LICA and partial occlusion of the RICA

on the outflows through the cerebral arteries.

Partial occlusion was defined by a reduction in ICA radius to 50% of its healthy value. This definition was chosen as it is the lower boundary of the degree of stenosis for which carotid endarterectomy has been found to be beneficial [133]. Total occlusion of the LICA and the LVA were both considered individually because the circle of Willis geometries under investigation are those that were identified by Papantchev *et al.* [11] as being at high risk of cerebral ischaemia during disruption of the supply to the left side of the circle. Combinations of stenosis and occlusions of both internal carotid ateries were also considered. This was because atherosclerosis of the carotid arteries is generally bilaterally symmetrical [134]. Moreover, a carotid endarterectomy procedure to reduce stenosis in one ICA would involve occlusion of that ICA and, therefore, reliance on collateral flow through the circle of Willis from the contralateral ICA, which may also be stenosed. Finally, the circles of Willis with no available collateral flow route to arteries downstream of the LICA (i.e. variants 8, 10 and 13) were also modelled with hypoplastic rather than absent circulus arteries to examine the availability of flow through narrowed collateral vessels. In these simulations the radii of 'hypoplastic' arteries were reduced to 50% of their values in variant 1 (a 75% reduction in area).

The model was also used to replicate the carotid endarterectomy simulations carried out by Liang *et al.* [66]. In their study, Liang *et al.* coupled a non-linear 1D model of the arterial network supplying the brain to an autoregulating, lumped-parameter model of the distal cerebral vascular network. They used the model to simulate stenotic conditions then, once the modelled network had reached steady state, the autoregulating cerebral resistances were fixed and one of the ICAs was widened. In the current work, Liang's five stenotic conditions: LICA, RICA, bilateral ICA, concurrent BA and LICA, and concurrent BA and RICA stenoses, were simulated in the nine circle of Willis geometries that Liang *et al.* considered [66]. Stenosis was modelled as a 60% reduction in vessel radius. Any circle in which a cerebral territory saw a flow increase of $> 100\%$ after ICA widening was considered to be at risk of cerebral hyperperfusion [66], which can lead to cerebral oedema, haemorrhage, and death.

3.3 Results

3.3.1 Healthy flows

Table 3.3 lists the 'healthy' flow rates of blood through the efferent and communicating arteries in the thirteen variants of the circle of Willis considered in this study. The values given are those calculated using the non-autoregulating version of the arterial network model. These flows were used as the baseline condition for the autoregulating version of the model. Variant 13 refers to a circle of Willis configuration that lacks the posterior and anterior communicating arteries; thereby completely lacking capacity for collateral flow.

Table 3.3 shows that the circle that produced the greatest deviations from the 'full circle' flows was variant 10: a circle missing the A1 segment of the RACA and the P1 segment of the LPCA. The vessel in variant 10 with the lowest flow relative to its value for variant 1 is the LPCA which, rather than being fed by the vertebrals, is fed by the LICA, via the LPCoA. However, it received 1.00 mls^{-1} of blood, a

Table 3.3: Flows in the efferent and communicating arteries of thirteen circle of Willis geometries. The numbers in the left-most column are used to refer to different network variants later in the text and figures. Flow values are given in ml/s. Negative values of flow indicate that the direction of flow is reversed relative to the positive direction indicated in Figure 3.2b. The bottom row shows blood flow rates presented by Fahrig *et al.* [50], for comparative purposes, these values are averages from a number TCD studies.

		Cerebral arteries						Communicating arteries		
Variant	Absent vessel(s)	LMCA	RMCA	LACA	RACA	LPCA	RPCA	LPCoA	RPCoA	ACoA
1	None	2.06	2.06	1.42	1.42	1.09	1.09	0.06	0.03	-0.07
2	LPCoA	2.06	2.06	1.42	1.42	1.10	1.10	—	0.05	-0.09
3	ACoA	2.06	2.06	1.42	1.42	1.09	1.09	0.07	0.02	—
4	RVA	2.05	2.05	1.42	1.42	1.08	1.08	-0.23	-0.26	-0.07
5	LPCAP1	2.04	2.06	1.41	1.42	1.03	1.10	-1.03	0.39	-0.49
6	RACAA1	2.03	2.10	1.39	1.37	1.09	1.10	0.37	-0.28	1.37
7	PCoAs	2.06	2.06	1.42	1.42	1.10	1.10	—	—	-0.08
8	ACoA & LPCoA	2.06	2.06	1.42	1.42	1.10	1.10	—	0.03	—
9	ACoA & RVA	2.05	2.06	1.41	1.42	1.08	1.08	-0.21	-0.27	—
10	RACAA1 & LPCAP1	1.99	2.11	1.36	1.34	1.00	1.12	-1.00	0.10	1.34
11	RACAA1 & RVA	2.02	2.09	1.38	1.37	1.07	1.08	0.08	-0.57	1.37
12	LPCoA & RPCAP1	2.05	2.04	1.41	1.41	1.12	1.03	—	-1.03	0.21
13	ACoA & PCoAs	2.06	2.06	1.42	1.42	1.10	1.10	—	—	—
	Fahrig *et al.* [50] (range)	2.0 (1.8 – 2.7)		1.1 (1.0 – 1.4)		0.8 (0.7 – 0.9)		—	—	—

reduction of only 8.3% from the 1.09 mls^{-1} received by the LPCA in variant 1, illustrating the robustness of the collateral network in this particular case.

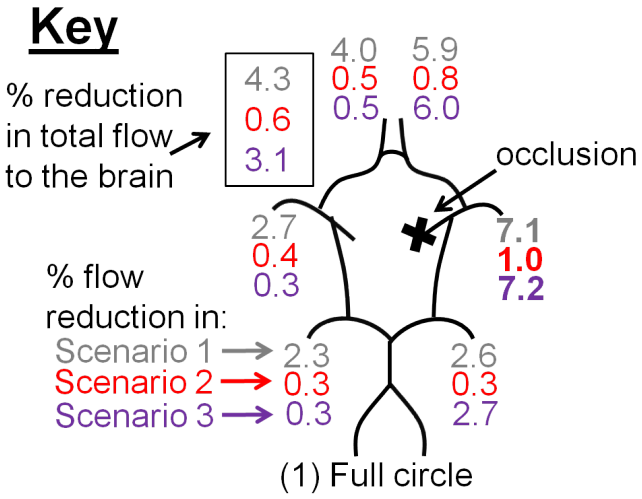


Figure 3.6: Percentage reductions in the flow rates through the cerebral arteries of the full circle of Willis (variant 1 in Table 3.3) during total LICA occlusion. The maximum reduction in each scenario is highlighted in bold. The boxed numbers give the total percentage reduction in flow to the brain. Colours are used to differentiate between the three autoregulation secnarios.

3.3.2 Arterial occlusions

This chapter focuses primarily on the results of model simulations performed under healthy conditions, and under conditions of LICA occlusion, which are presented and compared in detail. Simulations of four other network disruptions were also performed: LICA stenosis, LVA occlusion, combined LICA stenosis and RICA occlusion, and combined LICA occlusion and RICA stenosis. The results of these network simulations are presented in Appendix A.1 in the form of tables of absolute blood volume flow rates through the afferent and efferent arteries of each of the thirteen circle of Willis variants, exposed to each network disruption.

Figure 3.6 shows the effect of occlusion of the LICA on flows through the efferent arteries of the complete, well balanced circle of Willis (variant 1). The numbers next to each artery give the percentage **reductions** in flow through that artery, relative to the no-occlusion 'healthy' flows given for variant 1 in Table 3.3, for each of the three autoregulation scenarios. For example, Figure 3.6 shows that in the complete circle of Willis, occlusion of the LICA results in a 7.1% reduction in blood flow to the LMCA if none of the cerebral territories autoregulate, a 1.0% reduction if all of the territories autoregulate, and a 7.2% reduction if only the right-sided territories autoregulate.

Figure 3.7 shows the effects of LICA occlusion on flows in the efferent arteries of the remaining twelve circle of Willis variants (note that for variant 13, 75% area reduction was applied, rather than total occlusion). Figures 3.6 and 3.7 demonstrate that collateral flow alone (Scenario 1) is unable to ensure adequate ($> 90\%$) cerebral flows in all but three variants of the circle of Willis (1, 2, and 4). It is also evident that complete autoregulation (Scenario 2) enables improved maintenance of blood flow to the cerebral tissue. This is true for all networks in which there is some capacity for collateral flow (see Appendix A.1 for the remaining occlusion conditions), i.e. excluding the networks in Figures 3.7(8) and 3.7(10), whose blood supply to the brain was reduced by 38.0% and 63.8% respectively.

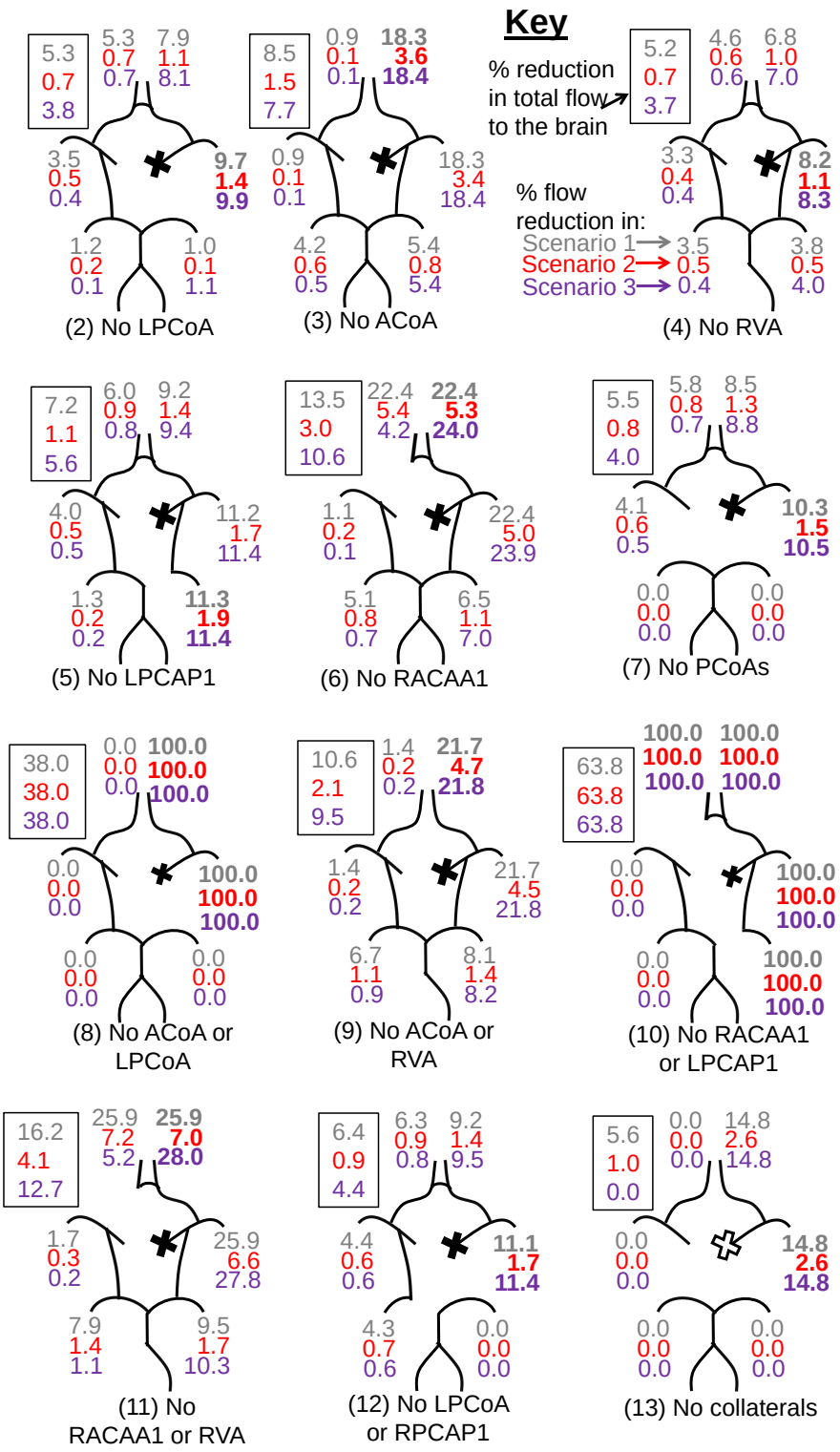


Figure 3.7: Percentage reductions in flow rates through the cerebral arteries of various circle of Willis configurations when the LICA is occluded. The hollow cross in variant 13 indicates 75% area reduction. The maximum reduction in each case is highlighted in bold. Full data are provided in Appendix A.1.

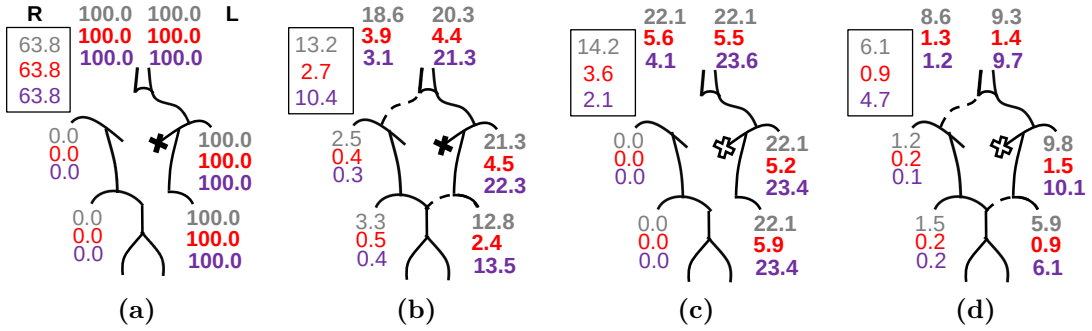


Figure 3.8: Percentage reductions in flow rates through the cerebral arteries of the circle of Willis in which the proximal segments of the RACA and the LPCA are absent or hypoplastic (variant 10). A solid black cross denotes total occlusion, whereas a hollow cross indicates a 75% reduction in area. A dashed vessel line indicates that an arterial segment is hypoplastic (75% area reduction). a) Total LICA occlusion in circle with absent RACAA1 and LPCAP1. b) Total LICA occlusion in circle with hypoplastic RACAA1 and LPCAP1. c) Partial LICA occlusion in circle with absent RACAA1 and LPCAP1. d) Partial LICA occlusion in circle with hypoplastic RACAA1 and LPCAP1. The maximum reduction in each case is shown in bold text. Boxed numbers give the total percentage reduction in blood supplied to the brain. Flow reductions are colour coded according to Figure 3.5 to denote the simulated status of the cerebral autoregulatory response.

These are the two most vulnerable networks: in variant 8 (Figure 3.7(8)) both the left middle and anterior cerebral territories, and in variant 10 (Figure 3.7(10)) the entire left hemisphere and the right anterior cerebral territory are at very high risk of ischaemia. However the results demonstrate that autoregulation only preserves cerebral flows locally. The Scenario 3 results show that the reduction in total flow to the brain is ameliorated as autoregulation preserved flows contralateral to the occluded afferent artery. But they also show that this occurs at the expense of the ipsilateral cerebral territories, which are most at risk.

Table 3.4 classifies the thirteen circle of Willis geometries as at either low, medium or high risk of ischaemia based on the cerebral blood flow reductions seen in Figures 3.6 and 3.7. These risk classifications are made based on the flow reductions seen in Scenarios 1 and 2. It should be noted that if Scenarios 1 and 3 are compared instead, all of the medium risk circle variants are re-classified as high risk.

Table 3.4: Risk classifications of circle of Willis variants under different occlusion conditions based on the following categories: Low (L) - none of the efferent arteries sees a flow rate reduction of $> 10\%$ whether autoregulation is taken into account or not. Medium (M) - at least one efferent artery sees a flow rate reduction of $> 10\%$, which is reduced to $< 10\%$ when bilateral autoregulation is taken into account. High (H) - at least one efferent artery experiences a flow rate reduction of $> 10\%$ even when bilateral autoregulation is taken into account. All risk classifications that worsen in Scenario 3 are highlighted in bold

Variant	Absent vessel(s)	LICA stenosed	LICA occluded	LVA occluded	LICA stenosed RICA occluded	LICA occluded RICA stenosed
1	None	L	L	L	**M**	**M**
2	LPCoA	L	L	L	**M**	**M**
3	ACoA	L	**M**	L	**M**	**M**
4	RVA	L	L	L	**M**	**M**
5	LPCAP1	L	**M**	L	**M**	**M**
6	RACAA1	**M**	**M**	L	**M**	**M**
7	PCoAs	L	**M**	L	H	H
8	LPCoA & ACoA	**M**	H	L	**M**	H
9	ACoA & RVA	L	**M**	L	**M**	**M**
10	RACAA1 & LPCAP1	**M**	H	L	**M**	H
11	RACAA1 & RVA	**M**	**M**	L	**M**	**M**
12	LPCoA & RPCAP1	L	**M**	L	H	H
13	ACoA & PCoAs	**M**	H	L	H	H

Figure 3.8 shows several simulations of network 10. The figure shows combinations of two levels of LICA stenosis (100% and 75%), with either complete absence of the RACAA1 and LPCAP1, or with the areas of these vessels reduced by 75% from their values in variant 1. 'Partial occlusion' refers to a reduction of vessel radius to 50% of the 'healthy' value, i.e. a 75% reduction in the vessel area. A dashed line in the circle of Willis drawing is used to denote a circulus artery whose radius is 50% of the value used when modelling the 'complete' circle of Willis (network 1). The figure demonstrates that autoregulation ameliorates the reduction in efferent flows; this is seen in all but the most severe combination of total LICA occlusion, with no capacity for right-side to left-side collateral flow (Figure 3.8a).

The effect of anterior communicating (Figure 3.9a), and left posterior communicating (Figure 3.9b) artery areas on flows through the LACA, LMCA, ACoA and LPCoA, when the LICA was occluded, was then examined. The results are

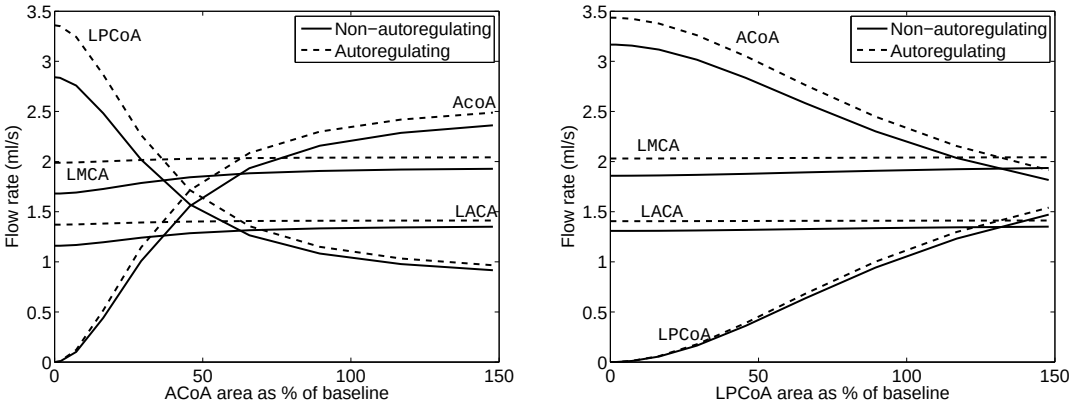


Figure 3.9: Flows through the LMCA, LACA, LPCoA and ACoA, in variant 1, during LICA occlusion, shown as a function of: a) ACoA area; b) LPCoA area

shown for both Scenario 1 (solid lines) and Scenario 2 (dashed lines). Figure 3.9a shows that the autoregulating components of the model allowed the network to compensate for absence of the ACoA. Flow through the LPCoA was raised to more than 3 times its value when the ACoA was present, meaning that flows through the cerebral arteries were maintained within 3% of their healthy values (Table 3.3) when the LICA of variant 1 was occluded. Hence, the autoregulating version of the network model was better able to make use of the collateral flow route through the LPCoA in order to maintain flows to the cerebral arteries at near their healthy levels.

In Figure 3.9a, as the area of the ACoA increases from $10 - 90\%$ of its reference value (in Table 3.1), its flow capacity increases sharply, levelling off thereafter. At an area of around 45%, the ACoA becomes the dominant collateral flow route to the LACA and LMCA. Similarly, as the area of the LPCoA increases (Figure 3.9b) its flow capacity rapidly increases. However, absence of the LPCoA is less detrimental to flows through the LACA and LMCA during LICA occlusion, than absence of the ACoA. Additionally, the LPCoA does not become the dominant collateral flow route until its area is increased to approximately 180% of its reference value (not shown in Figure 3.9b).

The results of simulations replicating those of Liang *et al.* [66] are shown in Tables 3.5 – 3.10. The tables give the percentage increase in flow through each cerebral artery when the simulated state is changed from a stenotic condition (including stenosis of at least one ICA), to a post carotid artery surgery (post-CAS) condition. In the post-CAS condition the radius of one 'stenotic' ICA was returned to its 'healthy' value, and the six autoregulating resistances were held at their stenotic condition values. The post-CAS flow rates in Tables 3.5 – 3.10 are given as a percentage of the flow rate through the same artery under stenotic conditions. Bold text indicates cerebral territories and circle of Willis configurations at high risk of cerebral hyperperfusion, defined as a flow rate increase of $> 100\%$. The circle variants that saw large efferent flow increases after carotid endarterectomy are circles 7, 8 and 12, and an additional circle considered by Liang *et al*, in which the RACAA1 and RPCAP1 segments were absent.

Table 3.5: Percentage increases in flows through the cerebral arteries resulting from carotid artery surgery – simulations of nine variants of the circle of Willis. LICA stenosis followed by LICA carotid artery surgery - Comparison with Figure 7A of Liang *et al.* [66]

Circle	Absent vessel(s)	LMCA	RMCA	LACA	RACA	LPCA	RPCA
1	None	5.7	2.1	4.7	3.1	2.0	1.8
6	RACAA1	22.1	0.9	22.1	22.1	5.5	4.3
—	RPCAP1	5.8	2.2	4.8	3.2	2.0	2.2
—	RACAA1 & RPCAP1	22.7	0.0	22.7	22.7	6.8	0.0
3	ACoA	16.3	0.7	16.3	0.7	4.3	3.3
8	**LPCoA & ACoA**	**180.2**	0.0	**180.2**	0.0	0.0	0.0
2	LPCoA	7.9	2.7	6.4	4.1	0.8	0.9
12	LPCoA & RPCAP1	9.2	3.5	7.6	5.0	0.0	3.4
7	PCoAs	8.5	3.2	6.9	4.6	0.0	0.0

3.4 Discussion

3.4.1 Healthy flows

The results of simulations of 'healthy' networks, i.e. those in which the radii of the four afferent arteries of the circle of Willis were unchanged (Table 3.3), showed that the absence of one, or even two, of the circulus arteries did not reduce the efferent

Table 3.6: Percentage increases in flows through the cerebral arteries resulting from carotid artery surgery – simulations of nine variants of the circle of Willis. RICA stenosis followed by RICA carotid artery surgery - Comparison with Figure 7B of Liang *et al.* [66]

Circle	Absent vessel(s)	LMCA	RMCA	LACA	RACA	LPCA	RPCA
1	None	2.3	6.1	3.4	5.0	1.9	2.2
6	RACAA1	0.5	10.9	0.5	0.5	2.4	3.0
—	RPCAP1	3.5	10.1	5.2	8.1	1.2	10.1
—	**RACAA1 & RPCAP1**	0.0	**160.8**	0.0	0.0	0.0	**160.8**
3	ACoA	0.8	16.7	0.8	16.7	3.4	4.4
8	LPCoA & ACoA	0.0	18.0	0.0	18.0	4.8	5.6
2	LPCoA	2.4	6.1	3.4	5.0	1.8	2.1
12	LPCoA & RPCAP1	4.3	11.1	6.1	9.1	0.0	11.2
7	PCoAs	3.5	9.1	5.0	7.5	0.0	0.0

Table 3.7: Percentage increases in flows through the cerebral arteries resulting from carotid artery surgery – simulations of nine variants of the circle of Willis. Bilateral ICA stenosis followed by LICA carotid artery surgery - Comparison with Figure 8A of Liang *et al.* [66]

Circle	Absent vessel(s)	LMCA	RMCA	LACA	RACA	LPCA	RPCA
1	None	19.9	15.2	18.6	16.5	8.0	7.7
6	RACAA1	27.1	5.7	27.1	27.1	7.7	6.5
—	RPCAP1	31.5	29.3	30.9	29.9	8.8	29.2
—	RACAA1 & RPCAP1	22.7	0.0	22.7	22.7	6.8	0.0
3	ACoA	22.0	4.8	22.0	4.8	6.5	5.5
8	**LPCoA & ACoA**	**180.2**	0.0	**180.2**	0.0	0.0	0.0
2	LPCoA	35.9	24.3	32.5	27.4	5.9	6.9
12	**LPCoA & RPCAP1**	**181.1**	**154.5**	**173.7**	**162.0**	0.0	**154.1**
7	**PCoAs**	**164.8**	**142.0**	**158.4**	**148.4**	0.0	0.0

flows through the cerebral arteries by more than 10%. In these healthy networks the results of simulations of autoregulation scenarios 1, 2, and 3 were identical. The efferent flow rates themselves are similar to the values presented in Fahrig *et al.* [50], which are weighted averages of values obtained from a literature review of measurement studies estimating flow rates of blood entering and exiting the circle of Willis.

Some differences between measured estimates of flow rates, and those from the simulations carried out in this work, were expected. This is because the

Table 3.8: Percentage increases in flows through the cerebral arteries resulting from carotid artery surgery – simulations of nine variants of the circle of Willis. Bilateral ICA stenosis followed by RICA carotid artery surgery - Comparison with Figure 8B of Liang *et al.* [66]

Circle	Absent vessel(s)	LMCA	RMCA	LACA	RACA	LPCA	RPCA
1	None	15.5	20.3	16.9	19.0	7.9	8.2
6	RACAA1	3.9	17.0	3.9	3.9	4.4	5.3
—	RPCAP1	27.6	41.7	31.4	37.6	7.7	41.9
—	**RACAA1 & RPCAP1**	0.0	**160.8**	0.0	0.0	0.0	**160.8**
3	ACoA	4.9	22.4	4.9	22.4	5.6	6.6
8	LPCoA & ACoA	0.0	18.0	0.0	18.0	4.8	5.6
2	LPCoA	27.3	29.3	27.9	28.8	7.2	8.4
12	**LPCoA & RPCAP1**	**158.3**	**185.8**	**165.9**	**178.0**	0.0	**186.2**
7	**PCoAs**	**143.5**	**166.5**	**149.9**	**160.1**	0.0	0.0

Table 3.9: Percentage increases in flows through the cerebral arteries resulting from carotid artery surgery – simulations of nine variants of the circle of Willis. Concurrent BA and LICA stenosis followed by LICA carotid artery surgery - Comparison with Figure 9A of Liang *et al.* [66]

Circle	Absent vessel(s)	LMCA	RMCA	LACA	RACA	LPCA	RPCA
1	None	8.7	3.5	7.2	4.9	5.4	5.1
6	RACAA1	39.5	2.7	39.5	39.5	16.4	14.1
—	RPCAP1	8.9	3.3	7.3	4.8	6.8	3.3
—	RACAA1 & RPCAP1	85.6	0.0	85.6	85.6	54.5	0.0
3	ACoA	30.1	2.2	30.1	2.2	13.2	11.4
8	**LPCoA & ACoA**	**180.2**	0.0	**180.2**	0.0	0.0	0.0
2	LPCoA	9.3	3.4	7.6	5.0	2.5	2.5
12	LPCoA & RPCAP1	9.2	3.5	7.6	5.0	0.0	3.4
7	PCoAs	8.5	3.2	6.9	4.6	0.0	0.0

simplified structure of the circle of Willis modelled here does not take account of the small perforating arteries that arise from its segments. These vessels include, for example, the spinal artery, which arises from the vertebral arteries, and the cerebellar and pontine arteries, all of which arise from the basilar artery [4]. Hence, the measurements averaged by Fahrig *et al.* [50] estimate that 11.8 ml/s enters the circle of Willis and 7.8 ml/s leaves via the cerebral arteries, whereas the model presented here sees 9.1 ml/s passing into and out from the full circle under healthy conditions. While the perforating arteries were omitted for simplicity in this study,

Table 3.10: Percentage increases in flows through the cerebral arteries resulting from carotid artery surgery – simulations of nine variants of the circle of Willis. Concurrent BA and RICA stenosis followed by RICA carotid artery surgery - Comparison with Figure 9B of Liang *et al.* [66]

Circle	Absent vessel(s)	LMCA	RMCA	LACA	RACA	LPCA	RPCA
1	None	3.9	9.4	5.4	7.8	5.5	5.8
6	RACAA1	1.8	21.7	1.8	1.8	8.8	10.1
—	RPCAP1	4.1	11.3	6.1	9.2	3.1	11.4
—	**RACAA1 & RPCAP1**	0.0	**160.8**	0.0	0.0	0.0	**160.8**
3	ACoA	2.4	30.9	2.4	30.9	11.8	13.6
8	LPCoA & ACoA	0.0	77.0	0.0	77.0	48.5	50.2
2	LPCoA	3.9	10.2	5.6	8.3	7.5	7.7
12	LPCoA & RPCAP1	4.3	11.1	6.1	9.1	0.0	11.2
7	PCoAs	3.5	9.1	5.0	7.5	0.0	0.0

it would be possible to include them in the network model; furthermore, doing so might bring the posterior cerebral artery flow rates down into the range of measured values presented in Fahrig *et al.* [50].

There are differences between modelling studies in the total blood flow through the circle of Willis, which makes direct comparison of efferent flow rates between studies difficult. In most cases, the difference in total flux is due to differences in arterial geometries, boundary conditions, and peripheral resistances. Several models [54], [62], [63], [71] have assigned the cerebral peripheral resistances as being inversely proportional to the relative masses of brain tissue supplied by each of the cerebral arteries, such that the $R_{ACA} : R_{MCA} : R_{PCA}$ ratio is $6 : 3 : 4$. This results in greater flow through the PCAs than the ACAs, an assumption that is, however, not supported by the data of Fahrig *et al.* [50]. Alastruey et al. [58] report lower flows through the circle of Willis than were seen in the results presented in this Chapter. This is likely to be due to the fact that Alastruey *et al.* modelled the arteries below the neck as more compliant than those in the neck and the circle of Willis. As a vessel's steady-state resistance (equation 3.1) varies non-linearly with radius this leads to a greater reduction of the time-averaged resistance relative to the steady-state resistance in these vessels, than occurs in the cerebral vessels, an

effect which thereby draws blood away from the head.

Between different circle variants, there are large variations in the flows through the communicating arteries. In the 'full circle' geometry, the flows in these vessels are two orders of magnitude lower than the flows through the efferent vessels (Table 3.3). This fact, along with the normal cerebral flows in variant 13, indicates that in the absence of afferent vessel occlusion the complete circle of Willis does not require the communicating arteries in order to adequately supply all six cerebral arteries. However, in certain circle variants (e.g. variants 6, 11, and 12), under normal afferent vessel conditions, the flows through the communicating arteries can be $20-35$ times their values in variant 1, indicating that some of the circle variants rely on this substantial redundant flow capacity through the communicating arteries.

The circle of Willis configuration in which the efferent flows are most affected under healthy conditions is the one missing the proximal segments of both the RACA and the LPCA (variant 10), which was detected in $< 1\%$ of the circles examined by Papantchev *et al.* [11]. In this variant of the circle, the distal RACA and LPCA are both supplied by collateral flow from the LICA, via the ACoA and the LPCoA, respectively. Hence, the LICA carries the blood supply to all three left-sided cerebral territories, as well as the RACA territory. This circle configuration was identified by Papantchev *et al.* [11] as one of the most high risk variations of the circle of Willis structure.

3.4.2 Arterial occlusions

Figure 3.7 shows that blood flow rates through the cerebral arteries fall under conditions of ICA occlusion. Without the effect of autoregulation (Scenario 1), most of the circle of Willis configurations considered here see a flow reduction of $> 10\%$ in at least one of the efferent arteries. The circle variants that were less severely affected were 1, 2, and 4, which therefore present a low risk of cerebral ischaemia

when subjected to LICA occlusion. However, complete cerebral autoregulation (Scenario 2) is able to substantially mitigate flow deficits, i.e. limit them to flow reductions of $< 10\%$, in circle variants 3, 5, 6, 7, 9, 11, and 12. This is because cerebral flow deficits trigger reductions in the R_{sa} values of the autoregulation models coupled to the cerebral arteries, thereby drawing blood through the circle of Willis to these arteries. These circle variants, therefore, present only a moderate risk of ischaemia under LICA occlusion.

The only circle of Willis geometries whose flow reductions were not ameliorated by complete autoregulation were variants 8, 10 and 13. These are networks which lack an exploitable collateral flow route to the LMCA and LACA and, therefore, present a high risk of tissue ischaemia when the LICA is occluded. In these cases the blood supply to the brain is reduced by 38.0%, 63.8%, and 38.0% respectively. In Scenario 3, the net flow to the brain is improved by contralateral autoregulation in all but the high risk circle variants, but flow reductions in the ipsilateral hemisphere are exacerbated. As summarised in Table 3.4, the results presented in Figure 3.7 demonstrate that all of the circle of Willis variants classified as 'medium risk' when comparing Scenarios 1 and 2, are classified as 'high risk' when comparing Scenarios 1 and 3.

Circle of Willis variants that have been identified as 'low-risk', i.e. circles 1, 2 and 4, are likely to protect against significant tissue ischaemia after LICA occlusion. Detection of one of these circle variants might allow clinicians to identify these patients as good candidates for surgical procedures which rely on collateral flow to perfuse brain tissue ipsilateral to a clamped ICA, for example aortic arch repair and carotid endarterectomy [11], [18]. Additionally, stroke patients with these circle of Willis variants are likely to be good candidates for recanalisation therapies such as mechanical clot removal or thrombolysis, due to their relatively high likelihood of successful recanalisation [13] and preservation of autoregulation [45], and their

relatively low risk of haemorrhagic transformation [19].

The circle of Willis variants identified as 'medium-risk', i.e. variants 3, 5, 6, 7, 9, 11, and 12, are those in which cerebral autoregulation in the left hemisphere has critical influence on the health of cerebral tissue when the ipsilateral ICA is occluded. In the context of carotid stenosis, knowledge of the potential of these circle variants to provide collateral flow, and of the status of the autoregulatory response, could aid clinicians in deciding whether to perform carotid endarterectomy with shunting or without (see Section 1.4). The presence of a medium-risk circle of Willis variant would certainly indicate a requirement for perioperative cerebral monitoring during procedures which unilaterally disrupt the blood supply to the brain.

In stroke patients with medium-risk circle variants, assessment of collateral flow, along with ongoing assessment of cerebral autoregulation is essential. The results presented here show that, in these patients, both factors may have substantial influence on the rate at which blood is supplied to vulnerable brain tissue. As cerebral autoregulation has been shown here to be an essential facilitator of collateral flow through these circle variants it may be necessary to monitor autoregulation in the days after acute ischaemic stroke. Several studies have found that impairment of ipsilateral autoregulation can worsen [39], [43] and spread to the contralateral hemisphere [43] in the $5-7$ days after stroke. Such autoregulatory impairment would be likely to compromise the health of any cerebral tissue surviving on collateral blood flow, and therefore further a patient's neurological decline.

Circle variants 8, 10, and 13, are those identified as presenting particularly high risk of cerebral ischaemia during LICA occlusion. Variant 13 was not identified from anatomical or imaging studies, but was proposed in this work to provide the most extreme case of a circle of Willis without any potential for collateral flow. However, variants 8 and 10 have been identified [11]. The detection of these

circles in stenosis patients would allow clinicians to identify the individuals as being at very high risk of stroke, potentially prioritising them as candidates for surgery and indicating that they would require routine shunting during carotid endarterectomy. During stroke, angiography would identify these patients as having 'poor' collateral flow to ischaemic tissue (see Section 2.1.3), signalling a lower likelihood of successful recanalisation therapy, and a higher chance of subsequent haemorrhagic transformation [13], [19].

Figure 3.8 demonstrates that the presence of an available blood flow route, be it through a stenosed LICA, or through narrow proximal ACA and PCA segments, permits autoregulation to return efferent flows to within 6% of their baseline rates (red cerebral arterial flows in Figures 3.8b and 3.8c). Additionally Figure 3.9 shows that if a vessel's area is greater than around 25% of its healthy value, it can permit blood flow at a high enough rate to affect flows through the downstream cerebral arteries. Figure 3.9 indicates that in the event of LICA occlusion, the ACoA is the more valuable collateral route, which is in agreement with previous modelling studies [54], [58].

Figures 3.9a and 3.9b also show that the potential flow capacities of the ACoA and the PCoAs are greater than 3 mls^{-1}, which is up to 100 times the flow rates in these vessels in variant 1, under healthy conditions. This is in agreement with the notion that the communicating arteries are redundant collateral vessels, which are 'recruited' when required. It has been shown using transcranial Doppler measurements during carotid endarterectomy, that this 'switching-on' of collateral vessels can occur within two or three heartbeats [129]. It may be that fortification of these newly recruited collateral routes then occurs, through vessel remodelling, over a period of weeks [129], although this remains very poorly understood. It is possible that, without such remodelling, collateral routes are only able to provide a temporary boost to cerebral blood flows. The endurance of collateral blood supply could be a factor in determining the length of the treatment-window for

recanalisation therapies, and could be implicated in the worsening of cerebral autoregulation which can be seen in the days after stroke [39], [43]. Gradual arterial remodelling occurring over a period of weeks could be one cause of the improvements in the function cerebral autoregulation that have been observed in weeks and months after acute ischaemic stroke [39], [44]

The results of carotid endarterectomy simulations shown in Tables 3.5 – 3.10 are in agreement with the results of Liang *et al.* [66], as the current model identifies the same circle of Willis variants as high risk. The results differ slightly in the case of concurrent BA and ICA stenosis, possibly due to differences in the physiological data used to create the two models. The current model identifies only circle 8 as high risk when the BA and LICA are stenosed, and only the additional circle in which the RACAA1 and RPCAP1 are absent as high risk when the BA and RICA are stenosed. The flow rates in the two circle variants each only reach the 'high risk' threshold in one case of concurrent BA and ICA stenosis, whereas Liang *et al.* identified both of these circle variants as being at high risk, irrespective of which ICA was stenosed. However, in the results presented here both circles do experience substantial increases in flow after surgery, irrespective of which ICA is occluded. The general agreement between the two models provides additional support for the use of the Poiseuille equation as an approximation to the steady state 1D flow equation.

3.4.3 Analysis of the model

The results of modelling blood flow through the complete circle of Willis (Table 3.3 and Figure 3.6) show good agreement with previous studies that have included a model of cerebral autoregulation. For example, the model very closely replicates the results shown in Fig. 4 of Moorhead *et al.* [63]. The main difference is a lower supply of blood to the posterior circulation in the current work, due to higher peripheral resistances distal to the posterior cerebral arteries, and lower blood pressures at the proximal ends of the VAs relative to the ICAs.

In contrast, previous studies [54], [62], [63], [71] have demonstrated autoregulatory control returning efferent flow rates to their reference values in most anatomical variants, after a pressure drop in an ICA. These results have not been reproduced by the modelling work presented here (Figure 3.7). This is due to two differences between the models: firstly, the current work simulates ICA occlusion by setting $r = 0$ when calculating the vessel's resistance, rather than reducing a pressure boundary condition proximal to the ICA. Secondly, the values of the autoregulating peripheral resistances are constrained within this physiological model by the limits of the function for arteriolar compliance (equation 3.6). In the case of LICA occlusion, the maximum changes in the peripheral resistances are seen in the ACA territories of circle of Willis variant 11, which reduce to $R_{sa} + R_v = 0.69R_p$. This limited variation of the peripheral resistance explains the good agreement with the results of Alastruey *et al.* [65] and Moore *at al.* [72]. In the study by Alastruey *et al.* [65] the peripheral resistances were constrained to: $0.74R_p < R < 1.30R_p$ and in the study by Moore *et al.* [72] the range of arterial blood pressures over which the peripheral resistances could be adjusted was bounded to $75 - 175\ mmHg$. In contrast, several modelling works [62], [63], [71] have included autoregulation in the peripheral resistances of the cerebral arterial network using PID control techniques, without modelling the physiological mechanism that causes vasodilation and vasoconstriction of the cerebral arterioles. These modelling studies have constrained the peripheral resistances to $0.05R_p < R < 1.95R_p$, providing the cerebral territories with a greater ability to draw blood through the low pressure ICA and the communicating arteries.

Many modelling studies of blood flow through the circle of Willis use Poiseuille's law. This is because most blood flow in humans is laminar; Reynold's numbers in the circle of Willis are well below $Re = 2000$, the value at which transition to turbulence begins. Also, in contrast to the compliant, elastic-walled arteries close to the heart such as the aorta, the common carotid arteries and the subclavian arteries, the arteries that constitute the circle of Willis are muscular walled and much more rigid. Stergiopulos *et al.* [131] give values of compliance for the internal

and external carotid arteries that are two orders of magnitude lower than the compliance of the aorta. The elasticity of the aorta and its major branches allows these vessels to constrain the high pressure of blood at peak systole, to reduce the variation in blood pressure over the cardiac cycle, and to thereby reduce the pulsatility of blood. Still, blood flow in the circle of Willis is somewhat pulsatile and, therefore, unsteady. However, as this work aimed to model blood flows over timescales much longer than the cardiac cycle, flow pulsatility was neglected. Payne [135] presents a mathematical justification for the use of Poiseuille's law as a highly accurate approximation to the linearised 1D flow equation in steady state.

Some research groups have compared the results of unsteady flow simulations, made using models of the circle of Willis in higher dimensions, with similar simulations made using models based on the assumption of Poiseuille flow. For example, Hillen *et al.*'s 1988 study [54] gave a lumped parameter representation of their 1986 1D flow model of the circle [53]. While the total flow rate of blood through the circle was 8% lower in the lumped-parameter model, there was almost no difference ($< 0.2\%$) in the distribution of blood flows between the afferent arteries, between the circulus arteries, or between the efferent arteries. The authors concluded that the assumption of Poiseuille flow was acceptable and explained that the difference in total flow occurred due to the larger time-averaged diameters and hence lower resistances of the vessels in the 1D flow model.

Moore *et al.*'s 2005 study produced lumped-parameter and non-pulsatile 3D representations of the circle of Willis of one person [71]. They found that the 3D model required lower peripheral resistances to match the efferent flows of the lumped-parameter model, which they attributed to greater losses in blood pressure in the 3D model. While the two models in Moore *et al.*'s study produced very similar efferent flows, the distributions of blood flow between the circulus arteries differed substantially. The study found that this difference could be corrected by modifying the individual vessel resistances. The authors postulated that the differences in flow

distributions were due to an incorrect assumption of Poiseuille flow in the arteries of the circle of Willis, particularly in the ACoA, which did not provide flow rates of $> 0.4\ ml/s$ in their 3D model. However, it is also possible that these differences resulted from the different boundary conditions imposed at the efferent arteries of the two models through the use of different peripheral resistances. A 3D modelling study by the same authors in 2006 did not report such low flows through the ACoA [72].

The non-autoregulating model presented in this chapter provides a lumped-parameter representation of the 1D flow model of Alastruey *et al.* [58]. The magnitude of the total blood flow through the circle of Willis is higher in the present lumped-parameter model than in the Alastruey *et al.* model, which has been explained (in Section 3.4.1) as resulting from the absence of flow pulsatility and deformable arterial walls. However, the percentage distributions of blood flows to the cerebral arteries and through the circulus arteries are extremely closely matched in the two models. Furthermore, in contrast to the 3D modelling results of Moore *et al.* [71], but in agreement with the lumped-parameter modelling in the same study, and the later 3D modelling results of Moore *et al.* [72], both the model presented in this Chapter, and the model of Alastruey *et al.* [58], show the ACoA as able to permit blood flow at rates above 1 ml/s (Table 3.3). Thus, the work presented here, in line with the theoretical justification provided by Payne [135], supports the conclusion that the assumption of Poiseuille flow is valid in the case of blood flow in the large arteries supplying the brain.

The model presented here has provided insight into the importance of collateral flow pathways and autoregulation in the maintenance of cerebral blood flows during afferent vessel occlusion. It is novel in that it incorporates a spatially variable model of cerebral autoregulation, enacted through peripheral resistance variations, which are brought about by pressure induced changes in arteriolar compliance. The network model in this study was based on averaged physiological data measured in

healthy young adults [58]. These data may differ from those of a cerebrovascular disease cohort, for example stroke patients often present as hypertensive [2], a factor which will affect the results of network simulations. Thus, the main limitations of this study lie in its lack of specificity to individual subjects and the lack of experimental validation. Refinement of the model, using patient-specific information on arterial geometry, arteriolar resistance, and network boundary conditions could provide potentially clinically useful information about individual patients with carotid stenosis or stroke. This could then be used to inform personalised treatment planning for these patients.

3.5 Summary

A simplified cerebral arterial network was modelled in steady state. The model has been shown to compare well with 1D flow models of the same network, and with data of measured flow rates in the cerebral arteries. The results of simulations of LICA occlusion show that collateral flow alone is unable to ensure adequate blood flow ($> 90\%$ normal flow) to the cerebral arteries in several common variants of the circle of Willis. In contrast to a passive vascular bed, the model indicates that cerebral autoregulation is better able to exploit available collateral flow and to maintain flows within 10% of baseline. This is true for nearly all configurations of the arterial circle. However, results showed that if the autoregulatory response is partially impaired then, in the autoregulating hemisphere, cerebral flows are preserved at the expense of those on the ipsilateral side. Autoregulation is a crucial facilitator of collateral flow through the circle of Willis. However, contralateral autoregulation can exacerbate flow reductions if not balanced by the same response in the vascular beds on the ipsilateral side. Hence, the status of the autoregulatory response in both hemispheres can strongly influence cerebral blood flows and tissue survival and should, therefore, be monitored in stroke over the period of likely changes.

4
ASL angiography models

As discussed in Chapter 2, cerebral angiography is an essential method for visualising the arterial lumen in the assessment of, and treatment planning for, cerebrovascular disease. Angiography can be used to detect arterial stenoses and occlusions. Its utility in detecting collateral flow can be valuable in the planning of surgical interventions, such as aortic arch repair and carotid endarterectomy, and in the monitoring of intra-arterial interventions such as carotid artery stenting and mechanical clot retrieval.

An ideal cerebral angiography modality would provide quantitative, time-resolved visualisation of the internal carotid arteries, the vertebral arteries, the circulus arteries of the circle of Willis and the six cerebral arteries, without the need for the injection of a potentially toxic contrast agent or exposure to ionising radiation. The most clinically-important parameters that could be determined using cerebral angiography are the flow rates of blood through individual arteries. An ideal cerebral angiography modality would enable flow rate measurements to be performed over small vessel segments as this would allow flow rate quantification in smaller arteries. For example, the ability to quantify flow in short vessel segments could allow direct measurement of blood flow rates in the posterior communicating arteries and in

branches from the cerebral arteries.

Unfortunately, as discussed in Section 2.3, most conventional cerebral angiography techniques fall short of the ideal standard described above. Only transcranial doppler ultrasound (TCD), phase contrast (PC) MRA, and arterial spin labelling (ASL) MRA avoid the potentially harmful effects of toxic contrast medium or ionising radiation. Both TCD and PC-MRA are quantitative techniques, but it is not possible to visualise the entire circle of Willis using TCD [2], and PC-MRA measures blood flow velocity rather than blood volume flow rate, meaning that flow rates must be subsequently calculated using additional measurements of vessel area. Furthermore PC-MRA is time consuming to acquire and can suffer from partial voluming effects.

ASL is essentially a contrast enhanced angiography technique in which arterial blood becomes an endogenous contrast agent through spin labelling of its water protons. Attempts have been made, by van Osch *et al.* [90] and Okell *et al.* [22], [91], [126], to measure blood volume flow rates from ASL angiograms. van Osch *et al.*'s model fitting method used vessel-selective, dynamic, 2D pulsed ASL (PASL) data to estimate blood flow rates in the cerebral arteries. In tests of the technique on images of a flow phantom, they showed that the method consistently quantified flow rates in the range $0.1 - 4\ mls^{-1}$ with an underestimation of $10 - 15\%$. However, the method required acquisition of an additional calibration scan.

Okell *et al.* [91] attempted to quantify flow rates using dynamic, vessel-encoded, pseudo-continuous ASL (PCASL) images of 2D thick slabs showing transverse and coronal views of the circle of Willis. Using their technique, Okell *et al.* quantified flows in a phantom, in the range: $0.3 - 8.1\ mls^{-1}$, with an underestimation of only $2 \pm 3\%$. However, as described in Section 2.4.4, the Okell *et al.* method required consideration of an image region-of-interest (ROI) which covered the entire simulated labelled blood bolus. In practice this limited the resolution of blood flow

measurements to one measurement in each of the large afferent and efferent arteries of the circle of Willis and meant that direct measurements of flow through the small circulus arteries were impossible.

The work presented in this chapter aims to provide a method for flow quantification in smaller arterial segments than those used by Okell *et al.* [91]. A new, model-based method for performing blood volume flow rate estimation from PCASL MRA is proposed. The chapter outlines the mathematical fluid flow modelling theory underpinning the PASL technique of van Osch *et al.* [90] and develops a novel PCASL flow model based on the same principles. It then explains the use of the PCASL and PASL models to perform quantitative angiography. Measurements of flow rates in vessel-encoded PCASL (VEPCASL) MRA images were carried out using curve fitting to estimate parameters of the PCASL flow model. The chapter describes this curve fitting process and then examines the performance of the technique on VEPCASL angiography images of both a flow phantom and of the cerebral vasculature of healthy individuals.

4.1 Theory

The ASL MR signal measured in an ROI of a vessel can be modelled by considering the mass transport of an ASL labelled bolus of fluid and integrating the signal it produces over the volume of the region. Consider a bolus of a detectable fluid (ASL labelled blood or water) flowing through a straight, axisymmetric cylinder. The concentration of the label, c, decays at a rate determined by T_{1b}, the longitudinal relaxation of the ASL signal (discussed in Section 2.4.1). In this work, the ASL tracer concentration c, is defined as the ratio of the volume of ASL labelled blood to the volume of non-labelled blood. At any point along the vessel, c is given by the general mass transport equation:

$$\frac{\partial c(x,r,t)}{\partial t} + U(r)\frac{\partial c(x,r,t)}{\partial x} = -\frac{c(x,r,t)}{T_{1b}} \tag{4.1}$$

where t is time, x is axial distance along the tube and $U(r)$ is the axial velocity profile of the fluid. Assuming that the fluid is incompressible, $U(r)$ can be approximated by the following flow profile:

$$U(r) = \bar{U}\left(\frac{\gamma+2}{\gamma}\right)\left(1-\left(\frac{r}{R}\right)^{\gamma}\right) \tag{4.2}$$

In equation 4.2, $\bar{U}$ is the average axial velocity of the fluid. $U(r)$ can take a range of forms: from uniform plug flow to fully developed, parabolic, Hagen-Poiseuille flow [136]. The parameter γ controls the shape of the velocity profile; it can take any value greater than 2 (parabolic flow) and as $\gamma \to \infty$ the velocity profile tends towards uniform plug flow. Hence, γ controls the variation in the axial velocity with radius and, therefore, incorporates the element of bolus dispersion which results from this effect. As $\gamma \to \infty$, the effect of bolus dispersion resulting from a non-uniform axial velocity profile disappears.

The aim of this flow modelling exercise is to produce an expression that successfully models detected ASL difference signals. In order to use the model to estimate blood flow rates through arteries by curve fitting, the model must include the flow rate of blood as one of its defining parameters. The ASL difference signal, at any point in an artery, is related to the concentration of ASL labelled blood, through the calibration factor, S_0:

$$s(x,r,t) = S_0 c(x,r,t) \tag{4.3}$$

MR signals are measured over the small volumes of voxels, the total ASL difference signal measured from a volume of blood V is:

$$S(x,r,t) = \int_V s(x,r,t)dV \tag{4.4}$$

as V becomes small relative to the length scale over which c varies:

$$S(x,r,t) \to Vs(x,r,t) \tag{4.5}$$

Thus, over a small volume, such as the volume of a voxel, the detectable signal $S(x,r,t)$ is scaled by the small volume of ASL labelled blood within the voxel. It is,

therefore, not possible to obtain voxel-wise information about blood flow. Instead, integration over a larger, multi-voxel, vessel segment is required, allowing timing information about the accumulation and wash out of ASL labelled blood to be observed in the region-wise signal. This modelling principle was adopted by both van Osch *et al.* [90] and Okell *et al.* [91], and is also applied in the work presented in this chapter. It is first used to model PASL angiography signals, as an expression for the PASL signal measured in an ROI can be obtained analytically, then the same techniques are applied in the context of PCASL angiography signals.

4.1.1 Pulsed arterial spin labelling

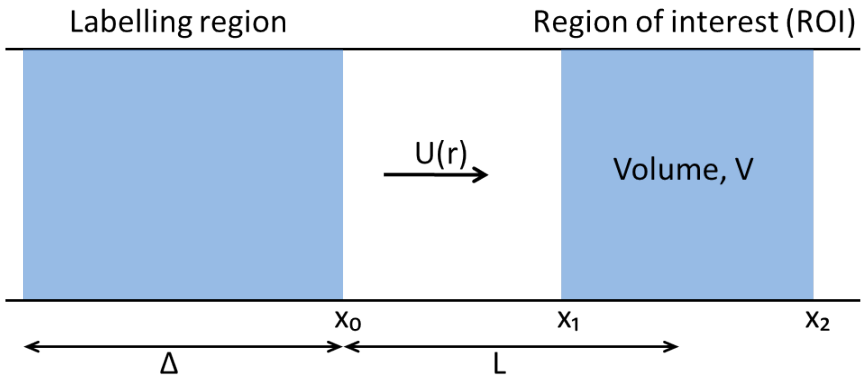


Figure 4.1: Schematic of pulsed arterial spin labelling of an artery modelled as a rigid-walled tube. PASL occurs in the labelling region, from $x_0 - \Delta$ to x_0, and the ASL MR signal is measured in the ROI, between x_1 and x_2. $U(r)$ is the axial flow velocity profile of blood, defined in equation 4.2.

Figure 4.1 provides a simplified representation of the PASL process. In PASL, the entire blood bolus is labelled simultaneously in a thick slab ($x_0 - \Delta$ to x_0 in Figure 4.1, creating a labelled bolus of length Δ). The labelled blood bolus is then assumed to flow through a straight rigid-walled, axisymmetric artery to the vessel ROI, with the axial velocity profile $U(r)$, as shown. Due to the rapid, simultaneous labelling of blood the label begins to decay immediately at every point in the bolus. PASL solutions to equation 4.1 thus take the form:

$$c(x, r, t) = f\left(x - U(r)t\right) e^{-t/T_{1b}} \tag{4.6}$$

where $$f\left(x - U(r)t\right) = f(x_0, r, t = 0) = c(x_0, r, 0)$$

The ASL signal created in the labelling plane is a rectangular pulse, which can be described mathematically as:

$$f(x) = H(x + \Delta) - H(x) \tag{4.7}$$

where $H(.)$ is the Heaviside unit step function and Δ is the spatial width of the labelled ASL bolus. Hence,

$$f\left(x - U(r)t\right) = H\left(x - U(r)t + \Delta\right) - H\left(x - U(r)t\right) \tag{4.8}$$

The ASL difference signal generated at any point in the vessel is:

$$s(x, r, t) = S_0 c(x, r, t) \tag{4.9}$$

$$= S_0 \left[H\left(x - U(r)t + \Delta\right) - H\left(x - U(r)t\right)\right] e^{-t/T_{1b}} \tag{4.10}$$

The ASL signal measured in an ROI (Figure 4.1) is given by the integration of equation 4.10 over the volume, V, of the ROI.

$$S_{ROI}(t) = S_0 \int_{ROI} c(x, r, t)\, \mathrm{d}V \tag{4.11}$$

As described in Section 2.4.4, the RF excitation pulses of the Look-Locker readout attenuate the ASL signal of labelled water in the imaging region. The modified relaxation time T_{1m} is shorter than T_{1b}, meaning that the signal decays faster when in the imaging plane. An ASL signal is continuous at the time of initiation of PASL imaging, $t = t_p$, when the modified relaxation time begins to apply, thus the following scaling factor is applied:

$$S_{ROI}(t_p) e^{-t_p/T_{1b}} = e^{-t_p\left(1/T_{1b} - 1/T_{1m}\right)} S_{ROI}(t_p) e^{-t_p/T_{1m}} \tag{4.12}$$

Meaning that

$$S_{ROI}(t < t_p) = S_0 e^{-t/T_{1b}} \int_{ROI} f(x - U(r)t)\, \mathrm{d}V \tag{4.13}$$

$$S_{ROI}(t > t_p) = S_0 e^{-t/T_{1m}} e^{-t_p\left(1/T_{1b} - 1/T_{1m}\right)} \int_{ROI} f(x - U(r)t)\, \mathrm{d}V \tag{4.14}$$

Hence,

$$\begin{aligned}
S_{ROI} &= S_0 e^{-t/T_{1b}} e^{(t-t_p)\ln(cos\alpha)/T_R} \Bigg\{ \int_{ROI} [H(x - U(r)t + \Delta) \\
&\qquad\qquad -H(x - U(r)t)] \, \mathrm{d}V \Bigg\} \\
&= S_0 e^{-t/T_{1b}} e^{(t-t_p)\ln(cos\alpha)/T_R} \Bigg\{ \int_{r=0}^{R} \int_{x_1}^{x_2} 2\pi r \, [H(x - U(r)t + \Delta) \\
&\qquad\qquad -H(x - U(r)t)] \, \mathrm{d}r \, \mathrm{d}x \Bigg\} \\
&= 2\pi R^2 S_0 e^{-t/T_{1b}} e^{(t-t_p)\ln(cos\alpha)/T_R} \Bigg\{ \int_{a=0}^{1} a \int_{x_1}^{x_2} [H(x - U(r)t + \Delta) \qquad (4.15) \\
&\qquad\qquad -H(x - U(r)t)] \, \mathrm{d}x \, \mathrm{d}a \Bigg\} \\
&= 2\pi R^2 g_p(t) \Bigg\{ \int_{a=0}^{1} a \int_{x_1}^{x_2} [H(x - U(r)t + \Delta) \qquad (4.16) \\
&\qquad\qquad -H(x - U(r)t)] \, \mathrm{d}x \, \mathrm{d}a \Bigg\}
\end{aligned}$$

where α is the flip angle, and T_R the repetition time, of the RF attenuation pulses, and $a = {}^{r}/_{R}$. The calibration factor and decay terms have been condensed into one time-dependent term, $g_p(t)$. Integrating the Heaviside functions with respect to x leads to:

$$\begin{aligned}
S_{ROI} &= 2\pi R^2 g_p(t) \int_{a=0}^{1} a \Big[(x - U(a)t + \Delta) \, H \, (x - U(a)t + \Delta) \qquad (4.17) \\
&\qquad\qquad - (x - U(a)t) \, H \, (x - U(a)t) \Big]_{x_1}^{x_2} \mathrm{d}a \\
&= 2\pi R^2 g_p(t) \Bigg\{ \; - \int_{a=0}^{1} (x_1 - U(a)t) \, H \, (U(a)t - x_1) \, a \, \mathrm{d}a \qquad (4.18) \\
&\qquad\qquad + \int_{a=0}^{1} (x_2 - U(a)t) \, H \, (U(a)t - x_2) \, a \, \mathrm{d}a \\
&\qquad\qquad + \int_{a=0}^{1} (x_1 - U(a)t + \Delta) \, H \, (U(a)t - x_1 - \Delta) \, a \, \mathrm{d}a \\
&\qquad\qquad - \int_{a=0}^{1} (x_2 - U(a)t + \Delta) \, H \, (U(a)t - x_2 - \Delta) \, a \, \mathrm{d}a \Bigg\}
\end{aligned}$$

The four integrals in equation 4.18 can all be solved using the same process, which is demonstrated here just for the first integral. Firstly, a Heaviside function

is only equal to one when its argument is greater than zero, so:

$$H\left(U(a)t - x_1\right) = 1$$

when $$U(a)t > x_1$$

i.e. $$\bar{U}t\left(\frac{\gamma+2}{\gamma}\right)\left(1-a^{\gamma}\right) > x_1$$

$$\left(1-a^{\gamma}\right) > \frac{\gamma x_1}{(\gamma+2)\,\bar{U}t}$$

$$\left[1-\frac{\gamma x_1}{(\gamma+2)\,\bar{U}t}\right]^{1/\gamma} > a \tag{4.19}$$

Including the flow profile model (equation 4.2) in the first integral, termed I_1, and using equation 4.19 to redefine the limits of integration with respect to a gives:

$$\begin{aligned} I_1 &= \int_{a=0}^{1}\left(x_1 - U(a)t\right)H\left(U(a)t - x_1\right)a\,\mathrm{d}a \\ &= \int_{a=0}^{\left[1-\frac{\gamma x_1}{(\gamma+2)\bar{U}t}\right]^{1/\gamma}}\left[a\,x_1 - \bar{U}t\left(\frac{\gamma+2}{\gamma}\right)\left(a-a^{\gamma+1}\right)\mathrm{d}a\right]\cdot H\left(t-t_1\right) \end{aligned} \tag{4.20}$$

This exists when the upper limit of integration is larger than the lower limit:

$$0 < \left[1-\frac{\gamma x_1}{(\gamma+2)\,\bar{U}t}\right]^{1/\gamma}$$

Hence, $$t_1 = \frac{\gamma x_1}{(\gamma+2)\bar{U}} \tag{4.21}$$

Integration and simplification of equation 4.20 gives:

$$I_1 = \frac{L}{2T}\left[t_1 - t\right]\left[1-\frac{t_1}{t}\right]^{2/\gamma}\cdot H\left(t-t_1\right) \tag{4.22}$$

where $T = L/\bar{U}$. The three further integrals that made up equation 4.18 can all be solved in the same way as the first integral (equations 4.19-4.22) leading to the following results:

$$I_2 = \frac{L}{2T}\left[t_2 - t\right]\left[1-\frac{t_2}{t}\right]^{2/\gamma}\cdot H\left(t-t_2\right) \qquad \text{where } t_2 = \frac{\gamma x_2}{(\gamma+2)\bar{U}}$$

$$I_3 = \frac{L}{2T}\left[t_3 - t\right]\left[1-\frac{t_3}{t}\right]^{2/\gamma}\cdot H\left(t-t_3\right) \qquad \text{where } t_3 = \frac{\gamma\left(x_1+\Delta\right)}{(\gamma+2)\bar{U}}$$

$$I_4 = \frac{L}{2T}\left[t_4 - t\right]\left[1-\frac{t_4}{t}\right]^{2/\gamma}\cdot H\left(t-t_4\right) \qquad \text{where } t_4 = \frac{\gamma\left(x_2+\Delta\right)}{(\gamma+2)\bar{U}}$$

Thus, the final model of a PASL signal, integrated over an ROI is:

$$S_{ROI} = BFg_p(t)\Bigg\{ -[t_1 - t]\left[1 - \frac{t_1}{t}\right]^{2/\gamma} \cdot H(t - t_1) + [t_2 - t]\left[1 - \frac{t_2}{t}\right]^{2/\gamma} \cdot H(t - t_2) + [t_3 - t]\left[1 - \frac{t_3}{t}\right]^{2/\gamma} \cdot H(t - t_3) - [t_4 - t]\left[1 - \frac{t_4}{t}\right]^{2/\gamma} \cdot H(t - t_4)\Bigg\} \quad (4.23)$$

The BF parameter represents the volume flow rate of blood through the ROI: $BF = \frac{\pi R^2 L}{T} = \pi R^2 \bar{U}$.

4.1.2 Pseudo-continuous arterial spin labelling

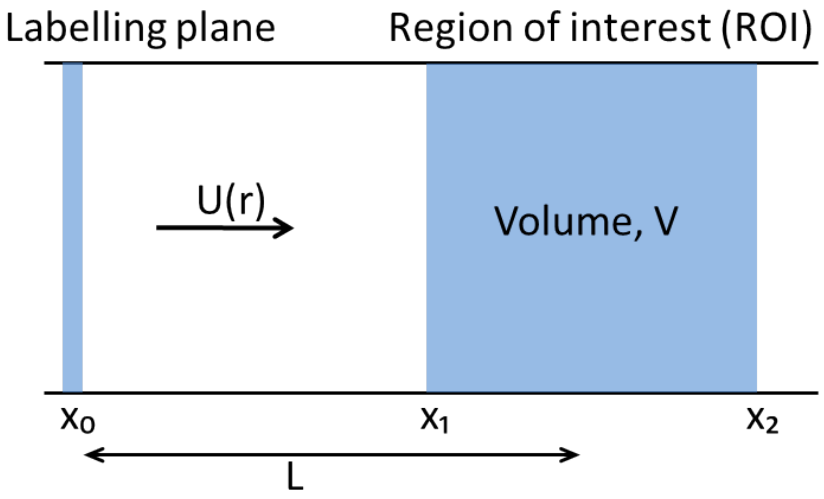


Figure 4.2: Schematic of pseudo-continuous arterial spin labelling of an artery modelled as a rigid-walled tube. PCASL occurs as blood flows through the labelling plane, at x_0, and the ASL MR signal is measured in the ROI, between x_1 and x_2. $U(r)$ is the axial blood flow velocity profile defined in equation 4.2.

Figure 4.2 provides a schematic representation of the PCASL process. PCASL differs from PASL in that blood is labelled over a relatively long period of time, the labelling duration τ, as it flows through a thin plane (at x_0 in Figure 4.2). As the whole of the blood bolus is not labelled simultaneously in PCASL, T_1 decay of the label begins at different times for different parts of the bolus. Hence, labelled

blood arriving at a point x within a vessel will all have been labelled for the same length of time and therefore, undergone the same amount of T_1 decay. Taking the Laplace transform of equation 4.1, with the initial condition, $c(x, r, 0) = 0$, gives the following Laplace-domain solution:

$$c(x, r, s) = B(s)e^{-sx/U(r)}e^{-x/U(r)T_{1b}} \tag{4.24}$$

where $B(s)$ is the constant of integration and s is frequency in the Laplace domain.

Equation 4.25 defines the boundary condition for PCASL at x_0, the labelling plane:

$$c\left(x_0, t\right) = H(t) - H(t - \tau) \tag{4.25}$$

The Laplace transform of equation 4.25 can be used to eliminate B, in equation 4.24. Hence, the exact time-domain PCASL solution to equation 4.1 is:

$$c\left(x, r, t\right) = \left[H\left(t - \frac{x}{U\left(r\right)}\right) - H\left(t - \frac{x}{U\left(r\right)} - \tau\right)\right] e^{-x/U(r)T_{1b}} \tag{4.26}$$

As in PASL imaging, the signal from the ASL label is attenuated by the readout RF excitation pulses it experiences as it passes through the imaging region. This effect is accounted for by multiplying equation 4.26 by a term which effectively shortens the longitudinal relaxation time of the ASL label, as in equation 4.15:

$$c\left(x, r, t < t_c\right) = e^{-x/U(r)T_{1b}}\left[H\left(t - \frac{x}{U\left(r\right)}\right) - H\left(t - \frac{x}{U\left(r\right)} - \tau\right)\right] \tag{4.27}$$

$$\begin{aligned} c\left(x, r, t > t_c\right) = e^{\left[-x/U(r)T_{1b}\right]}e^{\left[(t-t_c)\ln(cos\alpha)/T_R\right]}\Bigg[&H\left(t - \frac{x}{U\left(r\right)}\right) \\ &-H\left(t - \frac{x}{U\left(r\right)} - \tau\right)\Bigg] \end{aligned} \tag{4.28}$$

where t_c is the time at which PCASL imaging begins. In this work it is assumed that all of the ASL labelled blood bolus experiences all of the RF excitation pulses. However, this assumption is only strictly true for MRA images in which the labelling plane is immediately adjacent to, or contained within, the imaging slab.

The MR signal, at any point in an artery, is related to the volume of ASL labelled blood, through the calibration factor, S_0, as described by equation 4.9. In order to estimate the volume flow rate of blood through an artery, knowledge of the passage of the bolus into, and through, a vessel segment is required. Hence, equation 4.28 is integrated over the volume of an ROI (as shown in equation 4.11), as follows:

$$S_{ROI}\left(t > t_c\right) = S_0 e^{(t-t_c)lncos(\alpha)/T_R} \left\{ \int_{r=0}^{R} \int_{x_1}^{x_2} 2\pi r \left[H\left(t - \frac{x}{U\left(r\right)}\right) - H\left(t - \frac{x}{U\left(r\right)} - \tau\right)\right] e^{-x/U(r)T_{1b}} dx dr \right\} \tag{4.29}$$

$$= S_0 e^{(t-t_c)lncos(\alpha)/T_R} \pi R^2 \left\{ \int_{a=0}^{1} a \int_{x_1}^{x_2} 2 \left[H\left(t - \frac{x}{U(r)}\right) - H\left(t - \frac{x}{U(r)} - \tau\right)\right] e^{-x/U(r)T_{1b}} dx da \right\} \tag{4.30}$$

During the integration by parts of equation 4.30, the constants: $\bar{U}$, $\left(\gamma + 2\right)/\gamma$ and T_{1b} are taken outside of both of the integrals. In the case of plug flow ($\gamma \to \infty$ in equation 4.2), the radial integral in equation 4.30 is tractable and the solution is:

$$\begin{aligned} S_{ROI}(t > t_c) = BF S_0 T_{1b} e^{(t-t_c)ln(cos\alpha)/T_R} \cdot \Big\{ & \left[e^{-x_1/U(r)T_{1b}} - e^{-t/T_{1b}}\right] \cdot H(t - t_1) \\ & - \left[e^{-x_2/U(r)T_{1b}} - e^{-t/T_{1b}}\right] \cdot H(t - t_2) \\ & - \left[e^{-x_1/U(r)T_{1b}} - e^{\tau - t/T_{1b}}\right] \cdot H(t - t_3) \\ & + \left[e^{-x_2/U(r)T_{1b}} - e^{\tau - t/T_{1b}}\right] \cdot H(t - t_4) \Big\} \end{aligned} \tag{4.31}$$

where again BF is the net flow rate of blood through the arterial segment. In equation 4.31, $t_1 = x_1/\bar{U}$, $t_2 = x_2/\bar{U}$, $t_3 = t_1 + \tau$, $t_4 = t_2 + \tau$. However, for all other flow profiles the radial integral in equation 4.30 is not tractable and must be solved numerically. Like equation 4.31, its solutions are equations made up of four groups of terms, and each group of terms contributes to the signal only

after a certain time point has been reached.

$$t_1 = \frac{\gamma x_1}{(\gamma+2)\bar{U}} \tag{4.32}$$

$$t_2 = \frac{\gamma x_2}{(\gamma+2)\bar{U}} \tag{4.33}$$

$$t_3 = t_1 + \tau \tag{4.34}$$

$$t_4 = t_2 + \tau \tag{4.35}$$

These timing parameters, and those in the PASL model described in Section 4.1.1 (equation 4.23), mark the stages of the progression of an ASL labelled bolus of blood through a defined ROI. Figure 4.3 shows examples of both PASL and PCASL MRA signals modelled using equations 4.23 and 4.30, respectively, using equal bolus durations. The red dotted lines at $t = t_p$ and $t = t_c$ mark the initiations of PASL and PCASL imaging, respectively. At these time points, the boluses start to undergo the attenuating effects of the RF readout pulses; in the PCASL signal the effect of this can be seen as a change in gradient. The modelled signals in Figure 4.3 show five distinct stages:

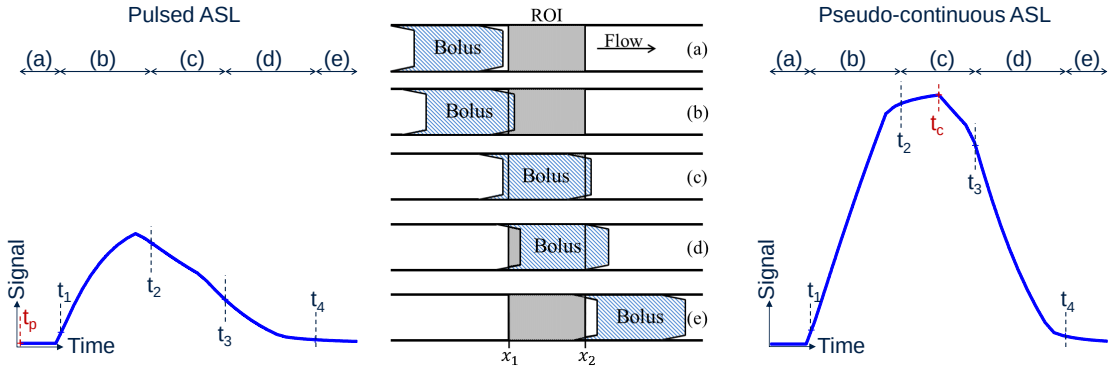


Figure 4.3: The modelled ASL MR signal in an ROI, and the bolus passage stages that produce it. In the figure the timing parameters t_1, t_2, t_3, and t_4 mark the progression of blood flowing at the **mean** axial velocity $\overline{U}$ through the ROI in five stages (a) to (e), which are described in the text below. As a non-uniform axial flow velocity profile was used to produce this figure ($\gamma = 3$) the timing parameters for the two signals lag behind the visible points of inflection, which mark the progression of the fastest flowing blood through the ROI.

(a) $t < t_1$: there is no ASL labelled blood in the ROI and, therefore, no signal.

(b) $t_1 < t < t_2$, the leading edge of the bolus has arrived in the ROI. The volume of ASL labelled blood in the ROI rapidly increases, as does the signal amplitude.

(c) $t_2 < t < t_3$: the leading edge of the bolus begins to leave the ROI. At this point the volume of ASL labelled blood in the ROI remains approximately constant as blood flows into and out of the region at the same flow rate. Even so, the PASL signal amplitude declines between these two time points, influenced by T_1 decay and RF attenuation. In the example PCASL signal, the initiation of imaging causes a sharp change in gradient at $t = t_c$. Prior to this time point the signal undergoes T_1 decay only, however this is not observed as a decline in the PCASL signal because all blood arriving at a distance x from the labelling plane has undergone T_1 decay for the same length of time due to delayed labelling of later parts of the PCASL bolus.

(d) $t_3 < t < t_4$: the trailing edge of the bolus arrives in the ROI, meaning the ASL signal amplitude decreases rapidly because more labelled blood leaves the ROI than enters it, as unlabelled blood has begun to enter the region again.

(e) $t_4 < t$: as the trailing edge of the bolus leaves the ROI, the ASL signal gradually tails away.

Fitting this ASL signal model to the measured angiography signal from an ROI allows estimation of the model parameters: BF, γ, t_1, t_2, t_3, t_4.

4.2 Materials and methods

4.2.1 Data

Phantom data

For the purpose of validating their method of quantifying blood flow rates in cerebral arteries, Okell *et al.* [91] acquired vessel encoded ASL dynamic angiography images of a flow phantom. The flow phantom was made by pumping water through two rubber tubes in the MR scanner bore, at known flow rates. An example image of

the flow phantom is shown in Figure 4.4. The images acquired were of a $50\,mm$ thick slab with $1.1\,mm$ x $1.1\,mm$ voxels interpolated to $0.55\,mm$ x $0.55\,mm$. Image acquisition began 1.028 seconds after the start of VEPCASL labelling and 20 frames were acquired, with a temporal resolution of $55\,ms$. Scans of the phantom were acquired over a flow rate range extending beyond the rates expected in the cerebral vasculature: $0.3 - 8.1\ ml/s$. The flow phantom images were used in this study to validate the proposed flow model based blood flow estimation technique. The fact that these data had already been used by Okell *et al.* [91] to measure blood flow rates in the circle of Willis meant that a direct comparison of the two techniques could also be made.

Healthy volunteers

The human data used here have been used in several previous studies [22], [91], [126], [137]. The data come from six healthy volunteers (4 male, 2 female, age range 24-39, mean age 32) scanned by Okell *et al.* [22], under a protocol agreed with local ethics and institutional committees [22]. None of the volunteers was known to have a neurological disease. Transverse and coronal vessel-encoded dynamic angiography views of the circle of Willis were acquired ($50\,mm$ and $100\,mm$ thick imaging slabs, respectively). The temporal resolution of the sequence of images was $55\,ms$ and the time sequence included 20 frames. Each image covered a 205x154 mm field-of-view with $1.1\,mm$ x $1.1\,mm$ voxels, interpolated to $0.55\,mm$ x $0.55\,mm$ [22]. The VEPCASL data from volunteers were used to test the proposed blood flow estimation technique. Figure 4.5 gives examples of coronal (Fig. 4.5a) and transverse (Fig. 4.5b) VEPCASL views of the circle of Willis of one of the healthy volunteers, with blood supplied by each of the four afferent arteries shown in a different colour.

4.3 Parameter estimation

The parameters $BF, \gamma, t_1, t_2, t_3, t_4$ were chosen as the set of parameters to be estimated from the data rather than of a possible alternative spatial parameter set which would include: BF, R, x_1, x_2, Δ, and γ in the case of PASL, or BF, R, x_1, x_2,

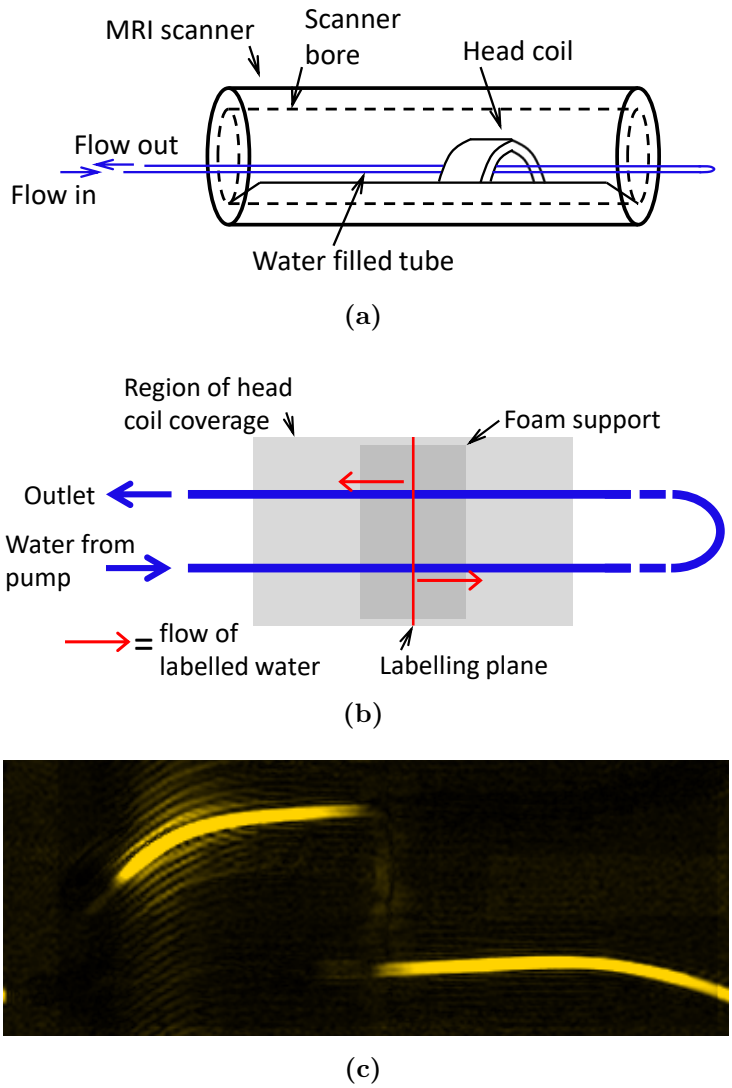
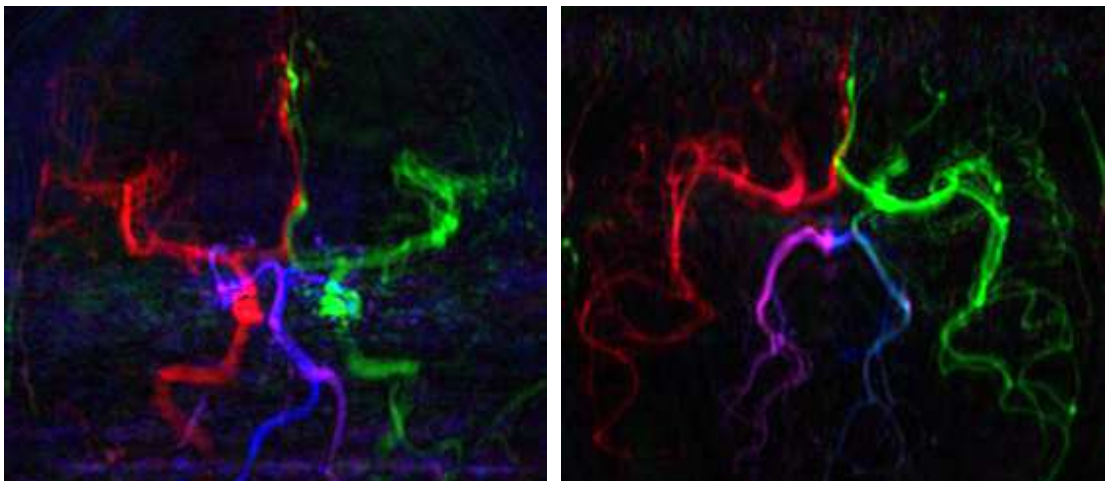


Figure 4.4: Water flow phantom used to validate the model-based flow quantification technique developed in this chapter: (a) schematic showing the position of the phantom in the MRI scanner bore; (b) schematic seen from above, showing labelling of water in the flow phantom; and (c) example PCASL image of the phantom, collected by Okell *et al.* [91]. The tube on the left of the image shows a substantial motion artefact.

and γ in the case of PCASL. The decision not to perform curve fitting to estimate the spatial parameter set resulted from the significant challenges of determining initial estimates of the spatial parameters from the data. Establishing initial estimates of the spatial parameters would require several additional measurements to be made from the angiography images. These measurements would likely prove unreliable due to the 2D thick-slab nature of the acquisitions and the tortuosity of the afferent and efferent arteries of the circle of Willis.



(a) Coronal view **(b)** Transverse view

Figure 4.5: Vessel encoded PCASL images of the circle of Willis of one healthy volunteer, created using the data acquired by [22]. Blood labelled in the RICA is shown in red, LICA blood is shown in green, RVA blood is in blue, and LVA blood is shown in magenta.

4.3.1 Calibration factor

As the data used here have previously been used for testing the flow quantification technique of Okell et al. [91], the value of the calibration parameter S_0 was already known for each data set, and did not have to be calculated in this work.

4.3.2 Vessel regions

The ASL signal measured in each voxel or region of an image can be thought of as the integral of $s(x, r, t)$ over the volume of blood in that voxel or region. Hence, the measured signal in any ROI is calculated by summing the ASL signals from each voxel within it. The parameters of the PASL and PCASL flow models can be estimated by finding the sets of parameters that minimise a cost function measured between the imaged region signal and the modelled signal.

The fact that imaging did not commence until labelling was complete meant that, in the case of PCASL, most of the vessels in the angiograms were already filled with ASL labelled blood by $t = t_c$, limiting the timing information captured

in the acquired signal (see Figure 4.3). In consideration of this, two possible vessel region conditions were used:

1. A single region covering a short segment of a single vessel.

2. The region described in (1) was used (and is referred to here using the subscript 'B'), along with an additional, shorter, upstream vessel segment, which is referred to using the subscript 'A'. This additional region was included to provide more timing information about the bolus' passage, by contributing an additional measured signal which can be described using a second set of model parameters, and which can be related to the parameters that describe the signal in region B.

4.3.3 Constraints

The modelled signals were fitted to the corresponding measured signals. Where only a single vessel region was used, the parameter set required to define the flow model was: BF, γ, t_1, t_2, t_3, t_4. When two coupled vessel regions were used, the blood flow rate, BF, and the dispersion parameter, γ, were assumed to be common to the blood flow between the two regions. This left the parameters required to define the two models as: BF, γ, t_{1_A}, t_{2_A}, t_{3_A}, t_{4_A}, t_{1_B}, t_{2_B}, t_{3_B}, t_{4_B}.

PASL

It is possible to reduce the model parameter space using relations between the timing parameters. Firstly, it can be assumed that the duration of the labelled ASL bolus does not change within a vessel region, meaning that:

$$t_3 - t_1 = t_4 - t_2 \tag{4.36}$$

$$t_1 = t_2 + t_3 - t_4 \tag{4.37}$$

Hence

$$t_{1_B} = t_{2_B} + t_{3_B} - t_{4_B} \tag{4.38}$$

$$t_{1_A} = t_{2_A} + t_{3_A} - t_{4_A} \tag{4.39}$$

Secondly, when two coupled vessel regions are used, it can be assumed that the duration of the ASL bolus does not change between the two regions, thus:

$$\begin{aligned} t_{4_A} - t_{2_A} &= t_{4_B} - t_{2_B} \\ t_{2_A} &= t_{4_A} + t_{2_B} - t_{4_B} \end{aligned} \tag{4.40}$$

After making these assumptions, the PASL parameters which must be estimated during curve fitting are BF, γ, t_2, t_3, and t_4 when fitting to a signal from only one region, or BF, γ, t_{2_B}, t_{3_B}, t_{4_B}, t_{3_A}, and t_{4_A} when fitting to coupled signals from two regions. The remaining time parameters can be further subjected to inequality constraints:

$$t_2, t_3 \leq t_4 \tag{4.41}$$

$$t_{3_B} \leq t_{4_B} \tag{4.42}$$

$$t_{2_B} \leq t_{4_B} \tag{4.43}$$

$$t_{4_A} \leq t_{3_B} \tag{4.44}$$

$$t_{3_A} \leq t_{4_A} \tag{4.45}$$

PCASL

In PCASL, imaging begins later than in PASL ($t_c > t_p$) meaning that fewer data points are available for use in the estimation of the model parameters. However, in PCASL imaging the initial duration of the ASL bolus is known, and it can again be assumed that the duration of the bolus does not change between two coupled regions. Thus, equations 4.34 and 4.35 can be used to reduce the PCASL model parameter space with the following relations:

$$t_{1_B} = t_{3_B} - \tau \tag{4.46}$$

$$t_{1_A} = t_{3_A} - \tau \tag{4.47}$$

$$t_{2_B} = t_{4_B} - \tau \tag{4.48}$$

$$t_{2_A} = t_{4_A} - \tau \tag{4.49}$$

where τ refers to the PCASL bolus duration introduced in equation 4.25.

This leaves a total of four PCASL parameters to be estimated from curve fitting when the model is fitted to the signal from a single region (BF, γ, t_3, t_4). Six parameters are estimated when the model is fitted to signals from two coupled regions, A and B (BF, γ, t_{3_B}, t_{4_B}, t_{3_A}, and t_{4_A}). Inequality constraints 4.41, 4.42, 4.44 and 4.45 can also be applied in the fitting of the PCASL signal flow model.

4.3.4 Curve fitting

Parameter estimation was performed by minimisation of a 'cost function' which provided a measure of the difference between the measured and modelled signals from either a single region, or from two coupled regions. A Bayesian maximum *a posteriori* (MAP) method was used, as it allowed prior information about the values of the model parameters to be taken into account during their estimation. The method assumes normally distributed priors on each of the model parameters. In MAP estimation, Bayes' theorem gives the posterior probability $p(\mathbf{\Theta} \mid \mathbf{y}, \mathcal{M})$ of the parameters $\mathbf{\Theta}$, given the data $\mathbf{y}$ and the model $\mathcal{M}$, as directly proportional to the product of the likelihood function $p(\mathbf{y} \mid \mathbf{\Theta}, \mathcal{M})$ and the prior distributions on the parameters $p(\mathbf{\Theta})$.

Assuming Gaussian noise on the data, with standard deviation σ, the likelihood function is:

$$p(\mathbf{y} \mid \mathbf{\Theta}, \mathcal{M}) = \frac{1}{(2\pi)^{N/2}\,\sigma^N} \cdot e^{-\frac{1}{2\sigma^2}[\mathbf{y}-\mathbf{f}(\mathbf{\Theta})]^T[\mathbf{y}-\mathbf{f}(\mathbf{\Theta})]} \tag{4.50}$$

where $\mathbf{f}(\mathbf{\Theta})$ is a vector of the modelled signal sampled at the same N time points as the data $\mathbf{y}$. The posterior distribution, the maximum of which corresponds to the most likely set of model parameters, can be obtained by multiplying the likelihood function by the Gaussian prior distributions, each with mean μ_X and standard deviation σ_X:

$$p(\mathbf{\Theta} \mid \mathbf{y}, \mathcal{M}) = p(\mathbf{y} \mid \mathbf{\Theta}, \mathcal{M})\, p(\mathbf{\Theta}) \tag{4.51}$$

The maximum of the posterior probability distribution is found by minimising its negative logarithm. The parameter-dependent cost function is therefore:

$$C_1(\Theta)_{MAP} = -\ln\left[p\left(\mathbf{\Theta} \mid \mathbf{y}, \mathcal{M}\right)\right] \tag{4.52}$$

$$\propto N \ln\sigma + \frac{1}{2\sigma^2}\left[\mathbf{y} - \mathbf{f}\left(\mathbf{\Theta}\right)\right]^T\left[\mathbf{y} - \mathbf{f}\left(\mathbf{\Theta}\right)\right] + \frac{1}{2}\sum_{X\in\Theta}\frac{\left(X-\mu_X\right)^2}{\sigma_X^2} \tag{4.53}$$

Here the parameter set $\mathbf{\Theta}$ includes σ, the noise standard deviation, making it an additional parameter to be estimated in the curve fitting process. A second cost function can be obtained by marginalising out the noise parameter using a non-informative Jeffrey's prior: $p(\phi) = \phi^{-1}$ where $\phi = 1/\sigma^2$. This was done to remove noise from the set of parameters estimated by curve fitting:

$$p\left(\mathbf{y} \mid \mathbf{\Theta}, \mathcal{M}\right) = \int_0^\infty p\left(\mathbf{y} \mid \mathbf{\Theta}, \mathcal{M}, \phi\right) p\left(\phi\right) d\phi \tag{4.54}$$

$$= \int_0^\infty \frac{\phi^{\frac{N}{2}-1}}{\left(2\pi\right)^{N/2}} \cdot e^{-\frac{\phi}{2}[\mathbf{y}-\mathbf{f}(\mathbf{\Theta})]^T[\mathbf{y}-\mathbf{f}(\mathbf{\Theta})]} d\phi \tag{4.55}$$

If $\chi^2 = \left[\mathbf{y} - \mathbf{f}\left(\mathbf{\Theta}\right)\right]^T\left[\mathbf{y} - \mathbf{f}\left(\mathbf{\Theta}\right)\right]$

$$p\left(\mathbf{y} \mid \mathbf{\Theta}, \mathcal{M}\right) = \int_0^\infty \frac{\phi^{\frac{N}{2}-1}}{\left(2\pi\right)^{N/2}} \cdot e^{-\frac{\phi\chi^2}{2}} d\phi \tag{4.56}$$

Using the substitution $t = \phi\chi^2/2$ and therefore, $d\phi = 2dt/\chi^2$ gives:

$$p\left(\mathbf{y} \mid \mathbf{\Theta}, \mathcal{M}\right) = \frac{2}{\left(2\pi\right)^{N/2}} \int_0^\infty \left(\frac{2t}{\chi^2}\right)^{\frac{N}{2}-1} \cdot e^{-t}\frac{dt}{\chi^2} \tag{4.57}$$

$$= \frac{2}{\left(2\pi\right)^{N/2}} \int_0^\infty \left(\frac{1}{\chi^2}\right)^{\frac{N}{2}} (2t)^{\frac{N}{2}-1} \cdot e^{-t} dt \tag{4.58}$$

$$= \frac{2}{\left(2\pi\right)^{N/2}} \left(\frac{1}{\chi^2}\right)^{N/2} \int_0^\infty (2t)^{\frac{N}{2}-1} \cdot e^{-t} dt \tag{4.59}$$

This expression for the likelihood function is now composed of a parameter dependent factor (outside of the integral), multiplied by an integral over all t. The value of this integral is only dependent on the value of N, the number of time points at which the signal and the modelled signal are each sampled. The posterior distribution is obtained as before:

$$p\left(\mathbf{\Theta} \mid \mathbf{y}, \mathcal{M}\right) = \frac{2}{\left(2\pi\right)^{N/2}} \left(\frac{1}{\chi^2}\right)^{N/2} \int_0^\infty (2t)^{\frac{N}{2}-1} \cdot e^{-t} dt \cdot \prod_{X\in\Theta} e^{-\frac{(X-\mu_X)^2}{2\sigma_X^2}} \tag{4.60}$$

$$= \frac{2}{\left(2\pi\right)^{N/2}} \left(\frac{1}{\chi^2}\right)^{N/2} \int_0^\infty (2t)^{\frac{N}{2}-1} \cdot e^{-t} dt \cdot \prod_{X\in\Theta} e^{-\frac{\phi_X}{2}(X-\mu_X)^2} \tag{4.61}$$

The negative logarithm of the posterior distribution is:

$$-\ln\left[p\left(\mathbf{\Theta}\mid\mathbf{y},\mathcal{M}\right)\right]=\frac{N}{2}\ln\left(\chi^2\right)+\sum_{X\in\Theta}\left(X-\mu_X\right)^2\frac{\phi_X}{2}$$
$$-\ln\left\{\frac{2}{(2\pi)^{N/2}}\int_0^\infty(2t)^{\frac{N}{2}-1}\cdot e^{-t}dt\right\} \tag{4.62}$$

Thus, the parameter-dependent cost function is:

$$C_2(\Theta)_{MAP}=\frac{N}{2}\ln\left\{\left[\mathbf{y}-\mathbf{f}(\mathbf{\Theta})\right]^T\left[\mathbf{y}-\mathbf{f}(\mathbf{\Theta})\right]\right\}+\frac{1}{2}\sum_{X\in\Theta}\frac{\left(X-\mu_X\right)^2}{\sigma_X^2} \tag{4.63}$$

Optimisation

The cost functions (equations 4.52 and 4.63) were minimised using the 'MultiStart' facility from the Matlab Global Optimisation toolbox. This optimisation tool generates $n-1$ pseudo-random initial points within a bounded parameter space, then uses these start points and a user supplied initial point to run $n=500$ instances of the multivariate constrained optimisation algorithm (*fmincon.m*). The bounds used to constrain the parameter space are given in Table 4.1. The MultiStart algorithm was run on one node of the University of Oxford Advanced Research Computing resource with the n instances on *fmincon.m* sent to the 16 parallel processing cores of that one node. MultiStart was assigned a maximum duration of 10 *minutes*. After this time period, MultiStart collected the optimisation solutions that defined local minima found by *fmincon.m* and identified the parameter set which gave the lowest value of the cost function, and then selected this parameter set as the optimum solution.

Table 4.1: Constraints placed on the PCASL model parameters during curve fitting.

	BF	γ	$t_4(t_{4B})$	$t_3(t_{3B})$	t_{4A}	t_{3A}
Units	ml/s	—	s	s	s	s
Lower bound	0	2	τ	τ	τ	τ
Upper bound	12	15	4	4	4	4

Initial Conditions

The use of the Matlab MultiStart algorithm resulted in the generation of 499 initial parameter sets in addition to the one user-supplied set. Thus, the use of this algorithm is likely to have minimised the influence of the given initial condition on the optimised parameter set. However, initialisation of the model parameters was performed on the phantom and human data signals, as described below.

When testing the quantification technique on signals from images of the flow phantom and of human circles of Willis, the initial model parameter estimates were derived from the region-wise ASL signals. The region signals were re-sampled at five times their temporal resolution using the Matlab *interp.m* function. This function inserts zeros into a signal and applies a low-pass interpolating filter to the resulting extended signal, leaving the data points of the original signal unchanged. From the interpolated signal the t_3 and t_4 values for each region signal were estimated as the times at which the signal amplitude fell to 70% and 10% of the peak amplitude, respectively. If the image acquisition period captured the in-flow, rather than the wash-out, of the bolus in a region of interest, then t_1 and t_2 were estimated as the times at which the signals first rose to 30% and 90% of the signal peak, respectively. These thresholds were determined based on visual assessment of the ROI signals. The values of t_3 and t_4 were then obtained by adding the bolus duration, τ, using equations 4.34 and 4.35.

An initial estimate of the axial flow profile shape parameter, γ, was obtained by fitting a decaying exponential to the tail end of the ROI signal i.e. to all of the time points recorded after the estimated value of t_4. The relaxation rate of the fitted exponential decay curve was then taken to be γ. An initial estimate of BF was made by fixing the values of t_3, t_4, and γ at their initial estimates and then fitting the PCASL flow model to the measured ROI signal with BF as the only free variable. The noise standard deviation, σ, was initially taken to be equal to the number of voxels contained within the ROI mask.

Priors

The use of a maximum *a posteriori* cost function allowed 'prior information' about each parameter to be taken into account in parameter estimation. This information was included in the form of Gaussian prior probability distributions. For the phantom and human data signals, the priors on the model parameters had means equal to the estimated initial values obtained from simple analysis of the region signals (described above). The standard deviations of the parameter priors were set such that, in these early validation and testing experiments, the priors were close to flat within the range of the constraints (Table 4.1): $\sigma_{BF} = 8\ ml/s$, $\sigma_{\gamma} = 8$, and $\sigma_{t_4,t_3,t_{4B},t_{3B},t_{4A},t_{3A}} = 10\ seconds$. The standard deviation of the prior on the noise parameter, σ_{σ}, was equal to the number of voxels contained within the ROI mask.

4.3.5 Experiments performed

The flow phantom data was acquired with water flowing through it at a range of eight known flow rates ($0.3 - 8.1\ ml/s$). This meant that the data could be used to validate the performance of the flow model technique against a ground truth. Thus, the results of this process were used to obtain the optimal conditions for application of the technique to flow quantification using the human data.

Validation using phantom data

Parameter estimation using the VEPCASL images of a flow phantom (Section 4.2.1) was performed over a range of possible region sizes, with a 10 mm region A, and a variable-length region B. Region A began 10 mm from the labelling plane and there was a separation between the end of region A and the start of region B, equal to 5 mm. A total of 15 region B lengths were considered, from 5 mm to 74 mm. Using these regions, the parameter estimation technique was used on phantom data signals of the eight different phantom flow rates. The PCASL flow model was fitted to the signals from all 15 region B signals alone, using cost function $C_1(\Theta)_{MAP}$. The PCASL flow model was also fitted to the signals from region A coupled to

the 15 region B signals, using cost function $C_2(\Theta)_{MAP}$. Thus, the flow model was used for parameter estimation using two methods:

Method 1 – Cost function $C_1(\Theta)_{MAP}$ was used to fit the PCASL model to signals from a single ROI.

Method 2 – Cost function $C_2(\Theta)_{MAP}$ was used to fit the PCASL model to signals from two coupled ROIs.

The flow quantification methods were evaluated through analysis of their ability to estimate the eight phantom flow rates (0.3–8.1 ml/s). As van Osch *et al.* [90] had tested their technique on phantom data with flow rates in the range 0–4 ml/s, the performance of Method 1 and Method 2 was also analysed over just the first six flow rates seen in the VEPCASL phantom images (0.3–3.8 ml/s). The performance of the technique was deemed 'successful' if, over the considered flow rates, the mean error and one standard deviation were within 15% of the known values. Furthermore, the technique was also directly compared with the existing method of Okell *et al.* [91]. This was done by running the Okell *et al.* quantification technique on the region B vessel segments used here in testing the flow model parameter estimation technique. It should be noted that the longest ROI used in the work described in this chapter (74 mm) was shorter than the (100 mm) vessel region used to produce Figure 6d in Okell *et al.* [91].

Testing on human data

Informed by the results of flow phantom experiments, 'Method 1' was used to apply the flow model quantification technique to the human data (Section 4.2.1). Using the VEPCASL images of six healthy volunteers, estimates of blood flow rates in the afferent and efferent arteries of the circle of Willis were made. For each volunteer data set, vessel regions were outlined on eight arteries (ICAs, MCAs, VAs, BA, and combined ACAs) in the coronal view of the circle, and on five arteries in the transverse view (MCAs, PCAs, and combined ACAs). The left and right ACAs were considered together in both the coronal and the transverse

views of the circle as they could not be clearly distinguished as separate vessels. Where possible, the outlined vessel regions were within the length range $30 - 45$ mm. Again, the blood flow parameter estimates, made using the signals summed over these regions, were compared directly to the estimates made by applying the existing method of Okell *et al.* [91].

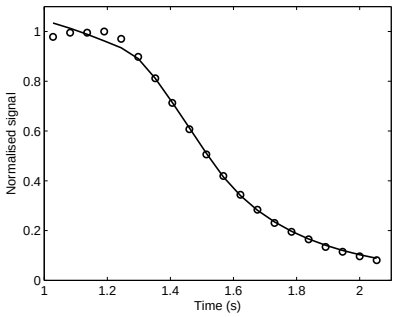
4.4 Results

4.4.1 Phantom data

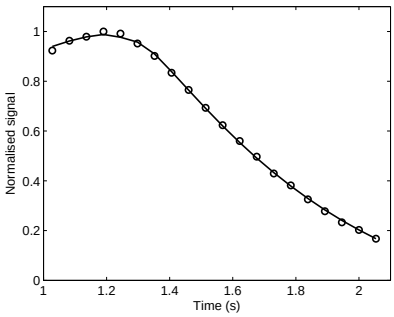
Curve fits

Figure 4.6 shows PCASL signals from the flow phantom images (circle markers). The signals are from water flowing at three different flow rates, and were detected in two vessel regions, a 35 mm long region (Figures 4.6a, c, and e) and a 74 mm long region (Figures 4.6b, d, and f). The plots also show the PCASL flow models optimised to represent the measured signals most closely (solid lines). These optimised model fits were obtained using Method 1 (see Section 4.3.5). The caption beneath each subfigure in Figure 4.6 gives the resulting estimates of blood flow, BF, and the axial velocity profile shape parameter, γ. The signals in Figures 4.6a – d show that the ability to fit the PCASL flow model to the signals from the flow phantom is dependent on both the length of the considered vessel region, and the flow rate of water through the vessel. For example, at the lower flow rate of 0.73 ml/s, the model was unable to represent the bolus inflow part of the signal (seen at $1 - 1.3$ *seconds* in Figure 4.6a) when the 35 mm region was used, but the curve fit to this section of the signal was improved when the larger 74 mm region was used (Figure 4.6b) and slightly more of the bolus' inflow was detected.

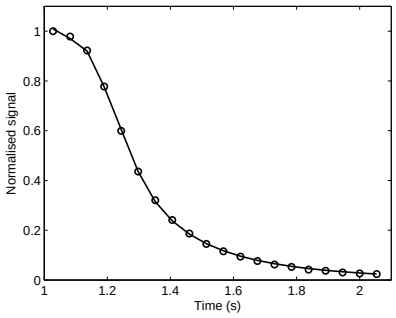
Figures 4.6e and 4.6f show that at the highest water flow rate of 8.13 ml/s, only the very tail end of the ASL bolus signal was captured in the images due to the late onset of imaging in PCASL. At this flow rate very little additional information about the shape of the signal was obtained through the use of larger vessel regions. Even when the largest region length of 74 mm was used (Fig. 4.6f)



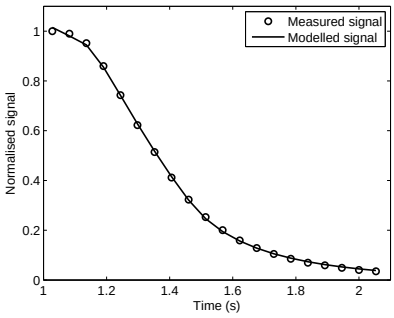
(a) 0.73 ml/s in a 35 mm vessel segment. $BF = 0.76$ ml/s, $\gamma = 2.00$



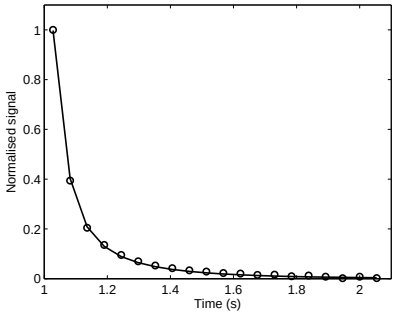
(b) 0.73 ml/s in a 74 mm vessel segment. $BF = 0.56$ ml/s, $\gamma = 5.10$



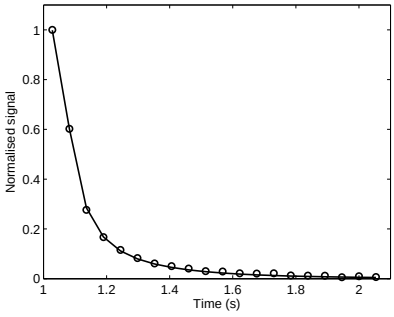
(c) 1.57 ml/s in a 35 mm vessel segment. $BF = 1.55$ ml/s, $\gamma = 2.55$



(d) 1.57 ml/s in a 74 mm vessel segment. $BF = 1.51$ ml/s, $\gamma = 2.73$



(e) 8.13 ml/s in a 35 mm vessel segment. $BF = 6.86$ ml/s, $\gamma = 2.20$



(f) 8.13 ml/s in a 74 mm vessel segment. $BF = 6.67$ ml/s, $\gamma = 3.28$

Figure 4.6: Example curves produced using Method 1 to fit the proposed PCASL flow model (solid lines) to flow phantom signals (circle markers). Both the data and the model in each subfigure have been normalised with respect to the maximum of the data time series in that subfigure.

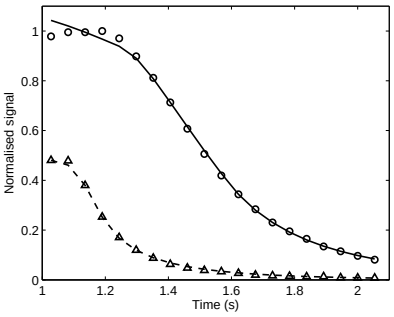
the measured signal did not show the sudden change in gradient associated with the model parameter t_3 and the transition of the bolus' passage from stage (c) to stage (d) (shown in Figure 4.3).

Figure 4.7 shows example results from curve fitting using Method 2. In Figure 4.7, the region B signals are identical to the signals seen in Figure 4.6 because the same regions were used in both cases. Note that vessel region A was outlined in exactly the same place on all of the flow phantom images. Thus, while the region A signals varied with water flow rate, they did not vary with the size of region B. This is not immediately evident from the signals in Figure 4.7 because both the measured and modelled signals in each subfigure have been normalised with respect to the maximum value of the measured region B signal in that subfigure.

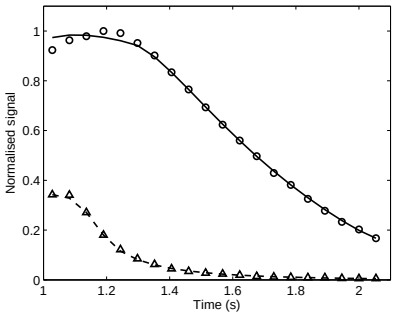
The Method 2 results in Figure 4.7, can be compared to the corresponding Method 1 results in Figure 4.6. The coupling of two region signals appears to have had little effect on the model fit to the measured region B signal in Figure 4.7a, but the fit to the inflow part of the measured region B signal in Figure 4.7b worsened slightly. However, the region-coupling involved in Method 2 has prevented the underestimation of BF which was seen in the Method 1 results when the 74 mm ROI was used (see Figure 4.6b caption). The region B curve fits seen in Figures 4.7c – 4.7f are remarkably similar to those seen in Figures 4.6c – f. In Figures 4.7c and 4.7d, the coupled curve fits produce estimates of the flow rate and flow profile parameters which are very close to those estimated with the curve fits in Figures 4.6c and 4.6d (see subfigure captions). However, the model fits in Figures 4.7e and 4.7f result in BF estimates much higher than those obtained by fitting to just the signal from region B using Method 1 (Figures 4.6e and 4.6f).

Flow rate estimates

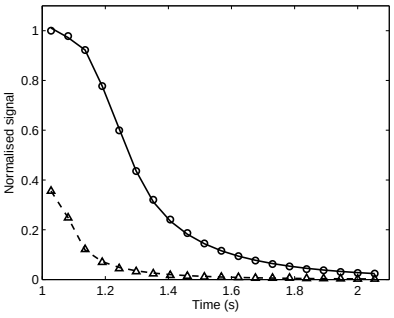
Figures 4.8 and 4.9 show the results of flow rate quantification performed on one of the tubes seen in the VEPCASL images of the flow phantom (Figure 4.4); the



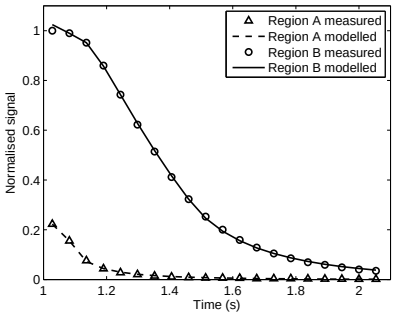
(a) 0.73 ml/s in a 35 mm vessel segment. $BF = 0.66$ ml/s, $\gamma = 2.36$



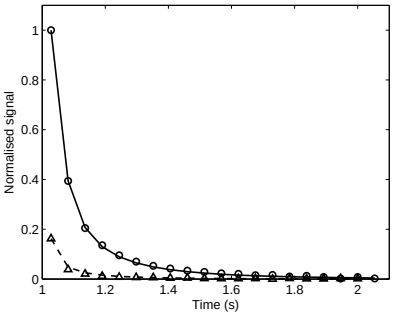
(b) 0.73 ml/s in a 74 mm vessel segment. $BF = 0.63$ ml/s, $\gamma = 2.65$



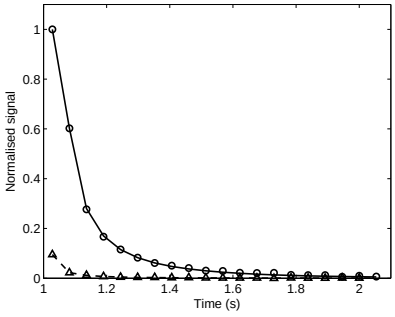
(c) 1.57 ml/s in a 35 mm vessel segment. $BF = 1.54$ ml/s, $\gamma = 2.64$



(d) 1.57 ml/s in a 74 mm vessel segment. $BF = 1.47$ ml/s, $\gamma = 2.81$



(e) 8.13 ml/s in a 35 mm vessel segment. $BF = 9.27$ ml/s, $\gamma = 2.00$



(f) 8.13 ml/s in a 74 mm vessel segment. $BF = 12.0$ ml/s, $\gamma = 2.82$

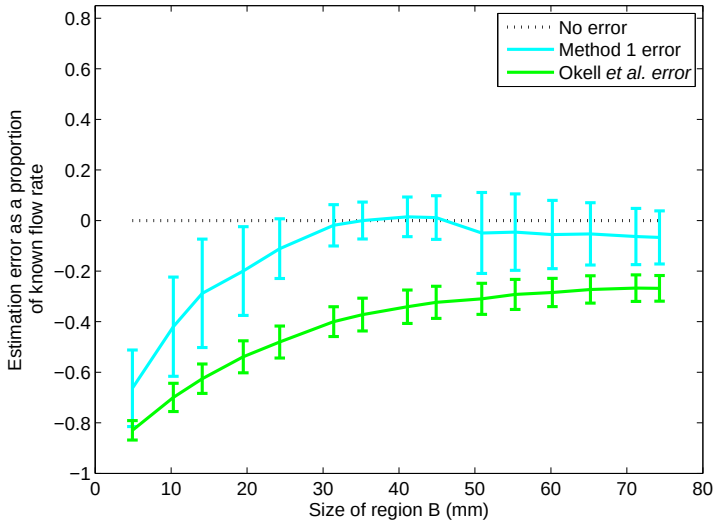
Figure 4.7: Example curves produced using Method 2 to fit the proposed PCASL flow model (solid and dashed lines) to flow phantom signals (circle and triangle markers). Both the region A and region B data and the two region models in each subfigure have been normalised with respect to the maximum of the region B data time series in that subfigure.

tube that showed a substantial motion artefact was excluded. The results in Figure 4.8 were obtained by fitting the PCASL flow model to flow phantom signals using Method 1 (pale blue lines), and by applying the technique of Okell *et al.* [91] to signals from the same vessel region (green lines). Each point on the graph gives the mean error of the phantom flow rate estimates, as a proportion of the known values, plotted against the length of the vessel segment used to obtain the estimates. In Figure 4.8a the plotted error values are the averages over all eight phantom flow rates. Figure 4.8b gives the error over just the lowest six phantom flow rates, i.e. those less than 4 ml/s. The error bars show one standard deviation above and below the mean value.

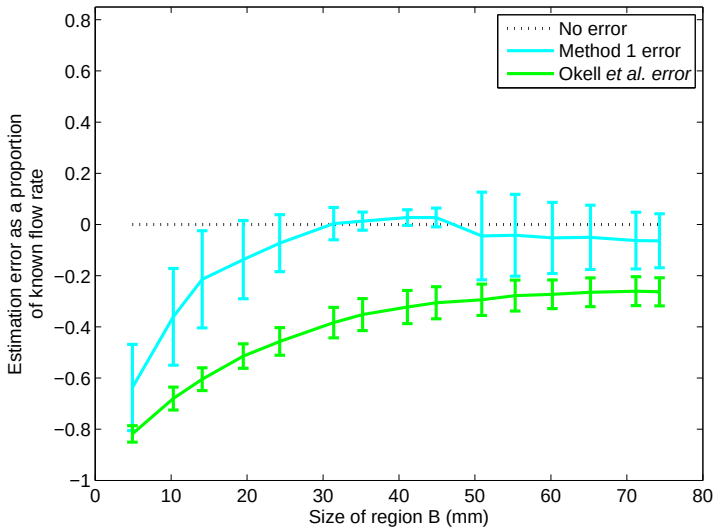
Figure 4.8a shows that the use of Method 1, in which the noise parameter σ was included in the set of parameters estimated from the data, provided accurate estimates of blood flow rates (in terms of the mean and one standard deviation of the error: $-0.15 < \mu \pm \sigma < 0.15$, as defined in Section 4.3.5) when the considered vessel segment length was in the range 30 mm to 45 mm. In vessel segments shorter than 30 mm, water flow rates were underestimated, with the degree of underestimation decreasing with increasing ROI size. There is an increase in the standard deviation of the estimation error as region size increases from 45 to 50 mm. This was a result of the problem of fitting the model to the short inflow section of the PCASL signal, which was seen in Figures 4.6a and 4.6b and will be discussed later with reference to those figures.

Figure 4.8a also shows that the PCASL flow model technique for flow rate estimation applied using Method 1 was more accurate than the Okell *et al.* [91] method, across all of the vessel region lengths considered here. The aim of the work described in this chapter was to develop a quantification technique that could be applied to short vessel segments. Thus, the range of ROIs considered here did not extend to particularly long regions which covered all of the flow phantom tube (Figure 4.4), which is the range of region lengths over which the Okell *et al.*

technique produces highly accurate flow rate estimates.



(a) Mean error, and standard deviation of the error, on estimates of all eight flow rates measured in the flow phantom.



(b) Mean error, and standard deviation of the error, on estimates of the first six flow rates measured in the flow phantom, i.e. excluding the 7th and 8th flow rates, which were greater than 4 ml/s.

Figure 4.8: Results of water flow rate estimation performed by fitting the proposed PCASL model to flow phantom signals using Method 1.

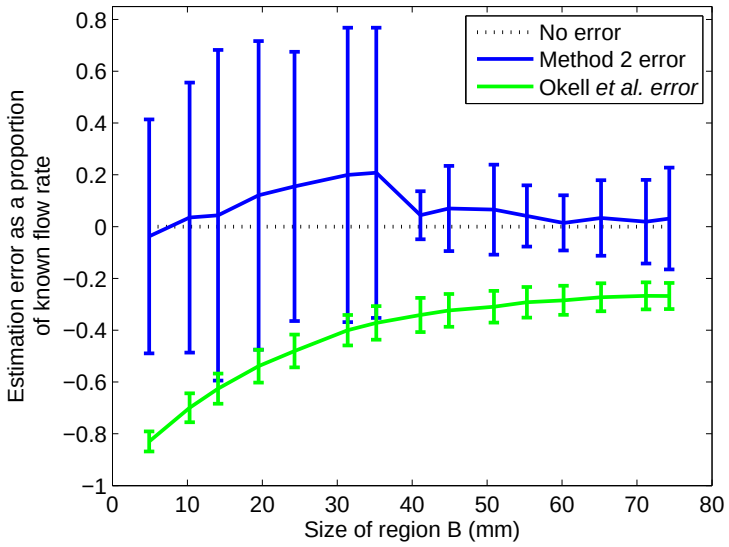
Figure 4.9a shows results of water flow rate quantification obtained using Method 2 over all eight flow rates measured in the phantom. It shows that the use of Method

2 leads to substantially larger variability in flow rate estimates. This method only provided acceptable flow rate estimates at two separate region B lengths: 40 mm and 60 mm. Unlike the Method 1 results in Figure 4.8a, when using Method 2 there was not a range of region lengths that provide accurate estimates of water flow rates.

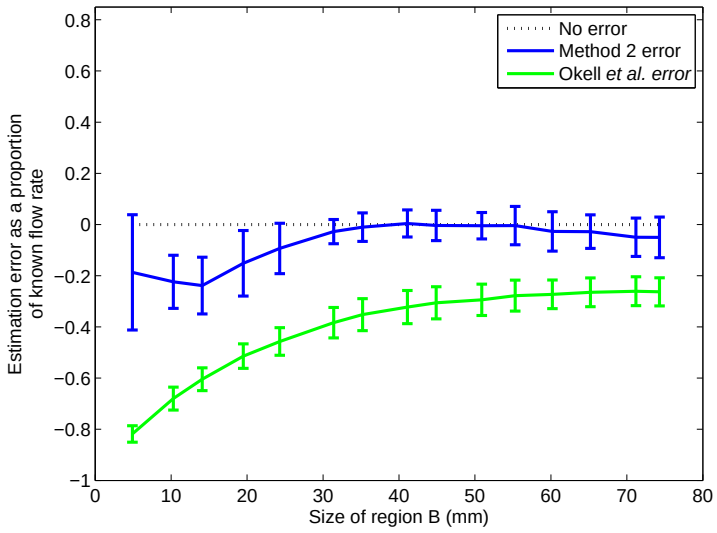
The performance of the flow model technique was also evaluated over the flow rate range considered by van Osch *et al.* [90], i.e. over just the lowest six phantom flow rates seen in the PCASL phantom data ($0.3 - 3.8$ ml/s). Figures 4.8b and 4.9b show that flow rate estimation performed using both Method 1 and Method 2 was more accurate over the six lower flow rates. When the model was applied using Method 1 (Fig. 4.8b), the exclusion of the two highest phantom flow rates reduced the standard deviation of flow rate estimation errors in the vessel segment length range $30 - 45$ mm, although it did not widen this 'acceptable' range. Conversely, Figure 4.9b shows that, when considering only the six slower phantom flow rates, the performance of Method 2 improved markedly. The mean errors across the six flow rates, and one standard deviation either side of these values, remained within ± 0.15, for all region B lengths in the range $30 - 75$ mm.

4.4.2 Human data testing

Based on the results of the flow phantom experiments, the proposed PCASL flow model technique was next applied, using Method 1, to estimate flow rates in the arteries of the circles of Willis of healthy volunteers, from the VEPCASL images described in Section 4.2.1. In Figures 4.10 – 4.13 the subfigures labelled (a) show image masks used to define the vessel segments over which the ROI signals were summed. The signals from these regions were used to obtain the blood flow rate estimates with the PCASL flow model. These estimates are shown, in subfigures labelled (c), as coloured stacked bars with thick black borders. Also included in Figures 4.10 – 4.13 (in subfigures labelled (b)) are images showing the vessel-region masks used by Okell *et al.* [91] to perform blood flow rate quantification on the same images. The flow rates estimated using the Okell technique with these region



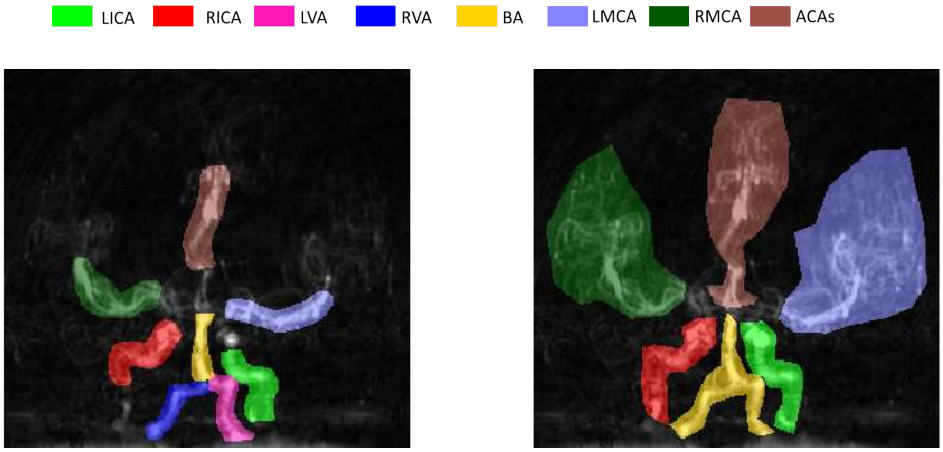
(a) Mean error, and standard deviation of the error, on estimates of all eight flow rates measured in the flow phantom.



(b) Mean error, and standard deviation of the error, on estimates of the first six flow rates measured in the flow phantom, i.e. excluding the 7th and 8th flow rates, which were greater than 4 ml/s.

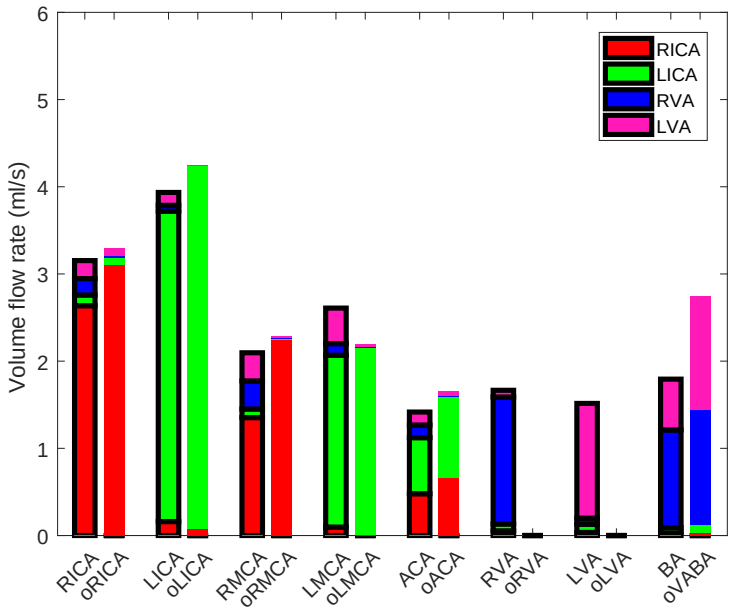
Figure 4.9: Results of water flow rate estimation performed by fitting the proposed PCASL model to flow phantom signals using Method 2.

masks are shown, in the subfigures labelled (c), as coloured stacked bars with no line border, and labelled with the prefix 'o-' before each artery name. The bar charts of the results of flow quantification are listed by artery with the results from the two techniques displayed side-by-side for easy comparison. The colours of



(a) ROI masks for the flow model technique.

(b) ROI masks used by Okell *et al.* [91].

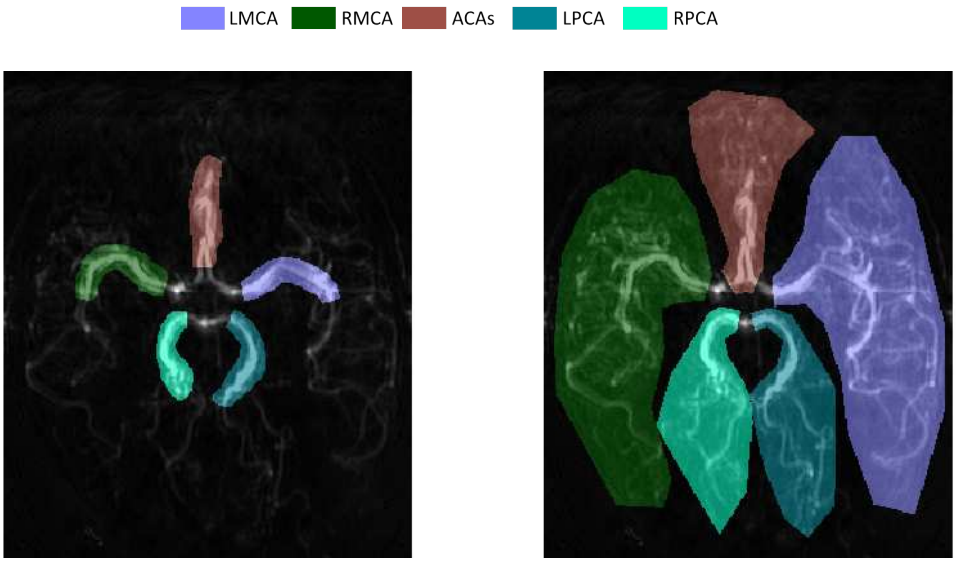


(c) Estimated arterial blood flow rates.

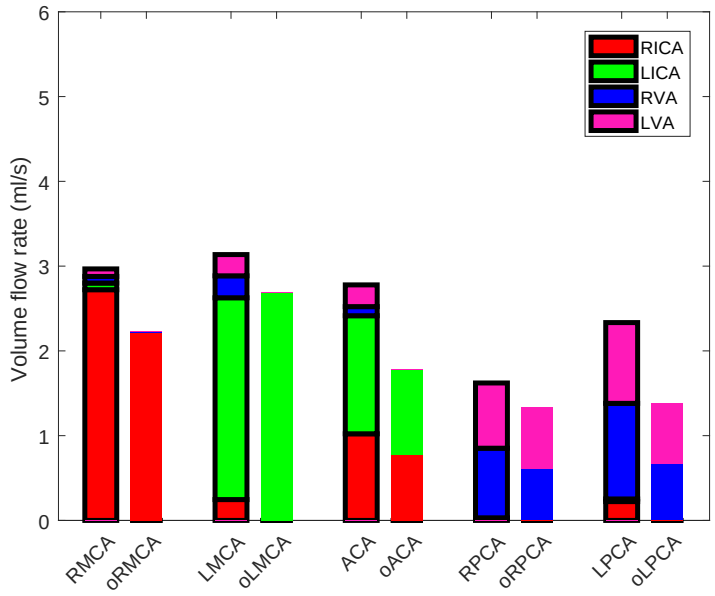
Figure 4.10: Coronal view of the circle of Willis of human subject A, showing vessel masks used for the flow model technique (a), and the Okell *et al.* technique (b). (c) shows the resulting flow rate estimates. Bars with thick black borders show the flow model estimates, and bars with no border and the prefix 'o-' on the artery name show the Okell estimates. The Okell *et al.* technique estimated the RVA, LVA and BA flow contributions within a single VAs-and-BA mask (shown in yellow in (b)), these estimates are attributed to the BA in (c).

the bar segments identify the afferent artery in which the detected blood was labelled.

The goal of using a region-wise PCASL flow modelling technique in the work presented in this chapter was to develop a method of blood flow rate quantification



(a) ROI masks for the flow model technique. **(b)** ROI masks used by Okell *et al.* [91].

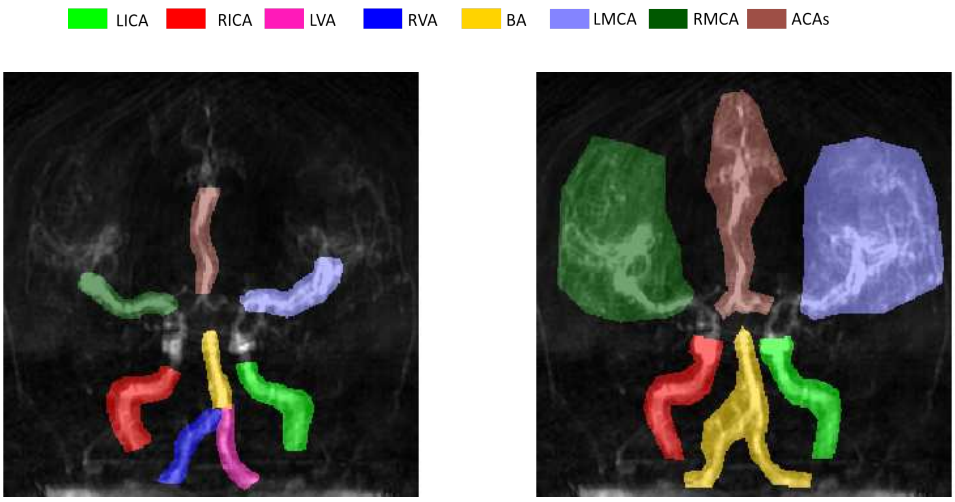


(c) Estimated arterial blood flow rates.

Figure 4.11: Transverse view of the circle of Willis of human subject A, showing vessel masks used for the flow model technique (a), and the Okell *et al.* technique (b). (c) shows the resulting flow rate estimates. For explanations of the bar styles refer to the caption of Figure 4.10.

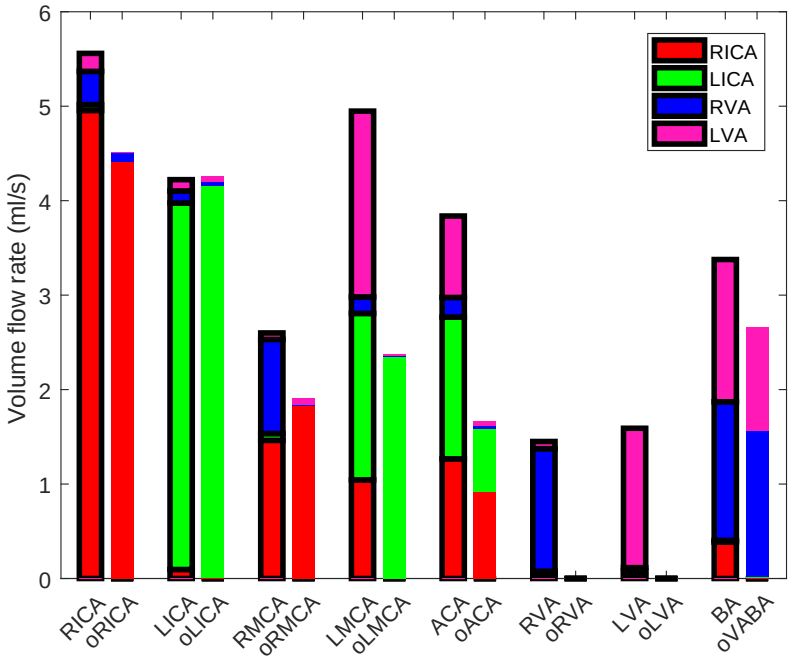
that could be applied over much smaller vessel masks than those used by Okell *et al.* [91], whose vessel masks needed to encompass the entire simulated labelled blood bolus (the wash-in portion of which was simulated through the fitting of a kinetic model [126]). Subfigures (a) and (b) in Figures 4.10 – 4.13 demonstrate this

difference in region size, and show that the new flow model technique permitted separate consideration of the RVA, the LVA, and the BA, which were considered together by Okell *et al.* [91].



(a) ROI masks for the flow model technique.

(b) ROI masks used by Okell *et al.* [91].



(c) Estimated arterial blood flow rates.

Figure 4.12: Coronal view of the circle of Willis of human subject B, showing vessel masks used for the flow model technique (a), and the Okell *et al.* technique (b). (c) shows the resulting flow rate estimates. For explanations of the bar styles refer to the caption of Figure 4.10.

Figures 4.10 – 4.13 show flow rate quantification results obtained using the coronal (Figures 4.10 and 4.12) and transverse (Figures 4.11 and 4.13) views of the circle of Willis of two human subjects. Considering the results of flow rate estimation from the human data sets, in all four figures (4.10c – 4.13c) there are several areas of good agreement between the results from the current flow model technique, and the results from the Okell technique. For example, in the coronal view of human subject A (Figure 4.10c) there was excellent agreement between the two quantification techniques on the rate at which blood labelled in the LICA was delivered to the LMCA, which was estimated to be 2.0 ml/s by the flow model technique, and 2.1 ml/s by the Okell technique. Also in Figure 4.10c, the flow rate of RVA labelled blood in the RVA was estimated at 1.5 ml/s and the flow rate of LVA labelled blood in the LVA was 1.3 ml/s. The Okell technique measured these flow rates using a mask that covered both of the VAs and the BA, and estimated 1.3 ml/s of blood labelled in the RVA and 1.3 ml/s of blood labelled in the LVA. However, when the flow model technique was applied to signals summed over the BA mask alone (shown in yellow in Figure 4.10a) flows of 1.1 ml/s of RVA labelled blood and 0.6 ml/s of LVA blood are estimated.

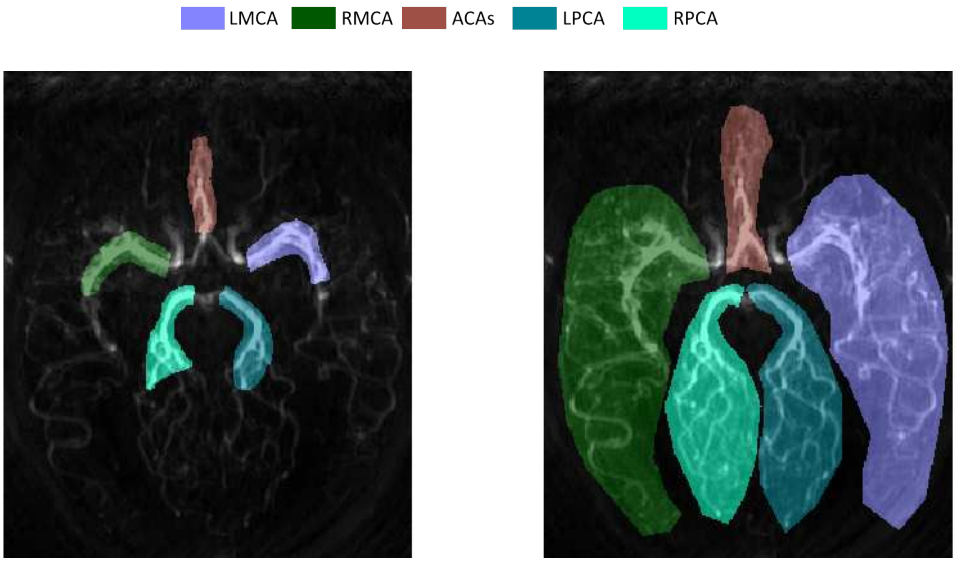
In the transverse view of the same volunteer (Figure 4.11), there is again good agreement between the two techniques on the flow rates of blood through the MCAs. However, the Okell method measures a lower blood flow rate to the ACAs: 0.8 ml/s of blood that was labelled in the RICA, and 1.0 ml/s of blood that was labelled in the LICA. This is in contrast to the 1.0 ml/s of RICA labelled blood and 1.4 ml/s of LICA labelled blood estimated using the flow model technique. In this volunteer the two methods appear to agree on the level of blood flow through the PCAs.

In the results of flow quantification from the images of human subject B (Figures 4.12 and 4.13), the flow model technique has again produced many blood flow estimates that are in line with the results of the Okell technique and values from the literature. For examples, consider the flow rates of RICA labelled blood in the

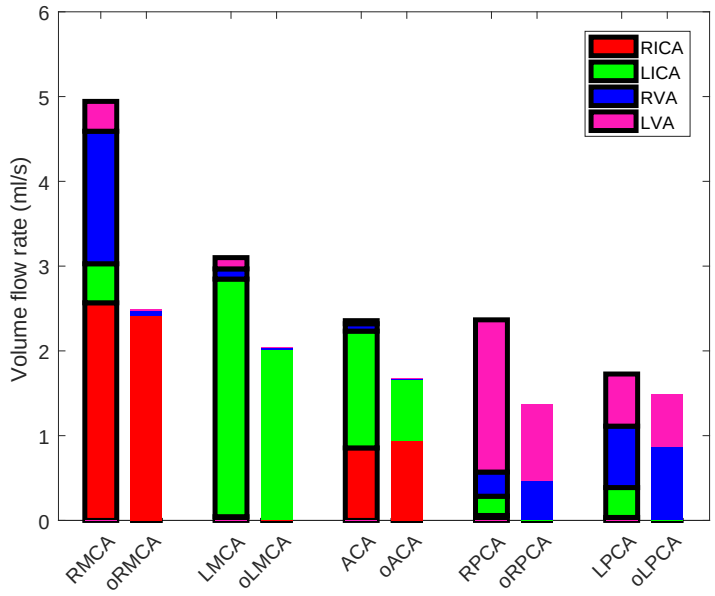
RICA and the RMCA, and LICA labelled blood in the LICA and LMCA. In the ACAs of this subject the flow model estimates are again higher than the estimates from the Okell technique. In Figure 4.12c there is fairly good agreement between the two techniques on the RVA and LVA labelled blood flows through the BA, and there is excellent consistency between the flow model estimates made in the VAs and in the BA.

Some examples of poor performance of the flow model technique can however also be seen in Figures 4.12c and 4.13c. The technique tends to estimate large flow rate contributions to cerebral arteries from afferent arteries that are unlikely to be involved in their supply, resulting in total flow rates through those cerebral arteries that are above the reasonable range of cerebral artery flow rates. For example, in Figure 4.12c the bar representing flows through the LMCA shows a total blood flow rate of 5.0 ml/s, of which 1.0 ml/s was labelled in the RICA, 1.8 ml/s was labelled in the LICA, 0.2 ml/s was labelled in the RVA, and 2.0 ml/s was labelled in the LVA. While the flow contribution from the LICA is in line with expectations, and alone provides a reasonable volume flow rate of blood to the LMCA [50], [89], [90], the contributions from the three remaining afferent arteries seem less reasonable. Similarly unlikely blood flow contributions can be seen in Figures 4.12c and 4.13c in the ICAs, RMCA, and ACAs and, at a lower level, in the flow model results from human subject A (Figures 4.10c and 4.11c) in the ICAs, MCAs and ACAs. Similar, but much smaller, blood flow contributions from the corresponding supply arteries are seen in the results from the Okell method.

Figure 4.14 shows the four PCASL signals detected in the LMCA mask on the coronal view of human subject B, which is shown in pale blue on the right of Figure 4.12a. These four signals are the ASL blood signal contributions from each of the four afferent arteries. Curve fitting of the flow model developed in this chapter to these signals using Method 1 (Section 4.3.5) leads to the LMCA flow rate estimates shown in Figure 4.12c. The signal shown in Figure 4.14b is



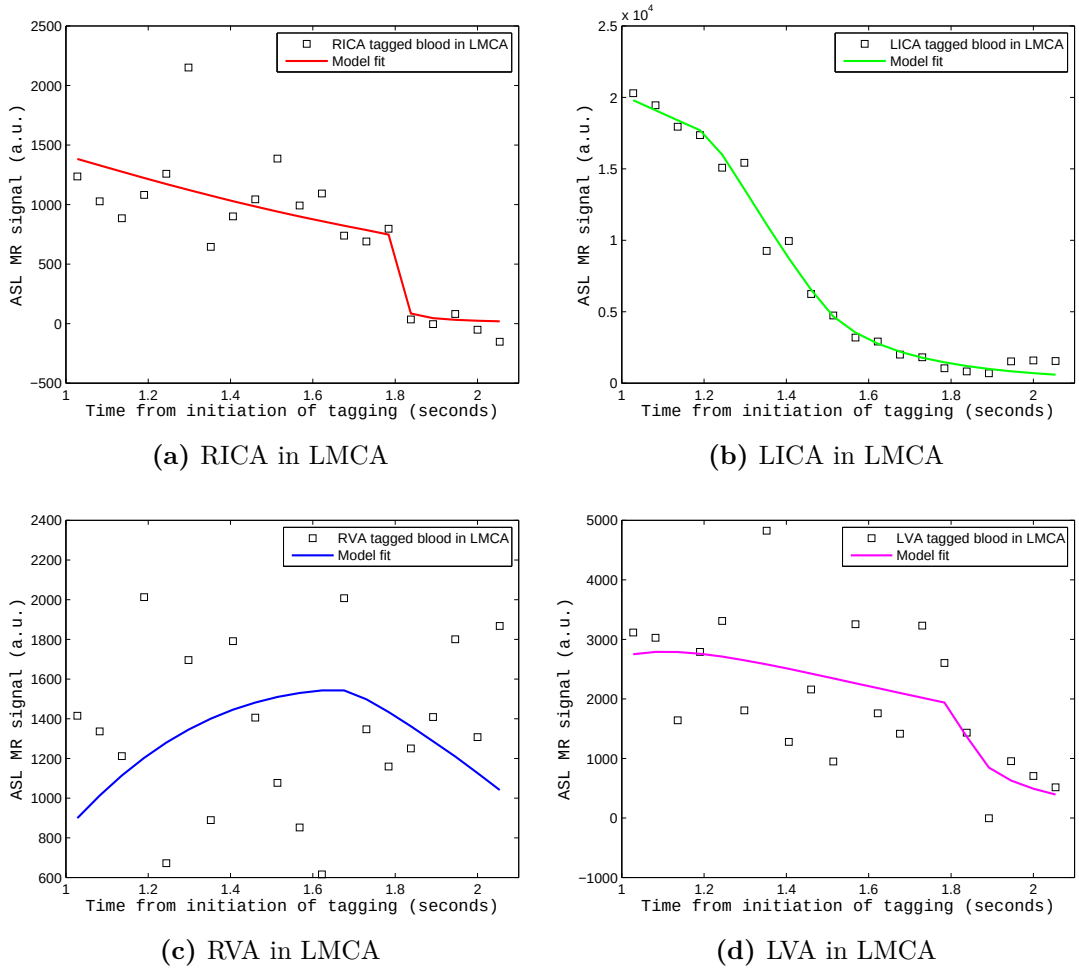
(a) ROI masks for the flow model technique. **(b)** ROI masks used by Okell *et al.* [91].



(c) Estimated arterial blood flow rates.

Figure 4.13: Transverse view of the circle of Willis of human subject B, showing vessel masks used for the flow model technique (a), and the Okell *et al.* technique (b). (c) shows the resulting flow rate estimates. For explanations of the bar styles refer to the caption of Figure 4.10.

the LMCA signal from blood that was labelled in the LICA; it has the highest amplitude and the highest signal-to-noise ratio ($SNR_b = 19.5$) of all four signals detected in the LMCA. The signals shown in Figures 4.14a, 4.14c, and 4.14d were also measured in the LMCA and are signals from blood labelled in the RICA,



(a) RICA in LMCA

(b) LICA in LMCA

(c) RVA in LMCA

(d) LVA in LMCA

Figure 4.14: PCASL signals summed over the LMCA mask outlined on the coronal view of human subject B (Figure 4.12a).

RVA, and LVA, respectively. These signals are of much lower amplitudes and are noisier than the LICA labelled blood signal ($SNR_a = 8.0$, $SNR_c = 8.5$, and $SNR_d = 7.0$). These signals are also far noisier than those detected in the phantom images, which have SNRs in the range $29 - 39$.

4.5 Discussion

This chapter has presented the development and testing of a blood volume flow rate quantification technique, for use in PCASL angiography, based on modelling of the mass transport of tracer through an artery. The results of validating and testing this technique on VEPCASL images of a water flow phantom and of the

circles of Willis of healthy volunteers were shown in Section 4.4. These results demonstrate that the technique was successfully able to quantify water flow rates from VEPCASL images of a flow phantom, and blood flow rates from VEPCASL cerebral angiography images of healthy volunteers. The flow model technique and the results from Section 4.4 are discussed in more detail in this section.

4.5.1 Flow phantom validation

The water flow phantom data used in validation of the flow model quantification technique provided very low noise signals from a simplified model of a cerebral artery. The results of fitting the flow model to signals from the flow phantom (Figures 4.6 and 4.7) show that the PCASL flow model developed in Section 4.1.2 fitted the ROI signals seen in the data well. This suggests that the model is able to successfully represent the fluid mechanics of the flow of an ASL blood bolus and the stages of its passage through an ROI. These features included a change in gradient at time point t_3 (seen most clearly in Figures 4.6c and 4.6d at $t \approx 1.15$ *seconds*) as the trailing edge of the bolus arrived in the ROI, and bolus dispersion caused by a non-uniform axial velocity profile. However, it should be noted that additional causes of bolus dispersion, which were not included in the development of the flow model, such as flow pulsatility, differences in path length, and diffusion of the labelled blood water, are likely to have had a lesser effect on the labelled water bolus seen in the phantom images compared with blood boluses seen in the human data. This is due to the fact that the phantom consisted of a short, straight tube in place of arteries which can be highly tortuous.

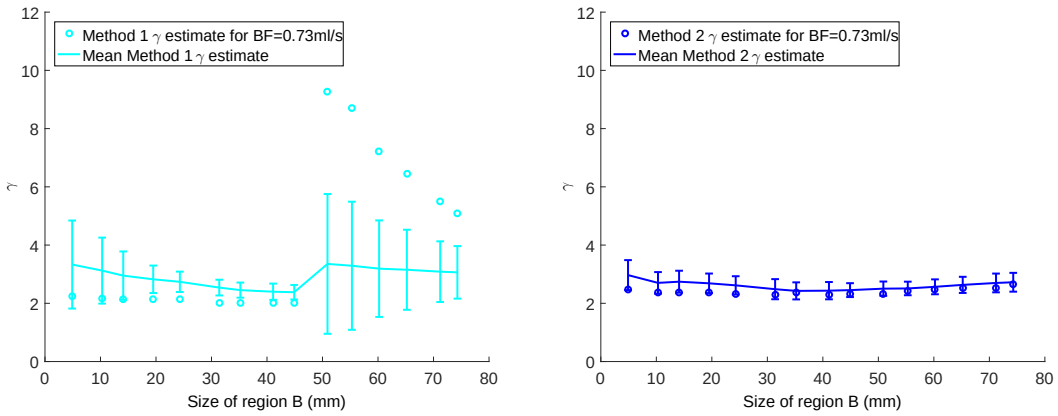
The water flow rate quantification results in Figures 4.8 and 4.9 showed that fitting the flow model to VEPCASL signals detected in the images of the flow phantom allowed successful quantification of water flow rates. When the flow model technique was applied using Method 1 (see Section 4.3.5), flow rates of up to 8.1 ml/s could be accurately estimated in ROIs between 30 and 45 mm long. Over this region length range, the technique also provided more accurate estimates of

flow rates than the Okell *et al.* [91] method.

In vessel segments shorter than 30 mm the flow model technique tended to underestimate flow rates, possibly indicating that below 30 mm the ROI was too small to allow sufficient accumulation of the ASL label within the region, preventing the detection of temporal information about the bolus' passage through the ROI. According to Table 3.1, this lower limit on ROI size means that the flow model technique cannot be used to quantify blood flow rates in any of the circulus arteries of the circle of Willis, i.e. the distal segments of the ICAs, the proximal segments of the ACAs and PCAs, the PCoAs, or the ACoA.

In Figures 4.8a and 4.8b, the use of ROIs longer than 45 mm led to a slightly negative mean error, indicating underestimation of flow rates, and one standard deviation below the mean fell below -15%, i.e. outside the error range deemed as acceptable. The underestimation, and the larger standard deviation of the error with an ROI of 50 mm compared with an ROI of 45 mm can be understood by considering the inflow section of the signals in Figures 4.6a and 4.6b, and by considering Figure 4.15. The latter shows the estimated values of the flow profile parameter, γ, averaged over the eight phantom flow rates, for both Method 1 (Figure 4.15a), and Method 2 (Figure 4.15b). The figure also shows (as circle markers) the specific value of γ estimated from the 0.73 ml/s signals in Figures 4.6a and 4.6b (Method 1), and Figure 4.7a and 4.7b (Method 2). Figure 4.15a shows that, using Method 1, the partial presence of the inflow section of the bolus' passage in the 0.73 ml/s signal leads to a much higher estimate of γ and subsequent underestimation of BF. This apparent overestimation of γ results from a compromised curve fit to the tail end of the signal, which allows fitting to the inflow part (results not shown), which begins to recover as the size of the ROI increases further.

When the flow model technique was applied to signals from the flow phantom data using Method 2, flow rates of up to 3.8 ml/s could be accurately estimated



(a) Estimated γ values from Method 1 **(b)** Estimated γ values from Method 2

Figure 4.15: γ values obtained when fitting the proposed PCASL flow model to signals from the water flow phantom images.

if the length of the downstream ROI (region B) was within $30 - 74$ mm (Figure 4.9b). In Method 2, the coupling of two ROIs appears to have constrained the flow model such that the issue of partial inclusion of the inflow part of the signal did not result in under-fitting of the signal tail. This led to blood flow rate errors (Figure 4.9b) and γ estimates (Figure 4.15b) that were consistent for all region B lengths greater than 30 mm. For these region lengths and for phantom flow rates of up to 3.8 ml/s, Method 2 provided more accurate water flow rate estimates than the Okell *et al.* technique. However, the technique was not able to accurately estimate the two highest water flow rates of 4.6 ml/s and 8.1 ml/s. While the latter flow rate is highly unlikely to be observed in the arteries of the cerebral vasculature [50], [89], [90], a flow rate of 4.6 ml/s falls within the range of values expected in the ICAs. Thus, only Method 1 was used to fit the flow model to the *in vivo* data. Furthermore, based on the optimal ROI length range identified in the Method 1 flow phantom results (Figure 4.8), the vast majority of the ROIs in Figures 4.10a–4.13a were outlined with lengths in the range: $30 - 45$ mm.

4.5.2 Human results

The results of *in vivo* flow quantification show that the flow model technique is able to successfully quantify blood volume flow rates in the healthy volunteer data set.

However, it is worth noting that for individual *in vivo* blood flow rate quantification there exists no ground truth with which to compare the results. Thus, the flow rate estimates made using the flow model technique are discussed here in reference to the results obtained by applying the technique of Okell *et al.* [91] to the same data, and to the results of other studies in which flow rate measurements were made using PASL MRA [90], PC-MRA [89], and TCD [50]. For example, the flow model technique and the Okell technique [91], respectively, measured 2.0 ml/s and 2.1 ml/s of LICA labelled blood in the LMCA, from the coronal view of human subject A (Figure 4.10c). These flow rates estimates are in good agreement, and are within the range of values reported in the literature from measurement studies using alternative imaging modalities, such as PC–MRA [89], [90] and TCD [50]. In the same image, the two techniques also strongly agree with the literature on the blood flows in the VAs [50], [89], [90].

In the transverse view of the same volunteer (Figure 4.11c), the flow model technique estimated higher blood flow rates through the ACAs than were estimated by the Okell method. In this case, the flow model results, of 1.0 ml/s of RICA labelled blood and 1.4 ml/s of LICA labelled blood, were more in line with the values presented in the literature [50], [89], [90]. The flow model method also measures higher ACA flows than the Okell technique in both the coronal and transverse views of human subject B (Figures 4.12 and 4.13, respectively). In fact, the Okell technique seemed to consistently estimate low flows through the ACAs compared with values reported in previous studies [50], [89], [90]. This may be due to some loss of ACA signal in the 2D thick-slab data, resulting from the path of ACAs not being entirely contained within in the imaging slab. The flow model technique was more robust to absence of part of a vessel from the imaging plane, as the technique can perform successful flow quantification on shorter arterial segments than the Okell technique.

As identified in Section 4.4.2, there are several instances in the *in vivo* flow quantification results (Figures 4.10–4.13) in which the flow model technique estimates large blood flow contributions from afferent arteries which are unlikely to be involved in the supply of the artery of interest. These 'unlikely' contributions are more apparent in subject B than in subject A. Some of these flow contributions can clearly be identified as erroneous. Take the RICA labelled blood detected in the LMCA in Figure 4.12c as an example: for blood labelled in the RICA to be present in the LMCA requires collateral flow from the RICA clockwise around the circle of Willis via the ACoA and the LACAA1, or anticlockwise via the PCoAs and the PCAP1s. In the first case, the ACAs would not receive any blood that was labelled in the LICA, as there would be reversed flow through the LACAA1, which is not indicated in Figure 4.12c. In the second case, the RPCA would be supplied by the RICA rather than the VAs, due to reversed flow in the RPCAP1, which again is not indicated in Figure 4.13c. Thus, it is possible to identify many of the suspicious flow contributions as erroneous. Further examples include the RVA and LVA labelled blood in the RICA and LICA.

Some suspicious blood flow contributions are less obviously spurious, for example in Figure 4.12c, the large flow rates of VA labelled blood supplied to the ipsilateral MCAs, and to the ACAs. Collateral flow to the MCAs and ACAs from the VAs, via the PCoAs, is physiologically plausible, and not so easily contradicted by inference of the flow directions in the circulus arteries using flow rate estimates for other vessels. These results, however, are clearly questionable due to the magnitudes of the flow contributions and the resulting total flow rates through the MCAs and the ACAs.

Collateral flow through the circle of Willis is the focus of this thesis, and the aim of performing quantitative cerebral angiography is to use flow rate measurements to personalise a cerebral arterial network model like the one developed in Chapter 3. The phantom experiments demonstrated that the flow model technique cannot

be applied over small ROIs, which would allow flow rate quantification in the small circulus arteries of the circle of Willis. It is therefore important that the technique be able to produce reliable flow rate estimates from low amplitude signals in the efferent arteries, such that the magnitudes of collateral flows around the circle of Willis can be determined. Figure 4.14 shows the measured VEPCASL signals and the associated fitted PCASL flow models used to obtain the four flow rate estimates for the LMCA in Figure 4.12c. The figure shows that the proposed flow model is able to successfully describe the high SNR LICA signal shown in Figure 4.14b. The signals in Figures 4.14a, c, and d, and the associated LMCA flow rate estimates show that the flow quantification technique is not robust to the presence of noise on signals.

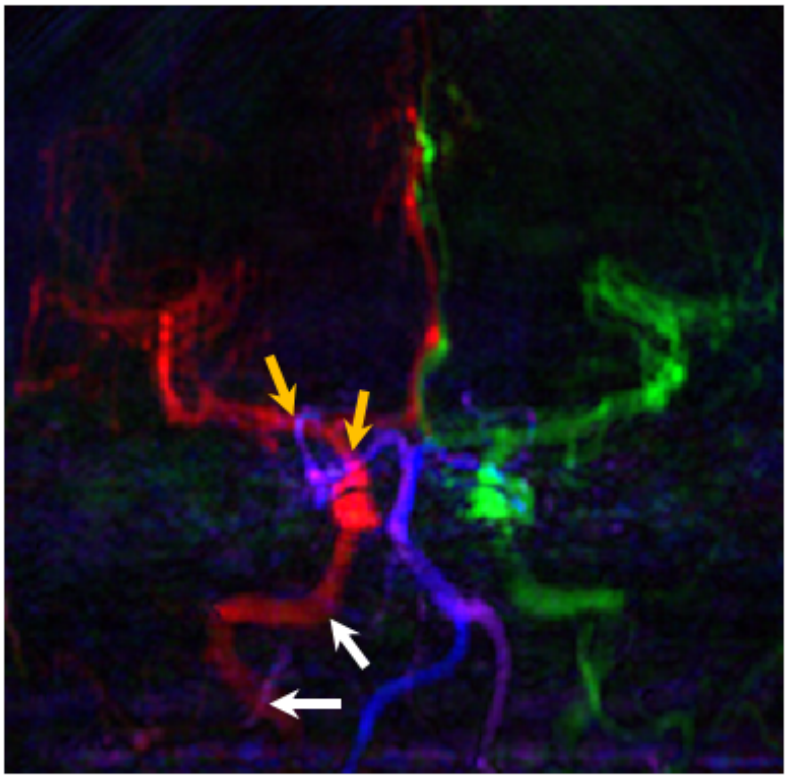


Figure 4.16: Coronal view of the circle of Willis of one healthy volunteer. The white arrows identify points at which a small branch of the BA crosses the RICA, orange arrows show points at which the RPCA overlaps with the RICA and the RMCA.

The nature of the VEPCASL data used in this study is a factor that contributes to the unreliable flow rate estimates seen in the results of flow model quantification.

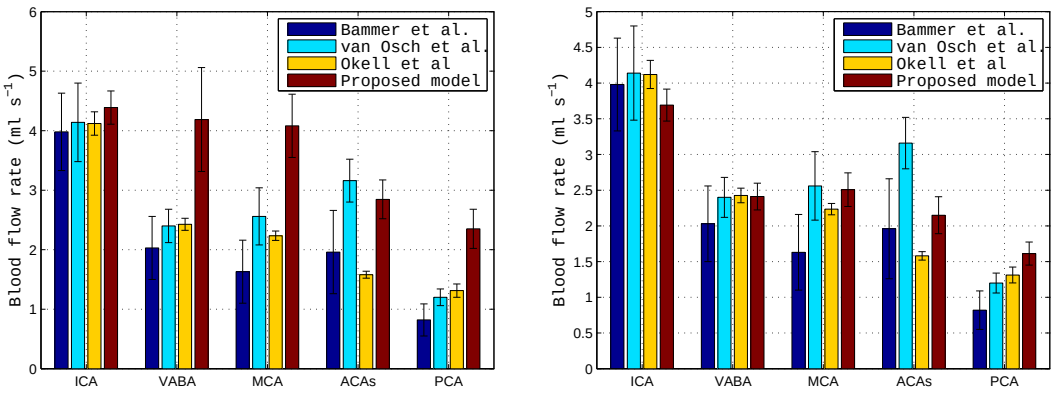
In part, flow rate quantification problems, like those identified in the LMCA in Figure 4.12c, arise due to the use of a 2D thick-slab image acquisition. This acquisition allows all of the arteries of the circle of Willis to be captured in just two orthogonal images (Figure 4.5). However, the circle of Willis is a complex 3D structure and the use of a 2D thick-slab acquisition means that signals from blood in two or more vessels may be detected in a single voxel. This effect is most easily observable in the coronal views of the circle, which have a slab thickness of 100 mm, twice the thickness of the transverse slabs.

In Figure 4.16, the white arrows identify a small branch off the BA, containing blood labelled in the RVA and LVA, crossing the RICA. One of the short segments of this artery that intersect with the RICA was included in the ROI outlined along the RICA for the purposes of blood flow rate quantification, thereby contributing RVA and LVA labelled blood signal to the signals detected in the ROI. These contaminating signals resulted in 0.2 ml/s of RVA labelled blood and 0.2 ml/s of LVA labelled blood being attributed to the RICA (Figure 4.10c).

The orange arrows in Figure 4.16a show the RPCA overlapping the distal part of the RICA and the proximal part of the RMCA in the coronal view of the circle of Willis. As the RPCA runs roughly perpendicular to the plane of the image, its structure is not well visualised in the coronal view. However, some voxels can contain ASL signal from up to several centimetres of the PCA, which leads to contaminating signals from RVA and LVA labelled blood being detected in the MCA. Shifting the ROI masks to exclude the contaminating vessels leads to the RICA ROI covering the section of the vessel that is overlapped by the RPCA, and to the RMCA ROI excluding the high signal trunk of the RMCA, which results in lower estimates of RICA labelled blood in the RMCA.

Contaminating signals are also present in the vascular territory masks outlined by Okell *et al.*. However, the Okell flow quantification technique is more robust to

their presence, due to its requirement that the entire simulated labelled blood bolus in a vessel be included in the mask in order for the flow estimate to be accurate. As the flow model technique developed in this chapter avoided such a requirement, it is therefore more sensitive to these contaminating signals. Figure 4.17 allows for comparison of the results of PCASL flow model quantification, with the results of Okell *et al.* [91], and with values published in the literature [89], [90]. Figure 4.17a shows the results of flow model quantification with the signals that could clearly be identified as erroneous included, and Figure 4.17b shows the flow model results when these flow contributions are removed.



(a) Flow quantification with noisy and contaminating signals included.

(b) Flow quantification with noisy and contaminating signals excluded.

Figure 4.17: Mean estimated blood flow rates in the afferent and efferent arteries of the circle of Willis. The flow rate values are averaged across all of the subjects and both views of the circle. Also shown are the equivalent estimates from Bammer *et al.* [89], van Osch *et al.* [90] and Okell *et al.* [91]. Error bars show the standard error in the mean.

Figure 4.17 summarises the results of blood flow estimation performed on VEPCASL images of all six healthy volunteers. Each red bar shows blood flow rates estimated in that vessel, averaged across the left and right sides of the circle of Willis, the transverse and coronal views, and the six individual subjects. As an example, the ICA blood flow rate was estimated twice per subject: in the RICA and the LICA, which were only visible in the coronal view, hence, the red ICA bar in Figure 4.17 is the mean of 12 blood flow estimates. The results of Bammer

et al. [89] (dark blue), van Osch *et al.* [90] (light blue) and Okell *et al.* [91] (yellow) are also plotted for comparison. van Osch's estimates of blood flow in the afferent arteries are the sum of the values estimated in the efferent arteries, assuming no collateral flow (e.g. ICA = MCA + ACA). It is clear from the figure that the flow model technique can demonstrate similar performance to existing methods, but relies on a certain SNR and is sensitive to contaminating vessel signals.

Okell *et al.* [91] eliminated non-vascular noisy voxels from consideration. This was done by using a mask to filter out voxels in which the maximum and mean signal intensity was below a threshold of 40% of the 99th percentile of the maximum or mean signal intensity for the image, respectively. Their kinetic model was then only fitted to the voxels contained within this high-signal mask and only these voxels were included in flow quantification. The same technique could also be applied before the use of the PCASL flow model quantification method to estimate flow rates. Its use would likely minimise errors in flow estimation caused by noise on signals, such as those seen in Figures 4.14a, c, and d. However, it is unlikely to reduce or to eliminate the flow contributions from contaminating signals resulting from regions of vessel overlap (Figure 4.16). The effect of these signals could perhaps be reduced through the use of higher levels of precision on the BF parameter prior.

4.6 Summary

In this chapter a model-based method for blood flow rate quantification from dynamic ASL MR angiography has been proposed. The flow model method was designed to allow blood volume flow rate quantification over shorter arterial segments than those used by the existing technique of Okell *et al.*, which required all of the simulated ASL blood bolus to be included within the considered vessel mask. While the method presented here was developed specifically for use on PASL and PCASL MRA data, it is based on modelling the mass transfer of an imaging tracer through the vasculature and could, therefore, be adjusted for application to data from other

contrast enhanced angiography imaging modalities.

In this work the method was used to quantify flow rates from vessel-encoded PCASL MRA images of a water flow phantom, and of the arteries of the circles of Willis of six healthy volunteers. The results of flow phantom experiments demonstrated that the technique could produce highly accurate estimates of water flow rates, and that these estimates could be obtained over far shorter arterial segments than those required for accuracy in the application of the technique proposed by Okell *et al.* [91]. The phantom results also showed that the accuracy of flow rate estimates could be affected by the length of the vessel segment over which flow quantification was performed, and thereby permitted identification of an optimal range of ROI lengths.

Having defined the optimal range of ROI lengths, further testing on human data demonstrated that the technique could be successfully applied to the task of blood flow rate quantification in the major arteries of the cerebral vasculature, with the technique showing good agreement with the method of Okell *et al.*, and with reported values of arterial blood flows in the circle of Willis. However, the results of testing the technique using the human data set also showed that the technique was sensitive to low amplitude contaminating signals that arise in the 2D thick-slab images due to the potential presence of blood from more than one vessel within a voxel. The human results also showed that the flow model quantification technique requires a certain SNR. This factor could, in future, be mitigated through the application of a high-signal mask to eliminate noisy non-vascular voxels.

5 Tracer Model

5.1 Introduction

As discussed in Chapter 3, two of the major limitations in the use of cerebral arterial network modelling are the lack of specificity to individual subjects and the lack of experimental validation. In order to personalise the network model outlined in Chapter 3, it is first necessary to identify any absent, or non-functional hypoplastic, circulus arteries and afferent arteries. Then, measurements of the lengths and radii of all of the afferent, circulus, and efferent arteries, along with measurements of the flow rates of blood through these arteries, would be required. Many of the physiological parameters (Table 3.1) required to model an individual's cerebral arterial network can, in theory, be measured from imaging data. However, the small arteries of the circle of Willis can be difficult to visualise.

It is possible to acquire information about blood flow rates in an individual subject's circle of Willis, and about the autoregulatory status of cerebral tissue territories. However, using such information to personalise cerebral arterial network models presents a substantial challenge which is beyond the scope of this thesis. The work described in this chapter aims, however, to help address the first requirement for personalisation of a network model i.e. identification of the structure of the

circle of Willis. This work involved modelling the progression of an imaging tracer through the cerebral arterial network by solving the mass transport equation over the network described in Chapter 3. This modelling work was carried out in order to observe the effects of occlusion and autoregulatory status on the ASL MR signals that could be detected in the arteries of several variants of the circle of Willis. Understanding the movement of imaging tracers through the circle of Willis could allow greater knowledge of circle structure, particularly the presence or absence of small circulus arteries, to be gleaned from imaging studies.

5.2 Model equations

Modelling the concentration of ASL tracer in the circle of Willis allows observation of the passage of a bolus through the arterial network. As in Section 4.1, this was done using the general mass transport equation. In the bloodstream the Péclet number, i.e. the ratio of the advective transport rate to the diffusive transport rate, is very high, which means that mass transport in the cerebral vasculature is dominated by advection. Hence, mass transport by diffusion is negligible and the general mass transport equation becomes the advection equation:

$$\frac{\partial c}{\partial t} + U\nabla c = -R \tag{5.1}$$

In equation 5.1, c is the concentration of the ASL tracer, U is the flow velocity of blood, and R is a sink term, which results from the attenuation of the ASL signal due to T_1 decay and RF attenuation. Thus, in one-dimension, equation 5.1 becomes:

$$\frac{\partial c}{\partial t} + U\frac{\partial c}{\partial x} = -\frac{c}{\tau} \tag{5.2}$$

Note that equation 5.2 is the 1D form of equation 4.1. For numerical solutions it is assumed that the blood flow velocity does not vary axially (i.e. $U \neq U(x)$), and equation 5.2 can be rewritten in conservation form:

$$\frac{\partial \mathbf{U}}{\partial t} + \frac{\partial \mathbf{F}(\mathbf{U})}{\partial x} = \mathbf{S}(\mathbf{U}) \tag{5.3}$$

where

$$\begin{aligned} \mathbf{U} &= [c] \\ \mathbf{F}(\mathbf{U}) &= [Uc] \\ \mathbf{S}(\mathbf{U}) &= \left[-\frac{c}{\tau}\right] \end{aligned} \tag{5.4}$$

The system was then solved over the arterial network outlined in Chapter 3. This was done numerically using the two-step Lax-Wendroff method [138]:

$$\begin{aligned} \mathbf{U}_x^{t+1} =& \mathbf{U}_x^t - \frac{\Delta t}{\Delta x}\left[\mathbf{F}\left(\mathbf{U}_{x+1/2}^{t+1/2}\right) - \mathbf{F}\left(\mathbf{U}_{x-1/2}^{t+1/2}\right)\right] \\ &+ \frac{\Delta t}{2}\left[\mathbf{S}\left(\mathbf{U}_{x+1/2}^{t+1/2}\right) + \mathbf{S}\left(\mathbf{U}_{x-1/2}^{t+1/2}\right)\right] \end{aligned} \tag{5.5}$$

where

$$\begin{aligned} \mathbf{U}_j^{t+1/2} =& \frac{\mathbf{U}_{j+1/2}^t + \mathbf{U}_{j-1/2}^t}{2} \\ &- \frac{\Delta t}{2\Delta x}\left[-\mathbf{F}\left(\mathbf{U}_{j+1/2}^t\right) + \mathbf{F}\left(\mathbf{U}_{j-1/2}^t\right)\right] \\ &+ \frac{\Delta t}{4}\left[\mathbf{S}\left(\mathbf{U}_{j+1/2}^t\right) + \mathbf{S}\left(\mathbf{U}_{j-1/2}^t\right)\right] \end{aligned} \tag{5.6}$$

where $j = x + 1/2$ and $j = x - 1/2$.

The Lax-Wendroff method is a standard solution technique used in the approximation of the advection equation (equation 5.1). It is used in these cases because it is an explicit solution scheme of second order accuracy in space and time and it does not result in non-physical pulse spreading during propagation of a waveform. For stability of the numerical scheme, the length and time increments, Δx and Δt respectively, must satisfy the condition that:

$$max|\lambda|\frac{\Delta t}{\Delta x} < 1 \tag{5.7}$$

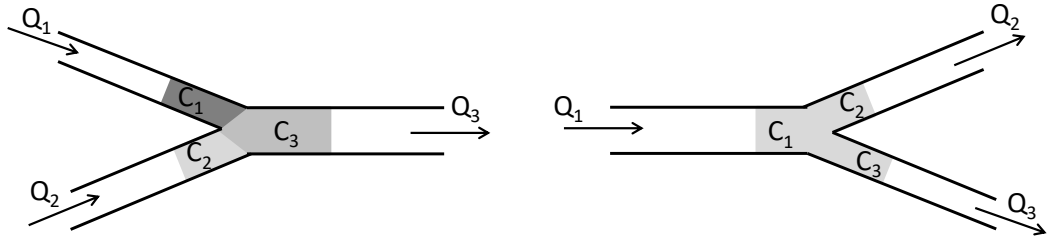
where λ is the eigenvalue of matrix $\mathbf{F}(\mathbf{U})$. In the case of equations 5.3 and 5.4 $\lambda = U$ and thus, for stability the numerical scheme is subject to the Courant-Friedrichs-Lewy (CFL) condition:

$$U\frac{\Delta t}{\Delta x} < 1 \tag{5.8}$$

in which the dimensionless number on the left of the inequality is known as the Courant number. The CFL condition essentially states that, for such a numerical scheme to be stable, the time increment must be less than the time taken for the modelled wave to travel between adjacent spatial grid points. Hence, the step size combination of $\Delta t = 1\ \mu s$ and $\Delta x = 1\ mm$ was used here.

5.2.1 Junctions and bifurcations

The possibility of collateral flow through the circle of Willis is provided by the potential for flow reversal in the circulus arteries, i.e. the distal ICAs, the proximal segments of the ACAs and PCAs, the PCoAs, and the ACoA (Figure 3.2a). The directions of blood flow through the circulus arteries for thirteen variants of the circle of Willis, under various occlusion conditions, were calculated in the arterial network modelling work in Chapter 3. For each network, this information was used to determine whether arterial connections in the circle of Willis were functioning as junctions or as bifurcations. At a junction, flows from two upstream vessels merge in one downstream vessel (Figure 5.1a). At an arterial bifurcation, flow from one upstream vessel divides between two downstream vessels (Figure 5.1b).



(a) Blood flows, Q, and tracer concentrations, C, at an arterial junction

(b) Blood flows and tracer concentrations at an arterial bifurcation

Figure 5.1: Schematic illustration of the effects of arterial junctions and bifurcations on the concentration of an endovascular imaging tracer.

At junctions, C_1 and C_2, the tracer concentrations at the ends of the two parent vessels, are known and conservation of mass can be used to calculate the concentration of the ASL tracer at the start of the downstream vessel, denoted by C_3:

$$C_3 = \frac{C_1 Q_1 + C_2 Q_2}{Q_3} \tag{5.9}$$

In the case of a bifurcation, flow from one vessel divides between two downstream vessels, hence: $C_1 = C_2 = C_3$.

5.2.2 The final node in each vessel

At the most distal grid point in each vessel the two-step Lax-Wendroff solver cannot be used as it requires a value of concentration at one spatial grid point forward i.e. beyond the end of the vessel. Instead, backward difference approximations to the two partial derivatives in equation 5.2 were made:

$$\frac{c_x^{t+1} - c_x^t}{\Delta t} + U \cdot \frac{c_x^t - c_{x-1}^t}{\Delta x} = -\frac{c_x^t}{T_{1b}} \tag{5.10}$$

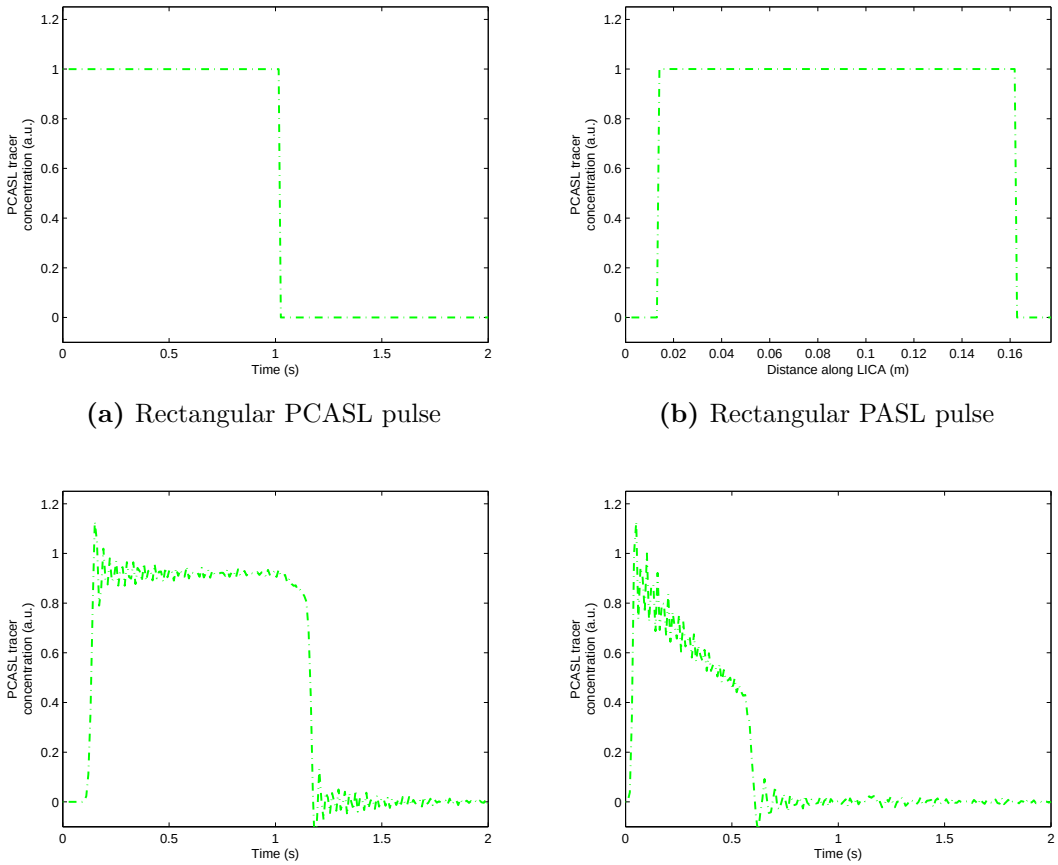
$$c_x^{t+1} = c_x^t \left(1 - \frac{\Delta t}{T_{1b}}\right) + U \cdot \frac{\Delta t}{\Delta x} \left(c_{x-1}^t - c_x^t\right) \tag{5.11}$$

5.2.3 ASL labelling conditions

As explained in Chapters 2 and 4, PASL is applied rapidly over a wide volume in the neck, whereas PCASL is applied over a much longer time period as blood flows through a very narrow labelling plane in the neck. The resulting PASL and PCASL boluses undergo T_1 signal decay differently. This difference is because the whole of the PASL pulse is created simultaneously, whereas the leading edge of the PCASL pulse is typically created around 1 *second* before the trailing edge, meaning that at any imaging time point the leading edge has existed for longer and has been decaying for longer.

Ideally, in order to most closely represent realistic ASL angiography labelling schemes, such as the PCASL angiography of Okell *et al.* [22] and the PASL

angiography of van Osch *et al.* [90], the simulated boluses in the afferent arteries would have rectangular pulse profiles. To represent PCASL, a rectangular pulse would be applied over time, and to represent PASL, a rectangular pulse would be applied spatially.



(a) Rectangular PCASL pulse

(b) Rectangular PASL pulse

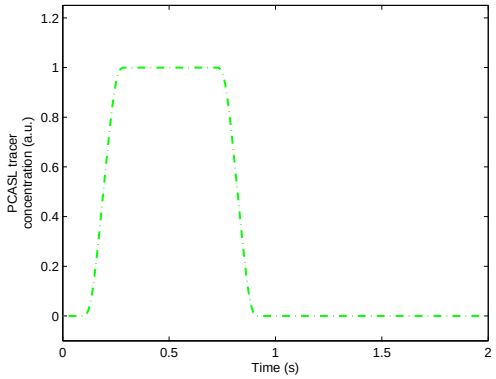
(c) Temporal profile of the resulting PCASL bolus

(d) Temporal profile of the resulting PASL bolus

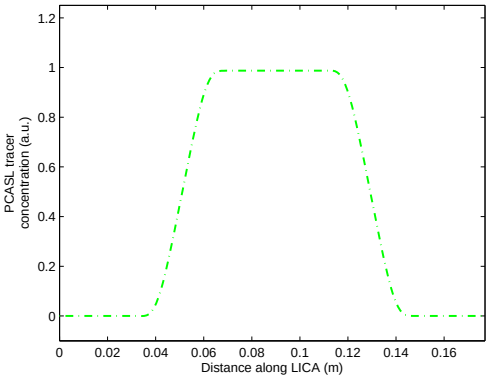
Figure 5.2: Rectangular ASL labelling pulses and resulting ASL signals detected 4 mm proximal to the end of the left internal carotid artery (LICA I1 in Table 3.1) showing non-physical oscillations (ringing) in the solution.

Figure 5.2 illustrates the use of rectangular labelling pulses to simulate PCASL (Figure 5.2a) and PASL (Figure 5.2b) tracer creation in the LICA of the full circle of Willis (variant 1 in Figure 3.6). The PCASL labelling pulse in Figure 5.2a produces a simulated bolus of duration 1 *second*, identical to the VEPCASL boluses in the phantom and human data used in Chapter 4. The PASL labelling pulse in Figure 5.2b produces a 148 *mm* wide labelled blood bolus, which, under healthy conditions

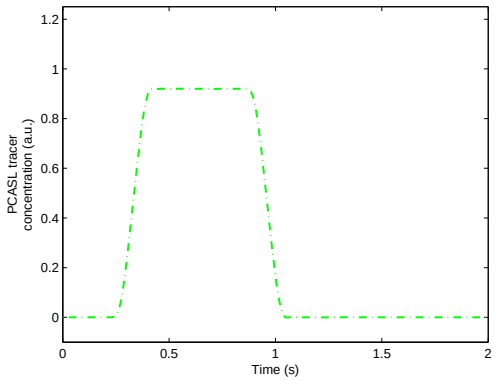
in circle variant 1, has a duration of 0.55 *seconds*. The PASL bolus width of 148 *mm* was used because it is equal to the full length of each of the vertebral arteries in the network model (Table 3.1). The PCASL and PASL labelling pulses define the tracer concentration 1 *a.u.* (Figures 5.2a and 5.2b); the magnitudes of all other tracer concentration signals in this Chapter are relative to this value.



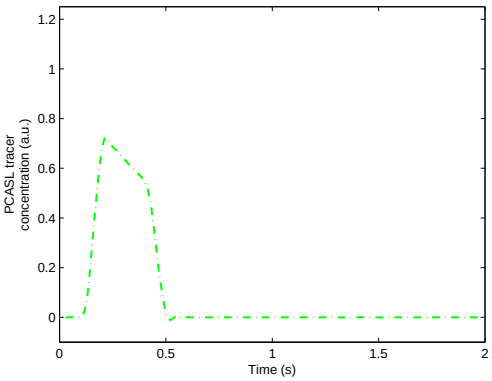
(a) Smoothed PCASL pulse



(b) Smoothed PASL pulse



(c) Temporal profile of the resulting PCASL bolus



(d) Temporal profile of the resulting PASL bolus

Figure 5.3: Smoothed ASL labelling pulses and the resulting ASL signals detected 4 mm proximal to the end of the left internal carotid artery (LICA I1 in Table 3.1), without the non-physical ringing seen in Figure 5.2.

Figures 5.2c and 5.2d show the simulated tracer concentrations seen downstream of the PCASL labelling plane, and PASL labelling slab, at a point 4 *mm* proximal to the distal end of the LICA. Unfortunately, the instantaneous step changes in the simulated tracer concentration signals, which result from the use of rectangular labelling pulses, lead to substantial, non-physical ringing effects in the two solutions.

Both the downstream PCASL (Figure 5.2c) and downstream PASL (Figure 5.2d) signals show concentration values above 1.10 $a.u.$, as the oscillations cause an overshoot when the boluses arrive, and concentrations below -0.1 $a.u.$ as the boluses leave, neither of which are physically possible. In order to avoid this ringing effect, the smoothed rectangular pulse profiles shown in Figures 5.3a and 5.3b were used as the PCASL and PASL concentration inputs to this model, respectively. These pulse profiles were obtained by smoothing the rectangular pulses using locally weighted linear regression. It can be seen from the resulting downstream concentration signals (Figures 5.3c and 5.3d, respectively) that the use of these smoothed pulses eliminates the non-physical ringing effects seen in Figure 5.2.

5.2.4 Decay

The longitudinal relaxation rate of labelled blood, T_{1b} is the same in both PASL and PCASL imaging. As described in Chapter 4, the RF pulses used in Look-Locker MR acquisition also attenuate the concentration of the ASL tracer. This leads the label to decay at a modified relaxation rate T_{1m} (equation 5.12) once imaging commences. In the simulated PASL signal in Figure 4.3, this occurred at $t = t_p = 0.002$ seconds and in PCASL data used in Chapter 4, it occurred at $t = t_c = 1.028$ seconds.

$$\frac{1}{T_{1m}} = \frac{1}{T_{1b}} - \frac{\ln\left[\cos\alpha\right]}{T_R} \tag{5.12}$$

Using the imaging parameters set out in Chapter 4 gives $T_{1m} = 0.6890$ seconds, whereas $T_{1b} = 1.664$ seconds. The difference in PASL and PCASL input conditions and the different times at which imaging commences thus result in two boluses that have different spatial and temporal profiles, as shown in Figure 4.3.

5.3 Materials and methods

Information about the cerebral arterial network and the flow rates through its arteries was taken from the results of the network modelling work described in Chapter 3. Flow velocities used in the Lax-Wendroff update step were calculated

using the blood flow rate and cross sectional area of each vessel. To fully examine the behaviour of an imaging tracer in the network, four factors were considered:

1. Circle of Willis structure: the low-risk full circle configuration was modelled (variant 1 in Figure 5.4a and Table 3.3), along with two medium-risk circle variants as defined in Chapter 3. One of these (variant 5 in Figure 5.4b and Table 3.3), saw a flow reduction of $> 10\%$ and $< 20\%$, and the other (variant 11 in Figure 5.4c and Table 3.3) saw a very large ($> 20\%$) reduction in flow to at least one cerebral artery which was ameliorated by a complete autoregulatiory response. Finally, one of the high-risk circles of Willis was modelled for comparison (variant 10 in Figure 5.4d and Table 3.3).

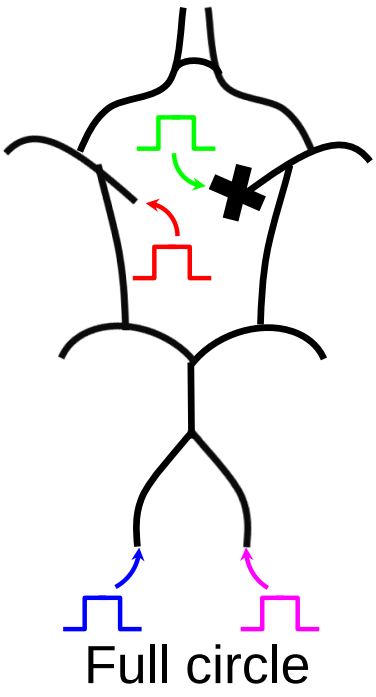
2. Arterial occlusion: the networks of interest were modelled with the LICA open and with it occluded.

3. Autoregulation: the cases of complete autoregulation and absent autoregulation were considered.

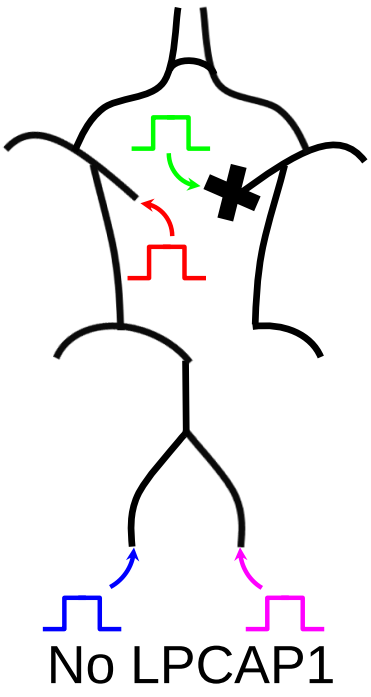
4. Labelling condition: separate instances of the tracer model were run with different afferent arteries labelled: first, only the LICA was labelled, then only the RICA, then only the LVA, and finally only the RVA was labelled (Figure 5.4). This allowed the tracer contributions from each of these arteries to be observed separately, which provides a good representation of the vessel encoded ASL data used in Chapter 4.

5.4 Results

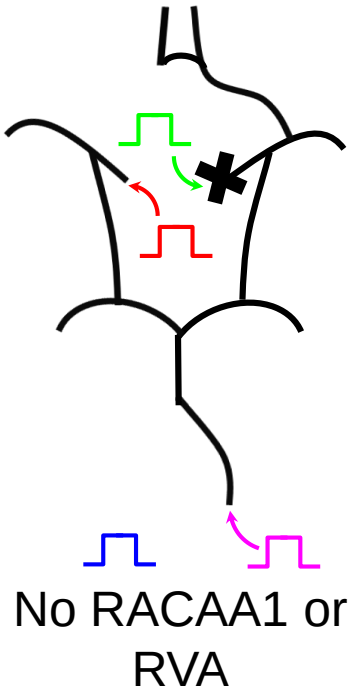
This section sets out the results of tracer modelling, showing the tracer signals detected in the six cerebral arteries for each of the four tracer-modelled network scenarios. Figure 5.4 shows the colour coding of ASL labelling conditions used in the tracer model to create Figures 5.5–5.9. Note that in Figures 5.5–5.9, dash-dot lines show signals from simulations with the LICA open, solid lines show signals modelled with the LICA occluded and no autoregulation response (described as



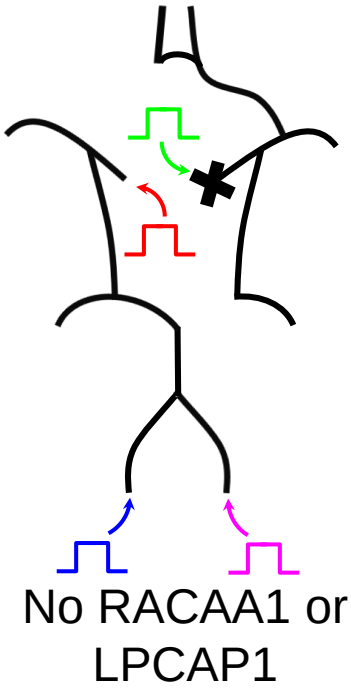
(a) Variant 1 labelling conditions used to produce the results in Figures 5.5 and 5.6



(b) Variant 5 labelling conditions used to produce the results in Figure 5.7



(c) Variant 11 labelling conditions used to produce the results in Figure 5.8



(d) Variant 10 labelling conditions used to produce the results in Figure 5.9

Figure 5.4: Labelling conditions applied to the tracer model in order to represent the VEPCASL data introduced in Chapter 4. The coloured square pulses represent boluses of ASL tracer.

autoregulation Scenario 1 in Figure 3.5), whereas dashed lines show signals modelled with the LICA occluded and a complete autoregulation response (autoregulation Scenario 2).

Figure 5.5 shows the modelled tracer concentration signals seen in the six cerebral arteries of the complete circle of Willis (variant 1) after modelling the progression of PCASL boluses from the LICA (green lines), RICA (red lines), RVA (blue lines), and LVA (magenta lines). The figure shows that, under baseline (no-occlusion) conditions, the delivery of tracer to the cerebral arteries is almost symmetrical. It takes approximately 0.3 *seconds* for tracer to be delivered to all six cerebral arteries, during which time little longitudinal relaxation has occurred: the concentration pulses in the LMCA and RMCA reach values of 0.88 and 0.89 *a.u.*, respectively.

Symmetry in the posterior circulation means that the RVA and LVA labelled blood boluses arrive simultaneously and the blue RVA concentration pulses are therefore obscured by the magenta LVA pulses in all six subfigures. Under healthy conditions (dot-dashed lines) in the PCAs, the RVA and LVA labelled boluses arrive 0.45 *seconds* after the start of labelling, each with a concentration of 0.41 *a.u.*. The PCA baseline signals also show the onset of tracer concentration attenuation due to RF imaging pulses, applied after 1.03 *seconds*, which can be seen as a slight downturn in concentration just before the concentration falls away as the boluses pass the points of interest 5 *mm* distal to the origins of the PCAs.

At baseline, Figure 5.5c shows no discernible evidence of collateral flow through the RPCoA, although there are, in fact, RVA and LVA concentration pulses of 0.001 *a.u.* arriving in the RMCA after 1.3 *seconds*, demonstrating very low level posterior-to-anterior collateral flow through the RPCoA. Similar very slight (0.005 *a.u.*) RVA and LVA tracer pulses are present after 0.9 *seconds* in the LMCA (just visible in Figure 5.5d) and 1 *second* in the LACAA2 (Figure 5.5b). There is also baseline right-to-left collateral flow, which can be seen in Figure 5.5b (the LACAA2)

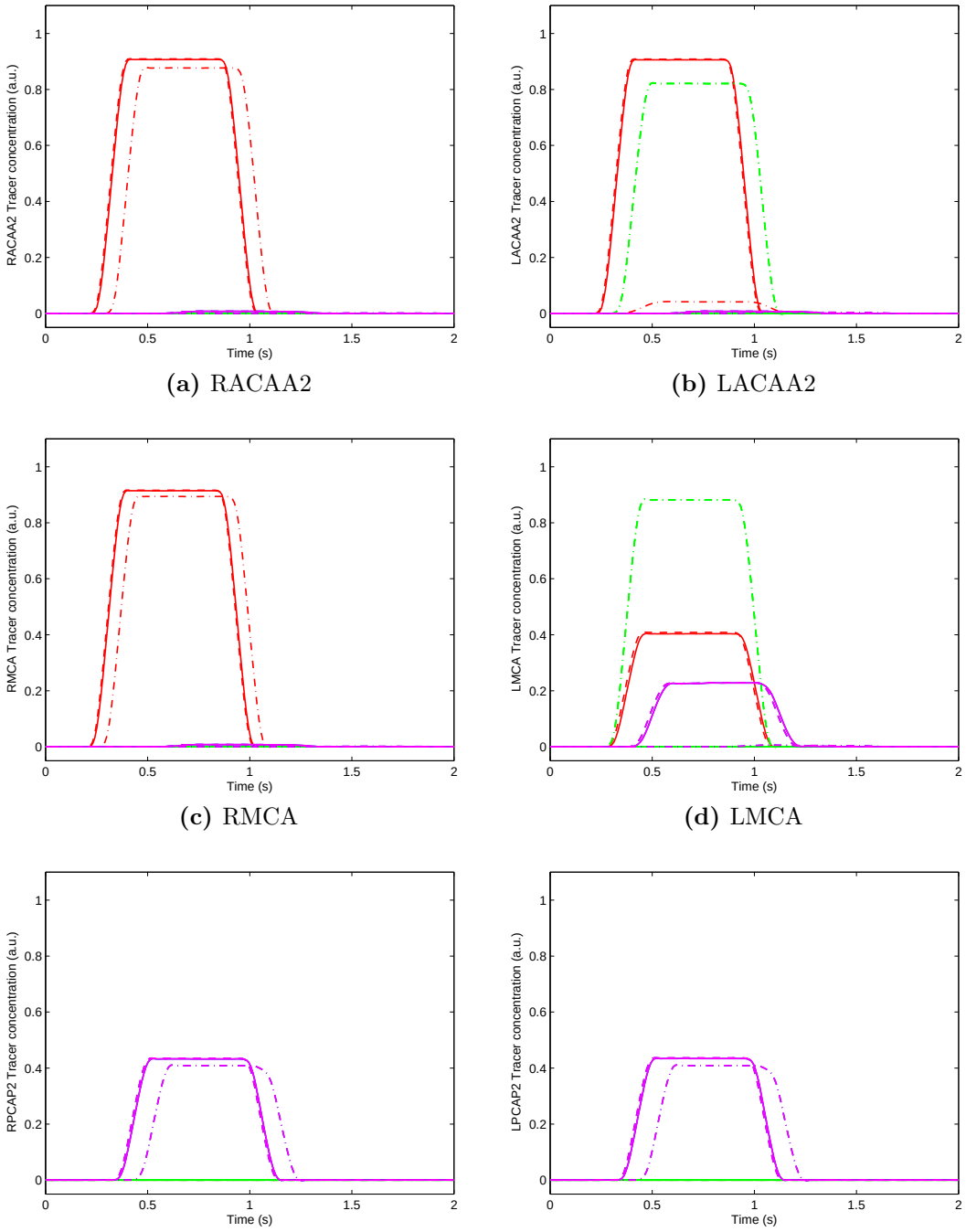


Figure 5.5: PCASL tracer concentrations seen 5 *mm* distal to the origins of the six cerebral arteries of the complete circle of Willis (variant 1). Green lines show ASL tracer from the bolus labelled in the LICA; red is from the RICA; blue is from the RVA; magenta is from the LVA. Dot-dashed lines show the results of modelling the network with no LICA occlusion, solid lines show the results modelling with the LICA occluded and no autoregulatory response, and dashed lines are from the network modelled with the LICA occluded and a complete autoregulatory response.

as RICA labelled tracer, arriving after 0.37 seconds, at a concentration of 0.04 *a.u.*.

Figure 5.5 also shows that when the LICA of variant 1 is occluded, tracer is rapidly delivered to the LACAA2 from the RICA (Figure 5.5b), and to the LMCA from the RICA and both VAs (Figure 5.5d). In the LMCA, a blood bolus from the RICA arrives 0.28 *seconds* after the start of labelling, with a tracer concentration of 0.4 *a.u.*, and boluses from the two VAs arrived 0.12 *seconds* later, each at a concentration of 0.23 *a.u.*. Compared to healthy conditions, when the LICA is occluded tracer labelled in the RICA arrives in the RMCA, RACAA2, and LACAA2 around 0.06 *seconds* earlier, and the tracer is delivered at higher concentrations e.g. 0.91 *a.u.* to the RMCA versus 0.88 *a.u.* under healthy conditions. Similar differences due to LICA occlusion were seen in the VA tracer signals detected in the PCAs. As expected, Figure 5.5 shows that when the LICA of variant 1 is occluded there are no substantial differences in ASL tracer delivery to the cerebral arteries related to the status of the cerebral autoregulatory response. When autoregulation was intact globally (dashed lines), tracer boluses tended to arrive in the cerebral arteries only 0.01 *seconds* earlier than when autoregulation was impaired globally (solid lines).

Figure 5.6 shows the results of modelling the passage of PASL boluses through the full circle of Willis. The figure provides all of the same information about collateral flow and flow directions in the circulus arteries as does Figure 5.5. The primary differences between the two figures are the amplitudes, shape, and arrival times of the PASL boluses, differences that result from the way that the PASL label is applied, as explained in Section 5.2.

Figure 5.7 shows PCASL tracer signals from the cerebral arteries of circle of Willis variant 5, in which the LPCAP1 is absent. From the baseline (no occlusion) signals in Figure 5.7f, it is clear that the proximal segment of the LPCA is not involved in the delivery of tracer to the LPCAP2, as no tracer labelled in either of

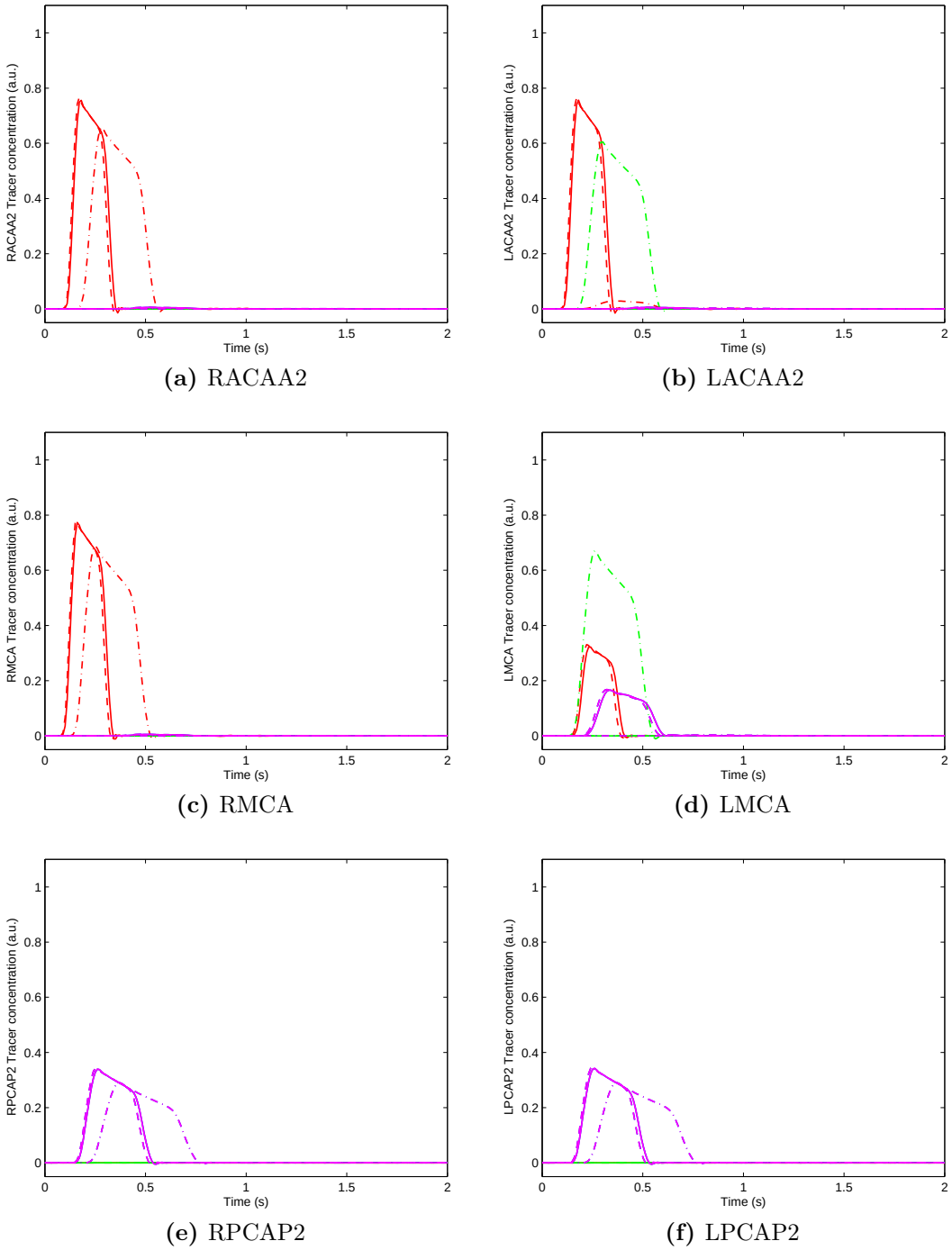
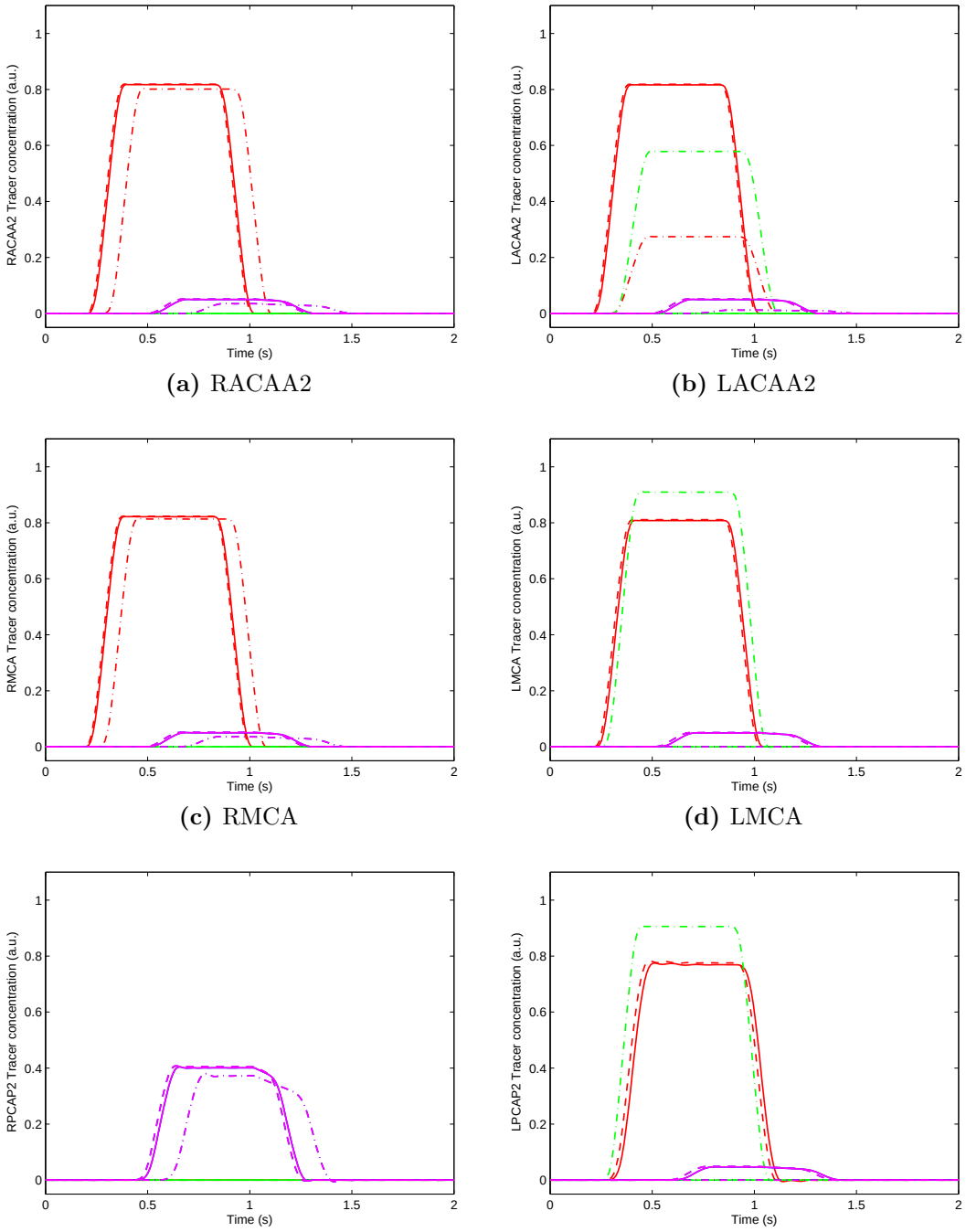


Figure 5.6: PASL tracer concentrations seen 5 *mm* distal to the origins of the cerebral arteries of the complete circle of Willis (variant 1). For explanations of the line styles refer to the caption of Figure 5.5.

the VAs is detected. Under these conditions, only tracer that was labelled in the LICA is seen in the LPCAP2, supplied via the LPCoA and arriving 0.27 *seconds* after the start of labelling, at a concentration of 0.91 *a.u.*. Compared to the baseline



(a) RACAA2 **(b)** LACAA2

(c) RMCA **(d)** LMCA

(e) RPCAP2 **(f)** LPCAP2

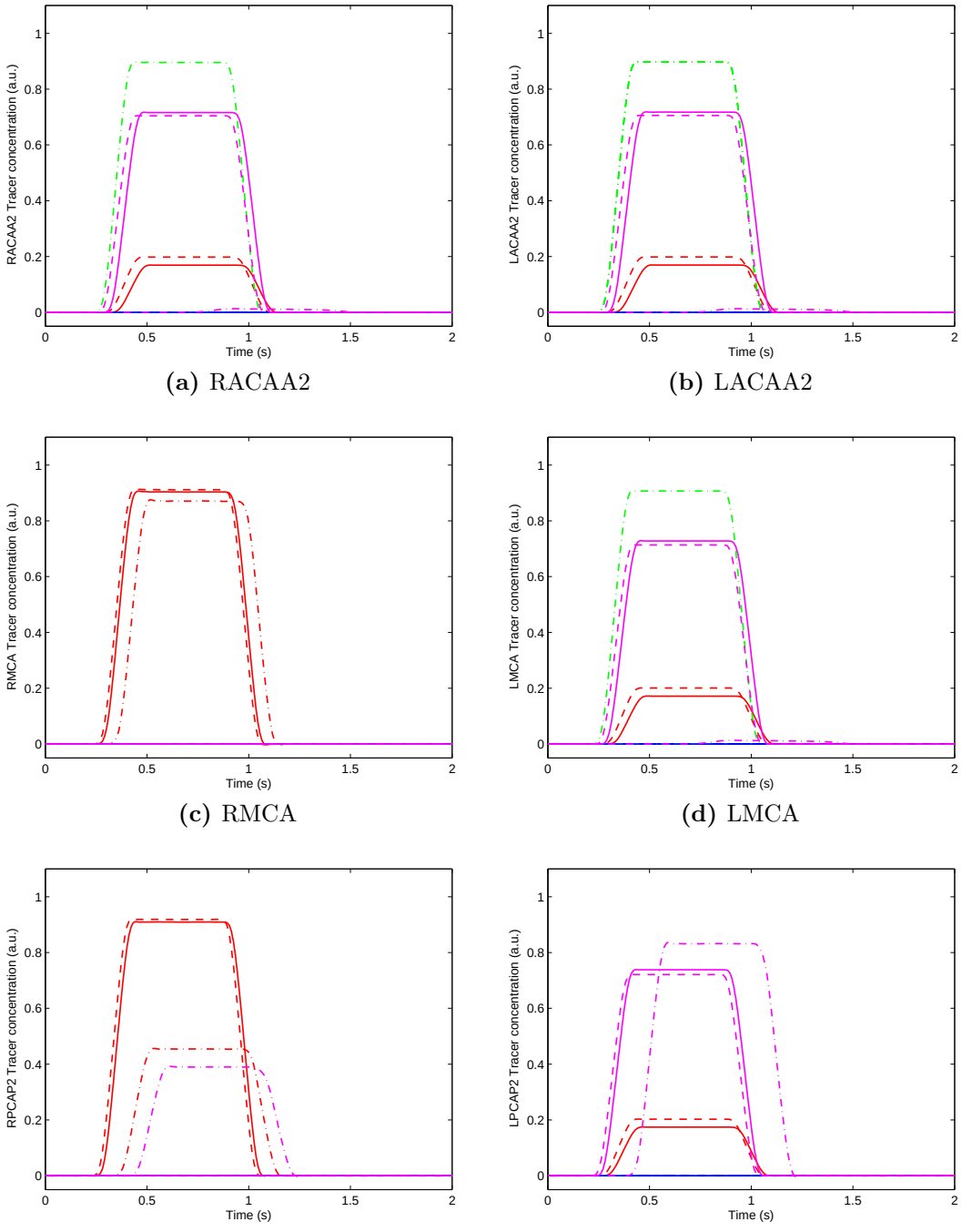
Figure 5.7: PCASL tracer concentrations seen 5 *mm* distal to the origins of the cerebral arteries of circle of Willis variant 5 (No LPCAP1). For explanations of the line styles refer to the caption of Figure 5.5.

conditions for the full circle of Willis (Figure 5.5e), RVA and LVA labelled tracer arrived in the RPCAP2 of variant 5 0.15 *seconds* later, at 0.61 *seconds* (Figure 5.7e). The RVA and LVA bolus tracer concentrations were also lower at 0.37 *a.u.*,

compared with 0.41 *a.u.* seen in variant 1. RVA and LVA labelled tracer can be seen in the RMCA, the RACAA2, and the LACAA2, as late arriving (> 0.7 *seconds*), low concentration pulses: 0.04 *a.u.* in the RMCA, 0.03 *a.u.* in the RACAA2, and 0.01 *a.u.* in the LACAA2. Similarly, RICA labelled tracer is seen to flow clockwise around the circle, as seen in Figure 5.5. In the variant 5 results, the RICA provides tracer at slightly lower concentrations to the RMCA and RACAA2 which were reduced by 0.07 *a.u.* and 0.09 *a.u.*, respectively, compared to variant 1 under healthy conditions. However, RICA labelled tracer is seen at a much higher concentration in the LACAA2, which increased from 0.04 *a.u.* in variant 1 to 0.27 *a.u.* in variant 5. The LICA labelled tracer contribution to the LACAA2 is reduced from 0.82 *a.u.* in variant 1 to 0.58 *a.u.* in variant 5, due to the addition of the LPCAP2 to the set of vessels dependent on the LICA.

It can be seen in Figure 5.7 that, when the LICA is occluded, tracer from both of the VAs and the RICA is supplied clockwise all the way around the circle such that, other than in the RPCA which is supplied by the VAs only, tracer contributions from all three remaining supply arteries are detected in every cerebral artery. On the right side of the circle, RICA and VA labelled tracer arrive more rapidly when the LICA is occluded than under healthy conditions. On the left side of the circle, tracer seen in the cerebral arteries is largely supplied by the RICA, which provides a 0.82 *a.u.* tracer bolus to the LACAA2, a 0.81 *a.u.* bolus to the LMCA, and a 0.78 *a.u.* bolus to the LPCAP2. These tracer signals arrive either faster than the corresponding LICA tracer boluses seen under healthy conditions, or at most, 0.03 *seconds* later, in the case of the LPCAP2.

Figure 5.8 shows the modelled tracer signals seen in the cerebral arteries of circle of Willis variant 11, which is lacking the proximal segment of the anterior cerebral artery, and the right vertebral artery. Absence of the RVA from the circle leads to RVA labelled tracer boluses of zero concentration in all six subfigures in Figure 5.8. This is not immediately evident because in Figures 5.5–5.7 and Figure 5.9, the blue



(a) RACAA2 **(b)** LACAA2

(c) RMCA **(d)** LMCA

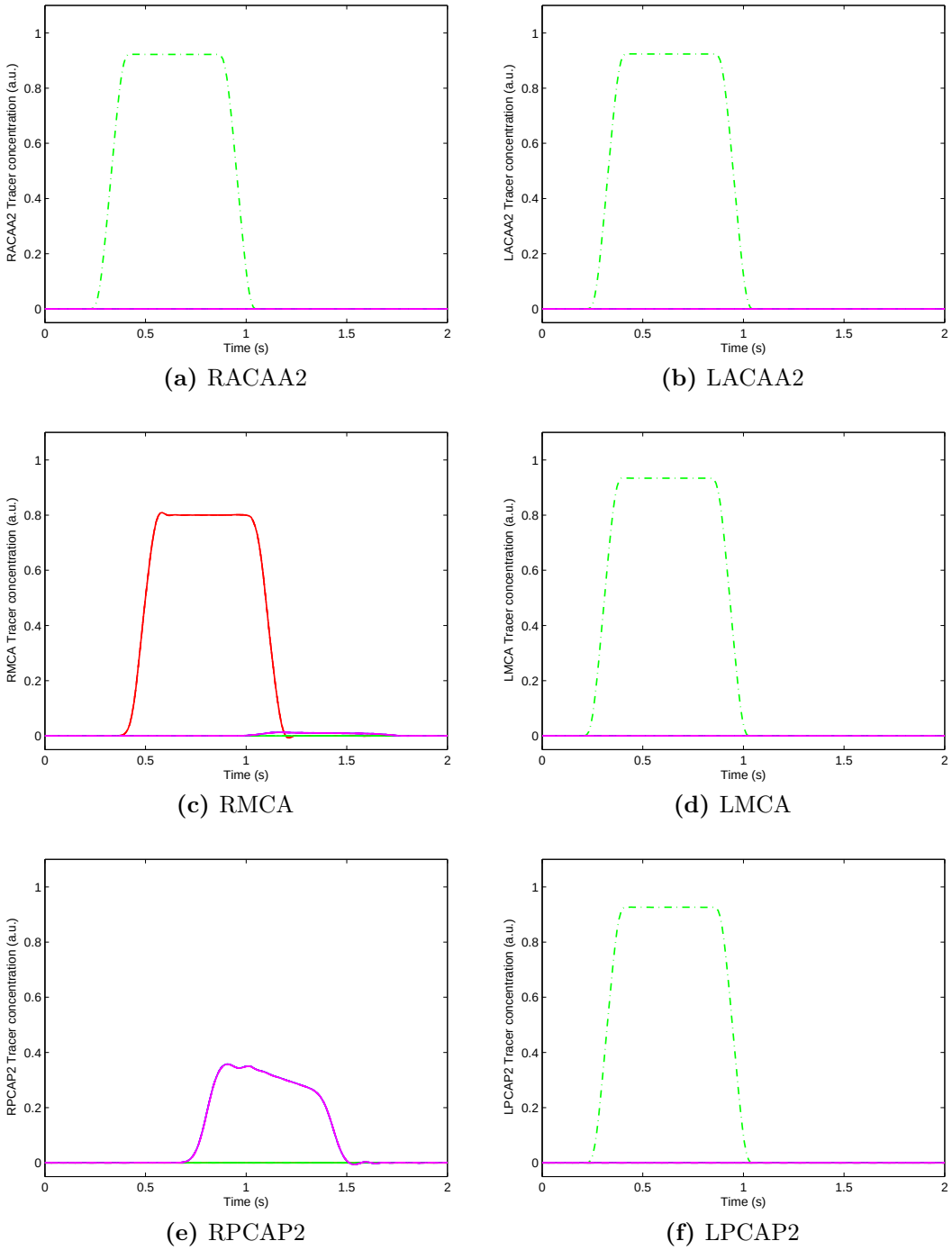
(e) RPCAP2 **(f)** LPCAP2

Figure 5.8: PCASL tracer concentrations seen 5 *mm* distal to the origins of the cerebral arteries of circle of Willis variant 11 (No RACAA1 or RVA). For explanations of the line styles refer to the caption of Figure 5.5.

RVA tracer signals are obscured by the extremely similar LVA tracer signals shown in magenta.

The modelled tracer signals in Figure 5.8 show that, under healthy conditions, the LICA supplies tracer to the LMCA, LACAA2 and, due to the absence of the RACAA1, the RACAA2, at concentrations of 0.91 *a.u.*, 0.90 *a.u.*, and 0.90 *a.u.*, respectively. Flow through the anterior communicating artery is therefore left-to-right. These boluses arrive in their respective cerebral arteries $0.24 - 0.26$ *seconds* after the start of PCASL labelling. Under healthy conditions, the RICA supplies tracer to the RMCA and is the larger contributor to the RPCAP2, providing a bolus, that arrives after 0.35 *seconds*, with a tracer concentration of 0.45 *a.u.*, while a 0.39 *a.u.* tracer bolus is supplied by the LVA and arrives after 0.42 *seconds*. In the case of LICA occlusion, tracer in the RPCAP2 is solely supplied by the RICA, and anticlockwise flow around the circle of Willis provides RICA and LVA labelled tracer to the LPCAP2, LMCA, LACAA2 and RACAA2. The LVA provides these arteries with tracer at higher concentrations than the RICA: $0.70 - 0.72$ *a.u.* compared to $0.17 - 0.20$ *a.u.* provided by the RICA.

Figure 5.9 shows similar vessel-specific tracer concentrations modelled in one of the circle of Willis variants identified as 'high-risk' in Chapter 3: the circle missing the proximal segments of both the RACA and the LPCA (variant 10). The figure shows that due to isolation of the RACAA2, LACAA2, LMCA and LPCAP2 from the RICA, RVA and LVA blood supplies, under healthy conditions these cerebral arteries only receive tracer labelled in the LICA. When the LICA is occluded, the blood supply to its four dependent arteries is cut off and the arteries do not receive any tracer. For the remaining cerebral arteries (the RMCA and RPCAP2) there is no difference in tracer delivery between healthy conditions and LICA occlusion in this circle variant. The RICA supplies a tracer bolus of 0.8 *a.u.* to the RMCA 0.4 *seconds* after the start of labelling, and the two VAs deliver tracer boluses to the RPCAP2 , which arrive after 0.72 *seconds*, each at a concentration of 0.35 *a.u.*. The VAs also supply a small amount of tracer (0.01 *a.u.*) to the RMCA, which arrives after 1 *second*. Compared to the signals seen in the full circle of Willis (Figures 5.5c and 5.5e), both under healthy conditions



(a) RACAA2 **(b)** LACAA2

(c) RMCA **(d)** LMCA

(e) RPCAP2 **(f)** LPCAP2

Figure 5.9: PCASL tracer concentrations seen 5 *mm* distal to the origins of the cerebral arteries of circle of Willis variant 10 (No RACAA1 or LPCAP1). For explanations of the line styles refer to the caption of Figure 5.5.

and when the LICA is occluded, the RMCA and RPCAP2 tracer signals are late arriving, by 0.1 *seconds* in the case of RICA tracer in the RMCA and by 0.26 *seconds* in the case of the VA tracers in the RPCAP2.

5.5 Discussion

In this chapter a mathematical model of ASL tracer transport through the circle of Willis has been described. The tracer model involved the application of the general mass transport equation over the arterial network defined by the physiological parameters from Table 3.1 in Chapter 3.

5.5.1 The tracer model

An angiography tracer modelling framework has been set out which links the lumped-parameter cerebral arterial network model of Chapter 3 to the two-dimensional mass transport-based angiographic flow quantification technique developed in Chapter 4. The tracer modelling work was applied over the arterial network geometry from Chapter 3 and included specific features of vessel-selective generation of an ASL tracer, longitudinal relaxation of both PCASL and PASL labelled blood boluses, and the attenuating effects of a Look-Locker dynamic MR acquisition (Sections 2.4.4 and 5.2.4) [128].

While the tracer model presented in this chapter does not perfectly describe the VEPCASL imaging data used in Chapter 4, it does provide a good understanding of the factors which affect tracer transport in such angiography acquisitions. For example, due to the 1D nature of the the tracer transport model, it was not possible to include radial variation of the blood flow velocity, as was done in Chapter 4 (equation 4.2). However, the model provides a middle ground between the lumped-parameter network model and the 2D angiography model. Also, as outlined in Section 5.2, the tracer advection equation was solved numerically using the two-step Lax-Wendroff. However, as non-physical ringing arose in the Lax-Wendroff solution when sharp-cornered rectangular functions were used to represent the PASL and PCASL labelling pulses, smoothed rectangular pulses were used instead. The smoothing of these pulses reduced the proportion of time, in the case of PCASL, and space, in the case of PASL, that the pulses were at their maximum value. This

effectively reduced the widths of the applied labelling pulses.

The tracer model was used to simulate vessel-specific PCASL and PASL labelling of the four afferent arteries of the circle and the passage of the resulting labelled blood boluses through several variants of the circle of Willis under healthy conditions, and under conditions of LICA occlusion. This modelling work was carried out in order to provide an indication of the extent to which vessel-selective angiography imaging can provide information about the structure and function of the circle of Willis.

5.5.2 Circle of Willis variant results

The modelling results in Section 5.4 confirm that collateral flow through the communicating arteries of the circle of Willis can be identified, and the direction of blood flow around the circle can be determined, based on the tracer signals seen in the six efferent arteries of the circle. For example, from Figure 5.7 it could be determined from the cerebral artery tracer concentration-time curves of circle variant 5 (missing the LPCAP1) that, under healthy conditions, there was posterior-to-anterior collateral flow through the RPCoA, as 0.4 *a.u.* of both RVA and LVA labelled blood was seen in the RMCA. There was also right-to-left collateral flow through the ACoA, demonstrated by 0.27 *a.u.* of RICA labelled blood delivered to the LACAA2, and anterior-to-posterior collateral flow through the LPCoA, which was demonstrated by 0.91 *a.u.* of LICA labelled blood delivered to the LPCAP2. In addition, in healthy conditions, blood in the LACAA1 could be identified as flowing anteriorly, as 0.58 *a.u.* of LICA labelled blood was delivered to the LACAA2. Absence of this tracer signal in the LACAA2 when the LICA was occluded, along with a higher concentration of RICA labelled blood (0.82 *a.u.*, compared with 0.27 *a.u.* under healthy conditions), and the presence of RICA labelled blood in the LMCA and LPCAP2, demonstrated that the direction of blood flow had changed, such that blood flowed posteriorly through the LACAA1 when the LICA was occluded.

While the presence of specific tracers can be used to identify the directions of flows through the circulus arteries, absence of such tracer signals does not necessarily provide evidence of absence of circulus arteries, only evidence of very low, or absent, flow through those arteries. As an example of vessel absence, consider the tracer concentration curves in variant 10 (Figure 5.9) under healthy conditions. The results show substantial LICA labelled tracer concentrations in the LPCAP2 and the RACAA2 (0.93 *a.u.* and 0.92 *a.u.*, respectively), demonstrating significant collateral flow through both the ACoA and LPCoA. The absence of RICA labelled tracer from the RACAA2, and the absence of RVA and LVA labelled tracers from the LPCAP2 demonstrates that there is no flow through both the RACAA1 and the LPCAP1. These arteries would typically be the primary flow routes to the RACAA2 and LPCAP2, respectively. From the complete absence of these expected tracer signals, it is reasonable to assume that the proximal segments of the RACA and LPCA are absent or non-functional. Examination of the tracer signals obtained from modelling LICA occlusion in this network show that this assumption is correct. When the LICA was occluded, there was no flow through these vessels to the RACAA2 or any of the cerebral arteries on the left of the circle.

Figure 5.9 also shows that there was no change to the tracer signals seen in the RMCA or the RPCAP2 when the LICA was occluded. These signals showed slight posterior-to-anterior collateral flow through the RPCoA. Thus, from the healthy-condition tracer signals it was possible to identify the presence and functionality of all of the circulus arteries, other than the RACAA1 and the LPCAP1. Using the signals modelled with the LICA occluded, it was only possible to identify the presence and functionality of: the distal segment of the RICA, the RPCoA, and the RPCAP1. The tracer signals seen in the RMCA and RPCAP2 were delayed relative to the same tracer signals seen in these arteries in variant 1 (Figure 5.5) under healthy conditions. This resulted from lower blood flow rates through the RICA and the VAs in this circle variant, due to the smaller set of efferent arteries

dependent on them for blood supply.

In the full circle of Willis (variant 1) it is less simple to determine the structure of the circle based on the tracer signals seen in the cerebral arteries. Considering the 'no-occlusion' signals (dot-dashed lines), Figure 5.5a, 5.5c, and 5.5e show almost no evidence of collateral flow through the RPCoA. Figure 5.5d shows a very slight posterior-to-anterior collateral flow signal through the LPCoA based on the late arriving 0.005 *a.u.* of RVA and LVA labelled tracers in the LMCA. Also, Figure 5.5b shows slight right-to-left collateral flow through the ACoA, based on 0.04 *a.u.* of RICA labelled tracer in the LACAA2. However, these very low amplitude tracer concentration signals are not indicative of low capacity circulus vessels, they instead reflect the the fact that, for variant 1 under baseline conditions, the communicating arteries sustain very little collateral flow as they are not necessary to adequately supply blood to the cerebral arteries (see Table 3.3).

The tracer signals in Figure 5.5 obtained when network variant 1 was modelled with the LICA occluded (dashed lines and solid lines) show that the ACoA and the LPCoA are able to provide substantial collateral flow. This is demonstrated by the 0.91 *a.u.* and 0.41 *a.u.* of RICA labelled blood in the LACAA2 and LMCA, respectively, and the 0.23 *a.u.* of both RVA and LVA labelled blood in the LMCA. Thus, regardless of whether the LICA in variant 1 was modelled as open or occluded, it was possible to identify the ACoA as present and functional. However, there was only clear evidence of flow through the LPCoA when the circle was modelled with the LICA occluded, and neither LICA condition provided clear evidence of the presence of the RPCoA. This is because the very low VAs tracer concentrations detected in the RMCA and LMCA (0.001 and 0.005 *a.u.*, respectively) would very likely be obscured by noise in a real angiography acquisition.

The tracer signals in Figure 5.7 are of interest when considering the different levels of structural information available under healthy conditions and under conditions

of LICA occlusion. When considering the 'no-occlusion' signals, it is reasonable to assume that the LPCAP1 is absent or non-functional due to absence of RVA or LVA labelled tracer in the LPCAP2. Such signals would typically be expected as these afferent arteries are the primary suppliers of this cerebral artery in the complete circle of Willis (see Figure 5.5f). However, in Figure 5.7f the LICA was the sole supplier to the LPCAP2, and supplied tracer at a concentration of 0.91 *a.u.*.

When the LICA was occluded, flow through the LACAA1 was reversed so that tracer labelled in the RICA, the RVA, and the LVA was supplied to the LMCA and LPCAP2. This led to the presence of RVA and LVA labelled tracer in the LPCAP2, which caused greater difficulty in identifying the absence of the LPCAP1 in this circle variant. This is because RVA and LVA labelled tracer signals are to be expected in the LPCAP2 if the LPCAP1 is present. However, the RVA and LVA tracer signals in Figure 5.7f were later arriving and of lower amplitude (0.28 *seconds* later and 0.39 *a.u.* lower) compared to those seen in Figure 5.5f during LICA occlusion. The signals also showed VA tracers at much lower concentrations than the concentration of RICA labelled tracer in the LPCAP2 (present at a concentration of 0.78 *a.u.*).

From the LICA-occlusion signals in Figure 5.7f it is not possible to determine whether the RVA and LVA tracer signals result from very slow flow through the LPCAP1, or from collateral flow clockwise around the entire circle of Willis. The latter conclusion is supported by the fact that RVA and LVA labelled tracers were also seen in the RMCA, RACAA2, LACAA2, and LMCA. The two tracers are present at the same concentrations (0.05 *a.u.*) in all four of these cerebral arteries. Furthermore, the arrival times of the RVA and LVA labelled boluses in the cerebral arteries indicate they travelled clockwise around the circle: arriving in the RMCA 0.50 *seconds* after the start of labelling, in the RACAA2 after 0.51 *seconds*, in the LACAA2 after 0.53 *seconds*, in the LMCA after 0.54 *seconds*, and in the LPCAP2 0.63 *seconds* after the start of labelling. Such clear evidence of slow,

long range collateral flow around the circle in the LICA occluded situation is a strong indication that the LPCAP1 is absent.

		Variant			
		1	5	11	10
Artery	LICA occluded?	Full circle	No LPCAP1	No RACAA1 or RVA	No RACAA1 or LPCAP1
LICA 2	No	✓	✓	✓	✓
	Yes	✓	✓	✓	✗
RICA 2	No	✓	✓	✓	✓
	Yes	✓	✓	✓	✓
LACAA1	No	✓	✓	✓	✓
	Yes	✓	✓	✓	✗
RACAA1	No	✓	✓	✗	✗
	Yes	✓	✓	inference	✗
LPCAP1	No	✓	✗	✓	✗
	Yes	✓	inference	✓	✗
RPCAP1	No	✓	✓	✓	✓
	Yes	✓	✓	✓	✓
LPCoA	No	SNR	✓	SNR	✓
	Yes	✓	✓	✓	✗
RPCoA	No	SNR	SNR	✓	SNR
	Yes	✓	✓	✓	SNR
ACoA	No	SNR	✓	✓	✓
	Yes	✓	✓	✓	✗

Table 5.1: Summary of the modelling results presented in this chapter, indicating whether presence or absence of the circulus arteries can be confirmed based on angiography signals detected in the cerebral arteries. A tick symbol (✓) shows that an artery can be confirmed as present, a cross (✗) shows an artery that can be confirmed as absent, 'inference' indicates cases where inference based on signal arrival times is required to determine the presence or absence of an artery, and 'SNR' indicates cases in which the relevent downstream signals are very low amplitude, and would likely be obscured by noise.

Table 5.1 presents a summary of the results in Figures 5.5 and 5.7–5.9, in terms of whether or not it is possible to confirm the presence of each of the circulus arteries, based on the vessel-encoded angiography signals detected in the cerebral arteries. The table indicates that, due to low flow and consequent low signal amplitude, the presence of the communicating arteries (LPCoA, RPCoA, and ACoA) may be difficult to confirm in some circle variants when the LICA has a healthy diameter. All of the other circulus arteries are detectable, both when the LICA diameter is

normal, and when the LICA is occluded. The RPCoA of variant 10 is the only circulus artery, in the variants considered in this chapter, that is likely to remain undetectable when the LICA is occluded.

Figures 5.5–5.9 show that, as expected, the status of the cerebral autoregulatory response had very little effect on tracer delivery to the cerebral arteries when the LICA was occluded. In Figures 5.5–5.7, under conditions of intact autoregulation (dashed lines), tracer generally arrived at the cerebral artery points of interest 0.01 *seconds* earlier than under conditions of globally-impaired autoregulation (solid lines). The tracer bolus concentrations in these cases were generally within 0.01 $a.u.$. This is because Figures 5.5 and 5.6 relate to circle variant 1, which was classified as 'low-risk' during LICA occlusion, meaning that the collateral circulation was able to provide robust blood supply ($> 90\%$ of healthy flows) to arteries downstream of LICA occlusion, even when cerebral autoregulation was globally impaired.

Although circle variant 5 was classified as 'medium-risk', Figure 5.7 shows little difference between the two autoregulation conditions. This is again due to the fact that the maximum reduction in cerebral artery blood flow caused by LICA occlusion and globally impaired autoregulation was only 11.2% (Figure 3.7), i.e. only just above the threshold for classification as 'medium-risk'. Figure 5.9 also showed no difference in tracer concentrations and delivery times between the two autoregulation conditions. This is because this circle of Willis (variant 10) is one that was identified as 'high-risk' in Chapter 3, in which the status of cerebral autoregulation had no effect at all on flows to any of the six cerebral arteries (see Figure 3.7).

Variant 11 (Figure 5.8) provided a case in which the status of the autoregulatory response had a more substantial effect on delivery of tracer to the cerebral arteries. In this case, autoregulatory status (complete autoregulation or absent autoregulation) caused $0.02 - 0.03$ *second* differences in arrival times during LICA occlusion, and

$0.01 - 0.03$ *a.u.* differences in tracer concentration. The difference between the autoregulating and non-autoregulating conditions was clearer in the results for this circle of Willis variant as it was classed as a 'medium-risk' variant, but was one in which autoregulation protected against very substantial flow reductions, particularly those seen by the LMCA and the LACAA2. For example, without autoregulation (scenario 1 in Figure 3.7) when the LICA was occluded, the LACAA2 saw a 25.9% reduction in blood flow rate relative to healthy conditions for that circle of Willis whereas, when autoregulation was intact globally (scenario 2), the same artery saw a flow rate reduction of only 7%. However, such large differences in flow rates in the cerebral arteries cause only the very slight differences in tracer delivery seen in Figure 5.8.

5.6 Summary

The angiographic tracer model described in this chapter has helped to determine the extent to which contrast enhanced cerebral angiography can be used to obtain information, beyond the measurement of arterial blood flow rates demonstrated earlier in this thesis, about the structure and function of the circle of Willis. Similar to the flow rate quantification method developed in Chapter 4, the modelling work in this chapter has focussed on the use of vessel-selective pseudo-continuous and pulsed arterial spin labelled (ASL) angiography data. However, as the tracer transport model is based on the general mass transport equation, the model could be reformulated to describe the kinetics of other contrast-enhanced angiographic imaging modalities, for example X-ray DSA.

The use of vessel-selective ASL tracer generation has been shown here to be extremely useful in identification of circle of Willis structure. However, as seen in Figures 5.7f, there are cases in which tracer signals detected in the cerebral arteries could be the result of delivery via either very slow direct flow, or very long range collateral flow. Study of the arrival times of tracer signals detected in the other cerebral arteries can be of use in distinguishing between these two situations.

Similar bolus arrival time information is routinely obtained during the analysis of dynamic ASL perfusion images. Such information could also aid the inference of structural features of the cerebral arterial network.

The results of tracer modelling demonstrate that angiography tracer signals do, in certain cases, show differences resulting from the status of cerebral autoregulation. However, the observed differences are simply caused by the resulting differences in flow rates through the arteries of the circle of Willis. As expected, there are no distinctive angiographic features which would allow inference of information about the status of the autoregulatory response.

In conclusion, the results presented in this chapter show that dynamic ASL cerebral angiography data can play a role, beyond quantification of arterial blood flows, in the identification of the structure and function of an individual's circle of Willis. As shown in Table 3.3, under healthy conditions (no occlusion), flows through the anterior communicating artery and both posterior communicating arteries are non-zero in all circle of Willis variants, provided that those arteries are present. However, Figures 5.5, 5.6, and 5.7 show that, in some circle of Willis variants, in which collateral flow occurs at very low levels, the tracer signals from collateral flow through the communicating arteries, seen in the cerebral arteries, are very low amplitude. In the context of the vessel-encoded PCASL angiography data used in Chapter 4, such low amplitude collateral flow signals are likely to be obscured by noise. This would be more problematic in the case of PASL angiography data, which is of inherently lower SNR (see Figures 4.3 and 5.6). However, cerebral angiography is most likely to be acquired in the context of afferent artery stenosis and occlusion, when cerebral blood flows are partially or fully dependent on collateral flows around the circle of Willis. As summarised in Table 5.1, it is under these conditions that more information is available about the structure and function of the small communicating arteries.

6 Conclusions and future work

6.1 Conclusions

The work presented in this thesis aimed to use mathematical modelling of the cerebral arterial network to explore the extent to which primary collateral blood flow routes and cerebral autoregulation, both individually and in combination, are able to preserve blood flows through the cerebral arteries during afferent vessel occlusion. Both of these mechanisms are of interest as they have been shown to be associated with improved outcomes of endovascular therapies (see Sections 2.1.3 and 2.1.4). However, as discussed in Section 2.1.3, the structure of the circle of Willis, which provides primary collateral flow routes to brain tissue, can vary significantly between individuals. Furthermore, the cerebral autoregulatory mechanisms can be impaired in one, or both, brain hemispheres during arterial stenoses and occlusions.

6.1.1 Network modelling

The results presented in Chapter 3 identified certain circles of Willis variants as presenting a higher risk of stroke during left internal carotid artery occlusion. For example, a patient possessing circle of Willis variant 8, in which the ACoA and the LPCoA are both absent, would be at much higher risk of stroke if experiencing LICA occlusion. This is because they lack a primary collateral flow route to either

the LACA or the LMCA. Thus, the LACA and LMCA territories would be entirely dependent on much smaller secondary collateral flow pathways. Such a patient may also be a poor candidate for recanalisation therapies, as the lack of collateral flow to the LACA and LMCA territories would be likely to result in large tissue regions that rapidly progress to infarction. This could potentially leave the patient vulnerable to haemorrhagic transformation [19].

The results in Chapter 3 also demonstrated that cerebral autoregulation is a crucial facilitator of collateral flow through the circle of Willis. When intact globally, autoregulation boosts cerebral blood flows, during LICA occlusion, to all six cerebral arteries. In doing so, autoregulation is able to ameliorate substantial flow reductions to cerebral arteries directly downstream of the arterial occlusion. However, impairment of the cerebral autoregulatory response ipsilateral to an arterial occlusion actually reduces flows directly downstream of an occlusion more than global impairment of autoregulation.

Consider circle of Willis variant 6, in which the proximal segment of the RACA is absent. If a patient possessing this circle of Willis variant presented with LICA occlusion, and with autoregulation impaired globally, the patient's cerebral tissue downstream of both ACAs and the LMCA would be at risk of infarction. With globally intact autoregulation this tissue would be at much lower risk. However, if autoregulation were impaired ipsilateral to the arterial occlusion, but intact contralaterally, the LACA and LMCA territories would be at risk, but the RACA territory would not. Autoregulation of the right hemisphere would draw blood through the LACAA1 and ACoA to preserve flow to the RACA, at the expense of flows to the vessels at risk en route. These results show the influence of autoregulation on cerebral blood flows, and therefore on cerebral tissue survival. Thus, the work suggests that cerebral autoregulation should be monitored in both hemispheres in acute ischaemic stroke patients, in the hours and days following stroke onset.

6.1.2 Flow quantification

Chapter 4 addressed the lack of a reliable method for absolute blood volume flow rate quantification in short segments of the intracranial arteries from angiography imaging data. The proposed model-based flow quantification technique was successfully validated using dynamic PCASL images of a flow phantom. It was shown to accurately estimate flow rates in this data set over shorter vessel segments than an existing technique. In many cases, when applied to flow rate quantification using dynamic PCASL images of the circles of Willis of healthy volunteers, the flow quantification technique showed good agreement with estimates of blood flow rates in the arteries of interest, obtained using established techniques such as PC-MRA, as well as existing ASL analysis methods.

During in vivo testing, the flow quantification technique was found to be very sensitive to contamination from small vessels overlapping the arterial segments of interest within the 2D thick-slab images. These areas of vessel overlap often resulted in estimates of high blood flow rates from afferent arteries unlikely to be involved in the supply of the artery of interest. Furthermore, the technique was found to be SNR dependent, a factor which also caused flow rate quantification errors.

The quantification issues listed above may limit the use of the proposed technique to make measurements of blood flow rates in the arteries of the circles of Willis of patients. The reasons for this are two-fold. Firstly, clinical data from patients, as opposed to healthy volunteers, is often more noisy. In part, this is because patients may find it harder to remain still for the duration of an MRI scan. The scan time required for the acquisition of two dynamic, vessel-encoded, thick-slab images of the circle of Willis was approximately 10 minutes. Example images from such an acquisition are shown in Figure 4.5. The second factor that may limit the application of the proposed flow quantification technique to clinical data, in its current iteration, is the need for reliable estimates of collateral blood flows to the cerebral arteries. If a method cannot be devised to eliminate contaminating

signals from overlapping vessels, or to distinguish between these signals and signals derived from true collateral flow, then the technique cannot be applied to the assessment of collateral flow. Both of the factors limiting the application of the technique to clinical data will be discussed further, in Section 6.2, with a view to methods that could improve its robustness.

6.1.3 Model personalisation

Chapter 5 considered the angiography signals that would be observed in some of the variants of the circle of Willis presented in Chapter 3. The inverse task, in which angiography signals are used to define the imaged arterial network, is a challenging problem which was beyond the scope of this thesis. However, this challenge will be discussed, in terms of the possible next steps to be taken, in Section 6.2.

The model presented in Chapter 5 demonstrated that vessel-selective angiography signals can be used to obtain additional information about the structure and function of an individual's circle of Willis. This information could be used in conjunction with that which can be obtained from a high-resolution TOF MRA scan. Such scans are typically acquired in the planning stage of a dynamic VEPCASL angiography acquisition, but do not provide temporal information. The tracer modelling work in Chapter 5 showed that vessel-selective angiography signals measured in the cerebral arteries could often be used to infer the direction of blood flow around the circle of Willis. In most cases, the signals could thereby be used to determine which, if any, of the circulus arteries were absent. This additional structural information can be of benefit in cases of arterial stenoses and occlusions, when slow or turbulent flows may lead to the loss of TOF MRA signal. It was noted in Chapter 5 that the relatively low SNR of some collateral flow signals seen on ASL angiography may mean that very low level collateral flow signals, such as those seen in variant 1 under healthy conditions (Figure 5.5), may be obscured by noise. However, imaging of the cerebral vasculature is most likely to be performed after a patient presents with neurological symptoms. If such symptoms are a result of arterial stenosis

or occlusion, the cerebral artery tracer signals resulting from collateral flow will be likely to have higher values of SNR.

6.2 Future work

The work presented in this thesis is a step towards the development of an arterial network modelling framework which could be rapidly personalised, and could thereby allow simulations of arterial stenoses and occlusions, or of recanalisation therapies, to be used as tools to aid clinical decision making. However, a substantial body of work remains before such a network model could be used in a clinical context. This section presents recommendations of the next steps to be taken in the process of developing such a framework.

6.2.1 Measurements of arterial blood flows

In the short term, the robustness of the blood flow quantification technique, presented in Chapter 4, may be improved through the use of a masking technique to eliminate noisy non-vascular voxels from consideration. A technique like that used by Okell *et al.* [91] could be applied for this task. The technique used by Okell *et al.* eliminated voxels from a high-signal mask if both their mean and maximum signal intensities were below certain thresholds. These thresholds were set at 40% of the 99$^{\text{th}}$percentiles of the mean and maximum voxel signal intensities within the image. It is likely that the addition of a similar noise masking procedure to post-processing of the VEPCASL angiography images would significantly improve the noise performance of the blood flow quantification technique. In addition to this, simulations of cerebral angiography signals with a variety of SNRs could be used to systematically test the performance of the technique in the presence of noise, and identify the minimum SNR required for the technique to accurately quantify flow rates.

Contaminating signals from overlapping vessels within the imaging plane are unlikely to be eliminated through the application of the noise masking technique

described above. However, it is possible that noise reduction could improve flow quantification such that the technique could be applied over shorter vessel segments than those identified as optimal in Figure 4.8. The ability to apply the technique over shorter vessel segments may mean that vessel ROIs can be drawn in such a way as to avoid regions of vessel overlap (see Figure 4.16).

Dynamic ASL MRA images are generally acquired as 2D thick-slabs in order to limit acquisition time while achieving high spatial and temporal resolution. If it is found to be too challenging to apply the blood flow rate quantification technique to 2D thick-slab data, it may instead be possible to apply it to 3D data, in which the problem of vessel overlap would be significantly reduced. Such data are likely to become increasingly available. Several authors have recently demonstrated the acquisition of dynamic 3D ASL MRA images of the cerebral arterial network [139]–[141]. Lindner *et al.* [139] in 2015, and Okell *et al.* in 2016 [141] demonstrated vessel-selective 3D dynamic ASL MRA.

6.2.2 Model personalisation

Structural information

The comparisons of the 0D steady-state modelling work presented in Chapter 3, with 1D and 3D models of the cerebral arterial network from literature, has demonstrated that steady-state modelling can be used to provide good approximations to higher dimensional models. This is particularly beneficial in the clinical context of stroke, as a simpler model that can be used to perform simulations rapidly is likely to be of most use.

A 2005 article by Moore *et al.* [71] showed that simple scaling parameters were all that was required to match the distributions of blood flows in and around a 0D model of the circle of Willis to those seen in a 3D model whose arterial structure was derived from TOF MRA images. In much of the literature covering personalised modelling (see Section 2.2) authors have extracted morphological

information about the cerebral arterial network from high-resolution 3D TOF MRA. A useful next step in the process of personalised steady-state modelling of the network would be to devise a method of rapidly extracting vessel measurements from such structural scans, in order to automatically generate an equivalent 0D representation of the network based on Poiseuille's law.

Functional information

As mentioned in Section 2.2, measurements of network flow parameters, such as velocity flow profiles, that can be derived from functional angiography imaging modalities, have typically been included in personalised arterial network models as boundary conditions. Or, such information has been used to validate the results of simulations performed using arterial network models personalised only on the basis of structural information. Finding the optimal way to personalise models using both structural information, and functional information, such as the blood volume flow rate measurements obtained in Chapter 4, is a challenging task, which forms the bulk of the required future work relating to the project presented in this thesis. The challenge lies in determining how much, and what kind, of information is required, and how a variety of measurements, each of which will be measured with a certain level of confidence, can be combined to uniquely identify an individual's cerebral arterial network.

It is possible that model sensitivity analysis could be used to identify parameters of the arterial network model, presented in Chapter 3, that could reasonably be considered generic, i.e. if uncertainty on the values of such parameters had limited influence on the simulated blood flows through the arteries of the circle of Willis. For example, sensitivity analysis could reveal that the outputs of interest, which are the calculated flows through the circle of Willis, are fairly insensitive to the parameters defining the arteries below the neck. If this were the case, the model could be truncated at the base of the neck, or the network of arteries below the

neck could be considered common to all subjects.

As already mentioned, measurements of arterial structure can be made from high-resolution structural angiography imaging modalities, and estimates of arterial blood flow rates can be obtained from dynamic angiography data. However, every measurement made within a cerebral arterial network will be taken with some level of confidence, or of possible measurement error. In some cases such a confidence level relates to the spatial resolution of imaging data, and in other cases it relates to the uncertainty of parameter estimation. Attempting to directly combine these measurements would be likely to produce a set of coupled network equations with no solution, due to inconsistencies at junctions and bifurcations, or the lack of a unique solution.

Personalised arterial network models may need to be solved iteratively to optimise the set of parameters that describe them best. This process may be easier if a network were considered in a series of smaller subdivisions, for example the two vertebral arteries and the basilar artery could be considered as one such subdivision. With knowledge of the initial measured estimates of vessel radii, lengths and flow rates, and of the uncertainties of those estimates, a Bayesian parameter inference technique, similar to that used in Section 4.3.4, would allow identification of the set of most likely parameters that allow for conservation of mass at the node joining the three arteries. A Bayesian technique would allow propagation of the uncertainty through the parameter estimation process. Iteration of this process around the various small network subdivisions that make up the circle of Willis should then allow the network to converge upon a unique solution.

6.3 Summary

This thesis has presented a novel investigation of the interaction between cerebral autoregulation and collateral flow through the circle of Willis, and has developed a method for blood volume flow rate quantification in short vessel segments from

dynamic ASL angiography images. The work has also suggested that information from vessel-encoded angiography signals, including bolus arrival times, could be used to infer further information about the structure of the circle of Willis. In the short term, work is required to identify and improve the SNR threshold of the quantitative angiography technique. In the longer term, further work is also required to develop methods to accurately personalise the cerebral arterial network modelling framework presented here, such that it can be used to aid clinical decision making in the context of cerebrovascular disease.

Appendices

A

A.1 Blood flow rates through the circle of Willis from network simulations

This appendix provides the results of modelling simulations of the thirteen variants of the circle of Willis, presented in Chapter 3, performed under healthy conditions, and under conditions of LICA stenosis, LICA occlusion, LVA occlusion, combined LICA stenosis and RICA occlusion, and combined LICA occlusion and RICA stenosis. Each of these network insults was simulated in each circle variant with each of the three possible autoregulation scenarios. The results are provided in the form of tables of absolute blood volume flow rates through the afferent and efferent arteries of the circle of Willis.

Variant 1: Full circle							
Artery	Scenario	Healthy	LICA stenosed	LICA occluded	LVA occluded	LICA stenosed RICA occluded	LICA occluded RICA stenosed
LICA	1	3.35	1.36	0.00	3.62	2.73	0.00
	2	3.35	1.40	0.00	3.64	3.10	0.00
	3	3.35	1.37	0.00	3.63	2.90	0.00
RICA	1	3.52	4.68	5.48	3.80	0.00	2.76
	2	3.52	4.79	5.71	3.82	0.00	3.13
	3	3.52	4.73	5.56	3.81	0.00	2.94
LVA	1	1.14	1.44	1.64	0.00	2.62	2.61
	2	1.14	1.47	1.70	0.00	2.93	2.92
	3	1.14	1.45	1.66	0.00	2.75	2.74
RVA	1	1.14	1.44	1.64	1.67	2.62	2.61
	2	1.14	1.46	1.70	1.69	2.93	2.91
	3	1.14	1.44	1.66	1.68	2.75	2.74
LMCA	1	2.06	1.97	1.91	2.05	1.78	1.74
	2	2.06	2.05	2.04	2.06	2.01	2.00
	3	2.06	1.97	1.91	2.05	2.02	1.72
RMCA	1	2.06	2.03	2.01	2.05	1.74	1.79
	2	2.06	2.06	2.05	2.06	2.01	2.02
	3	2.06	2.06	2.06	2.06	1.72	2.02
LACA	1	1.42	1.37	1.34	1.42	1.22	1.21
	2	1.42	1.42	1.41	1.42	1.39	1.38
	3	1.42	1.37	1.34	1.42	1.39	1.19
RACA	1	1.42	1.39	1.37	1.42	1.21	1.22
	2	1.42	1.42	1.42	1.42	1.38	1.39
	3	1.42	1.42	1.42	1.42	1.19	1.39
LPCA	1	1.09	1.08	1.07	1.08	1.02	1.01
	2	1.09	1.09	1.09	1.09	1.08	1.08
	3	1.09	1.08	1.07	1.08	1.08	1.01
RPCA	1	1.09	1.08	1.07	1.08	1.01	1.02
	2	1.09	1.09	1.09	1.09	1.08	1.08
	3	1.09	1.09	1.09	1.09	1.01	1.08

Table A.1: Flow rates (in ml/s) through the afferent and efferent arteries of variant 1. Scenario 1 included a vascular bed modelled as passive. In Scenario 2 all of the cerebral tissue territories were modelled as autoregulating. In Scenario 3 only cerebral territories contralateral to the main stenosis or occlusion were modelled as autoregulating.

Variant 2: No LPCoA							
Artery	Scenario	Healthy	LICA stenosed	LICA occluded	LVA occluded	LICA stenosed RICA occluded	LICA occluded RICA stenosed
LICA	1	3.39	1.54	0.00	3.49	3.25	0.00
	2	3.39	1.59	0.00	3.51	3.77	0.00
	3	3.39	1.54	0.00	3.50	3.51	0.00
RICA	1	3.53	4.87	5.99	3.80	0.00	3.25
	2	3.53	5.01	6.32	3.83	0.00	3.83
	3	3.53	4.92	6.09	3.82	0.00	3.49
LVA	1	1.12	1.24	1.34	0.00	2.29	2.22
	2	1.12	1.26	1.38	0.00	2.57	2.52
	3	1.12	1.25	1.36	0.00	2.40	2.35
RVA	1	1.12	1.24	1.34	1.79	2.29	2.22
	2	1.12	1.26	1.38	1.81	2.57	2.51
	3	1.12	1.25	1.36	1.80	2.40	2.34
LMCA	1	2.06	1.95	1.86	2.06	1.71	1.60
	2	2.06	2.04	2.03	2.06	1.99	1.96
	3	2.06	1.95	1.86	2.05	2.00	1.57
RMCA	1	2.06	2.02	1.99	2.05	1.70	1.72
	2	2.06	2.06	2.05	2.06	1.99	2.00
	3	2.06	2.06	2.05	2.06	1.67	2.01
LACA	1	1.42	1.36	1.31	1.42	1.18	1.13
	2	1.42	1.41	1.41	1.42	1.38	1.36
	3	1.42	1.36	1.31	1.42	1.38	1.11
RACA	1	1.42	1.38	1.35	1.42	1.17	1.16
	2	1.42	1.42	1.41	1.42	1.38	1.37
	3	1.42	1.42	1.41	1.42	1.15	1.38
LPCA	1	1.10	1.09	1.08	1.07	1.04	1.04
	2	1.10	1.09	1.09	1.09	1.09	1.09
	3	1.10	1.09	1.08	1.07	1.09	1.03
RPCA	1	1.10	1.09	1.08	1.07	1.03	1.03
	2	1.10	1.09	1.09	1.09	1.08	1.09
	3	1.10	1.09	1.09	1.09	1.02	1.08

Table A.2: Flow rates (in ml/s) through the afferent and efferent arteries of variant 2. Scenario 1 included a vascular bed modelled as passive. In Scenario 2 all of the cerebral tissue territories were modelled as autoregulating. In Scenario 3 only cerebral territories contralateral to the main stenosis or occlusion were modelled as autoregulating.

Variant 3: No ACoA							
Artery	Scenario	Healthy	LICA stenosed	LICA occluded	LVA occluded	LICA stenosed RICA occluded	LICA occluded RICA stenosed
LICA	1	3.40	1.93	0.00	3.67	2.35	0.00
	2	3.40	2.05	0.00	3.69	2.64	0.00
	3	3.40	1.93	0.00	3.68	2.53	0.00
RICA	1	3.47	3.76	4.15	3.75	0.00	2.38
	2	3.47	3.82	4.33	3.77	0.00	2.66
	3	3.47	3.78	4.18	3.76	0.00	2.56
LVA	1	1.14	1.56	2.12	0.00	2.76	2.75
	2	1.14	1.62	2.34	0.00	3.14	3.13
	3	1.14	1.57	2.13	0.00	2.86	2.85
RVA	1	1.14	1.56	2.12	1.67	2.76	2.75
	2	1.14	1.62	2.34	1.69	3.14	3.13
	3	1.14	1.57	2.13	1.68	2.86	2.85
LMCA	1	2.06	1.89	1.68	2.05	1.84	1.63
	2	2.06	2.03	1.99	2.06	2.02	1.97
	3	2.06	1.89	1.68	2.05	2.03	1.62
RMCA	1	2.06	2.06	2.04	2.06	1.63	1.84
	2	2.06	2.06	2.06	2.06	1.97	2.03
	3	2.06	2.06	2.06	2.06	1.62	2.03
LACA	1	1.42	1.31	1.16	1.41	1.27	1.13
	2	1.42	1.40	1.37	1.42	1.40	1.36
	3	1.42	1.31	1.16	1.41	1.40	1.12
RACA	1	1.42	1.42	1.41	1.42	1.12	1.27
	2	1.42	1.42	1.42	1.42	1.36	1.40
	3	1.42	1.42	1.42	1.42	1.12	1.40
LPCA	1	1.09	1.07	1.04	1.08	1.01	1.00
	2	1.09	1.09	1.09	1.09	1.08	1.08
	3	1.09	1.07	1.03	1.08	1.08	1.00
RPCA	1	1.09	1.07	1.05	1.08	1.00	1.01
	2	1.09	1.09	1.09	1.09	1.08	1.08
	3	1.09	1.09	1.09	1.09	1.00	1.08

Table A.3: Flow rates (in ml/s) through the afferent and efferent arteries of variant 3. Scenario 1 included a vascular bed modelled as passive. In Scenario 2 all of the cerebral tissue territories were modelled as autoregulating. In Scenario 3 only cerebral territories contralateral to the main stenosis or occlusion were modelled as autoregulating.

Variant 4: No RVA							
Artery	Scenario	Healthy	LICA stenosed	LICA occluded	LVA occluded	LICA stenosed RICA occluded	LICA occluded RICA stenosed
LICA	1	3.62	1.50	0.00	4.36	3.29	0.00
	2	3.62	1.55	0.00	4.43	3.84	0.00
	3	3.62	1.51	0.00	4.39	3.52	0.00
RICA	1	3.80	5.16	6.12	4.56	0.00	3.32
	2	3.80	5.30	6.42	4.64	0.00	3.88
	3	3.80	5.21	6.23	4.60	0.00	3.58
LVA	1	1.67	2.15	2.49	0.00	4.29	4.27
	2	1.67	2.20	2.60	0.00	4.96	4.93
	3	1.67	2.17	2.53	0.00	4.57	4.54
RVA	1	0.00	0.00	0.00	0.00	0.00	0.00
	2	0.00	0.00	0.00	0.00	0.00	0.00
	3	0.00	0.00	0.00	0.00	0.00	0.00
LMCA	1	2.05	1.95	1.88	2.03	1.71	1.65
	2	2.05	2.04	2.03	2.05	1.99	1.97
	3	2.05	1.95	1.88	2.03	2.00	1.62
RMCA	1	2.05	2.02	1.99	2.03	1.65	1.71
	2	2.05	2.05	2.05	2.05	1.97	1.99
	3	2.05	2.05	2.05	2.05	1.62	2.00
LACA	1	1.42	1.36	1.32	1.40	1.17	1.15
	2	1.42	1.41	1.40	1.41	1.37	1.36
	3	1.42	1.36	1.32	1.40	1.37	1.13
RACA	1	1.42	1.38	1.35	1.40	1.15	1.17
	2	1.42	1.41	1.41	1.42	1.36	1.37
	3	1.42	1.41	1.41	1.42	1.13	1.38
LPCA	1	1.08	1.05	1.03	1.02	0.95	0.95
	2	1.08	1.07	1.07	1.07	1.05	1.05
	3	1.08	1.05	1.03	1.02	1.06	0.94
RPCA	1	1.08	1.05	1.04	1.02	0.95	0.95
	2	1.08	1.07	1.07	1.07	1.05	1.05
	3	1.08	1.07	1.07	1.07	0.94	1.06

Table A.4: Flow rates (in ml/s) through the afferent and efferent arteries of variant 4. Scenario 1 included a vascular bed modelled as passive. In Scenario 2 all of the cerebral tissue territories were modelled as autoregulating. In Scenario 3 only cerebral territories contralateral to the main stenosis or occlusion were modelled as autoregulating.

Variant 5: No LPCAP1							
Artery	Scenario	Healthy	LICA stenosed	LICA occluded	LVA occluded	LICA stenosed RICA occluded	LICA occluded RICA stenosed
LICA	1	4.00	1.79	0.00	4.07	3.54	0.00
	2	4.00	1.87	0.00	4.08	4.16	0.00
	3	4.00	1.80	0.00	4.07	3.89	0.00
RICA	1	3.57	5.12	6.39	3.76	0.00	3.42
	2	3.57	5.32	6.85	3.77	0.00	4.12
	3	3.57	5.18	6.51	3.77	0.00	3.68
LVA	1	0.75	0.90	1.02	0.00	2.00	1.95
	2	0.75	0.92	1.06	0.00	2.30	2.28
	3	0.75	0.91	1.03	0.00	2.13	2.08
RVA	1	0.75	0.90	1.01	1.21	2.00	1.94
	2	0.75	0.92	1.06	1.22	2.31	2.28
	3	0.75	0.90	1.03	1.22	2.13	2.08
LMCA	1	2.04	1.91	1.81	2.04	1.67	1.55
	2	2.04	2.02	2.01	2.04	1.97	1.93
	3	2.04	1.91	1.81	2.04	1.98	1.52
RMCA	1	2.06	2.02	1.98	2.06	1.68	1.69
	2	2.06	2.05	2.05	2.06	1.99	1.99
	3	2.06	2.06	2.05	2.06	1.64	2.00
LACA	1	1.41	1.34	1.28	1.41	1.16	1.10
	2	1.41	1.40	1.39	1.41	1.36	1.34
	3	1.41	1.34	1.28	1.41	1.37	1.07
RACA	1	1.42	1.37	1.33	1.42	1.16	1.14
	2	1.42	1.41	1.41	1.42	1.37	1.36
	3	1.42	1.41	1.41	1.42	1.13	1.37
LPCA	1	1.03	0.96	0.91	1.03	0.84	0.78
	2	1.03	1.02	1.01	1.03	0.99	0.96
	3	1.03	0.96	0.91	1.03	0.99	0.76
RPCA	1	1.11	1.10	1.10	1.10	1.04	1.04
	2	1.11	1.11	1.11	1.11	1.10	1.10
	3	1.11	1.11	1.11	1.11	1.03	1.10

Table A.5: Flow rates (in ml/s) through the afferent and efferent arteries of variant 5. Scenario 1 included a vascular bed modelled as passive. In Scenario 2 all of the cerebral tissue territories were modelled as autoregulating. In Scenario 3 only cerebral territories contralateral to the main stenosis or occlusion were modelled as autoregulating.

Variant 6: No RACAA1							
Artery	Scenario	Healthy	LICA stenosed	LICA occluded	LVA occluded	LICA stenosed RICA occluded	LICA occluded RICA stenosed
LICA	1	4.42	2.44	0.00	4.68	2.76	0.00
	2	4.42	2.65	0.00	4.71	3.09	0.00
	3	4.42	2.49	0.00	4.69	2.95	0.00
RICA	1	2.38	2.75	3.21	2.65	0.00	1.89
	2	2.38	2.82	3.47	2.67	0.00	2.14
	3	2.38	2.78	3.29	2.67	0.00	2.02
LVA	1	1.14	1.67	2.32	0.00	2.61	2.82
	2	1.14	1.76	2.66	0.00	2.90	3.29
	3	1.14	1.69	2.41	0.00	2.71	2.98
RVA	1	1.14	1.67	2.32	1.67	2.61	2.82
	2	1.14	1.76	2.66	1.68	2.90	3.29
	3	1.14	1.69	2.41	1.68	2.71	2.97
LMCA	1	2.03	1.82	1.57	2.02	1.78	1.53
	2	2.03	2.00	1.92	2.03	1.99	1.91
	3	2.03	1.82	1.54	2.02	1.99	1.50
RMCA	1	2.10	2.08	2.07	2.09	1.75	1.91
	2	2.10	2.09	2.09	2.09	2.04	2.07
	3	2.10	2.09	2.09	2.09	1.74	2.07
LACA	1	1.39	1.25	1.08	1.38	1.22	1.05
	2	1.39	1.37	1.31	1.39	1.36	1.30
	3	1.39	1.24	1.05	1.38	1.36	1.02
RACA	1	1.37	1.23	1.06	1.37	1.20	1.04
	2	1.37	1.35	1.30	1.37	1.34	1.28
	3	1.37	1.35	1.31	1.37	1.18	1.31
LPCA	1	1.09	1.06	1.02	1.07	1.02	1.00
	2	1.09	1.09	1.08	1.09	1.08	1.08
	3	1.09	1.06	1.02	1.07	1.08	0.99
RPCA	1	1.10	1.07	1.04	1.08	1.02	1.01
	2	1.10	1.09	1.09	1.09	1.08	1.08
	3	1.10	1.09	1.09	1.09	1.01	1.08

Table A.6: Flow rates (in ml/s) through the afferent and efferent arteries of variant 6. Scenario 1 included a vascular bed modelled as passive. In Scenario 2 all of the cerebral tissue territories were modelled as autoregulating. In Scenario 3 only cerebral territories contralateral to the main stenosis or occlusion were modelled as autoregulating.

Variant 7: No PCoAs							
Artery	Scenario	Healthy	LICA stenosed	LICA occluded	LVA occluded	LICA stenosed RICA occluded	LICA occluded RICA stenosed
LICA	1	3.40	1.57	0.00	3.40	4.87	0.00
	2	3.40	1.63	0.00	3.40	6.30	0.00
	3	3.40	1.58	0.00	3.40	5.49	0.00
RICA	1	3.56	5.12	6.46	3.56	0.00	4.89
	2	3.56	5.29	6.89	3.56	0.00	6.31
	3	3.56	5.18	6.60	3.56	0.00	5.51
LVA	1	1.10	1.10	1.10	0.00	1.10	1.10
	2	1.10	1.10	1.10	0.00	1.10	1.10
	3	1.10	1.10	1.10	0.00	1.10	1.10
RVA	1	1.10	1.10	1.10	2.11	1.10	1.10
	2	1.10	1.10	1.10	2.18	1.10	1.10
	3	1.10	1.10	1.10	2.14	1.10	1.10
LMCA	1	2.06	1.94	1.85	2.06	1.49	1.40
	2	2.06	2.04	2.03	2.06	1.89	1.84
	3	2.06	1.94	1.84	2.06	1.93	1.31
RMCA	1	2.06	2.02	1.98	2.06	1.39	1.50
	2	2.06	2.06	2.05	2.06	1.84	1.90
	3	2.06	2.06	2.05	2.06	1.31	1.94
LACA	1	1.42	1.36	1.30	1.42	1.01	0.98
	2	1.42	1.41	1.40	1.42	1.29	1.28
	3	1.42	1.35	1.30	1.42	1.33	0.93
RACA	1	1.42	1.38	1.34	1.42	0.98	1.01
	2	1.42	1.42	1.41	1.42	1.27	1.30
	3	1.42	1.42	1.41	1.42	0.92	1.33
LPCA	1	1.10	1.10	1.10	1.05	1.10	1.10
	2	1.10	1.10	1.10	1.09	1.10	1.10
	3	1.10	1.10	1.10	1.05	1.10	1.10
RPCA	1	1.10	1.10	1.10	1.05	1.10	1.10
	2	1.10	1.10	1.10	1.09	1.10	1.10
	3	1.10	1.10	1.10	1.09	1.10	1.10

Table A.7: Flow rates (in ml/s) through the afferent and efferent arteries of variant 7. Scenario 1 included a vascular bed modelled as passive. In Scenario 2 all of the cerebral tissue territories were modelled as autoregulating. In Scenario 3 only cerebral territories contralateral to the main stenosis or occlusion were modelled as autoregulating.

Variant 8: No LPCoA or ACoA							
Artery	Scenario	Healthy	LICA stenosed	LICA occluded	LVA occluded	LICA stenosed RICA occluded	LICA occluded RICA stenosed
LICA	1	3.47	2.96	0.00	3.47	2.96	0.00
	2	3.47	3.38	0.00	3.47	3.38	0.00
	3	3.47	2.96	0.00	3.47	3.38	0.00
RICA	1	3.45	3.45	3.45	3.82	0.00	1.99
	2	3.45	3.45	3.45	3.85	0.00	2.13
	3	3.45	3.45	3.45	3.84	0.00	2.13
LVA	1	1.11	1.11	1.11	0.00	2.43	1.67
	2	1.11	1.11	1.11	0.00	2.76	1.75
	3	1.11	1.11	1.11	0.00	2.45	1.74
RVA	1	1.11	1.11	1.11	1.79	2.43	1.67
	2	1.11	1.11	1.11	1.82	2.76	1.75
	3	1.11	1.11	1.11	1.80	2.45	1.74
LMCA	1	2.06	1.75	0.00	2.06	1.75	0.00
	2	2.06	2.00	0.00	2.06	2.00	0.00
	3	2.06	1.75	0.00	2.06	2.00	0.00
RMCA	1	2.06	2.06	2.06	2.05	1.66	1.89
	2	2.06	2.06	2.06	2.06	1.98	2.04
	3	2.06	2.06	2.06	2.06	1.65	2.04
LACA	1	1.42	1.21	0.00	1.42	1.21	0.00
	2	1.42	1.38	0.00	1.42	1.38	0.00
	3	1.42	1.21	0.00	1.42	1.38	0.00
RACA	1	1.42	1.42	1.42	1.42	1.14	1.31
	2	1.42	1.42	1.42	1.42	1.37	1.41
	3	1.42	1.42	1.42	1.42	1.14	1.41
LPCA	1	1.10	1.10	1.10	1.07	1.03	1.07
	2	1.10	1.10	1.10	1.09	1.09	1.09
	3	1.10	1.10	1.10	1.07	1.09	1.06
RPCA	1	1.10	1.10	1.10	1.07	1.02	1.06
	2	1.10	1.10	1.10	1.09	1.08	1.09
	3	1.10	1.10	1.10	1.09	1.02	1.09

Table A.8: Flow rates (in ml/s) through the afferent and efferent arteries of variant 8. Scenario 1 included a vascular bed modelled as passive. In Scenario 2 all of the cerebral tissue territories were modelled as autoregulating. In Scenario 3 only cerebral territories contralateral to the main stenosis or occlusion were modelled as autoregulating.

Variant 9: No ACoA or RVA							
Artery	Scenario	Healthy	LICA stenosed	LICA occluded	LVA occluded	LICA stenosed RICA occluded	LICA occluded RICA stenosed
LICA	1	3.67	2.14	0.00	4.42	2.86	0.00
	2	3.67	2.30	0.00	4.49	3.33	0.00
	3	3.67	2.15	0.00	4.44	3.12	0.00
RICA	1	3.75	4.18	4.80	4.50	0.00	2.89
	2	3.75	4.27	5.12	4.57	0.00	3.36
	3	3.75	4.21	4.86	4.55	0.00	3.15
LVA	1	1.67	2.36	3.33	0.00	4.56	4.54
	2	1.67	2.47	3.77	0.00	5.39	5.37
	3	1.67	2.38	3.37	0.00	4.78	4.77
RVA	1	0.00	0.00	0.00	0.00	0.00	0.00
	2	0.00	0.00	0.00	0.00	0.00	0.00
	3	0.00	0.00	0.00	0.00	0.00	0.00
LMCA	1	2.05	1.86	1.61	2.03	1.77	1.52
	2	2.05	2.02	1.96	2.05	2.00	1.92
	3	2.05	1.86	1.60	2.03	2.00	1.50
RMCA	1	2.06	2.04	2.03	2.03	1.52	1.77
	2	2.06	2.05	2.05	2.05	1.92	2.01
	3	2.06	2.05	2.05	2.05	1.50	2.01
LACA	1	1.41	1.29	1.11	1.40	1.22	1.05
	2	1.41	1.40	1.35	1.41	1.38	1.32
	3	1.41	1.29	1.11	1.40	1.38	1.04
RACA	1	1.42	1.41	1.40	1.40	1.05	1.22
	2	1.42	1.42	1.42	1.42	1.32	1.38
	3	1.42	1.42	1.42	1.42	1.03	1.39
LPCA	1	1.08	1.04	0.99	1.02	0.94	0.93
	2	1.08	1.07	1.06	1.07	1.05	1.05
	3	1.08	1.04	0.99	1.02	1.06	0.92
RPCA	1	1.08	1.05	1.00	1.02	0.93	0.94
	2	1.08	1.07	1.06	1.07	1.05	1.05
	3	1.08	1.07	1.07	1.07	0.92	1.06

Table A.9: Flow rates (in ml/s) through the afferent and efferent arteries of variant 9. Scenario 1 included a vascular bed modelled as passive. In Scenario 2 all of the cerebral tissue territories were modelled as autoregulating. In Scenario 3 only cerebral territories contralateral to the main stenosis or occlusion were modelled as autoregulating.

Variant 10: No RACAA1 or LPCAP1							
Artery	Scenario	Healthy	LICA stenosed	LICA occluded	LVA occluded	LICA stenosed RICA occluded	LICA occluded RICA stenosed
LICA	1	5.70	4.44	0.00	5.70	4.44	0.00
	2	5.70	5.39	0.00	5.70	5.39	0.00
	3	5.70	4.62	0.00	5.70	5.12	0.00
RICA	1	2.01	2.01	2.01	2.22	0.00	1.19
	2	2.01	2.01	2.01	2.23	0.00	1.25
	3	2.01	2.01	2.01	2.23	0.00	1.25
LVA	1	0.61	0.61	0.61	0.00	1.46	0.95
	2	0.61	0.61	0.61	0.00	1.59	0.98
	3	0.61	0.61	0.61	0.00	1.46	0.98
RVA	1	0.61	0.61	0.61	0.99	1.46	0.95
	2	0.61	0.61	0.61	1.00	1.59	0.98
	3	0.61	0.61	0.61	1.00	1.46	0.98
LMCA	1	1.99	1.55	0.00	1.99	1.55	0.00
	2	1.99	1.89	0.00	1.99	1.89	0.00
	3	1.99	1.52	0.00	1.99	1.90	0.00
RMCA	1	2.11	2.11	2.11	2.10	1.85	2.00
	2	2.11	2.11	2.11	2.11	2.07	2.09
	3	2.11	2.11	2.11	2.11	1.85	2.09
LACA	1	1.36	1.06	0.00	1.36	1.06	0.00
	2	1.36	1.29	0.00	1.36	1.29	0.00
	3	1.36	1.04	0.00	1.36	1.30	0.00
RACA	1	1.34	1.05	0.00	1.34	1.05	0.00
	2	1.34	1.27	0.00	1.34	1.27	0.00
	3	1.34	1.29	0.00	1.34	0.98	0.00
LPCA	1	1.00	0.78	0.00	1.00	0.78	0.00
	2	1.00	0.94	0.00	1.00	0.94	0.00
	3	1.00	0.77	0.00	1.00	0.95	0.00
RPCA	1	1.12	1.12	1.12	1.11	1.07	1.10
	2	1.12	1.12	1.12	1.12	1.11	1.12
	3	1.12	1.12	1.12	1.12	1.07	1.12

Table A.10: Flow rates (in ml/s) through the afferent and efferent arteries of variant 10. Scenario 1 included a vascular bed modelled as passive. In Scenario 2 all of the cerebral tissue territories were modelled as autoregulating. In Scenario 3 only cerebral territories contralateral to the main stenosis or occlusion were modelled as autoregulating.

Variant 11: No RACAA1 or RVA							
Artery	Scenario	Healthy	LICA stenosed	LICA occluded	LVA occluded	LICA stenosed RICA occluded	LICA occluded RICA stenosed
LICA	1	4.68	2.66	0.00	5.41	3.24	0.00
	2	4.68	2.91	0.00	5.50	3.73	0.00
	3	4.68	2.73	0.00	5.45	3.49	0.00
RICA	1	2.66	3.20	3.92	3.42	0.00	2.42
	2	2.66	3.32	4.37	3.48	0.00	2.87
	3	2.66	3.24	4.06	3.46	0.00	2.64
LVA	1	1.67	2.52	3.63	0.00	4.34	4.64
	2	1.67	2.68	4.27	0.00	5.00	5.61
	3	1.67	2.56	3.80	0.00	4.56	4.97
RVA	1	0.00	0.00	0.00	0.00	0.00	0.00
	2	0.00	0.00	0.00	0.00	0.00	0.00
	3	0.00	0.00	0.00	0.00	0.00	0.00
LMCA	1	2.02	1.79	1.50	2.00	1.71	1.43
	2	2.02	1.98	1.89	2.02	1.96	1.84
	3	2.02	1.78	1.46	2.00	1.97	1.37
RMCA	1	2.09	2.07	2.05	2.07	1.63	1.83
	2	2.09	2.09	2.08	2.09	1.99	2.04
	3	2.09	2.09	2.08	2.09	1.61	2.05
LACA	1	1.38	1.23	1.02	1.37	1.17	0.98
	2	1.38	1.36	1.29	1.38	1.34	1.26
	3	1.38	1.22	1.00	1.37	1.35	0.94
RACA	1	1.37	1.21	1.01	1.35	1.16	0.96
	2	1.37	1.34	1.27	1.36	1.33	1.24
	3	1.37	1.34	1.29	1.36	1.13	1.28
LPCA	1	1.07	1.03	0.97	1.02	0.95	0.93
	2	1.07	1.07	1.06	1.07	1.05	1.04
	3	1.07	1.03	0.96	1.02	1.06	0.91
RPCA	1	1.08	1.04	0.99	1.03	0.95	0.94
	2	1.08	1.07	1.06	1.07	1.05	1.05
	3	1.08	1.07	1.07	1.07	0.94	1.06

Table A.11: Flow rates (in ml/s) through the afferent and efferent arteries of variant 11. Scenario 1 included a vascular bed modelled as passive. In Scenario 2 all of the cerebral tissue territories were modelled as autoregulating. In Scenario 3 only cerebral territories contralateral to the main stenosis or occlusion were modelled as autoregulating.

Variant 12: No LPCoA or RPCAP1							
Artery	Scenario	Healthy	LICA stenosed	LICA occluded	LVA occluded	LICA stenosed RICA occluded	LICA occluded RICA stenosed
LICA	1	3.67	1.69	0.00	3.67	5.29	0.00
	2	3.67	1.76	0.00	3.67	6.93	0.00
	3	3.67	1.71	0.00	3.67	5.92	0.00
RICA	1	4.27	5.94	7.36	4.27	0.00	5.39
	2	4.27	6.14	7.86	4.27	0.00	7.03
	3	4.27	6.02	7.55	4.27	0.00	6.22
LVA	1	0.56	0.56	0.56	0.00	0.56	0.56
	2	0.56	0.56	0.56	0.00	0.56	0.56
	3	0.56	0.56	0.56	0.00	0.56	0.56
RVA	1	0.56	0.56	0.56	1.10	0.56	0.56
	2	0.56	0.56	0.56	1.12	0.56	0.56
	3	0.56	0.56	0.56	1.10	0.56	0.56
LMCA	1	2.05	1.93	1.82	2.05	1.43	1.33
	2	2.05	2.03	2.02	2.05	1.85	1.78
	3	2.05	1.93	1.82	2.05	1.91	1.22
RMCA	1	2.04	1.99	1.95	2.04	1.31	1.43
	2	2.04	2.03	2.03	2.04	1.75	1.84
	3	2.04	2.04	2.03	2.04	1.23	1.89
LACA	1	1.41	1.34	1.28	1.41	0.96	0.94
	2	1.41	1.40	1.39	1.41	1.25	1.23
	3	1.41	1.34	1.28	1.41	1.30	0.86
RACA	1	1.41	1.36	1.32	1.41	0.93	0.97
	2	1.41	1.40	1.40	1.41	1.22	1.26
	3	1.41	1.40	1.40	1.41	0.87	1.30
LPCA	1	1.12	1.12	1.12	1.10	1.12	1.12
	2	1.12	1.12	1.12	1.12	1.12	1.12
	3	1.12	1.12	1.12	1.10	1.12	1.12
RPCA	1	1.03	1.01	0.99	1.03	0.66	0.72
	2	1.03	1.03	1.02	1.03	0.86	0.92
	3	1.03	1.03	1.02	1.03	0.62	0.94

Table A.12: Flow rates (in ml/s) through the afferent and efferent arteries of variant 12. Scenario 1 included a vascular bed modelled as passive. In Scenario 2 all of the cerebral tissue territories were modelled as autoregulating. In Scenario 3 only cerebral territories contralateral to the main stenosis or occlusion were modelled as autoregulating.

Variant 13: No collaterals							
Artery	Scenario	Healthy	LICA stenosed	LICA occluded	LVA occluded	LICA stenosed RICA occluded	LICA occluded RICA stenosed
LICA	1	3.47	2.96	0.00	3.47	2.96	0.00
	2	3.47	3.38	0.00	3.47	3.38	0.00
	3	3.47	2.96	0.00	3.47	3.38	0.00
RICA	1	3.49	3.49	3.49	3.49	0.00	2.97
	2	3.49	3.49	3.49	3.49	0.00	3.40
	3	3.49	3.49	3.49	3.49	0.00	3.40
LVA	1	1.10	1.10	1.10	0.00	1.10	1.10
	2	1.10	1.10	1.10	0.00	1.10	1.10
	3	1.10	1.10	1.10	0.00	1.10	1.10
RVA	1	1.10	1.10	1.10	2.11	1.10	1.10
	2	1.10	1.10	1.10	2.18	1.10	1.10
	3	1.10	1.10	1.10	2.14	1.10	1.10
LMCA	1	2.06	1.75	0.00	2.06	1.75	0.00
	2	2.06	2.00	0.00	2.06	2.00	0.00
	3	2.06	1.75	0.00	2.06	2.00	0.00
RMCA	1	2.06	2.06	2.06	2.06	0.00	1.76
	2	2.06	2.06	2.06	2.06	0.00	2.01
	3	2.06	2.06	2.06	2.06	0.00	2.01
LACA	1	1.42	1.21	0.00	1.42	1.21	0.00
	2	1.42	1.38	0.00	1.42	1.38	0.00
	3	1.42	1.21	0.00	1.42	1.21	0.00
RACA	1	1.42	1.42	1.42	1.42	0.00	1.21
	2	1.42	1.42	1.42	1.42	0.00	1.39
	3	1.42	1.42	1.42	1.42	0.00	1.39
LPCA	1	1.10	1.10	1.10	1.05	1.10	1.10
	2	1.10	1.10	1.10	1.09	1.10	1.10
	3	1.10	1.10	1.10	1.07	1.10	1.10
RPCA	1	1.10	1.10	1.10	1.05	1.10	1.10
	2	1.10	1.10	1.10	1.09	1.10	1.10
	3	1.10	1.10	1.10	1.07	1.10	1.10

Table A.13: Flow rates (in ml/s) through the afferent and efferent arteries of variant 13. Scenario 1 included a vascular bed modelled as passive. In Scenario 2 all of the cerebral tissue territories were modelled as autoregulating. In Scenario 3 only cerebral territories contralateral to the main stenosis or occlusion were modelled as autoregulating.

References

[1] H. S. Markus, "Cerebral perfusion and stroke", *Journal of Neurology, Neurosurgery & Psychiatry*, vol. 75, no. 3, pp. 353–361, 2004.

[2] H. Markus, A. Pereira, and G. Cloud, *Stroke Medicine*, ser. Oxford specialist handbooks in neurology. Oxford University Press, 2016.

[3] Stroke Association. (Jan. 2017). State of the nation: Stroke statistics, [Online]. Available: `https://www.stroke.org.uk/sites/default/files/state_of_the_nation_2017_final_1.pdf` (visited on 08/20/2017).

[4] A. Crossman and D. Neary, *Neuroanatomy: An Illustrated Colour Text*, ser. An Illustrated Colour Text Series. Elsevier Science Health Science Division, 2014.

[5] S. J. Payne, *Cerebral Autoregulation: Control of Blood Flow in the Brain*. Springer, 2016.

[6] R. B. Panerai, "Cerebral autoregulation: From models to clinical applications", *Cardiovascular Engineering*, vol. 8, no. 1, pp. 42–59, 2008.

[7] R. D. Henderson, M. Eliasziw, A. J. Fox, P. M. Rothwell, H. J. M. Barnett, *et al.*, "Angiographically defined collateral circulation and risk of stroke in patients with severe carotid artery stenosis", *Stroke*, vol. 31, no. 1, pp. 128–132, 2000.

[8] A. Angermaier, S. Langner, M. Kirsch, C. Kessler, N. Hosten, and A. V. Khaw, "CT-angiographic collateralization predicts final infarct volume after intra-arterial thrombolysis for acute anterior circulation ischemic stroke", *Cerebrovascular Diseases*, vol. 31, no. 2, pp. 177–184, 2010.

[9] B. J. Alpers, R. G. Berry, and R. M. Paddison, "Anatomical studies of the circle of Willis in normal brain", *Archives of Neurology and Psychiatry*, vol. 81, no. 4, p. 409, 1959.

[10] H. E. Riggs and C. Rupp, "Variation in form of circle of Willis: the relation of the variations to collateral circulation: anatomic analysis", *Archives of Neurology*, vol. 8, no. 1, p. 8, 1963.

[11] V. Papantchev, V. Stoinova, A. Aleksandrov, D. Todorova-Papantcheva, S. Hristov, D. Petkov, G. Nachev, and W. Ovtscharoff, "The role of Willis circle variations during unilateral selective cerebral perfusion: a study of 500 circles", *European Journal of Cardio-Thoracic Surgery*, vol. 44, no. 4, pp. 743–753, Mar. 2013.

[12] S. Schwarz, D. Georgiadis, A. Aschoff, and S. Schwab, "Effects of induced hypertension on intracranial pressure and flow velocities of the middle cerebral arteries in patients with large hemispheric stroke", *Stroke*, vol. 33, no. 4, pp. 998–1004, 2002.

[13] O. Y. Bang, J. L. Saver, S. J. Kim, G.-M. Kim, C.-S. Chung, B. Ovbiagele, K. H. Lee, and D. S. Liebeskind, "Collateral flow predicts response to endovascular therapy for acute ischemic stroke", *Stroke*, vol. 42, no. 3, pp. 693–699, 2011.

[14] J. Wardlaw, E. Berge, G. del Zoppo, and T. Yamaguchi, "Thrombolysis for acute ischemic stroke", *Stroke*, vol. 35, no. 12, pp. 2914–2915, 2004.

[15] P. Orlowski, F. Kennedy McConnell, and S. Payne, "A mathematical model of cellular metabolism during ischemic stroke and hypothermia", *IEEE Transactions on Biomedical Engineering*, vol. 61, no. 2, pp. 484–490, 2014.

[16] H. B. van der Worp, E. S. Sena, G. A. Donnan, D. W. Howells, and M. R. Macleod, "Hypothermia in animal models of acute ischaemic stroke: A systematic review and meta-analysis", *Brain*, vol. 130, no. 12, pp. 3063–3074, 2007.

[17] L. P. Kammersgaard, B. H. Rasmussen, H. S. Jørgensen, J. Reith, U. Weber, and T. S. Olsen, "Feasibility and safety of inducing modest hypothermia in awake patients with acute stroke through surface cooling: A case-control study", *Stroke*, vol. 31, no. 9, pp. 2251–2256, 2000.

[18] G. McLatchie, N. Borley, and J. Chikwe, *Oxford Handbook of Clinical Surgery*, ser. Oxford Medical Handbooks. Oxford University Press, 2013.

[19] O. Y. Bang, J. L. Saver, S. J. Kim, G.-M. Kim, C.-S. Chung, B. Ovbiagele, K. H. Lee, D. S. Liebeskind, *et al.*, "Collateral flow averts hemorrhagic transformation after endovascular therapy for acute ischemic stroke", *Stroke*, vol. 42, no. 8, pp. 2235–2239, 2011.

[20] L. Gartner and J. Hiatt, *Color Textbook of Histology*. W.B. Saunders, 2001.

[21] S. Monkhouse, *Clinical Anatomy: A Core Text with Self-Assessment*, ser. Master medicine. Churchill Livingstone, 2001.

[22] T. W. Okell, M. A. Chappell, M. W. Woolrich, M. Günther, D. A. Feinberg, and P. Jezzard, "Vessel-encoded dynamic magnetic resonance angiography using arterial spin labeling", *Magnetic Resonance in Medicine*, vol. 64, no. 2, pp. 430–438, 2010.

[23] L. R. Williams and R. W. Leggett, "Reference values for resting blood flow to organs of man", *Clinical Physics and Physiological Measurement*, vol. 10, no. 3, p. 187, 1989.

[24] M. Donaghy, *Brain's Diseases of the Nervous System*. Oxford University Press, 2009.

[25] G. Fuller and M. Manford, *Neurology: An Illustrated Colour Text*, ser. Illustrated Colour Text. Elsevier Churchill Livingstone, 2006.

[26] A. Jaillard, C. Cornu, A. Durieux, T. Moulin, F. Boutitie, K. R. Lees, M. Hommel, *et al.*, "Hemorrhagic transformation in acute ischemic stroke", *Stroke*, vol. 30, no. 7, pp. 1326–1332, 1999.

[27] D. S. Liebeskind, "Collateral circulation", *Stroke*, vol. 34, no. 9, pp. 2279–2284, 2003.

[28] S. A. Sheth and D. S. Liebeskind, "Imaging evaluation of collaterals in the brain: Physiology and clinical translation", *Current Radiology Reports*, vol. 2, no. 1, p. 29, 2014.

[29] D. S. Liebeskind and N. Sanossian, "How well do blood flow imaging and collaterals on angiography predict brain at risk?", *Neurology*, vol. 79, no. 13 Supplement 1, S105–S109, 2012.

[30] P. D. Schellinger, M. Köhrmann, S. Liu, W. P. Dillon, R. G. Nogueira, A. Shuaib, and D. S. Liebeskind, "Favorable vascular profile is an independent predictor of outcome", *Stroke*, vol. 44, no. 6, pp. 1606–1608, 2013.

[31] A. Shuaib, N. M. Bornstein, H.-C. Diener, W. Dillon, M. Fisher, M. D. Hammer, C. A. Molina, J. N. Rutledge, J. L. Saver, P. D. Schellinger, *et al.*, "Partial aortic occlusion for cerebral perfusion augmentation", *Stroke*, vol. 42, no. 6, pp. 1680–1690, 2011.

[32] O. B. Paulson, S. Strandgaard, and L. Edvinsson, "Cerebral autoregulation.", *Cerebrovascular and Brain Metabolism Reviews*, vol. 2, no. 2, pp. 161–192, 1990.

[33] E. C. Peterson, Z. Wang, and G. Britz, "Regulation of cerebral blood flow", *International Journal of Vascular Medicine*, vol. 2011, 2011.

[34] M. Reinhard, M. Roth, T. Müller, B. Guschlbauer, J. Timmer, M. Czosnyka, and A. Hetzel, "Effect of carotid endarterectomy or stenting on impairment of dynamic cerebral autoregulation", *Stroke*, vol. 35, no. 6, pp. 1381–1387, 2004.

[35] K. Kitagawa, "Carotid stenosis, baroreceptor sensitivity and cerebral autoregulation", *Circulation Journal*, vol. 74, no. 10, pp. 2058–2059, 2010.

[36] R. P. White and H. S. Markus, "Impaired dynamic cerebral autoregulation in carotid artery stenosis", *Stroke*, vol. 28, no. 7, pp. 1340–1344, 1997.

[37] M. Reinhard, T. Müller, M. Roth, B. Guschlbauer, J. Timmer, and A. Hetzel, "Bilateral severe carotid artery stenosis or occlusion – cerebral autoregulation dynamics and collateral flow patterns", *Acta Neurochirurgica*, vol. 145, no. 12, pp. 1053–1060, 2003.

[38] S.-C. Tang, Y.-W. Huang, J.-S. Shieh, S.-J. Huang, P.-K. Yip, and J.-S. Jeng, "Dynamic cerebral autoregulation in carotid stenosis before and after carotid stenting", *Journal of Vascular Surgery*, vol. 48, no. 1, pp. 88–92, 2008.

[39] M. J. H. Aries, J. W. Elting, J. De Keyser, B. P. H. Kremer, and P. C. A. J. Vroomen, "Cerebral autoregulation in stroke", *Stroke*, vol. 41, no. 11, pp. 2697–2704, 2010.

[40] E. R. Atkins, F. G. Brodie, S. E. Rafelt, R. B. Panerai, and T. G. Robinson, "Dynamic cerebral autoregulation is compromised acutely following mild ischaemic stroke but not transient ischaemic attack", *Cerebrovascular Diseases*, vol. 29, no. 3, pp. 228–235, 2010.

[41] R. V. Immink, G. A. van Montfrans, J. Stam, J. M. Karemaker, M. Diamant, and J. J. van Lieshout, "Dynamic cerebral autoregulation in acute lacunar and middle cerebral artery territory ischemic stroke", *Stroke*, vol. 36, no. 12, pp. 2595–2600, 2005.

[42] M. Reinhard, T. A. Gerds, D. Grabiak, P. R. Zimmermann, M. Roth, B. Guschlbauer, J. Timmer, M. Czosnyka, C. Weiller, and A. Hetzel, "Cerebral dysautoregulation and the risk of ischemic events in occlusive carotid artery disease", *Journal of Neurology*, vol. 255, no. 8, pp. 1182–1189, 2008.

[43] M. Reinhard, S. Rutsch, J. Lambeck, C. Wihler, M. Czosnyka, C. Weiller, and A. Hetzel, "Dynamic cerebral autoregulation associates with infarct size and outcome after ischemic stroke", *Acta Neurologica Scandinavica*, vol. 125, no. 3, pp. 156–162, 2012.

[44] N. H. Petersen, S. Ortega-Gutierrez, A. Reccius, A. Masurkar, A. Huang, and R. S. Marshall, "Dynamic cerebral autoregulation is transiently impaired for one week after large-vessel acute ischemic stroke", *Cerebrovascular Diseases*, vol. 39, no. 2, pp. 144–150, 2015.

[45] M. Reinhard, T. Müller, B. Guschlbauer, J. Timmer, and A. Hetzel, "Dynamic cerebral autoregulation and collateral flow patterns in patients with severe carotid stenosis or occlusion", *Ultrasound in Medicine & Biology*, vol. 29, no. 8, pp. 1105–1113, 2003.

[46] S. P. Kramer, "On the function of the circle of willis", *The Journal of Experimental Medicine*, vol. 15, no. 4, p. 348, 1912.

[47] L. Rogers, "The function of the circulus arteriosus of willis", *Brain*, vol. 70, no. 2, pp. 171–178, 1947.

[48] N. Avman and E. A. Bering Jr, "A plastic model for the study of pressure changes in the circle of willis and major cerebral arteries following arterial occlusion", *Journal of Neurosurgery*, vol. 18, no. 3, pp. 361–365, 1961.

[49] V. A. Fasano, A. Portalupi, and G. Broggi, "Study of cerebral hemodynamics by analogic models", *Vascular Diseases*, vol. 3, no. 2, pp. 89–99, 1966.

[50] R. Fahrig, H. Nikolov, A. J. Fox, and D. W. Holdsworth, "A three-dimensional cerebrovascular flow phantom", *Medical Physics*, vol. 26, no. 8, pp. 1589–1599, 1999.

[51] K. D. Murray, "Dimensions of the circle of willis and dynamic studies using electrical analogy", *Journal of Neurosurgery*, vol. 21, no. 1, pp. 26–34, 1964.

[52] J. Duros and P. Nadvornik, "Mathematical model of cerebral circulation and its significance for current neurosurgery", *Zentralblatt fur Neurochirurgie*, vol. 39, no. 1, pp. 33–44, 1977.

[53] B. Hillen, H. W. Hoogstraten, and L. Post, "A mathematical model of the flow in the circle of Willis", *Journal of Biomechanics*, vol. 19, no. 3, pp. 187–194, 1986.

[54] B. Hillen, B. A. H. Drinkenburg, H. W. Hoogstraten, and L. Post, "Analysis of flow and vascular resistance in a model of the cricle of willis", *Journal of Biomechanics*, vol. 21, no. 10, pp. 807–814, 1988.

[55] M. Zagzoule and J.-P. Marc-Vergnes, "A global mathematical model of the cerebral circulation in man", *Journal of Biomechanics*, vol. 19, no. 12, pp. 1015–1022, 1986.

[56] C. L. de Lancea, T. David, J. Alastruey, and R. G. Brown, "Recruitment pattern in a complete cerebral arterial circle", *Journal of Biomechanical Engineering*, vol. 137, no. 11, p. 111 004, 2015.

[57] T. Köppl, M. Schneider, U. Pohl, and B. Wohlmuth, "The influence of an unilateral carotid artery stenosis on brain oxygenation", *Medical Engineering & Physics*, vol. 36, no. 7, pp. 905–914, 2014.

[58] J. Alastruey, K. H. Parker, J. Peiró, S. M. Byrd, and S. J. Sherwin, "Modelling the circle of Willis to assess the effects of anatomical variations and occlusions on cerebral flows", *Journal of Biomechanics*, vol. 40, no. 8, pp. 1794–1805, 2007.

[59] K. DeVault, P. A. Gremaud, V. Novak, M. S. Olufsen, G. Vernieres, and P. Zhao, "Blood flow in the circle of willis: Modeling and calibration", *Multiscale Modeling & Simulation*, vol. 7, no. 2, pp. 888–909, 2008.

[60] P. Perdikaris, L. Grinberg, and G. E. Karniadakis, "An effective fractal-tree closure model for simulating blood flow in large arterial networks", *Annals of Biomedical Engineering*, vol. 43, no. 6, pp. 1432–1442, 2015.

[61] S. K. Piechnik, M. Czosnyka, K. Cieślicki, and D. Cieśla, "Problems in application of purely linear models in cerebral circulation", *Journal of Biomechanics*, vol. 35, no. 4, pp. 553–554, 2002.

[62] A. Ferrandez, T. David, and M. D. Brown, "Numerical models of auto-regulation and blood flow in the cerebral circulation", *Computer Methods in Biomechanics & Biomedical Engineering*, vol. 5, no. 1, pp. 7–19, 2002.

[63] K. T. Moorhead, C. V. Doran, J. G. Chase, and T. David, "Lumped parameter and feedback control models of the auto-regulatory response in the circle of Willis", *Computer Methods in Biomechanics and Biomedical Engineering*, vol. 7, no. 3, pp. 121–130, 2004.

[64] C. A. Lodi and M. Ursino, "Hemodynamic effect of cerebral vasospasm in humans: A modeling study", *Annals of Biomedical Engineering*, vol. 27, no. 2, pp. 257–273, 1999.

[65] J. Alastruey, S. M. Moore, K. H. Parker, T. David, J. Peiró, and S. J. Sherwin, "Reduced modelling of blood flow in the cerebral circulation: Coupling 1-d, 0-d and cerebral auto-regulation models", *International Journal for Numerical Methods in Fluids*, vol. 56, no. 8, p. 1061, 2008.

[66] F. Liang, K. Fukasaku, H. Liu, and S. Takagi, "A computational model study of the influence of the anatomy of the circle of willis on cerebral hyperperfusion following carotid artery surgery", *Biomedical Engineering Online*, vol. 10, no. 1, p. 1, 2011.

[67] J. Ryu, X. Hu, and S. C. Shadden, "A coupled lumped-parameter and distributed network model for cerebral pulse-wave hemodynamics", *Journal of Biomechanical Engineering*, vol. 137, no. 10, p. 101 009, 2015.

[68] S. Moore and T. David, "A model of autoregulated blood flow in the cerebral vasculature", *Proceedings of the Institution of Mechanical Engineers, Part H: Journal of Engineering in Medicine*, vol. 222, no. 4, pp. 513–530, 2008.

[69] K. T. Moorhead, J. G. Chase, T. David, and J. Arnold, "Metabolic model of autoregulation in the circle of willis", *Journal of Biomechanical Engineering*, vol. 128, no. 3, pp. 462–466, 2006.

[70] J. R. Cebral, P. J. Yim, R. Löhner, O. Soto, and P. L. Choyke, "Blood flow modeling in carotid arteries with computational fluid dynamics and MR imaging", *Academic Radiology*, vol. 9, no. 11, pp. 1286–1299, 2002.

[71] S. M. Moore, K. T. Moorhead, J. G. Chase, T. David, and J. Fink, "One-dimensional and three-dimensional models of cerebrovascular flow", *Journal of Biomechanical Engineering*, vol. 127, no. 3, pp. 440–449, 2005.

[72] S. Moore, T. David, J. G. Chase, J. Arnold, and J. Fink, "3d models of blood flow in the cerebral vasculature", *Journal of Biomechanics*, vol. 39, no. 8, pp. 1454–1463, 2006.

[73] Q. Long, L. Luppi, C. S. König, V. Rinaldo, and S. K. Das, "Study of the collateral capacity of the circle of willis of patients with severe carotid artery stenosis by 3d computational modeling", *Journal of Biomechanics*, vol. 41, no. 12, pp. 2735–2742, 2008.

[74] F. Khodaee, B. Vahidi, and N. Fatouraee, "Analysis of mechanical parameters on the thromboembolism using a patient-specific computational model", *Biomechanics and Modeling in Mechanobiology*, vol. 15, no. 5, pp. 1295–1305, 2016.

[75] L. Grinberg, E. Cheever, T. Anor, J. R. Madsen, and G. E. Karniadakis, "Modeling blood flow circulation in intracranial arterial networks: A comparative 3D/1D simulation study", *Annals of Biomedical Engineering*, vol. 39, no. 1, pp. 297–309, 2011.

[76] S. N. Wright, P. Kochunov, F. Mut, M. Bergamino, K. M. Brown, J. C. Mazziotta, A. W. Toga, J. R. Cebral, and G. A. Ascoli, "Digital reconstruction and morphometric analysis of human brain arterial vasculature from magnetic resonance angiography", *Neuroimage*, vol. 82, pp. 170–181, 2013.

[77] F. Mut, S. Wright, G. A. Ascoli, and J. R. Cebral, "Morphometric, geographic, and territorial characterization of brain arterial trees", *International Journal for Numerical Methods in Biomedical Engineering*, vol. 30, no. 7, pp. 755–766, 2014.

[78] X. Liu, Z. Gao, H. Xiong, D. Ghista, L. Ren, H. Zhang, W. Wu, W. Huang, and W. K. Hau, "Three-dimensional hemodynamics analysis of the circle of willis in the patient-specific nonintegral arterial structures", *Biomechanics and Modeling in Mechanobiology*, vol. 15, no. 6, pp. 1439–1456, 2016.

[79] P. Reorowicz, D. Obidowski, P. Klosinski, W. Szubert, L. Stefanczyk, and K. Jozwik, "Numerical simulations of the blood flow in the patient-specific arterial cerebral circle region", *Journal of Biomechanics*, vol. 47, no. 7, pp. 1642–1651, 2014.

[80] G. Zhu, Q. Yuan, J. Yang, and J. H. Yeo, "The role of the circle of willis in internal carotid artery stenosis and anatomical variations: A computational study based on a patient-specific three-dimensional model", *Biomedical Engineering Online*, vol. 14, no. 1, p. 107, 2015.

[81] M. S. Alnæs, J. Isaksen, K.-A. Mardal, B. Romner, M. K. Morgan, and T. Ingebrigtsen, "Computation of hemodynamics in the circle of willis", *Stroke*, vol. 38, no. 9, pp. 2500–2505, 2007.

[82] A. R. Xavier, A. I. Qureshi, J. F. Kirmani, A. M. Yahia, and R. Bakshi, "Neuroimaging of stroke: a review.", *Southern Medical Journal*, vol. 96, no. 4, pp. 367–379, 2003.

[83] Q. Shen, J. Stuart, B. Venkatesh, J. Wallace, and J. Lipman, "Inter observer variability of the transcranial Doppler ultrasound technique: impact of lack of practice on the accuracy of measurement", *Journal of Clinical Monitoring and Computing*, vol. 15, no. 3-4, pp. 179–184, 1999.

[84] M. Correia, J. Provost, M. Tanter, and M. Pernot, "4d ultrafast ultrasound flow imaging: In vivo quantification of arterial volumetric flow rate in a single heartbeat", *Physics in Medicine and Biology*, vol. 61, no. 23, p. L48, 2016.

[85] R. Khan, K. Nael, and W. Erly, "Acute stroke imaging: what clinicians need to know", *The American Journal of Medicine*, vol. 126, no. 5, pp. 379–386, 2013.

[86] H. P. Adams, *Principles of Cerebrovascular Disease*. McGraw-Hill Education, 2007.

[87] P. J. van Laar, J. van der Grond, W. P. T. M. Mali, and J. Hendrikse, "Magnetic resonance evaluation of the cerebral circulation in obstructive arterial disease", *Cerebrovascular Diseases*, vol. 21, no. 5-6, pp. 297–306, 2006.

[88] D. E. Strandness and A. van Breda, *Vascular Diseases: Surgical and Interventional Therapy*, v. 1. Churchill Livingstone, 1994.

[89] R. Bammer, T. A. Hope, M. Aksoy, and M. T. Alley, "Time-resolved 3D quantitative flow MRI of the major intracranial vessels: Initial experience and comparative evaluation at 1.5 T and 3.0 T in combination with parallel imaging", *Magnetic Resonance in Medicine*, vol. 57, no. 1, pp. 127–140, 2007.

[90] M. J. P. van Osch, J. Hendrikse, X. Golay, C. J. G. Bakker, and J. van der Grond, "Non-invasive visualization of collateral blood flow patterns of the circle of Willis by dynamic MR angiography", *Medical Image Analysis*, vol. 10, no. 1, pp. 59–70, 2006.

[91] T. W. Okell, M. A. Chappell, and P. Jezzard, "A theoretical framework for quantifying blood volume flow rate from dynamic angiographic data and application to vessel-encoded arterial spin labeling MRI", *Medical Image Analysis*, vol. 17, no. 8, pp. 1025–1036, 2013.

[92] R. B. Buxton, *Introduction to Functional Magnetic Resonance Imaging: Principles and Techniques*. Cambridge University Press, 2009.

[93] F. Calamante, D. L. Thomas, G. S. Pell, J. Wiersma, and R. Turner, "Measuring cerebral blood flow using magnetic resonance imaging techniques", *Journal of Cerebral Blood Flow & Metabolism*, vol. 19, no. 7, pp. 701–735, 1999.

[94] E. C. Wong, "An introduction to ASL labeling techniques", *Journal of Magnetic Resonance Imaging*, vol. 40, no. 1, pp. 1–10, 2014.

[95] D. C. Alsop, J. A. Detre, X. Golay, M. Günther, J. Hendrikse, L. Hernandez-Garcia, H. Lu, B. J. MacIntosh, L. M. Parkes, M. Smits, *et al.*, "Recommended implementation of arterial spin-labeled perfusion mri for clinical applications: A consensus of the ISMRM perfusion study group and the european consortium for ASL in dementia", *Magnetic Resonance in Medicine*, vol. 73, no. 1, pp. 102–116, 2015.

[96] D. M. Garcia, C. de Bazelaire, and D. Alsop, "Pseudo-continuous flow driven adiabatic inversion for arterial spin labeling", in *Proceeding of the International Society for Magnetic Resonance in Medicine*, vol. 13, 2005, p. 37.

[97] W. Dai, D. Garcia, C. de Bazelaire, and D. C. Alsop, "Continuous flow-driven inversion for arterial spin labeling using pulsed radio frequency and gradient fields", *Magnetic Resonance in Medicine*, vol. 60, no. 6, pp. 1488–1497, 2008.

[98] E. C. Wong, R. B. Buxton, and L. R. Frank, "Quantitative imaging of perfusion using a single subtraction (QUIPSS and QUIPSS II)", *Magnetic Resonance in Medicine*, vol. 39, no. 5, pp. 702–708, 1998.

[99] X. Zhang, E. T. Petersen, E. Ghariq, J. B. Vis, A. G. Webb, W. M. Teeuwisse, J. Hendrikse, and M. J. P. Osch, "In vivo blood T1 measurements at 1.5 T, 3 T, and 7 T", *Magnetic Resonance in Medicine*, vol. 70, no. 4, pp. 1082–1086, 2013.

[100] R. R. Edelman, H. P. Mattle, G. V. O'reilly, K. U. Wentz, C. Liu, and B. Zhao, "Magnetic resonance imaging of flow dynamics in the circle of willis", *Stroke*, vol. 21, no. 1, pp. 56–65, 1990.

[101] J. D. Eastwood, C. A. Holder, P. A. Hudgins, and A. W. Song, "Magnetic resonance imaging with lateralized arterial spin labeling", *Magnetic Resonance Imaging*, vol. 20, no. 8, pp. 583–586, 2002.

[102] J. Hendrikse, J. van der Grond, H. Lu, P. C. M. Van Zijl, and X. Golay, "Flow territory mapping of the cerebral arteries with regional perfusion MRI", *Stroke*, vol. 35, no. 4, pp. 882–887, 2004.

[103] X. Golay, E. T. Petersen, and F. Hui, "Pulsed star labeling of arterial regions (PULSAR): A robust regional perfusion technique for high field imaging", *Magnetic Resonance in Medicine*, vol. 53, no. 1, pp. 15–21, 2005.

[104] F. F. Paiva, A. Tannús, S. L. Talagala, and A. C. Silva, "Arterial spin labeling of cerebral perfusion territories using a separate labeling coil", *Journal of Magnetic Resonance Imaging*, vol. 27, no. 5, pp. 970–977, 2008.

[105] J. A. Detre, W. Zhang, D. A. Roberts, A. C. Silva, D. S. Williams, D. J. Grandis, A. P. Koretsky, and J. S. Leigh, "Tissue specific perfusion imaging using arterial spin labeling", *NMR in Biomedicine*, vol. 7, no. 1-2, pp. 75–82, 1994.

[106] G. Zaharchuk, P. J. Ledden, K. K. Kwong, T. G. Reese, B. R. Rosen, and L. L. Wald, "Multislice perfusion and perfusion territory imaging in humans with separate label and image coils", *Magnetic Resonance in Medicine*, vol. 41, no. 6, pp. 1093–1098, 1999.

[107] R. Trampel, T. Mildner, U. Goerke, A. Schaefer, W. Driesel, and D. G. Norris, "Continuous arterial spin labeling using a local magnetic field gradient coil", *Magnetic Resonance in Medicine*, vol. 48, no. 3, pp. 543–546, 2002.

[108] R. Werner, K. Alfke, T. Schaeffter, A. Nabavi, H. M. Mehdorn, and O. Jansen, "Brain perfusion territory imaging applying oblique-plane arterial spin labeling with a standard send/receive head coil", *Magnetic Resonance in Medicine*, vol. 52, no. 6, pp. 1443–1447, 2004.

[109] R. Werner, D. G. Norris, K. Alfke, H. M. Mehdorn, and O. Jansen, "Continuous artery-selective spin labeling (CASSL)", *Magnetic Resonance in Medicine*, vol. 53, no. 5, pp. 1006–1012, 2005.

[110] M. Helle, S. Rüfer, K. Alfke, O. Jansen, and D. G. Norris, "Perfusion territory imaging of intracranial branching arteries–optimization of continuous artery-selective spin labeling (CASSL)", *NMR in Biomedicine*, vol. 24, no. 4, pp. 404–412, 2011.

[111] W. Dai, P. M. Robson, A. Shankaranarayanan, and D. C. Alsop, "Modified pulsed continuous arterial spin labeling for labeling of a single artery", *Magnetic Resonance in Medicine*, vol. 64, no. 4, pp. 975–982, 2010.

[112] M. Helle, D. G. Norris, S. Rüfer, K. Alfke, O. Jansen, and M. J. P. van Osch, "Superselective pseudocontinuous arterial spin labeling", *Magnetic Resonance in Medicine*, vol. 64, no. 3, pp. 777–786, 2010.

[113] E. C. Wong, "Vessel-encoded arterial spin-labeling using pseudocontinuous tagging", *Magnetic Resonance in Medicine*, vol. 58, no. 6, pp. 1086–1091, 2007.

[114] I. Zimine, E. T. Petersen, and X. Golay, "Dual vessel arterial spin labeling scheme for regional perfusion imaging", *Magnetic Resonance in Medicine*, vol. 56, no. 5, pp. 1140–1144, 2006.

[115] M. Helle, S. Rüfer, M. J. P. van Osch, O. Jansen, and D. G. Norris, "Selective multivessel labeling approach for perfusion territory imaging in pseudo-continuous arterial spin labeling", *Magnetic Resonance in Medicine*, vol. 68, no. 1, pp. 214–219, 2012.

[116] E. C. Wong and A. P. Kansagra, "Mapping middle cerebral artery branch territories with vessel encoded pseudo-continuous ASL: Sine/cosine tag modulation and data clustering in tagging efficiency space", in *Proceedings of the 16th Annual Meeting ISMRM Toronto, Canada*, vol. 182, 2008.

[117] S. Gevers, R. P. Bokkers, J. Hendrikse, C. B. Majoie, D. A. Kies, W. M. Teeuwisse, A. J. Nederveen, and M. J. van Osch, "Robustness and reproducibility of flow territories defined by planning-free vessel-encoded pseudocontinuous arterial spin-labeling", *American Journal of Neuroradiology*, vol. 33, no. 2, E21–E25, 2012.

[118] M. Günther, "Efficient visualization of vascular territories in the human brain by cycled arterial spin labeling MRI", *Magnetic Resonance in Medicine*, vol. 56, no. 3, pp. 671–675, 2006.

[119] P. M. Robson, W. Dai, A. Shankaranarayanan, N. M. Rofsky, and D. C. Alsop, "Time-resolved vessel-selective digital subtraction MR angiography of the cerebral vasculature with arterial spin labeling.", *Radiology*, vol. 257, no. 2, pp. 507–15, Nov. 2010.

[120] T. Lindner, N. Larsen, O. Jansen, and M. Helle, "Accelerated visualization of selected intracranial arteries by cycled super-selective arterial spin labeling", *Magnetic Resonance Materials in Physics, Biology and Medicine*, vol. 29, no. 6, pp. 843–852, 2016.

[121] M. A. Chappell, T. W. Okell, P. Jezzard, and M. W. Woolrich, "Vascular territory image analysis using vessel encoded arterial spin labeling", in *Medical Image Computing and Computer-Assisted Intervention–MICCAI 2009*, Springer, 2009, pp. 514–521.

[122] R. B. Buxton, L. R. Frank, E. C. Wong, B. Siewert, S. Warach, and R. R. Edelman, "A general kinetic model for quantitative perfusion imaging with arterial spin labeling", *Magnetic Resonance in Medicine*, vol. 40, no. 3, pp. 383–396, 1998.

[123] J. Hrabe and D. P. Lewis, "Two analytical solutions for a model of pulsed arterial spin labeling with randomized blood arrival times", *Journal of Magnetic Resonance*, vol. 167, no. 1, pp. 49–55, 2004.

[124] D. Gallichan and P. Jezzard, "Modeling the effects of dispersion and pulsatility of blood flow in pulsed arterial spin labeling", *Magnetic Resonance in Medicine*, vol. 60, no. 1, pp. 53–63, 2008.

[125] S. M. Kazan, M. A. Chappell, and S. J. Payne, "Modeling the effects of flow dispersion in arterial spin labeling", *IEEE Transactions on Biomedical Engineering*, vol. 56, no. 6, pp. 1635–1643, 2009.

[126] T. W. Okell, M. A. Chappell, U. G. Schulz, and P. Jezzard, "A kinetic model for vessel-encoded dynamic angiography with arterial spin labeling", *Magnetic Resonance in Medicine*, vol. 68, no. 3, pp. 969–979, 2012.

[127] M. A. Chappell, M. W. Woolrich, S. Kazan, P. Jezzard, S. J. Payne, and B. J. MacIntosh, "Modeling dispersion in arterial spin labeling: validation using dynamic angiographic measurements", *Magnetic Resonance in Medicine*, vol. 69, no. 2, pp. 563–570, 2013.

[128] M. Günther, M. Bock, and L. R. Schad, "Arterial spin labeling in combination with a look-locker sampling strategy: Inflow turbo-sampling EPI-FAIR (ITS-FAIR)", *Magnetic Resonance in Medicine*, vol. 46, no. 5, pp. 974–984, 2001.

[129] J. R. Romero, A. Pikula, T. N. Nguyen, Y. L. Nien, A. Norbash, and V. L. Babikian, "Cerebral collateral circulation in carotid artery disease", *Current Cardiology Reviews*, vol. 5, no. 4, pp. 279–288, 2009.

[130] S. J. Payne, "A model of the interaction between autoregulation and neural activation in the brain.", *Mathematical Biosciences*, vol. 204, no. 2, pp. 260–81, Dec. 2006.

[131] N. Stergiopulos, D. F. Young, and T. R. Rogge, "Computer simulation of arterial flow with applications to arterial and aortic stenoses", *Journal of Biomechanics*, vol. 25, no. 12, pp. 1477–1488, 1992.

[132] H. Lippert and R. Pabst, *Arterial Variations in Man: Classification and Frequency*. J. F. Bergmann Verlag, 1985.

[133] P. M. Rothwell, M. Eliasziw, S. A. Gutnikov, A. J. Fox, D. W. Taylor, M. R. Mayberg, C. P. Warlow, H. J. M. Barnett, C. E. T. Collaboration, *et al.*, "Analysis of pooled data from the randomised controlled trials of endarterectomy for symptomatic carotid stenosis", *The Lancet*, vol. 361, no. 9352, pp. 107–116, 2003.

[134] G. J. Adams, D. M. Simoni, C. B. Bordelon, G. W. Vick, K. T. Kimball, W. Insull, and J. D. Morrisett, "Bilateral symmetry of human carotid artery atherosclerosis", *Stroke*, vol. 33, no. 11, pp. 2575–2580, 2002.

[135] S. J. Payne, *Cerebral Blood Flow and Metabolism: A Quantitative Approach*. World Scientific Publishing, 2018.

[136] Y.-C. Fung, *Biomechanics: Circulation*. Springer, 1997.

[137] M. A. Chappell, T. W. Okell, S. J. Payne, P. Jezzard, and M. W. Woolrich, "A fast analysis method for non-invasive imaging of blood flow in individual cerebral arteries using vessel-encoded arterial spin labelling angiography", *Medical Image Analysis*, vol. 16, no. 4, pp. 831–839, 2012.

[138] K. Morton and D. Mayers, *Numerical Solution of Partial Differential Equations: An Introduction*. Cambridge University Press, 2005.

[139] T. Lindner, U. Jensen-Kondering, M. J. P. van Osch, O. Jansen, and M. Helle, "3D time-resolved vessel-selective angiography based on pseudo-continuous arterial spin labeling", *Magnetic Resonance Imaging*, vol. 33, no. 6, pp. 840–846, 2015.

[140] H. Wu, W. F. Block, P. A. Turski, C. A. Mistretta, D. J. Rusinak, Y. Wu, and K. M. Johnson, "Noncontrast dynamic 3D intracranial MR angiography using pseudo-continuous arterial spin labeling (PCASL) and accelerated 3D radial acquisition", *Journal of Magnetic Resonance Imaging*, vol. 39, no. 5, pp. 1320–1326, 2014.

[141] T. W. Okell, P. Schmitt, X. Bi, M. A. Chappell, R. H. N. Tijssen, F. Sheerin, K. L. Miller, and P. Jezzard, "Optimization of 4D vessel-selective arterial spin labeling angiography using balanced steady-state free precession and vessel-encoding", *NMR in Biomedicine*, vol. 29, no. 6, pp. 776–786, 2016.